SALTWATER INTRUSION IN COASTAL AQUIFERS

A Thesis
Presented to
The Academic Faculty

By

Chan-Hee Park

In Partial Fulfillment
of the Requirements for the Degree
Doctor of Philosophy in
Civil and Environmental Engineering

Georgia Institute of Technology

September 2004

SALTWATER INTRUSION IN COASTAL AQUIFERS

Approved by:

Dr. Mustafa M. Aral (Advisor)

Dr. Armistead G. Russell

Dr. Philip J. W. Roberts

Dr. Paul A. Work

Dr. Turgay Uzer

Date Approved: Nov., 15, 2004

DEDICATION

To my mother, my wife, and my children,

Without their endless support, this could not have been possible.

ACKNOWLEDGMENTS

I would like to say that my sincere gratitude and appreciation should go to my advisor, Dr. Mustafa M. Aral for his invaluable guidance, continuous support, and high standard that have led me throughout the whole period of my Ph.D. Without these, this thesis could never been completed.

I would also like to thank my committee members: Dr. Armistead G. Russell, Dr. Philip J. W. Roberts, Dr. Paul A. Work, and Dr. Turgay Uzer for their constructive comments, suggestions, and salient advice to help complete this thesis.

I would like to gratefully acknowledge the members of Multimedia Environmental Simulations Laboratory (MESL) for their comments and critiques. I would like to especially acknowledge Wonyong Jang for his detailed and thoughtful comments on numerous occasions to lead this thesis to crucial improvement. My further acknowledgments cheerfully go to the members of Georgia Tech CEE Korean Student Association.

Finally, my sincere warmhearted gratitude goes to my wife, Eun-Joo Kim, my daughter, Jennifer Park, my son, Justin Park, and my mother, Bo-Gyeong Kim for their endless love, understanding, and patience not only to complete this thesis but also to take a journey of my life this far and to the rest of my life.

TABLE OF CONTENTS

DEDICATION iii
ACKNOWLEDGMENTS iv
TABLE OF CONTENTS v
LIST OF FIGURES x
LIST OF TABLES xvii
LIST OF SYMBOLS xix
SUMMARY xxviii

CHAPTER 1 INTRODUCTION 1
1.1 Optimization of Pumping Rates and Well Placement in Coastal Aquifers 1
1.2 Variable Density Flow in a Variably Saturated Porous Medium 4
1.3 Statement of the Problems 6
1.4 Motivation and Objective 8
1.5 Organization of the Thesis 9

CHAPTER 2 LITERATURE REVIEW 11
2.1 Optimization of Pumping Rates and Well Placement in Coastal Aquifers 11
2.2 Variable Density Flow in a Variably Saturated Porous Medium 15
2.2.1 The Henry Problem (Saltwater intrusion) 15
2.2.2 The Elder Problem 16
2.2.3 The Salt Dome Problem (HYDROCOIN Level 1 Case 5) 18
2.2.4 Hydrodynamics in Beaches under the Influence of Tidal Effects 20
2.2.5 Saltwater Upconing 22

CHAPTER 3 MULTI-OBJECTIVE OPTIMIZATION OF PUMPING RATES AND WELL LOCATIONS IN COASTAL AQUIFERS 26
3.1 Introduction 26

3.2 Governing Equations for the Sharp Interface Model 27

3.3 Formulation of Saltwater Intrusion Problem 35

3.4 The Modified Optimization Model 37

3.5 Genetic Algorithm 40

3.6 Convergence 43

3.7 Applications 43

3.8 Discussions 59

3.9 Conclusions 61

CHAPTER 4 VARIABLE DENSITY FLOW IN A VARIABLY SATURATED POROUS MEDIUM 62

4.1 Governing Equations 62

4.1.1 Equation of the Bulk Fluid Density 63

4.1.2 Continuity Equation of Flow 64

4.1.3 Momentum Equation of Flow (the Darcy Equation) and Dispersive Flux 65

4.1.4 Contaminant Transport Equation 65

4.2 The Henry Problem 69

4.3 The Elder Problem 74

4.4 The Salt Dome Problem (HYDROCOIN Level 1 Case 5) 79

4.5 Discussions 83

4.6 Conclusions 87

CHAPTER 5 SENSITIVITY OF THE SOLUTION OF ELDER PROBLEM TO DENSITY, VELOCITY AND OTHER NUMERICAL PERTURBATIONS 89

5.1 Introduction 89

5.2 Sensitivity of the Elder Problem to Density Difference 93

5.3 Sensitivity of the Elder Problem Solution to Numerical Perturbations 99

5.4 Discussions 110

5.5 Concluding Remarks..... 112

CHAPTER 6 SALTWATER INTRUSION HYDRODYNAMICS IN A BEACH 114

6.1 Introduction..... 114

6.2 Verification of Flow in a Variably Saturated Porous Medium 116

6.2.1 Celia et al.'s Problem 117

6.2.2 Forsyth et al.'s Problem 121

6.3 Description of Saltwater Intrusion Problem at a Beach under Tidal Effects..... 124

6.3.1 Boundary Conditions 130

6.4 Results..... 138

6.5 Discussions 148

6.5.1 Comparison with Boufadel's Result 148

6.5.2 Effects of Using Two Different Grids 149

6.5.3 Effects of the Different Types of Boundary Conditions in Solute-transport Model..... 151

6.5.4 Sensitivity Analysis of Density Difference Associated with the Different Types of Boundary Conditions in Solute-transport model 153

6.5.5 Submarine Groundwater Discharge (SGD) along the Intertidal Zone and Saltwater Wedge..... 156

6.6 Conclusions..... 158

CHAPTER 7 SALTWATER UPCONING BENEATH PUMPING WELLS 161

7.1 Introduction..... 162

7.2 Reilly and Goodman [1987] – Saltwater Upconing Problem 163

7.3 The Saltpool Problem by Oswald and Kinzelbach [2004] 173

7.4 Discussions 184

7.5 Conclusions 188

CHAPTER 8 SALTWATER UPCONING DUE TO PUMPING UNDER TIDAL EFFECTS 189

8.1 Introduction 189

8.2 The Application of Saltwater Intrusion/Upconing Due to Pumping under Tidal Effects 192

8.2.1 Preparation of the Application 193

8.2.2 Saltwater Intrusion Due to Pumping with no Tidal Effects 197

8.2.3 Saltwater Intrusion Due to Pumping under Tidal Effects 204

8.2.4 Saltwater Upconing Due to Pumping under Tidal Effects for a Partially Penetrating Well 208

8.3 Dimensional Analysis and Scaling up 211

8.4 Discussions and Concluding Remarks 217

CHAPTER 9 CONCLUSIONS AND FURTHER RESEARCH CONSIDERATION 219

9.1 Conclusions 219

9.2 Further Research Consideration 221

APPENDIX A MULTI-OBJECTIVE OPTIMIZATION OF PUMPING RATES AND WELL LOCATIONS IN COASTAL AQUIFERS 222

A.1 An Example Problem of the Laplace Equation using Single Potential Theory with Appropriate Boundary Conditions 222

A.2 Derivatives of Equation 3.18 and 3.19 223

APPENDIX B VARIABLE DENSITY FLOW IN A VARIABLY SATURATED POROUS MEDIUM 226

B.1 Derivation of the Flow Equation for Variable Density Flow in a Variably Saturated Porous Medium 226

APPENDIX C THE GALERKIN FINITE ELEMENT FORMULATION OF VARIABLE DENSITY FLOW IN A VARIABLY SATURATED POROUS MEDIUM 230

C.1 The Flow Equation 230

C.2 The Darcy Equation (Momentum Equation) 233

C.3 Contaminant Transport Equation 235

C.4 Analytical integration 238

C.5 Time Marching Schemes 241

C.6 The Free Exit Boundary Condition (Type IV) 244

REFERENCES 246

VITA 259

LIST OF FIGURES

Figure 1.1 Schematic of pumping well near coastal area: Plan view and cross-section of a coastal aquifer assumed to have sharp a sharp interface..... 3

Figure 3.1 Cross-sections of coastal aquifers: a confined aquifer and an unconfined aquifer..... 29

Figure 3.2 Pumping wells near a coastline : (a) One pumping well un-intruded case; (b) One pumping well intruded case; (c) Two pumping well un-intruded case; (d) Two pumping well intruded case; (e) Symmetric two pumping well intruded case; (f) Asymmetric two pumping well intruded case..... 34

Figure 3.3 (a) The concept of eliminating unnecessary runs using perturbation method by choosing one path rather than searching the whole solution domain; (b) Coding and crossover of design variables..... 39

Figure 3.4 (a) One pumping well placement optimization path; (b) Two pumping well placement optimization path..... 46

Figure 3.5 (a) Three pumping well placement optimization path; (b) Four pumping well placement optimization path; (c) Five pumping well placement optimization path; (d) Four pumping well placement optimization path (an intermediate solution – similar toe pattern to that given in (a))..... 48

Figure 3.6 The relationship between the number of wells and the maximum pumping rates and the average pumping rate per well..... 50

Figure 3.7 Comparison of results between Cheng et al. [2000] and MOGA application; (a) Cheng et al. Case 1 results; (b) MOGA Case 1 results; (c) Cheng et al. Case 3 results; (d) MOGA Case 3 results. (e) MOGA results obtained after abandoning one well given in Case 3..... 54

Figure 3.8 (a) The pumping rate maximization objective for two pumping well case; (b) Placement of the well as close as possible to the shoreline objective for two pumping well case; (c) Use of multi-objective criteria for two well case..... 57

Figure 4.1 Boundary conditions of the Henry problem 70

Figure 4.2 Isochlor contours of steady state concentrations for the Henry problem: SUTRA [1987] (black solid line), the Ghyben-Herzberg interface (black dotted line), and TechFlow (red dotted line)..... 72

Figure 4.3 Isochlor contours of steady state results for the Henry problem: (a) TOUGH2 [1995] (solid line), TechFlow (red dotted line); (b) FEFLOW [1998] (solid line), TechFlow (red dotted line); (c) ROCKFLOW [1998] (solid line), TechFlow (red dotted line)..... 73

Figure 4.4 Boundary conditions of the Elder problem 75

Figure 4.5 Results for t = 1, 2, 2.5, 3, 4, 5, 6, 7, 10, 12, 15 and 20 yr at grid level 7 from Frolkovič and Schepper [2001] 77

Figure 4.6 Results of the Elder problem for 1, 2, 2.5, 3, 4, 5, 6, 7, 10, 12, 15 and 20 year at regular grid of level 7 from TechFlow 78

Figure 4.7 Boundary conditions and the problem domain for the salt dome problem..... 80

Figure 4.8 Results for the salt dome problem: steady-state solutions (a) NAMMU by Herbert et al. [1988] – recirculating flow pattern; (b) TOUGH2 by Oldenburg and Pruess [1995] – swept-forward flow pattern; (c) FEFLOW by Kolditz et al. [1998] – recirculating flow pattern; (d) TechFlow in this study – recirculating flow pattern..... 85

Figure 5.1 Stationary results obtained from various density differences on two different grids. 97

Figure 5.2 Comparison for 20 years between regular and irregular grid with density of the medium mesh (i.e. 2200 elements)..... 101

Figure 5.3 Various grids: (a) the medium regular grid, (b) half of the horizontal layer of the grid zigzagged in the top area, (c) One vertical column of

the grid three elements away from the center zigzagged, (d) two zigzagged in the top center area 103

Figure 5.4 Results for year 1, 2, 3, 4, and 30 at the medium level grid with various combinations of regular and irregular elements: (a) the medium regular grid, (b) half of the horizontal layer of the grid zigzagged in the top area, (c) One vertical column of the grid three elements away from the center zigzagged, (d) two zigzagged in the top center area..... 104

Figure 5.5 (a) TechFlow results of the Elder problem for 1, 2, 2.5, 3, 4, 5, 6, 7, 10, 12, 15 and 20 year at regular grid of level 6, (b) Results for 4, 7, and 20 year at grid Level 6 from Frolkovič and Schepper [2001] 106

Figure 5.6 TechFlow results of the Elder problem for year 4, 10, 15, and 20 at regular grid of level 4 (a) with continuous velocity method, (b) with discontinuous velocity method 109

Figure 6.1 The description of Celia et al.'s [1990] problem with initial and boundary conditions. Note ψ is a pressure head..... 118

Figure 6.2 Comparison of the result of TechFlow (red solid line) with the results by Rathfelder and Abriola [1994] at time 6 hrs..... 120

Figure 6.3 The description of Forsyth et al.'s [1995] problem with initial and boundary conditions 121

Figure 6.4 Comparison of the result of TechFlow (red solid line) with the results by Forsyth et al.[1995] at times 1.16 d, 4.16 d, and 7.16 d. 123

Figure 6.5 Schematic of the beach and flow boundary condition. Red line is the intertidal zone 125

Figure 6.6 Tidal effect (pressure head) represented by a linear relation with a period of 1320 seconds..... 126

Figure 6.7 Two grids; (a) Grid 1: 1942 combinational regular and irregular elements, (b) Grid 2: 2413 irregular elements..... 129

Figure 6.8 Trilinear brick elements on exit boundary..... 136

Figure 6.9 Concentration profiles at 80, 160, 240, 320, 400, and 480 time units, free exit boundary condition: (a) Pe=0.25, (b) Pe=0.5, (c) Pe=1.0, (d) Pe=2.0, (e) Pe=4.0, and (f) Pe=8.0..... 137

Figure 6.10 Concentration and Darcy flux distribution at four different times. The dashed lines represent the beach water table and the sea water level [Boufadel 2000]..... 140

Figure 6.11 Concentration and Darcy flux distribution at six different times from Grid 1. The red dashed lines represent the beach water table for Case 1 of boundary conditions..... 142

Figure 6.12 Concentration and Darcy flux distribution at six different times from Grid 2. The red dashed lines represent the beach water table for Case 1 of boundary conditions..... 143

Figure 6.13 Concentration and Darcy flux distribution at six different times from Grid 2. The red dashed lines represent the beach water table for Case 2 of boundary conditions..... 144

Figure 6.14 Concentration and Darcy flux distribution at six different times from Grid 2. The red dashed lines represent the beach water table for Case 3 of boundary conditions..... 145

Figure 6.15 Concentration and Darcy flux distribution at 3.0 % density difference. The red dashed lines represent the beach water table for (a) Case 1, (b) Case 2, and (C) Case 3 boundary conditions..... 147

Figure 6.16 Concentration and Darcy flux distribution for Case 3 boundary conditions at 3.0 % density difference. The red dashed lines represent the beach water table. 154

Figure 6.17 Concentration and Darcy flux distribution at the highest tide after three cycles for the 2.4 % density differences obtained with Type A boundary conditions. The red dashed line represents the water table..... 158

Figure 7.1 A schematic of saltwater upconing beneath a pumping well 165

Figure 7.2 Diagram of physical systems simulated in variable-density solute-transport system approach. 167

Figure 7.3 Two different grids of densities in Cartesian coordinate system used for TechFlow 171

Figure 7.4 Comparison of the results by TechFlow (red solid line) with the results from Reilly and Goodman [1987] (black solid line) and the results from the sharp interface model (black dotted line). 172

Figure 7.5 A schematic of the experiment [Oswald and Kinzelbach 2004] 174

Figure 7.6 Caparison of measured and simulated breakthrough curves for Cases 1 and 2. (a) Oswald and Kinzelbach [2004], (b) Johannsen et al. [2002] 178

Figure 7.7 Caparison of measured and simulated breakthrough curves for (a) Case 1 and (b) Case 2 from Kolditz et al. [1998]..... 179

Figure 7.8 Caparison of measured and simulated breakthrough curves for (a) Case 1 and (b) Case 2 from TechFlow..... 182

Figure 7.9 Caparison of measured and simulated concentration distributions in diagonal vertical cross-section for Cases 1 and 2: (a) Case 1 from Oswald and Kinzelbach [2004], (b) Case 1 from TechFlow, (c) Case 2 from Oswald and Kinzelbach [2004], and (d) Case 2 from TechFlow 183

Figure 7.10 Reference solutions obtained from Johannsen et al. [2002] (a) the breakthrough curve for both cases, concentration distribution in diagonal cross-section for (b) Case 1 and (c) Case 2 185

Figure 8.1 Problem description for three-dimensional saltwater intrusion in a phreatic aquifer subject to well pumping under tidal effects. 194

Figure 8.2 Idealization of the problem for three-dimensional saltwater intrusion in a phreatic aquifer subject to well pumping under tidal effects. Purpled surface indicates the intertidal zone. 195

Figure 8.3 Water tables delineated from the one-dimensional analytical solution and from TechFlow. Blue dotted line is obtained from the cross-section of the result at the center of the three-dimensional problem domain. 197

Figure 8.4 Cross-sectional concentration and Darcy flux distribution used as initial conditions for the simulation of saltwater intrusion or upconing (a) seawater level set at the mid point of tide used in the case of no tidal effects; (b) the lowest tide under tidal effects used in the case of tidal effects. Solid line in (a) is the analytical solution of the sharp interface between fresh water and saltwater..... 198

Figure 8.5 Cross-sectional concentration and Darcy flux distribution of transient solutions for no tidal effect..... 200

Figure 8.6 (a) Comparison of the result of TechFlow with that from analytical solution (b) 0.5 isochlor line at the bottom of the aquifer: a blue solid line and Darcy flux are taken at time = 3330 seconds while a blue dotted line is taken with no pumping rate. 202

Figure 8.7 Cross-sectional concentration and Darcy flux distribution of transient solutions under tidal effects..... 205

Figure 8.8 0.5 isochlor line at the bottom of the aquifer: a blue solid line and Darcy flux are taken at time = 4,650 seconds while a blue dotted line is taken from the steady-state solution of the lowest tide under tidal effects with no pumping rate..... 206

Figure 8.9 Saltwater Intrusion due to pumping under tidal effects..... 207

Figure 8.10 Cross-sectional concentration and Darcy flux distribution of transient solutions under tidal effects..... 209

Figure 8.11 0.5 isochlor line at the bottom of the aquifer: a red solid line and Darcy flux are taken at time = 5,970 seconds while a black dotted line

is taken from the steady-state solution of the lowest tide under tidal effects with no pumping rate 210

Figure 8.12 Saltwater Upconing after lateral saltwater encroachment due to pumping under tidal effects 214

Figure A.1 Tracking saltwater toe in a one-dimensional problem 223

Figure C. 1 Diagram of two parallel coordinates 240

Figure C. 2 Diagram for time schemes 242

LIST OF TABLES

Table 3.1 Summary of modeling parameters for one and two pumping well cases 44

Table 3.2 Summary of modeling parameters for three-, four- and five pumping well cases..... 49

Table 3.3 Summary of modeling parameters and the comparison of results with Cheng et al. [2000] fixed well optimization example 52

Table 3.5 Summary of modeling parameters and the results of pumping well placement - Case 3 of Cheng et al. [2000] 56

Table 3.6 Summary of modeling parameters and the results of MOGA simulation 58

Table 4.1 Parameters for the Henry problem..... 71

Table 4.2 Parameters for the Elder problem 76

Table 4.3 Parameters for the salt dome problem 84

Table 5.1 Simulation schemes for physical instability on regular grids..... 95

Table 6.1 Physical parameters for Celia et al.'s problem 119

Table 6.2 Physical parameters for Forsyth et al.'s problem 122

Table 6.3 Modeling parameters associated with porous medium and fluid 127

Table 6.4 Various boundary conditions for transport equation 132

Table 6.5 Discharge contribution along the intertidal zone and the saltwater wedge zone and the local circulation rate under the intertidal zone for six pseudo-steady state solutions..... 157

Table 6.6 Seawater recharge contribution along the intertidal zone and the saltwater wedge zone and the local circulation rate under the intertidal zone for six pseudo-steady state solutions 159

Table 7.1 Physical parameters for Comparison 1 from Reilly and Goodman [1987] 168

Table 7.2 Grid parameters for two compatible grids with the ones from Reilly and Goodman [1987]..... 170

Table 7.3 Parameters of the saltpool experiment..... 177

Table 7.4 The hierarchy of grids..... 181

Table 8.1 Modeling parameters associated with porous medium and fluid 195

Table 8.2 Dimensionless groups and physical meanings..... 213

Table 8.3 Scale-up of the application parameters..... 216

LIST OF SYMBOLS

a	half length of element in the ξ direction, $[L]$
A	tidal amplitude, $[L]$
b	half length of element in the η direction, $[L]$
b	thickness of fresh water for unconfined aquifers, $[L]$
B	thickness of fresh water for confined aquifers, $[L]$
c	half length of element in the ζ direction, $[L]$
c_1	any large constant in slack variable, $[-]$
C	relative concentration, $[ML^{-3}]$
C_0	initial concentration, $[ML^{-3}]$
$\hat{C}$	approximate solution of concentration, $[ML^{-3}]$
$\hat{C}_j$	approximate solution of concentration, $[ML^{-3}]$
ΔC	maximum difference of mass concentration, $[ML^{-3}]$
d	sea level measured from the base of the aquifer, $[L]$
D	dispersion coefficient, $[LT^{-2}]$
$\widehat{D}$	dispersion tensor, $[LT^{-2}]$
D_m	coefficient of molecular diffusion, $[LT^{-2}]$
D_{ij}	dispersion coefficient on the ij plane, $[LT^{-2}]$
D_n^*	dispersion tensor, $[LT^{-2}]$
$\vec{e}$	unit vector in the gravitational direction, $[L]$

f_i	objective function at the i th iteration
$\{F\}$	vector of flux
g	coefficient of gravitational acceleration, $[LT^{-2}]$
h	hydraulic head, $[L]$
h_0	the reference hydraulic head, $[L]$
h_f	piezometric head in fresh water, $[L]$
$\hat{h}$	approximate solution of hydraulic head, $[L]$
Δh	maximum difference of hydraulic head, $[L]$
H	height of the aquifer, $[L]$
I	recharge rate, $[ML^{-2}T^{-1}]$
J	matrix of the Jacobian
k	index of iteration
k	permeability, $[L^2]$
k_1	positive integer for subdomain perturbation of pumping rate
k_2	positive integer for x coordinate subdomain perturbation
k_3	positive integer for y coordinate subdomain perturbation
k_i	intrinsic permeability in the i direction, $[L^2]$
$\hat{k}$	tensor of permeability of a porous medium, $[LT^{-1}]$
K	hydraulic conductivity, $[LT^{-1}]$
K_{i0}	saturated hydraulic conductivity in the i direction, $[LT^{-1}]$
K_{ij}	saturated hydraulic conductivity in the ij plane, $[LT^{-1}]$

$\hat{K}$	tensor of freshwater hydraulic conductivity, $[LT^{-1}]$
$\hat{K}_0$	tensor of the saturated hydraulic conductivity, $[LT^{-1}]$
m	parameter of the van Genuchten model, $[-]$
$[M_{Advection}]$	matrix of advection
$[M_{\text{conductance}}]$	matrix of conductance
$[M_{Diffusion}]$	matrix of diffusion
$[M_{mass}]$	matrix of mass
n	parameter of the van Genuchten model, $[-]$
n	normal unit vector, $[L]$
n_i	normal unit vector in the i direction, $[L]$
$\vec{n}$	normal unit vector, $[L]$
p	pressure head, $[L]$
Δp	pressure difference, $[MLT^{-2}]$
Pe	a grid Peclet number, $[-]$
q	fresh water volume outflow rate per unit length of coastline, $[L^2T^{-1}]$
$\vec{q}$	the Darcy velocity vector, $[LT^{-1}]$
q_0	fresh water recharge, $[LT^{-1}]$
q_i	Darcy flux in the i direction, $[LT^{-1}]$
Q	pumping rate vector, $[L^3T^{-1}]$
Q_i	pumping rate of well i, $[L^3T^{-1}]$

Q_C source term of the solute in terms of mass concentration, $\left[ML^{-3}T^{-1}\right]$

Q_ρ source term of the solute in transport equation, $\left[L^3T^{-1}\right]$

$Q_{Critical}$ critical pumping rate, $\left[L^3T^{-1}\right]$

Q_{Tin} total inland recharge rate, $\left[L^3T^{-1}\right]$

Q^0 initial pumping rate vector, $\left[L^3T^{-1}\right]$

Q_i^0 initial pumping rate for well i, $\left[L^3T^{-1}\right]$

$Q_i^{\max}$ maximum pumping rate for well i, $\left[L^3T^{-1}\right]$

$Q_i^{\min}$ minimum pumping rate for well i, $\left[L^3T^{-1}\right]$

ΔQ_i perturbation of pumping rate for well i, $\left[L^3T^{-1}\right]$

ΔQ_{upper} upper bound of perturbation vector of pumping rate, $\left[L^3T^{-1}\right]$

ΔQ_{lower} lower bound of perturbation vector of pumping rate, $\left[L^3T^{-1}\right]$

$\Delta Q_i^{\max}$ maximum perturbation of pumping rate for well i, $\left[L^3T^{-1}\right]$

$\Delta Q_i^{\min}$ minimum perturbation of pumping rate for well i, $\left[L^3T^{-1}\right]$

ΔQ_i^{upper} upper bound of perturbation of pumping rate for well i, $\left[L^3T^{-1}\right]$

ΔQ_i^{lower} lower bound of perturbation of pumping rate for well i, $\left[L^3T^{-1}\right]$

δQ_i subdomain perturbation of pumping rate for well i, $\left[L^3T^{-1}\right]$

r_w radius of a well, $[L]$

R residual function

Ra Rayleigh number of solute, $[-]$

s density ratio of fresh water and saltwater, $[-]$

s	arbitrary time point, $[T]$
S	slack variable
S	saturation ratio, $[-]$
S_r	residual soil saturation ratio, $[-]$
S_w	saturation ratio of fresh water, $[-]$
$\hat{S}$	approximate solution of saturation ratio, $[-]$
S_0^h	specific storativity of a porous medium with respect to hydraulic head change, $[L^{-1}]$
T	tidal period, $[T]$
v	characteristic value of macroscopic velocity, $[LT^{-1}]$
$\vec{v}$	fluid velocity vector, $[LT^{-1}]$
v_i	velocity in i direction, $[LT^{-1}]$
$\vec{v}_i$	velocity in i direction, $[LT^{-1}]$
V_s	volume of saltwater recharged during phase 1, $[L^3]$
$\hat{V}_i$	approximate solution of the Darcy flux in i direction, $[LT^{-1}]$
w	recharge rate, $[ML^{-2}T^{-1}]$
w_i	basis function
x_i	x coordinate of well i, $[L]$
x_i^0	initial x coordinate of well i, $[L]$
$x_i^{\max}$	maximum of x coordinate of well i, $[L]$

$x_i^{\min}$ minimum of x coordinate of well i, $[L]$

x_c^i stagnation point for well i, $[L]$

x_{ref} reference coastline location, $[L]$

x_{toe}^i toe location for well i, $[L]$

$\Delta x_i^{\max}$ maximum perturbation of x coordinate of well i, $[L]$

$\Delta x_i^{\min}$ minimum perturbation of x coordinate of well i, $[L]$

Δx_i^{upper} upper bound of x perturbation for well i, $[L]$

Δx_i^{lower} lower bound of x perturbation for well i, $[L]$

δx_i subdomain perturbation of x coordinate for well i, $[L]$

X x coordinate vector, $[L]$

X^0 initial x coordinate vector, $[L]$

ΔX_{upper} upper bound of x perturbation vector, $[L]$

ΔX_{lower} lower bound of x perturbation vector, $[L]$

y_i y coordinate of well i, $[L]$

y_i^0 initial y coordinate of well i, $[L]$

$y_i^{\max}$ maximum of y coordinate of well i, $[L]$

$y_i^{\min}$ minimum of y coordinate of well i, $[L]$

$\Delta y_i^{\max}$ maximum perturbation of y coordinate of well i, $[L]$

$\Delta y_i^{\min}$ minimum perturbation of y coordinate of well i, $[L]$

Δy_i^{upper} upper bound of y perturbation for well i, $[L]$

Δy_i^{lower}	lower bound of y perturbation for well i, $[L]$
δy_i	subdomain perturbation of y coordinate for well i, $[L]$
Y	y coordinate vector, $[L]$
Y^0	initial y coordinate vector, $[L]$
ΔY_{upper}	upper bound of y perturbation vector, $[L]$
ΔY_{lower}	lower bound of y perturbation vector, $[L]$
z	z coordinate, $[L]$
z_m	vertical position of the initial mixing zone, $[L]$
Δz	characteristic vertical element length, $[L]$
α	objective weighting parameter for maximization of pumping rate, $[-]$
α	a weighted average of the time derivative, $[-]$
α	parameter of the van Genuchten model, $[L^{-1}]$
α_L	longitudinal dispersivity, $[L]$
α_T	transverse dispersivity, $[L]$
β	objective weighting parameter for minimization of the distance between stagnation point and the reference location, $[-]$
γ	coefficient of slack variable
γ	tortuosity, $[-]$
$\hat{\delta}$	Kronecker-delta (unit tensor), $[-]$

ε predefined tolerance, $[-]$

ε density difference divided by the reference density, $[-]$

η a positive coefficient

θ moisture content ratio, $[-]$

λ_C coefficient of expansivity resulting from the change of the mass concentration of the solute at constant hydraulic head, $\left[L^3 M^{-1}\right]$

λ_{CA} specific moisture capacity, $\left[L^{-1}\right]$

λ_h coefficient of compressibility of the fluid associated with the change of the hydraulic head at constant mass fraction of the solute, $\left[L^{-1}\right]$

μ dynamic viscosity, $\left[ML^{-1}T^{-1}\right]$

μ_f dynamic viscosity, $\left[ML^{-1}T^{-1}\right]$

ξ depth of the sharp interface from sea level, $[L]$

ρ density of fluid, $\left[ML^{-3}\right]$

ρ_0 the reference density of fluid, $\left[ML^{-3}\right]$

ρ_f density of fresh water, $\left[ML^{-3}\right]$

ρ_s density of seawater, $\left[ML^{-3}\right]$

ρQ_ρ source term of the fluid mass, $\left[ML^3T^{-1}\right]$

ϕ single potential, $\left[L^2\right]$

ϕ porosity, $[-]$

ϕ_{toe} potential defined at toe location, $\left[L^2\right]$

ψ	pressure head, $[L]$
ψ_{atm}	atmospheric pressure head, $[L]$
ψ_w	fresh water pressure head, $[L]$
ω	width of the transition zone, $[L]$

SUMMARY

Utilizing the analytical solution of the steady state sharp interface saltwater intrusion model in coastal aquifers, a multi-objective optimization formulation of pumping rates and well locations in a coastal aquifer is formulated to solve problems in water management practice. The proposed optimization problem uses progressive genetic algorithm technique and the method developed is applied to the previous work of Cheng et al. [2000]. Through this analysis, several other applications are provided to demonstrate the use of the model in practical applications. This work is the first to optimize pumping rates as well as well locations simultaneously in coastal aquifer management.

In the subsequent chapters of this thesis, the work is expanded to include concepts of variable density flow in a variably saturated porous medium. In this approach, mixing between two fluids can be described and the porous medium is also expanded to cover saturated and unsaturated zones together (i.e., a variably saturated porous medium). Thus, a three-dimensional finite element model of variable density flow in a variably saturated porous medium, named TechFlow, is developed in this study and tested through various benchmark test problems such as the Henry problem, the Elder problem, and HYDROCOIN Level 1 Case 5 (i.e., the salt dome problem) for comparison between codes and the saltpool problem for comparison between the developed model and the three-dimensional temporal experimental measurement.

TechFlow is used to investigate instability issues associated with the numerical solution of the Elder problem in the perspective that includes physical instability issues

associated with density differences used in numerical solutions, sensitivity of the solution to idealization irregularity, and the importance of accurate estimation of the velocity field and its association to the grid density levels that is necessary to solve the problem accurately.

Saltwater intrusion hydrodynamics in a beach under the influence of tidal effects is also investigated using TechFlow. Based on the results of TechFlow with the use of various boundary conditions for the transport equation, the saltwater intrusion hydrodynamics in a beach under the influence of tidal effects shows unique dynamics. These solutions are primarily affected by density differences, tidal effects on a mild slope, variably saturated porous medium and finite domain solution condition.

TechFlow is also used to investigate saltwater upconing beneath pumping wells. Two applications of the saltwater upconing problem are solved. The results obtained by TechFlow are in good or better agreement with their results obtained from the other researchers in the first application and the experimental data in the saltpool problem.

The last application addressed and solved using TechFlow, is saltwater upconing due to pumping under tidal effects. Three scenarios of the saltwater intrusion due to pumping under no tidal effects or under tidal effects are solved and investigated. A large pumping rate is intentionally assigned to induce extreme cases of saltwater intrusion. For practical usefulness of the results, a dimensional analysis is provided. In the analysis, the principle dimensionless number is chosen as a ratio of capillary force to gravity force. Thus, the analysis is focused on the physics of water flow between the unsaturated zone and the saturated zone. The results obtained from the application can be used for

interpretation of scaling-up of applications in which the principle dimensionless number is of interest.

CHAPTER 1

INTRODUCTION

This chapter provides an introduction to two topics that constitute the main research areas in the whole thesis. These topics are: (i) optimization of pumping rates and well placement in coastal aquifers for fresh water extraction and controlled saltwater intrusion and (ii) variable density flow modeling in subsurface. In addition, this chapter also reviews the applications covered in the thesis along with the motivation and objectives of these applications. Finally, the chapter provides the reader with the organization of the thesis.

1.1 Optimization of Pumping Rates and Well Placement in Coastal Aquifers

Groundwater is one of the major sources of drinking water all over the world [Bear, 1979]. In the United States, the usage of groundwater is up to about fifty percent of all drinking water and it may go up to eighty percent in some rural areas [OTA, 1984]. Some areas near the coast have potential saltwater intrusion problems which may be initiated due to excessive pumping. Thus, the management of groundwater pumping in these aquifers differs from groundwater supply areas which are not near coastal zones. Improper water management practices in coastal aquifers are the main cause of saltwater intrusion and thus degradation of freshwater aquifers as reported for twenty coastal states in the USA [Frind, 1982]. Once the degradation of aquifers occurs, it often results in a loss of fresh water resources and requires the need to seek alternative water supplies that are costly. [Frind, 1982; Cheng et al., 2000].

The mathematical solution of the saltwater intrusion problem is not a simple task. There are in general three ways to approach to the solution of this problem. The first is the use of analytical solution on the basis of the Ghyben-Herzberg relationship [Bear, 1972] and the single potential theory introduced by Strack [1976]. Using this approach, steady state solutions can be obtained for hydrogeologically homogeneous aquifers. The second is a more complex model that is based on the assumption of a sharp interface between freshwater and saltwater, employing numerical solution of governing equations (Figure 1.1). In this approach, one solves two nonlinear coupled partial differential equations for pressures or hydraulic heads of freshwater and saltwater numerically. The interface position is implicitly defined and arrived at as one of the outcomes of the numerical solution. This is a fairly reasonable approach for the aquifers which exhibit narrow mixing zones so that the interface can be inferred from freshwater and saltwater heads. The third is a relatively more complex approach that is based on solutions of variable density flow in both time and space dimensions [Frind, 1982; Voss and Souza, 1987; Herbert et al., 1988; Oldenburg and Pruess, 1995; Holzbecher, 1998; Kolditz et al., 1998]. This model allows the mixing of freshwater and saltwater in transition zone of the interface. Thus, it represents the processes of saltwater intrusion in a more realistic way. The use among these approaches is necessary to analyze saltwater intrusion problems to achieve sound water management practices. The choice of the proper methodology to be adopted would depend on the complexity of the aquifer system under study, the accuracy expected of the modeling outcome for the chosen aquifer system, and the allowable budget and time available to conduct the studies.

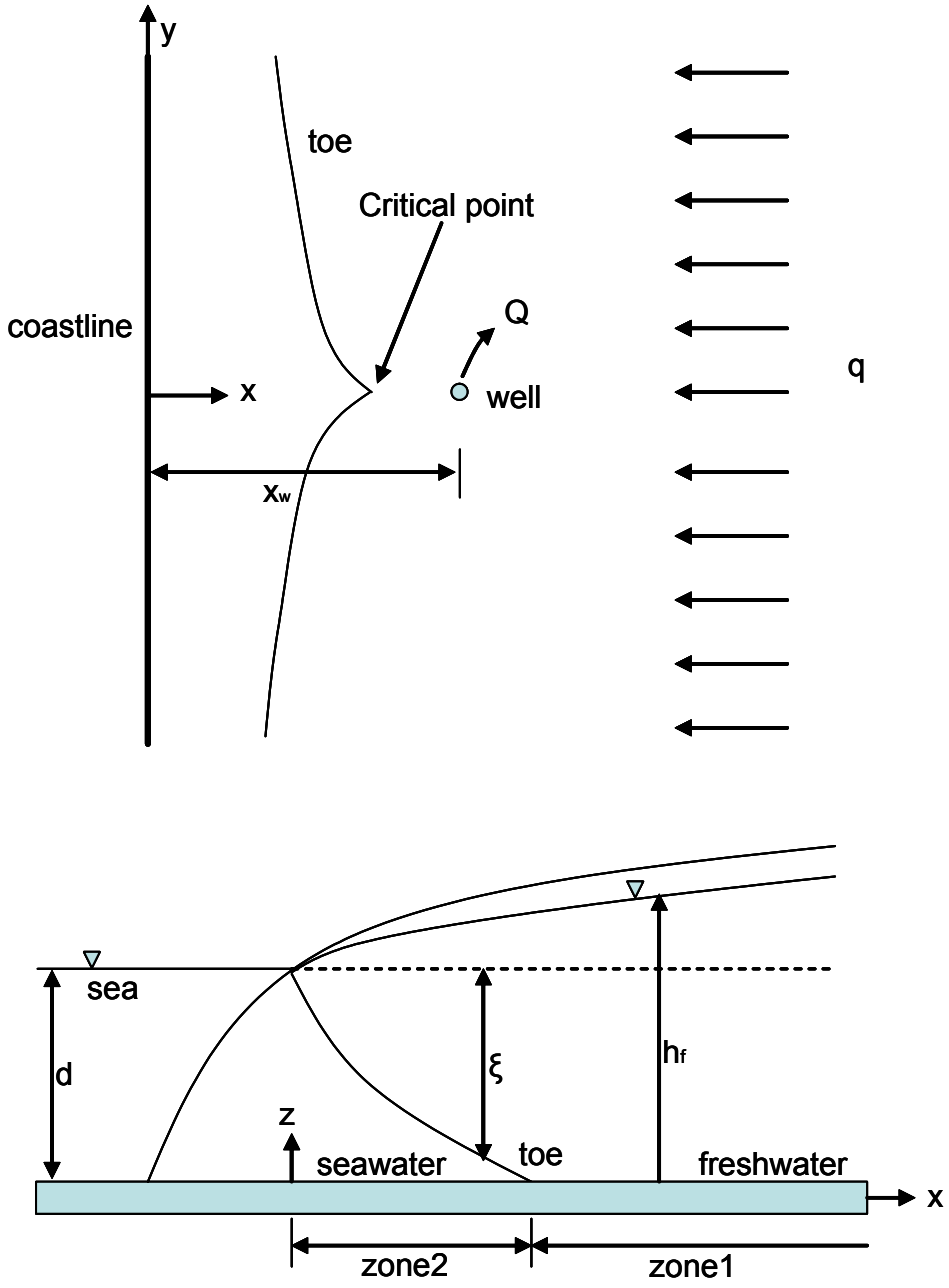

Figure 1.1 Schematic of pumping well near coastal area: Plan view and cross-section of a coastal aquifer assumed to have sharp a sharp interface

Two important goals can be identified as important issues associated with water resources management in coastal aquifers. These are freshwater production and environmental preservation. Accordingly, goals are to maximize freshwater extraction while minimizing saltwater intrusion into the aquifers and thus the extraction wells. These goals are of great importance and are mostly in conflict with one another in the proper management of coastal aquifers.

1.2 Variable Density Flow in a Variably Saturated Porous Medium

Variable density flow is the term that classifies the flow pattern influenced by density differences in the fluid system [Holzbecher, 1998]. Some scientists use the term density-driven flow since most of variable density flows in a porous medium in nature are generated by density differences. Here, the density referred to is the fluid density and not the density differences in the medium. Variable density flow analysis is associated not only with the density itself but also with the parameters that affect or change the density of the fluid. These parameters can be temperature, concentration (salinity) or both simultaneously.

A variably saturated porous medium means that the water saturation ratio of porous media also changes spatially and temporally. The division of saturated or unsaturated nature of porous media or both is due to the fact that the pattern of flow is significantly different depending on the degree of the saturation in porous media, which significantly affects the aquifer parameters and thus affects the head or pressure gradients in the flow system.

Examples of variable density flow can be found in many cases of flow in porous media. Saltwater intrusion is one of the popular examples in variable density flow between freshwater and saltwater. The well-known Elder problem is another application, which is a very instable problem because the heavier fluid is on the top of the lighter fluid and the density difference is 20 percent by mass [Elder, 1967; Voss and Souza, 1987]. A disposal of radioactive waste from nuclear power plants by burial in geological formations such as a salt dome is also another good example involving many complicated physical and chemical processes [Herbert et al., 1988; Oldenburg and Pruess, 1995; Holzbecher, 1998; Kolditz et al., 1998]. There are many other applications where or when density changes within the system such as advection-dispersion transport of dense organic vapors in the unsaturated zone and convection in groundwater below an evaporating salt lake [Mendoza and Frind, 1990a,b; Wooding et al., 1997a; Wooding et al., 1997b].

In the modeling of groundwater flow and transport, the density of groundwater is usually assumed constant because of little variation in either temperature or concentration of the miscible fluids. These are commonly termed as well mixed flow domains. The variable density flow is significantly different from these applications since the effect of density difference in association with the flow pattern needs to be considered in the numerical solution of the governing equations. To include this density effect on the flow domain, the governing equation of variable density flow leads to full coupling of two common groundwater models of flow and transport as will be discussed in detail throughout this thesis.

1.3 Statement of the Problems

The problems analyzed in this thesis cover two different topics, which are (i) optimization of pumping rates and well placement in coastal aquifers and (ii) variable density flow modeling in subsurface. The former mainly focuses on the engineering approach to water management practices. Thus, factors related to the science and engineering are considered while economical consideration is avoided. Under this topic two goals are set as (i) the maximization of freshwater extraction and (ii) the minimization of distance between wells and coastline as site specific criteria. The second goal is added to consider the unique situation of groundwater supply that coastal aquifers have. Note that this is a multiple-objective problem with two conflicting objectives. Multi-objective problems like this can be found in many other areas including science, technology, and business. Most often multi-objective problems narrow down to "Minimizing the cost while maximizing the profits" type of problems.

The other topic is focused on the physics of variable density flow problems. As mentioned previously, there are many applications where the solutions to variable density flow are of interest. The variable density flow analysis is a complex and computationally intensive problem. Some of the problems in the applications to be discussed in this thesis are still debated in the literature. Hopefully the work presented in this thesis will bring closure to some of these debates. The existing models that have been widely used in variable density flow analysis exhibit different solution strategies and techniques. This is due to the fact that the problems analyzed under this topic are so complex that the researchers are always in a process of refining their solution techniques to better represent the nonlinearities of the governing equations. In the chapters where variable

density flow is analyzed and solutions to the problem are presented, the different approaches to the solutions are discussed in detail. These solutions are first used for the validation of the model developed in this thesis. Further, the solutions obtained in this study lead to the important factors considered to obtain the accurate solution of density dependent flow. The problems in these chapters are presented in the following order: (i) saltwater intrusion problems (The Henry problem); (ii) the Elder problem; and, (iii) the salt dome problem (HYDROCOIN Level 1 Test Case 5) [Henry, 1964; Elder, 1967; Swedish Nuclear Power Inspectorate, 1984].

In addition, the model developed for variable density flow analysis is further applied to the recent applications such as hydrodynamics in a beach under the influence of tidal effects [Boufadel, 2000] and the salt pool problem (i.e. saltwater upconing) that has three-dimensional experimental data [Oswald and Kinzelbach, 2004]. The former application is provided by Boufadel [2000] and the problem domain is a variably saturated porous medium. For this application, the model validation for the saturated-unsaturated flow analysis is provided by comparing the results with those obtained by Celia et al. [1990] and Forsyth et al. [1995]. The numerical result obtained for the salt pool problem is also presented and compared with recently published results [Diersch and Kolditz, 2002; Johannsen et al., 2002; Oswald and Kinzelbach, 2004]. In addition, a discussion on the grid density effects in numerical solution is also presented in comparison with the recent results reported in other studies on the salt pool problem. Finally, the developed model is further used to solve problems in saltwater upconing due to pumping under tidal effects and the dimensional analysis for this three-dimensional problem is provided for scale-up of the results.

1.4 Motivation and Objective

The wise use of fresh water resources in coastal aquifers is of great importance to preserve available groundwater resources and environmental quality. To achieve this goal, it is necessary to understand the characteristics of the aquifer system so that a water management plan can be set for the proper management of these resources. The coastal aquifers are unique because of potential saltwater intrusion problems which may be initiated due to excessive pumping. To prevent saltwater intrusion, there are some important practical questions that need to be answered. These questions are (i) to meet the freshwater demand in a coastal aquifer how many wells are required; (ii) where those wells are to be placed; and, (iii) what pumping rates are to be assigned to those wells. The tool developed in this study may help us answer these questions with the certain limitation associated with the assumptions on which the tool is based.

The physical processes of variable density flow are very complex. In the literature, there are many works published and being published to understand these physical processes. However, many issues related to variable density flow in searching for the agreeable solutions on the benchmark test problems are still open to debate and remain unsolved. Thus, there are challenging questions in this field that needs to be answered by scientists and engineers.

The objective of this thesis is to develop two different models: (i) a model for optimization of the water management problems in coastal aquifers and (ii) a model for variable density flow in subsurface. The first is expected to help obtain water

management solutions in coastal aquifers. The user-friendly interface of the first model is implemented to help transfer an expert knowledge to the utility managers.

Second, the model for variable density flow was intended to meet the following requirements to investigate complex problems in the field of variable density flow.

i. The model should be able to solve three-dimensional problems.
ii. The model should be capable of creating three-dimensional grids as well as importing the grid created by other competent grid generator in an easy way.
iii. The model should be capable of handling variable density flow in both saturated and unsaturated porous media.
iv. The model should be efficient at least and beyond the level of the existing models developed in this field of study.
v. The model should be validated through the existing benchmarking test problems.
vi. The model should be capable of applying to problems in practice and providing reasonable solutions.

1.5 Organization of the Thesis

The thesis consists of nine chapters. A brief introduction is provided in this chapter. A comprehensive literature review is given in Chapter 2. The problem of optimization of pumping rates and well placement in coastal aquifers is presented in Chapter 3. Chapter 4 covers topics ranging from governing equations to the validation of the variable density flow model developed in this thesis. A discussion and comparison of results for three benchmark test problems are also provided in this chapter. The Galerkin finite element formulation of variable density flow used in the developed model is given in Appendix C.

In Chapter 5, sensitivity analysis of the solution of Elder problem to density, velocity and other numerical perturbations is investigated. In Chapter 6, the results of the model developed for solving hydrodynamics in a beach under the influence of tidal effect are discussed. Saltwater upconing and the validation with the saltpool experiment are provided in Chapter 7. Chapter 8 provides solutions for three different cases of saltwater intrusion or upconing due to pumping under tidal effects in three dimensions. Chapter 9 provides conclusions and further recommended studies.

CHAPTER 2

LITERATURE REVIEW

In this chapter, a comprehensive literature review is provided on the following topics: (i) optimization of pumping rates and well placement in coastal aquifers for fresh water extraction and controlled saltwater intrusion and (ii) variable density flow in a variably saturated porous medium. The review of the latter consists of the Henry, Elder, and salt dome problems for the benchmark tests, in addition to the applications to problems such as hydrodynamics under a beach under the influence of tidal effects and saltwater upconing with or without tidal effects.

2.1 Optimization of Pumping Rates and Well Placement in Coastal Aquifers

Optimization has been a commonly used method in the analysis of groundwater planning and management problems as demonstrated in numerous publications that appear in the current literature [Gorelick, 1983; Gorelick et al., 1984; Aral et al., 1993; Marryott et al., 1993; Rogers and Dowla, 1994; Mckinney and Lin, 1995; Peralta et al., 1995; Xiang et al., 1995; Aral and Guan, 1997; Aly and Peralta, 1999; Guan and Aral, 1999a; Guan and Aral, 1999b; Aral et al., 2001; Guan and Aral, 2004]. Even though the water management problem may be formulated in a unique way depending on the criteria for management and many other site specific conditions, most optimization problems in subsurface applications can be categorized into two groups: (i) extracting safe potable groundwater in the vicinity of a contaminant plume or providing safe yield in a clean aquifer system and (ii) containing and/or remediating contaminant plumes.

The first group includes a range from aquifers, contaminated, to coastal aquifers threatened by saltwater intrusion due to excessive pumping. Thus, the optimization analysis focuses on the control issues associated with the protection of aquifer resources. On the other hand, the second group is related to the remediation of aquifers that are already contaminated. Many researchers and scientists have used optimization tools to describe contaminated groundwater migration. One of the most commonly used groundwater remediation technologies is the pump and treat (P&T) approach. The basic design variables in a P&T system are most often the well locations and pumping schedules of these wells [Gorelick et al., 1984; Aral et al., 1993; Marryott et al., 1993; Rogers and Dowla, 1994; Mckinney and Lin, 1995; Peralta et al., 1995; Xiang et al., 1995; Aral and Guan, 1997; Aly and Peralta, 1999; Guan and Aral, 1999a; Guan and Aral, 1999b; Aral et al., 2001; Guan and Aral, 2004]. Similar to design of P&T systems, optimization problems in saltwater intrusion control are unique, in having goals such as to protect aquifers from saltwater intrusion and provide safe freshwater to consumers. Surprisingly, the use of optimization in the solution of saltwater intrusion problems is relatively recent [Shamir et al., 1984; Willis and Finney, 1988; Finney et al., 1992; Hallaji and Yazicigil, 1996; Das and Datta, 1999a,b; Cheng et al., 2000]. The consideration of different aspects of the saltwater intrusion problem such as inland aquifer intrusion, saltwater upconing, hammock formation in tidal estuaries etc. and the complexity of the solution of these problems has led to the formulation of many different optimization frameworks as well as the use of many different techniques to solve these optimization problems. As mentioned in Chapter 1, analytical solution with the sharp interface assumption allows greater flexibility in optimization because of the simplicity

of the solution. Variable density models that are more complex limit their use in optimization analysis due to the computational burden they impose on the optimization analysis. The solution of optimization problems requires repetitive solutions of the nonlinear equations governing the variable density models and this is not feasible given the current computational platforms.

Willis and Finney [1988], Finney et al. [1992], and Cheng et al. [2000] studied management models for coastal aquifers of saltwater intrusion with the assumption of a sharp interface between fresh water and saltwater. While most of the management problems addressed saltwater intrusion into wells in an indirect manner, such as constraining drawdown at control points or minimizing the intruded saltwater volume or concentration, Cheng et al. [2000] used an optimization approach to solve for pumping rates for an existing multiple well extraction scenario in a coastal aquifer using Genetic Algorithm (GA). In their study, the analytical solution of the sharp-interface saltwater intrusion model was used for simplicity. The use of a more complex model is deferred, in part due to the intensive computation time required by the repetitive use of the model during the optimization process. In their solution, they discretized the pumping rate and used the Structured Messy Genetic Algorithm (SMGA) approach with the pumping rate selected as the basic design variable. As for the discretized pumping rate, Park and Aral [2004a] successfully formulated an optimization problem to have continuous design variables of the pumping rate as well as well locations.

Depending on various design considerations on decision variables, optimization problems can be formulated from the simplest to the complex. For example, an optimization problem would be simple if the system is designed to have a small number

of basic design variables which are discrete so that the number of possible cases are limited. On the other hand, if the decision variables are for deciding some values from a continuous domain such as selecting pumping rates or well locations or both, then the number of possible values that the decision variables can take will be often infinite. This, in conjunction with the complexity of the physical model, is important in choosing the decision variables. In summary, there may be several combinations depending on the factors on computational burden and the accuracy of the solution that maybe linked to cases, such as the use of a simple model with a complex optimization formulation, the moderate physically based model coupled with a moderate optimization formulation, a complex physically based model with a simple optimization formulation, and so on. The work presented in this thesis may be categorized as a simple physically based model coupled with a complex optimization formulation.

Genetic Algorithms (GA) are a robust method when optimal solutions are sought for nonlinear problems. In the literature, numerous researchers have demonstrated that the GA could yield significant improvements in computational efficiency for the solution of these problems [Mckinney and Lin, 1994; Huang and Mayer, 1997]. This approach is used in various engineering fields to achieve optimal solutions to complex problems. The GA approach is further extended to progressive GA (PGA) approach to improve the efficiency of the solution process [Aral and Guan, 1997; Guan and Aral, 1999a; Guan and Aral, 1999b; Aral et al., 2001]. The basic idea in this method may be defined in the following way: “Search as little as possible, get the trend of the solution in a sub-domain and reach the optimal solution through a sequence of sub-domain optimal solutions.” Often in reality, the number of possible solutions are simply too many to complete an

exhaustive search for an optimization problem. Therefore, the formulation of the optimization problem is of great importance to reduce the unnecessary simulations (i.e., computational burden) before the search begins. The PGA is one of way to realize that objective.

2.2 Variable Density Flow in a Variably Saturated Porous Medium

The literature review on variable density flow in a variably saturated porous medium consists of the Henry, Elder, and salt dome problems for the benchmark test as well as the applications such as hydrodynamics in a beach under the influence of tidal effects and saltwater upconing with or without tidal effects. A review of each problem is covered separately in this section.

2.2.1 The Henry Problem (Saltwater intrusion)

Henry proposed an analytical solution of the saltwater intrusion for steady state conditions allowing the mixing of fluids with different densities [Henry, 1960]. Variable density analysis leads to a quantitative description of the dynamic balance between fresh water and saltwater in a coastal aquifer [Holzbecher, 1998]. Based on his assumption of a constant dispersive mechanism in the aquifer, he used Darcy's law, the continuity equation, and a steady state transport equation. Even though there have been some critical remarks in the literature on the unrealistic boundary condition on the seaside boundary and the use of the constant diffusivity, the Henry problem has become one of the most popular benchmark tests in variable density flow applications.

Pinder and Cooper [1970], Lee and Cheng [1974], Segol et al. [1975] have solved the Henry problem numerically. Frind [1982] and Huyakorn et al. [1987] solved the Henry problem using their finite element codes with slightly modified boundary condition on the seaside boundary. Konikow and Bredehoefs [1978] used the same problem and solved the problem with the use of method of characteristics (MOC) in the solution of the advective transport equation. The Henry problem is used as benchmark solutions by INTERA [1979] using SWIFT; by Voss and Souza [1987] using SUTRA [Voss, 1984]; by Kolditz [1994] using FEFLOW; by Strobl and Yeh [1994] using 2DFEMFAT; by Oldenburg and Pruess [1995] using TOUGH2; and by Bastian et al. [1997] using UG. Interestingly, none of the numerical solutions has been able to obtain results close to the solution of the semi-analytical results of Henry. This may be due to some form of inaccuracy in the original findings by Henry that requires that the contours of equipotential heads are not orthogonal to Darcy velocity vectors [Kolditz, 1994]. Nevertheless, it is a trend in variable density flow that the Henry problem is widely chosen as one of the test problems for validation of existing and newly developed codes prior to the use of the code in more complex applications.

2.2.2 The Elder Problem

Elder [1967] provided experimental and numerical studies of transient convection in a porous medium. He used a Hele-Shaw cell to generate thermal convection-dominated flow by constantly heating a part of the base of a porous medium. The Elder problem can be considered analogous to the density-driven problem from the hypothesis of Cooper [1959] “differing from it only in that changes in density are produced by changes in

concentration rather than by changes in temperature". Similar to the Henry problem, the Elder problem has also been another benchmark test problem for variable density flow applications.

Voss and Souza [1987] solved it using the SUTRA model [Voss, 1984] and obtained numerical results close to the result of Elder's numerical solution. Oldenburg and Pruess [1995] discovered that the original solution of the Elder problem was obtained on a coarse grid implying that the grid was not convergent. They showed that the different patterns of the solution obtained on a more refined grid while reproducing the same solution on the coarse grid with Voss and Souza [1987]. Kolditz et al. [1998] reproduced the results of Oldenburg and Pruess by using two models FEFLOW and ROCKFLOW on the different grid densities up to 9900 rectangular elements. This seemed to be in agreement with Oldenburg and Pruess [1995] until Frolkovič and Schepper [2001] showed a different pattern with an extremely dense grid that consisted of up to 32768 rectangular elements. They also presented results for various upwind methods and indicated that different transient behavior of the numerical solutions that can also be caused by the inconsistencies in the numerical method itself [Holzbecher, 1998]. Later, Woods et al. [2003] investigated the Elder problem with SUTRA [Voss, 1984], again showing that the Elder problem is prone to error, and confirmed that Elder problem results are extremely sensitive to the simulation method used. Unfortunately, they did not solve the problem on the extremely dense grid as Frolkovič and Schepper [2001] did. The compatible level of the grid density with Frolkovič and Schepper are also used in another recent paper [Boufadel et al., 1999b]. Unlike Frolkovič and Schepper [2001], the results of Boufadel et al. [Boufadel et al., 1999b] do not show the same pattern which Woods et

al. [2003] cast possibility of inaccuracy of the model because of distinctly asymmetric results of Boufadel et al.'s at lower grid resolutions. Considering different kinds of solutions of the Elder problem, Woods et al. [2003] commented that the nature of indeterminance of the Elder problem makes the problem inappropriate for the benchmark test problem in variable density flow. Recently, Park and Aral [2004b] investigated sensitivity of the solution of the Elder problem to density, velocity and other numerical perturbations.

2.2.3 The Salt Dome Problem (HYDROCOIN Level 1 Case 5)

A salt dome has been known to be a good geological formation for storage of radioactive wastes in several countries [Witherspoon, 1991; Holzbecher, 1998]. The proponents especially for heat producing waste refer to the facts that the flow of salt closes fractures in short times because of high plasticity and salt has high thermal conductivity. On the other hand, some doubts about the storage in the salt dome are that the impurity of the salt, salt dome diapirism, high solubility of salt, and the corrosive effect of salt may increase risks when keeping the radioactive wastes in these environments [Holzbecher, 1998]. Nonetheless, it is still considered as one of the good candidates for radioactive waste burial sites.

Because of the extremely slow decay of the waste, the USEPA requires radionuclide concentration in groundwater to remain below a certain limit for a time period of 100 years. Even longer cases, cumulative release of radionuclides to the environment from all significant processes must be limited for a period of 10000 years [Brown and Lemons, 1991]. Kastenberg and Gratton [1997] suggested that the 10000

year period is quite arbitrary and it is reasonable to consider even longer time periods. Thus, the slow decay of the waste and the uncertainty of the regulation on the time period significantly increase the risk to securely store the wastes in geological formations for such a long time. The first step for successful treatment of the wastes is to understand various scenarios that might be occurred with hydrogeological condition during the long time period of the burial.

As a first step for the task, the Hydrologic Code Intercomparison (HYDROCOIN) project was set in 1984 as multi-country effort for understanding groundwater flow in radioactive waste disposal scenarios. The objective of HYDROCOIN level 1 studies was to "verify the accuracy of groundwater flow codes" for a variety of hydrogeological settings [OECD, 1992]. Among HYDROCOIN level 1 studies, Case 5 has been studied extensively and created discussion and debate in the literature. Herbert et al. [1988] presented their results using NAMMU; SWIFT result by Bűtow and Holzbecher [1986]; Oldenburg and Pruess [1995] using TOUGH2; Konikow et al. [1997] and Kolditz et al. [1998] using both FEFLOW and ROCKFLOW. Case 5 was hypothetically made to focus on the mathematical model of variable density flow representing the test-case setup of the Gorleben salt dome in Germany [Langer et al., 1991]. Thus, the problem is highly simplified in terms of the geological and geometrical conditions and the aquifer homogeneity. The lateral dispersive mass flux from the top of the salt dome was originally set so that diffusivity has been the most discussed parameter in publications.

Herbert et al. [1988] used NAMMU and solved the problem for diffusivities ranging from 10^{-6} to 10^{-8} m^2/s by successfully using a parameter stepping technique. Oldenburg and Pruess [1995] obtained similar recirculating flow pattern only

for $D > 10^{-7}\ m^{-2}/s$. On the other hand, they discovered that the solution leads to a 'swept-forward' pattern in which concentrations were not found upstream of the salt dome. These results were contradicting those of Herbert et al. [1988]. Oldenburg and Pruess [1995] has put more credibility on their results because they believe that they used minimization of residual in convergence criterion while others (NAMMU by Herbert et al., [1988]; SUTRA by Voss, [1984]; CFEST by Gupta et al., [1982]; SWIFT by Reeves et al., [1986]) except TOUGH2 have used a criterion of small relative or absolute changes in primary variables to determine convergence. Hoping for resolving the arguments, Johns and Rivera [1996] recalculated the case with NAMMU and reconfirmed the results of Herbert et al. [1988]. Nonetheless, Oldenburg et al. [1996] solved the case using MOR3D and obtained the swept-forward solution. In spite of the debate, Kolditz et al. [1998] produced the same results as Herbert et al. [1988] in the recent publication. It was Konikow et al. [1997] that discovered the erroneous boundary conditions which lead to the different results. From the results of MOCDENSE which uses the method of characteristic (MOC), they concluded that the different ways to apply boundary conditions produce the different results regardless what models or methods are used and the concentration distribution of the case depends very little on which numerical model is used, as long as the selected model is solving the proper equations.

2.2.4 Hydrodynamics in Beaches under the Influence of Tidal Effects

Oil-contaminated beaches have been a major concern in coastal environments. Bioremediation is an emerging technology for remediation of oil-contaminated beaches. There are several bioremediation technologies: (i) a no-nutrient control (intrinsic

bioremediation), (ii) addition of water-soluble nutrients (biostimulation), and (iii) addition of water-soluble nutrients supplemented with a natural microbial inoculum from the site (bioaugmentation). Venoso et al. [1996] reported high rates of oil biodegradation with little difference between biostimulation and bioaugmentation. The effective implementation of this biostimulation or bioaugmentation requires long residence time of the added nutrients that are needed to be contacted on the oil-contaminated zone, which is mostly in shallow depths within the beach [Rosenberg et al., 1993]. Maximizing the residence time is the key for successful implementation of this bioremediation technology. Good understanding of hydrodynamics of saltwater intrusion in beaches under the influence of tidal effects is required for an optimal practice of bioremediation.

The hydrodynamics under tidal effects involves several complex physical processes such as mixing in porous medium, water flow in both unsaturated and saturated zones, and the effect of tidal wave. Due to the periodic nature of the tidal rise and fall, hydrodynamics in beaches becomes a transient problem. Excluding sediment erosions on beaches by wave, the height of tide becomes a boundary condition on the seaside which makes the water table higher than the average sea level at high tides and lower at low tides [Boufadel, 2000]. Philip [1973] showed analytically that the average water table in the beach is above the average sea water level using a rectangular beach application. Later, Nielsen [1990] also found out that the water table should be above the average sea level including sloping beaches. The Dupuit assumption was used in both works [Bear, 1979]. Recently, Boufadel [2000] did both experiments and numerical simulation on the sloping beach and cast doubts on analysis of hydraulics in a beach based on the Dupuit assumption, commenting that the Dupuit approach does not account for water flow in the

unsaturated zone and assumes horizontal flow below the water table. The hydrodynamics of beaches are complex due to the following: (i) beach geometry, (ii) periodic change of tide, (iii) flow both in unsaturated and saturated porous media, and (iv) wind and waves. When groundwater flow equation is solved in a variably saturated medium, in other words, both unsaturated and saturated zones together, the equation becomes highly nonlinear. The nonlinearity limits utilization of traditional numerical models of groundwater. A numerical scheme which solves a mixed form of flow equation has been developed to overcome the limitations for finite different method [Celia et al., 1990] together with a modified mixed form for finite element method [Rathfelder and Abriola, 1994]. Few studies of hydrodynamics of beaches can be found in the literature. Boufadel's work [2000] is the most recent and comprehensive covering variable boundary conditions describing concentration distribution, periodic seaside boundary conditions of hydraulic head, density-dependent flow and transport in a variably saturated porous medium. Thus, the hydrodynamics in a beach and salt water movement under the influence of tidal effects is another dynamic application in variable density flow which will be covered in details in Chapter 6.

2.2.5 Saltwater Upconing

Saltwater upconing is described by Reilly and Goodman [1987] as the movement of saltwater from a deeper saltwater zone into the fresh groundwater in response to pumping at a single well. It is a widespread problem reported in USA that is observed at Georgia, Michigan, Minnesota, Missouri, Nebraska, New Mexico, North Dakota, South Carolina, and Utah [ASCE, 1969; Krause and Clarke, 2001] as well as globally in other

countries such as Germany [Diersch et al., 1984; Diersch and Nillert, 1987], the Netherlands [Huisman, 1954], Israel [Dagan and Bear, 1968; Schmorak and Mercado, 1969], and Japan [Hosokawa et al., 1990].

There are mainly two different approaches for modeling saltwater upconing. The sharp interface approach and miscible displacement (i.e., variable density flow and transport). The first approach originates from the problem of oil recovery which is physically closer to the sharp interface assumption by Muskat and Wyckoff [1935]. Although the sharp interface approach has a physical limitation, it was used in well design and operation widely in the 60's, 70's, and even 80's. This is in part because of the simplicity of the conditions and the definition of critical pumping rate or rise that allows the saltwater to remain static [Wang, 1965; Bennett et al., 1968; Strack, 1972; Sahni, 1973; Strack, 1976; Motz, 1992]. The other underlying assumption of the sharp interface approach is that a steady state is reached in a relatively short time after the start of pumping [Holzbecher, 1998].

The variable density flow approach, which satisfies physical conditions more realistically by allowing a transition zone between fresh water and saltwater, is useful in answering the question why many case studies show a gradual salinity increase due to increasing aquifer exploitation. This in fact requires the variable density flow approach for the saltwater upconing problems. Thus, the difficulties associated with variable density flow accompanies naturally. Numerical modelers attempted to match their results of saltwater upconing problem with the analytical solution. Reilly and Goodman [1987] compared two results using SUTRA and indicated that even though a stable cone (i.e., valid zone that the sharp interface model can be applied to) exists below the well screen,

the well can discharge significant salt concentrations. Other contradicting discussions can also be found on the applications of two different approaches but they have different recommendations mainly because two different methods are used or the underlying assumptions are different. For example, Motz [1995] argued that the range of the design criterion that Panday et al. [1993] obtained from numerical model of variable density flow, DSTRAM, is greater than most previously reported results and it is significantly greater than the range generally recommended for design. Panday [1995] came back on the argument pointing out the limitation of the analytical solution due to the ideal assumptions. He also suggested that the Geneva lens system that is the site in the discussion is not a candidate for sharp-interface conceptualization due to large vertical mixing in the vicinity, and due to validity of the assumptions for the scale of the Geneva system.

The most recent work of the other approach up to now on saltwater upconing is started by Oswald and Kinzelbach [2004]. They conducted a series of laboratory experiments that a stable layering of saltwater below freshwater is affected by the recharge and discharge of freshwater on the top with 1% and 10% initial salt-mass fraction differences. They also conducted numerical work to reproduce experimental results within a reasonable accuracy but failed for the high concentration case. Johannsen et al. [2002] carried out detailed numerical investigations and obtained the reference solutions and suggested that for the high concentration, a very high spatial grid resolution using up to 16 million grid points are necessary. This grid density is obviously far beyond all of the previous numerical simulations conducted on saltwater upconing by previous researchers [Diersch et al., 1984; Wirojanagud and Charbeneau, 1985; Reilly and

Goodman, 1987; Voss and Souza, 1987]. Noticing that there is no three-dimensional experimental data for variable density flow before Oswald and Kinzelbach [2004], the validation of variable density flow models is required for matching the results with the experimental ones on the saltwater upconing problem known as the saltpool problem.

Based on the literature review on the topics (i) optimization of pumping rates and well placement in coastal aquifers for fresh water extraction and controlled saltwater intrusion and (ii) variable density flow in variably saturated porous medium, two models, one in each topic, have been developed in an effort to provide alternative water management solutions to problems in coastal aquifers. In this thesis, using these models several complex problems are investigate in an effort to answer some of the questions that are still debated in the literature. Further, the developed model is applied to solve saltwater intrusion or upconing due to pumping under tidal effects in three dimensions. This problem is never been solved previously. A dimensional analysis to scale up the results of the application is also provided.

CHAPTER 3

MULTI-OBJECTIVE OPTIMIZATION OF PUMPING RATES AND WELL LOCATIONS IN COASTAL AQUIFERS

In this chapter, a new multi-objective optimization approach is presented to determine pumping rates and well locations to prevent saltwater intrusion while satisfying desired extraction rates in coastal aquifers. The objective is formulated based on the analytical solution for the steady state sharp interface saltwater intrusion model. The optimization problem formulated is solved using the progressive genetic algorithm technique [Aral and Guan, 1997; Guan and Aral, 1999a; Guan and Aral, 1999b]. The method developed is applied to the previous work [Cheng et al., 2000] and several other applications are provided to demonstrate the use of the model.

3.1 Introduction

In developing the optimization model, the analytical solution of the steady state sharp-interface saltwater intrusion model is used in this study. This solution is based on the single-potential theory proposed by Strack [1976] for combined fresh water and saltwater problems. The concept of the stagnation point approach was expanded to two dimensions for multiple wells, which leads to the optimization criteria for pumping rates for each well. The process is also extended to include the determination of the optimal location for extraction wells as continuous variables. The comparison of the location of the stagnation point relative to the saltwater intrusion point is used as one of the constraints of the optimization model in analyzing this problem.

Utilizing the Progressive Genetic Algorithm (PGA) approach, which is a combinatorial optimization method introduced in the literature [Aral and Guan, 1997; Guan and Aral, 1999a; Guan and Aral, 1999b], the pumping rates and the locations of multiple wells can be optimized simultaneously while allowing the unknown variables to be continuous variables in the solution domain. In this chapter, the methodology of the PGA and the stagnation point model are discussed in the iterative sub-domain solution of the saltwater intrusion problem. This chapter shows that this approach can improve the results of the optimized solution significantly when compared with the solutions obtained in earlier studies [Cheng et al., 2000].

3.2 Governing Equations for the Sharp Interface Model

Analytical solutions used in this study are valid if the following assumptions can be made for the aquifer under study. First, it is assumed that a sharp interface exists between the fresh water zone and the saltwater zone rather than a miscible transition zone [Bear, 1972,1979]. Second, the aquifer is assumed to be homogeneous, and steady state conditions are considered. Third, the Dupuit assumption is used, which state that in regional groundwater flows, the slope of the phreatic surface is very small and the assumption of the small slope is equivalent to assuming that equipotential surfaces are vertical and the assumption of flow being essentially horizontal is justified. The important advantage gained from employing the Dupuit assumption is that a potential in three-dimensional geometry can be reduced to a new potential in a two-dimensional domain rendering the variable independent of the vertical coordinate (z) [Bear, 1972,1979]. Thus, employing the Dupuit assumption in the study, the flow is assumed to

be two-dimensional in the horizontal plane of the aquifer. Fourth, the interface location is deduced from the Ghyben-Herzberg assumption [Bear, 1972,1979]. Finally, a single-potential theory approach [Strack, 1976] is adopted to make use of a single governing potential equation across the saltwater and freshwater zones as seen in Figure 3.1.

The Ghyben-Herzberg approximation can be described as a ratio of the depth of saltwater interface below the sea level to the elevation of freshwater piezometric head above the sea level. This ratio can be given as a function of fresh water and saltwater densities and is approximately equal to 40. The piezometric head in the fresh water and saltwater zones respectively can be defined as

$$h_f = \frac{p}{\rho_f g} + z \tag{3.1}$$

$$h_s = \frac{p}{\rho_s g} + z \tag{3.2}$$

where p is the pore pressure, ρ_f and ρ_s are the fresh water and saltwater densities respectively, g is the gravitational acceleration, and positive z directional coordinate is defined in the negative gravitational acceleration direction. Since the pressure is continuous across the fresh water and saltwater interface and is the same at the interface as one approaches the interface from either of the two zones, the pressure can be expressed in terms of the saltwater density as

$$p = (d - z) g \rho_s \tag{3.3}$$

where d is the sea level measured from the base of the aquifer (Figure 3.1). For aquifers that are relatively shallow (i.e., flowlines are nearly horizontal), the Dupuit assumption [Bear, 1979] can be applied and h_f and h_s can be defined to be invariant in the vertical

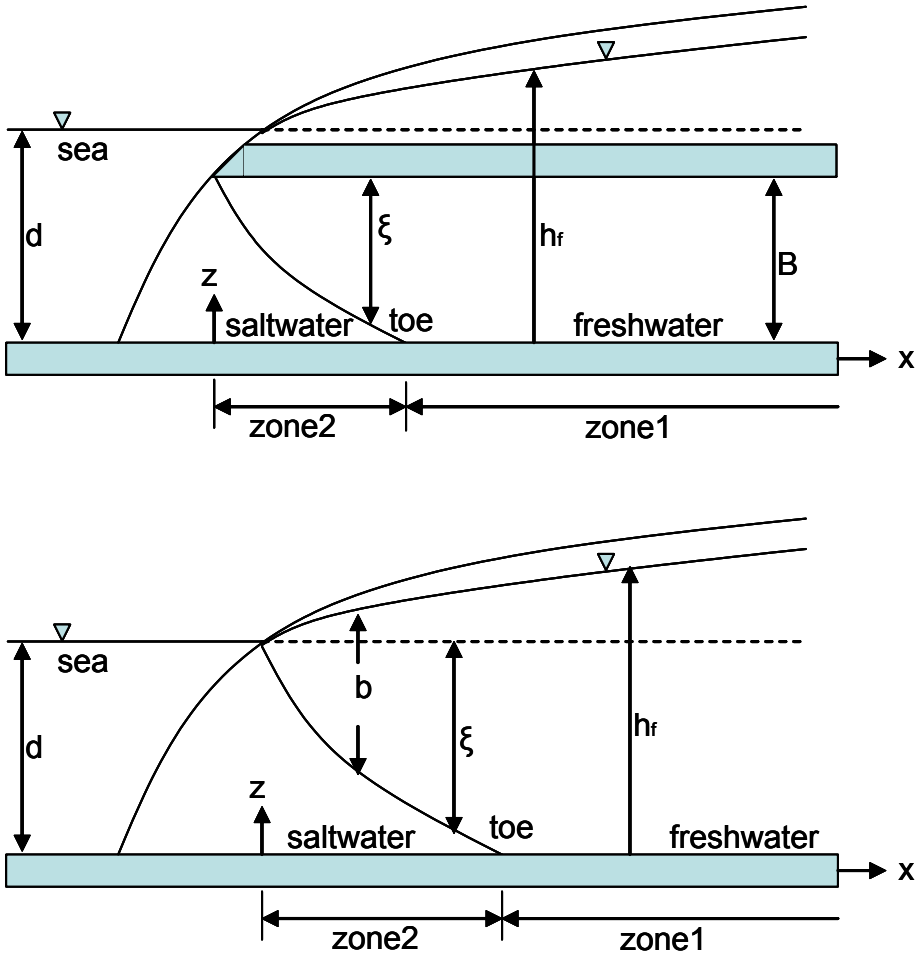

Figure 3.1 Cross-sections of coastal aquifers: a confined aquifer and an unconfined aquifer

direction by integrating the flow equation in the vertical direction. Substituting Equation (3.3) into Equation (3.1) and rearranging in terms of the ratio of the density difference to the density of the fresh water yields

$$h_f - d = \left(\frac{\rho_s - \rho_f}{\rho_f} \right) (d - z) \tag{3.4}$$

Defining the depth of the interface from the sea level, $\xi = d - z$, the relationship known as the Ghyben and Herzberg assumption is provided as

$$\xi = \frac{\rho_f}{(\rho_s - \rho_f)} (h_f - z) \approx 40 (h_f - z) \tag{3.5}$$

The corresponding densities for the fresh water and the saltwater are $\rho_f = 1.0\, g/cm^3$ and $\rho_s = 1.025\, g/cm^3$ respectively to obtain the constant in Equation (3.5).

Strack [1976] proposed a single potential for the two zones (i.e., zone 1 for the fresh water and zone 2 for the saltwater, Figure 3.1). The potential is continuous across the interface so that only a single governing equation can be applied to both the fresh water and saltwater zones. With the Ghyben-Herzberg relation to define the interface as well as the Dupuit assumption, the freshwater head can be described as a function of horizontal coordinates only. Assuming that the aquifer is homogeneous, a governing equation of the fresh water head valid for both zone 1 and zone 2 and for confined as well as unconfined aquifers can be written as

$$\nabla \cdot (b \nabla h_f) = 0 \tag{3.6}$$

where $b = b(x, y)$ is the thickness of freshwater for unconfined aquifers in Figure 3.1. Similarly for confined aquifers in Figure 3.1, aquifer thickness (B) can also be expressed in the form of $b = b(x, y)$. Thus, Equation (3.6) is also valid for the confined aquifer.

Following Strack [1976] and Cheng et al. [1999; 2000], a potential ϕ is defined for both confined and unconfined aquifers as follows:

For confined aquifers:

$$\phi = Bh_f + \frac{(s-1)B^2}{2} - sBd \qquad zone1 \tag{3.7}$$

$$\phi = \frac{1}{2(s-1)}\left[h_f + (s-1)B - sd\right]^2 \qquad zone2 \tag{3.8}$$

For unconfined aquifers:

$$\phi = \frac{1}{2}\left[h_f^2 - sd^2\right] \qquad zone1 \tag{3.9}$$

$$\phi = \frac{s}{2(s-1)}\left(h_f - d\right)^2 \qquad zone2 \tag{3.10}$$

where d is the elevation of mean sea level above the datum, Figure 3.1, and B is the confined aquifer thickness. The density ratio of the fresh water and saltwater is,

$$s = \frac{\rho_s}{\rho_f} \tag{3.11}$$

The potential defined by Equations (3.7) through (3.10) satisfies the Laplace equation $\nabla^2\phi = 0$ in the horizontal (x-y) plane. The problem is solved as a one-zone problem with appropriate boundary conditions that are provided as in the example in Appendix A.1. Once the problem is solved by analytical or numerical methods, the interface location ξ is evaluated as

For a confined aquifer:

$$\xi = \sqrt{\frac{2\phi}{s-1}} + d - B \tag{3.12}$$

For an unconfined aquifer:

$$\xi = \sqrt{\frac{2\phi}{s(s-1)}} \tag{3.13}$$

From Figure 3.1, the toe of saltwater can be evaluated at $\xi = d$. Hence, the potential at the toe can be calculated from Equation (3.12) and (3.13).

For a confined aquifer:

$$\phi_{toe} = \frac{s-1}{2} B^2 \tag{3.14}$$

For an unconfined aquifer:

$$\phi_{toe} = \frac{s(s-1)}{2} d^2 \tag{3.15}$$

Since the Laplace equation is linear, the freshwater potential for multiple pumping wells, in an aquifer with uniform flow, can be obtained using the method of superposition and the use of potential flow theory [Strack, 1976; Cheng et al., 2000].

$$\phi = \frac{q}{K} x + \sum_{i=1}^{n} \frac{Q_i}{4\pi K} \ln\left[\frac{(x-x_i)^2 + (y-y_i)^2}{(x+x_i)^2 + (y-y_i)^2}\right] \tag{3.16}$$

where Q_i is the pumping rate of well i, $\left[L^3T^{-1}\right]$, q is the fresh water volume outflow rate per unit length of coastline, $\left[L^2T^{-1}\right]$, and (x_i, y_i) are well coordinates. Based on potentials defined from Equation (3.7) to (3.10), Equation (3.16) is valid for both confined and unconfined aquifers. Using either Equation (3.14) or (3.15) in Equation (3.16), the toe location for the multiple wells can be solved.

The location of multiple stagnation points of the flow field is important to define the maximum pumping rate for the pumping wells. The locations of the stagnation points can be obtained from the following relation [Strack, 1976],

$$\frac{\partial \phi}{\partial x} = \frac{\partial \phi}{\partial y} = 0 \tag{3.17}$$

Differentiating Equation (3.16):

$$\frac{\partial \phi}{\partial x} = \frac{q}{K} + \sum_{i=1}^{n} \frac{Q_i}{4\pi K} \frac{(x+x_i)^2 + (y-y_i)^2}{(x-x_i)^2 + (y-y_i)^2} \left[\frac{2(x-x_i)}{(x+x_i)^2 + (y-y_i)^2} - 2(x+x_i) \frac{(x-x_i)^2 + (y-y_i)^2}{\{(x+x_i)^2 + (y-y_i)^2\}^2} \right] \tag{3.18}$$

$$\frac{\partial \phi}{\partial y} = \sum_{i=1}^{n} \frac{Q_i}{4\pi K} \frac{(x+x_i)^2 + (y-y_i)^2}{(x-x_i)^2 + (y-y_i)^2} \left[\frac{2(y-y_i)}{(x+x_i)^2 + (y-y_i)^2} - 2(y+y_i) \frac{(x-x_i)^2 + (y-y_i)^2}{\{(x+x_i)^2 + (y-y_i)^2\}^2} \right] \tag{3.19}$$

Equations (3.18) and (3.19) form a set of nonlinear equations. A Newton-Raphson method was used to find the stagnation points from these equations. These equations need to be further differentiated to make use of the Newton-Raphson method. The derivatives of these equations are provided in Appendix A.2. The stagnation point location is used to detect the well-intrusion, by comparing the location of this point relative to the toe location on the coastline.

The cases of well intrusion conditions are numerous depending on the interactions among the extraction wells as well as the physical parameters of aquifers. In general, the number of the well intrusion cases is increasing with increasing number of wells placed. To illustrate several examples of the well intrusion conditions, various cases of the well

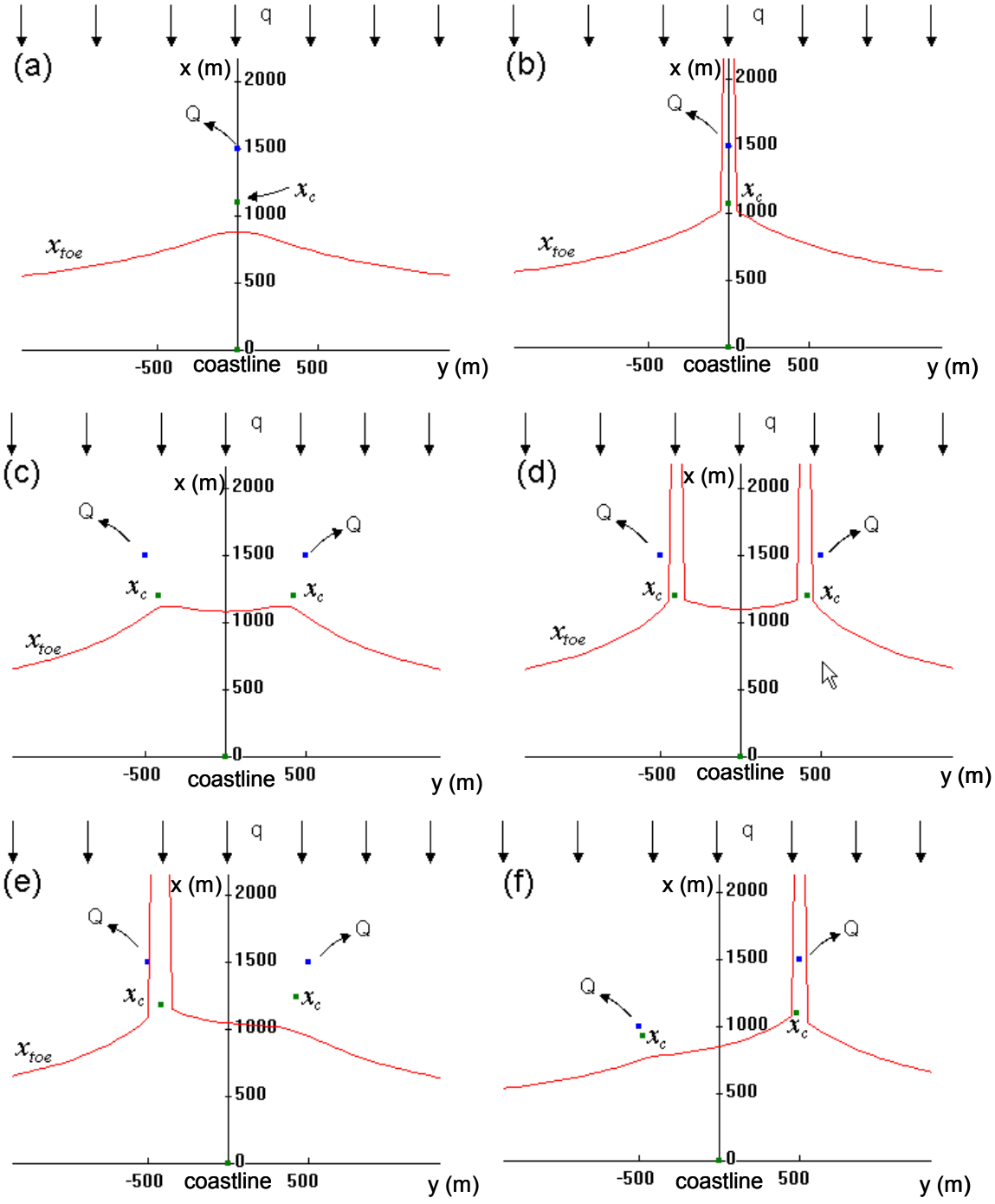

Figure 3.2 Pumping wells near a coastline : (a) One pumping well un-intruded case; (b) One pumping well intruded case; (c) Two pumping well un-intruded case; (d) Two pumping well intruded case; (e) Symmetric two pumping well intruded case; (f) Asymmetric two pumping well intruded case

intrusion condition for one- and two-pumping well conditions in an arbiturary selected unconfined aquifer are provided in Figure 3.2. Obviously, in reality the cases with more than one- and two-pumping well conditions are more realistic but more complex than these simple cases.

3.3 Formulation of Saltwater Intrusion Problem

In most cases, one of the objectives in the optimal solution of a saltwater intrusion problem is maximizing the pumping rate. The optimization of the saltwater intrusion problem becomes unique, if the extraction wells are forced to be placed as closely as possible to the coast, since the development region maybe selected close to the coastline. Excessive pumping in these situations, in practice, causes the saltwater intrusion problem. If the extraction wells can be placed further away from the coastline, all the extraction wells may be allowed to pump higher rates of fresh water with no limitations. In order to integrate this constraint into the saltwater intrusion problem, another objective is introduced such that all extraction wells should be placed as close to the coastline as possible. This, in turn, restricts the first objective, that is maximizing the pumping rate.

Researchers working on these multi-objective problems have attempted to solve the multi-objective optimization problem using various techniques. Fonseca and Fleming [1993; 1995] used the genetic algorithm (GA) for solving multi-objective problems and introduced the concept of dominated and non-dominated populations. There are other techniques associated with the solution of multi-objective problems, such as fitness sharing, niche approach, etc [Fonseca and Fleming, 1993; Fleming and Fonseca, 1995]. The GA uses the survival of the fittest idea for selecting competitive populations. This

selection process is linear in the scalar objective value of each population. However, the main difficulty originates from the multi-objective nature of the problem. There may be no simple way to differentiate the relative importance of each objective in the selection of the fittest. The easiest way to deal with multiple objectives is to use the summation of each objective function to form a single scalar objective function. However, this brings disadvantages such as the difficulty of adjusting the weight of each objective. This is basically because a single scalar objective function generated is not capable of representing the vector tendency of each objective. Nonetheless, in this work the single scalar objective function approach is used for simplicity. The two objectives of the optimization problem are given as follows:

The first objective: Maximizing the pumping rate.

$$Max \sum_{i=1}^{n} Q_i \tag{3.20}$$

The second objective: Minimizing the distance between the stagnation points and the reference coastline location.

$$Min \sum_{i=1}^{n} (x_c^i - x_{ref}) \tag{3.21}$$

Equation (3.21) is modified to convert the second objective to be a maximization problem,

$$Max \left(- \sum_{i=1}^{n} (x_c^i - x_{ref}) \right) \tag{3.22}$$

The combined and normalized objective function can be written as,

$$f\left(Q, x_{ref}, x_c^i\right) = \sum_{i=1}^{n} \left(\alpha \frac{Q_i}{Q_i^{\max}} + \beta \left(\frac{x_{ref}}{x_c^i} - 1 \right) \right) \tag{3.23}$$

Subject to the following conditions,

$$x_{toe}^{i}(Q,X,Y) < x_{c}^{i}(Q,X,Y) \tag{3.24}$$

$$Q_i^{\min} < Q_i < Q_i^{\max},\ x_i^{\min} < x_i < x_i^{\max},\ y_i^{\min} < y_i < y_i^{\max}\ \ i = 1,...,n \tag{3.25}$$

where Q_i is the pumping rate of well i, x_c^i is the stagnation point associated with the pumping well Q_i, x_{ref} is the coastline, x_{toe}^i is the toe location, and α and β are the objective function weighting parameters. The independent variable vectors, Q, X, Y, will be re-defined in the modified optimization formulation for the PGA application.

3.4 The Modified Optimization Model

Cheng et al. [2000] used the discretized pumping rate as an independent variable for optimizing pumping rates of fifteen fixed wells in a case study. This independent variable itself requires a large number of simulations for the solution of the optimization problem. For a typical application, it is almost impossible to complete an exhaustive search for the global optimal solution. To avoid this computationally intensive approach, the independent variables of the optimization problem are chosen differently. Rather than having pumping rates and well locations as independent variables, the perturbations of these variables were chosen as independent variables. In this way, the GA solution can eliminate a considerable amount of unnecessary simulations at each step of the iterative solution.

To achieve this, for each optimization step of each perturbation, a sub-domain needs to be defined, and the search is conducted within this sub-domain. No matter where the simulation starts, there is a path from this starting point to the optimal solution. The direction from the current to the next location on the correct path may be determined

easily by the GA within the pre-determined sub-domain, even if it is far away from an optimal solution. This approach allows the consequent sub-domains to move in the optimal direction as well, which leads the solutions closer to the global optimum. Thus, within each step the solution gets closer to the optimal solution by effectively eliminating the unnecessary paths, as shown in Figure 3.3a.

The saltwater intrusion problem is complex, due to the dependence of the pumping rates and well locations on each other. The sub-domain concept handles this dependence issue effectively and provides good feedback as the simulation proceeds. This approach filters out the unnecessary runs by taking the direction of the moving wells or adjusting the pumping rates during the iteration. One other advantage of this method is that the independent variables are continuous variables rather than discrete ones variation of which is fixed priori.

In this approach, the modified objective function, the constraints and the independent variables of the perturbations yield the following formulation:

$$f\left(Q, x_{ref}, x_c^i\right) = \sum_{i=1}^{n}\left(\alpha \frac{Q_i^0 + \Delta Q_i}{Q_i^{\max}} + \beta\left(\frac{x_{ref}}{x_c^i} - 1\right)\right) \tag{3.26}$$

$$\Delta Q_i^{\min} < \Delta Q_i < \Delta Q_i^{\max},\ \Delta x_i^{\min} < \Delta x_i < \Delta x_i^{\max},\ \Delta y_i^{\min} < \Delta y_i < \Delta y_i^{\max}\ \ i = 1,...,n \tag{3.27}$$

where

$$\Delta Q_i^{\min} = Q_i^{\min} - Q_i^0;\ \Delta Q_i^{\max} = Q_i^{\max} - Q_i^0 \tag{3.28a}$$

$$\Delta x_i^{\min} = x_i^{\min} - x_i^0;\ \Delta x_i^{\max} = x_i^{\max} - x_i^0 \tag{3.28b}$$

$$\Delta y_i^{\min} = y_i^{\min} - y_i^0;\ \Delta y_i^{\max} = y_i^{\max} - y_i^0 \tag{3.28c}$$

$Q_i^0, x_i^0, and\ y_i^0$ are initial starting points, and the bounding sub-domain is determined to be polyhedron having the starting points at the center of the polyhedron.

(a)

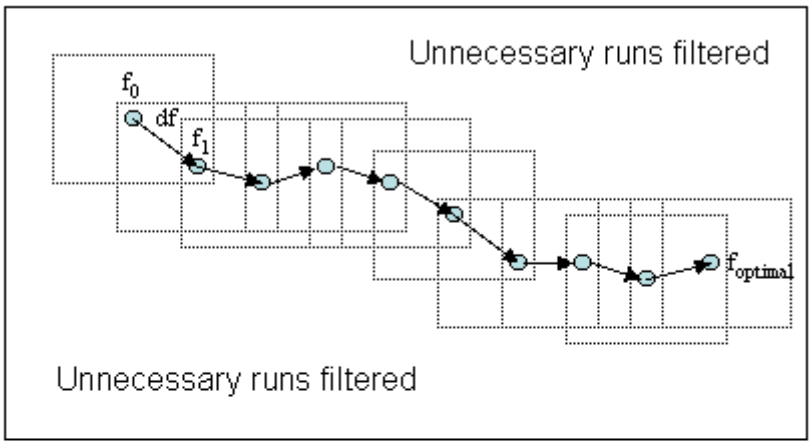

(b)

$$Parent\ 1: (\Delta Q_1, \Delta x_1, \Delta y_1)(\Delta Q_2, \Delta x_2, \Delta y_2)\cdots(\Delta Q_n, \Delta x_n, \Delta y_n)$$

$$Parent\ 2: (\Delta \tilde{Q}_1, \Delta \tilde{x}_1, \Delta \tilde{y}_1)(\Delta \tilde{Q}_2, \Delta \tilde{x}_2, \Delta \tilde{y}_2)\cdots(\Delta \tilde{Q}_n, \Delta \tilde{x}_n, \Delta \tilde{y}_n)$$

$$\Downarrow$$

$$Child: \begin{pmatrix} \Delta Q_1 & \Delta x_1 & \Delta y_1 \\ or & or & or \\ \Delta \tilde{Q}_1 & \Delta \tilde{x}_1 & \Delta \tilde{y}_1 \end{pmatrix} \begin{pmatrix} \Delta Q_2 & \Delta x_2 & \Delta y_2 \\ or & or & or \\ \Delta \tilde{Q}_2 & \Delta \tilde{x}_2 & \Delta \tilde{y}_2 \end{pmatrix} \cdots \begin{pmatrix} \Delta Q_n & \Delta x_n & \Delta y_n \\ or & or & or \\ \Delta \tilde{Q}_n & \Delta \tilde{x}_n & \Delta \tilde{y}_n \end{pmatrix}$$

n is the number of wells

Figure 3.3 (a) The concept of eliminating unnecessary runs using perturbation method by choosing one path rather than searching the whole solution domain; (b) Coding and crossover of design variables

In order to handle the inequality constraint of Equation (3.24) properly in the objective function of the GA, a slack vector and penalty functions are introduced. Thus, the modified objective function and constraints can be given as follows,

$$f\left(Q, x_{ref}, x_c^i\right) = \sum_{i=1}^{n}\left(\alpha \frac{Q_i^0 + \Delta Q_i}{Q_i^{\max}} + \beta\left(\frac{x_{ref}}{x_c^i} - 1\right)\right) - \sum_{\forall_i} \gamma s^2 \tag{3.29}$$

$$x_{toe}^i(Q, X, Y) + S = x_c^i(Q, X, Y) \qquad S \geq 0 \tag{3.30}$$

where $\gamma = \begin{cases} c_1 \ if \ s_i < 0 \\ 0 \ otherwise \end{cases}$ and c_1 is any large constant.

It should be noted that the independent variables of this formulation are the perturbations, $\Delta Q_i, \Delta x_i, \Delta y_i$.

3.5 Genetic Algorithm

In GA's [Davis, 1987; Goldberg, 1989; Holland, 1992], the parameter set of the optimization problem is coded as a finite-length string. Traditionally, binary numbers are used to represent such a string. Thus, each bit of a string can be either 0 or 1. Owing to the dramatic growth of computer technology, the use of the binary representation is somewhat cumbersome these days. Since the vector representation of real numbers for the real function optimization is more natural and of no difficulty, the real-number coding is used in this study [Obayashi et al., 2000]. Thus, the length of the real-number string corresponds to the number of design variables (i.e., independent variables).

In order for the modified model to work inside the sub-domain, the GA search process must be limited to a sub-domain in the neighborhood of $\left\{Q^0, X^0, Y^0\right\}$. The search sub-domains of the independent variables are evaluated as follows,

$$\delta Q_i = \frac{Q_i^{\max} - Q_i^{\min}}{k_1} \tag{3.31a}$$

$$\delta x_i = \frac{x_i^{\max} - x_i^{\min}}{k_2} \tag{3.31b}$$

$$\delta y_i = \frac{y_i^{\max} - y_i^{\min}}{k_3} \tag{3.31c}$$

In the neighborhood of $\{Q^0, X^0, Y^0\}$, the intervals, $[\Delta Q_{lower}, \Delta Q_{upper}]$, $[\Delta X_{lower}, \Delta X_{upper}]$, and $[\Delta Y_{lower}, \Delta Y_{upper}]$ are determined by,

$$\Delta Q_i^{lower} = \max\{\Delta Q_i^{\min}, -0.5e^{-\eta k}\delta Q_i\} \tag{3.32a}$$

$$\Delta Q_i^{upper} = \min\{\Delta Q_i^{\max}, 0.5e^{-\eta k}\delta Q_i\} \tag{3.32b}$$

$$\Delta x_i^{lower} = \max\{\Delta x_i^{\min}, -0.5e^{-\eta k}\delta x_i\} \tag{3.32c}$$

$$\Delta x_i^{upper} = \min\{\Delta x_i^{\max}, 0.5e^{-\eta k}\delta x_i\} \tag{3.32d}$$

$$\Delta y_i^{lower} = \max\{\Delta y_i^{\min}, -0.5e^{-\eta k}\delta y_i\} \tag{3.32e}$$

$$\Delta y_i^{upper} = \min\{\Delta y_i^{\max}, 0.5e^{-\eta k}\delta y_i\} \tag{3.32f}$$

where k_1, k_2, and k_3 are positive integers (e.g. $k_1 = k_2 = k_3 = 5$), k is the index of iteration, η is a positive coefficient (e.g. $\eta = 0.001$), $e^{-\eta k}$ is a contraction coefficient for the sub-domain. The sub-domain defined by Equation (3.32) forms a regular polyhedron, with the center located at $\{Q^0, X^0, Y^0\}$. The volume of the polyhedron decreases by the contraction function as the number of iterations increases. The idea of decreasing sub-domain size makes sense, especially when the solution approaches to a local (sub-domain) or to the global optimal solution. In this way, more precise populations can be

generated in the reproduction of the GA. Obviously, the sub-domain defined should satisfy,

$$\left[\Delta Q_{lower},\ \Delta Q_{upper}\right] \subseteq \left[\Delta Q_{\min},\ \Delta Q_{\max}\right] \tag{3.33a}$$

$$\left[\Delta X_{lower},\ \Delta X_{upper}\right] \subseteq \left[\Delta X_{\min},\ \Delta X_{\max}\right] \tag{3.33b}$$

$$\left[\Delta Y_{lower},\ \Delta Y_{upper}\right] \subseteq \left[\Delta Y_{\min},\ \Delta Y_{\max}\right] \tag{3.33c}$$

The GA approach consists of generating populations, applying genetic operators such as crossover and mutation. Normally, the populations are generated in the discretized domain randomly. Since each optimization step works within its sub-domain, the populations generated for that step should satisfy the sub-domain constraints. The other technique introduced here, is the contraction function used in defining the sub-domains. For this purpose, various contraction functions, including the one used in this study, can be defined. This approach would be similar to the definition of the energy used in the *Boltzmann* probability distribution, when simulated annealing approach is employed. This process reduces the number of iterations and thus the computational time [Dougherty and Marryott, 1991; Shonkwiler, 2000].

The crossover of the GA is designed such that the offspring inherits the gene from either parent with equal chance. Figure 3.3b illustrates the coding of the crossover. The purpose of the mutation operator in the GA is to give diversity to the genes in the population. This diversity is intended to seek a better optimum, when the solution is stuck in a lower local optimum. In this work, the mutation is designed to reassign different pumping rates to the selected population within the allowed bounds previously defined. Generally, the probability of the mutation is set much lower than that of the crossover.

3.6 Convergence

Since it is impossible to know if the solution has reached the global optimum, the relative error of the objective function was used to escape the GA loop. Thus, the convergence criterion is defined as,

$$\frac{|f_1 - f_0|}{f_0} \leq \varepsilon \tag{3.34}$$

ε is a predefined tolerance for the convergence of iterations. In this study, the tolerance of *0.001* was used for all the simulations. If two consecutive objective values satisfy the criterion given in Equation (3.34), then $\{Q^1, X^1, Y^1\}$ is chosen as a final solution in the corresponding sub-domain. Otherwise, the solution sequence continues with the new starting point at $Q_i^0 = Q_i^1,\ x_i^0 = x_i^1,\ y_i^0 = y_i^1,\ k = k+1,\ i = 1,...n$.

3.7 Applications

Several numerical experiments are performed to test the accuracy of the proposed model and the solution algorithm. The numerical examples included here are single- and multi-objective problems, where well locations and pumping rates are selected as independent variables. For single objective problems, maximization of the pumping rate is considered as the objective function. For one- and two-well cases, the global solution can be deduced from the heuristic observation that the pumping well needs to be placed farther inland, limited by the boundaries of the selected solution domain. This way, the pumping rates can be increased to a maximum value, given the constraint that the pumping wells are not to be intruded by saltwater. This constraint is evaluated by comparing the position of the stagnation point and the location of each well. Table 3.1

Table 3.1 Summary of modeling parameters for one and two pumping well cases

Aquifer parameters	**Value**	**MOGA (Multi-Objective Genetic Algorithm) parameters**	**Value**
Aquifer type	unconfined	**α**	1
Saltwater density	1.025 g/cm^3	**β**	0
Uniform flow rate	0.6 m^2/d	**Population size**	40
Saltwater depth	14 m	**Mating probability**	0.9
Hydraulic conductivity	100 m/d	**Mutation probability**	0.1
		Convergence	0.001

Sub-domain and bounding parameters (for all wells)

	Single well	**Double wells**
$\mathbf{k_1}$	250	250
$\mathbf{k_2}$	150	150
$\mathbf{k_3}$	150	150
η	0.00001	0.00001
$\mathbf{Q_{min}, Q_{max}}$ **m^3/d**	100, 6000	100, 5000
$\mathbf{x_{min}, x_{max}}$ **m**	0, 4000	0, 4000
$\mathbf{y_{min}, y_{max}}$ **m**	-3500, 3500	-3500, 3500

Starting Points			**Optimal Points**		
Q,m^3/d	***x*, m**	**y, m**	**Q,m^3/d**	***x*, m**	**y, m**
One well					
Q_1=300	x_1=1000	y_1 = 0	5433.74	3999.7	33.9
Two wells					
Q_1=300	x_1=1000	y_1 = 0	4474.88	3998.5	3497.1
Q_2=300	x_2=1000	y_2=1500	4477.56	3998.3	-3497.4

lists the physical parameters used in the examples included here, and the GA parameters used for the simulation of one- and two-pumping well cases for an unconfined aquifer. In these applications, the aquifer domain setting and physical parameters selected are similar to those used in Cheng et al. [2000].

Example 1: In this example, one-well and two-well cases are considered. The aquifer domain is 4,000 m by 7,000 m. A uniform freshwater flow of 0.6 m^2/d exists in the negative x direction. The aquifer is unconfined, with a hydraulic conductivity of 100 m/d. The saltwater depth at the coastline is 14 m. The minimum and maximum allowable pumping rates are selected as 100 m^3/d to 6,000 m^3/d for the one-well case and 100 m^3/d to 5,000 m^3/d for the two-well case. The starting position of the well (x, y) is at coordinates (1,000, 0) for the one-well case and (1,000, -1,500); (1,000, 0) for the two-well case. Other parameters of this problem can be found in Table 3.1.

As shown in Figure 3.4a, as the solution progresses, the extraction well moves farther inland for the one-well case, while the pumping rate increases, reaching a maximum value 6,000 m^3/d. In all figures, the dotted line shows the location of the saltwater interface, the cross marks show the location of the stagnation point and the plus sign shows the location of the pumping well. Since there is no pumping well interaction in the one-well case, there is an infinite number of solutions for this problem. That is, a well placed on any y-coordinate position at the domain boundary would yield the same results at all iteration steps as well as the final solution.

Unlike with the one-well case, there is only one global optimum for the two-well case. This is because of the interaction between the two wells. Obviously, in the two-well

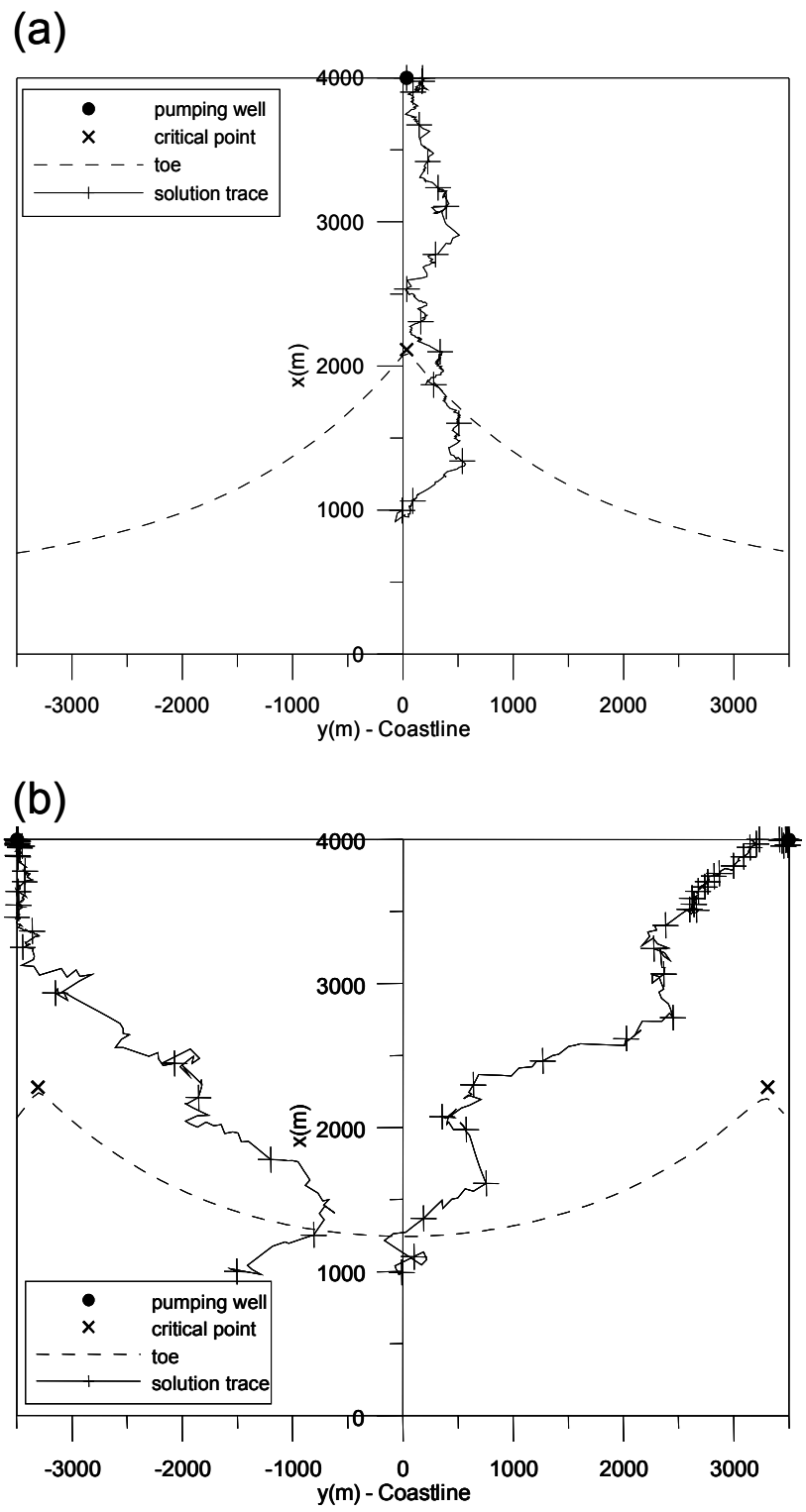

Figure 3.4 (a) One pumping well placement optimization path; (b) Two pumping well placement optimization path

application, the extraction wells spread as far as possible from each other to reduce the well interaction, which also leads to the maximization of the pumping rates. In Figure 3.4, it is shown that the trace of the well positions for these two cases, including the global optimum positions after the solution is completed.

Example 2: With the same single objective of maximizing the pumping rate, the results of three-, two of four- and five-well cases are shown in Figure 3.5. In these cases, the aquifer domain and aquifer parameters are the same as in Example 1. Other selected modeling parameters are given Table 3.2. Although the number of pumping wells for each of these four cases is different, the optimal total pumping rates are close to each other. This result indicates that, for the single objective problem, the optimal total pumping rate for a finite domain can be achieved by a finite number of wells, and adding more wells to the domain will not improve the maximum pumping rate significantly. This can be seen in Figure 3.6. The maximum economical number of wells for this domain is 3, since the total pumping rate does not increase significantly, if more wells are added to the solution. The average pumping rate for the wells is also shown in Figure 3.6.

Based on the heuristic point stated previously, the global maximum pumping rates for this simple application can be obtained, when the well locations and the pumping rates are perturbed simultaneously. It should be noted that once the critical number of wells is established within the problem domain, adding more wells often creates a similar shape of toe delineation to the case of the critical number of wells. This can be observed from Figure 3.5d, i.e. there are three peaks even though the number of wells is four. Note that this figure represents an intermediate solution obtained from the four-well solution. This

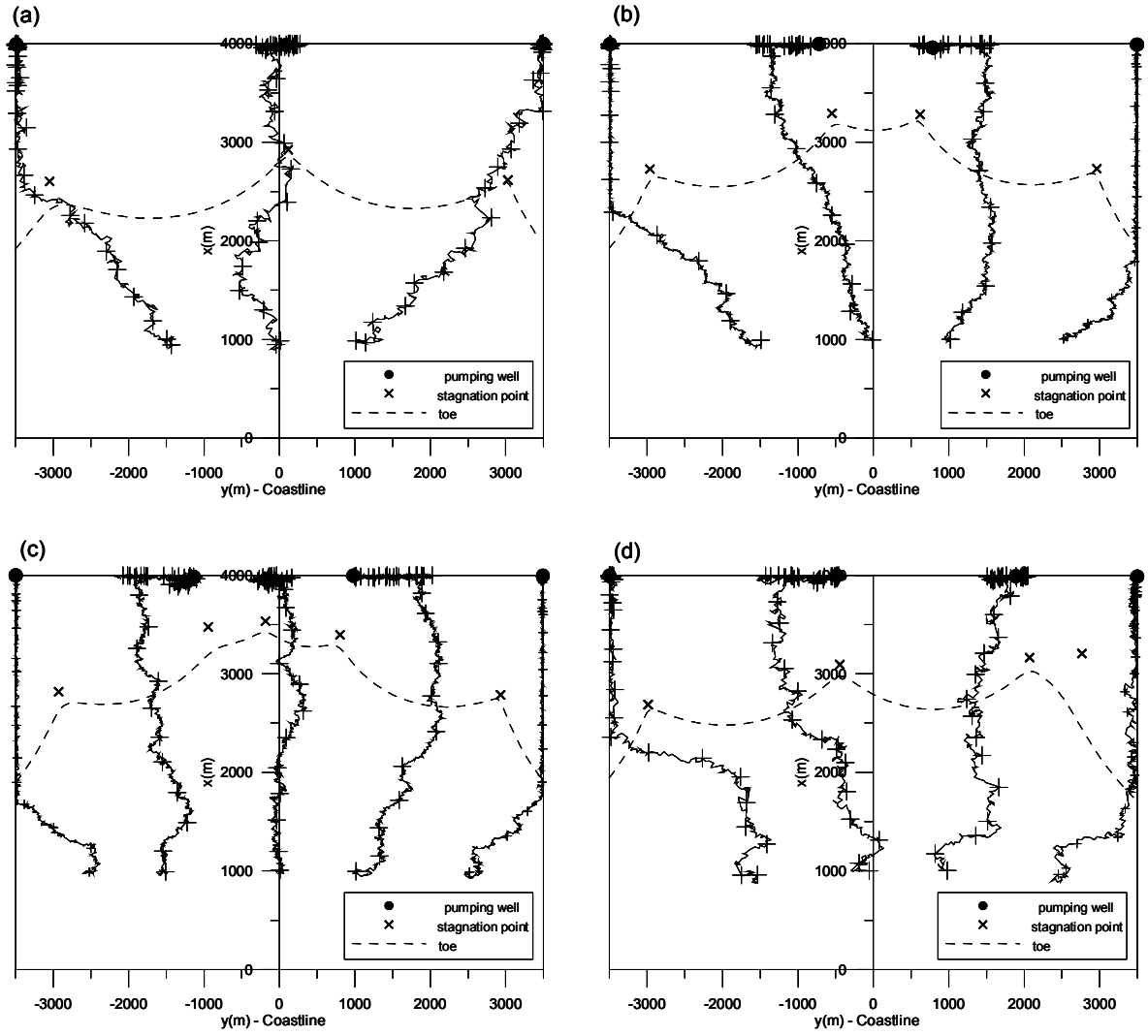

Figure 3.5 (a) Three pumping well placement optimization path; (b) Four pumping well placement optimization path; (c) Five pumping well placement optimization path; (d) Four pumping well placement optimization path (an intermediate solution – similar toe pattern to that given in (a))

Table 3.2 Summary of modeling parameters for three-, four- and five pumping well cases

Aquifer parameters	**Value**	**MOGA parameters**	**Value**
Same as Table 3.1.			
Sub-domain and bounding parameters (for all wells)			
	Three wells (a)	**Four wells (b)**	**Five wells (c)**	**Four wells (d)**
$\mathbf{k_1}$	250			
$\mathbf{k_2}$	150			
$\mathbf{k_3}$	150			
η	0.00001			
$\mathbf{Q_{min}, Q_{max}}$ $\mathbf{m^3/d}$	100, 4000			
$\mathbf{x_{min}, x_{max}}$ **m**	0, 4000			
$\mathbf{y_{min}, y_{max}}$ **m**	-3500, 3500			

Starting Points			**Optimal Points**		
Q,m^3/d	***x*, m**	**y, m**	**Q,m^3/d**	***x*, m**	**y, m**
Three wells (a)					
Q_1=300	x_1=1000	y_1 = 0	2195.6	3987.1	89.7
Q_2=300	x_2=1000	y_2=-1500	3561.5	3994.3	-3491.4
Q_3=300	x_3=1000	y_3=1000	3530.3	3997.3	3499.4
Four wells (b)					
Q_1=300	x_1=1000	y_1 = 0	1447.4	3997.1	-596.4
Q_2=300	x_2=1000	y_2=-1500	3371.9	3995.0	-3497.6
Q_3=300	x_3=1000	y_3=1000	1293.3	3975.4	993.9
Q_4=300	x_4=1000	y_4=2500	3207.5	3998.4	3495.0
Five wells (c)					
Q_1=300	x_1=1000	y_1 = 0	725.1	3966.2	-161.6
Q_2=300	x_2=1000	y_2=-1500	1031.2	3981.4	-1136.0
Q_3=300	x_3=1000	y_3=1000	1206.4	3997.0	978.7
Q_4=300	x_4=1000	y_4=2500	3200.2	3995.6	3492.0
Q_5=300	x_5=1000	y_5=-2500	3155.6	3999.9	-3498.8
Four wells (d)					
Q_1 = 300	x_1 = 1000	y_1 = 0	1817.5	3997.6	-474.9
Q_2 = 300	x_2 = 1000	y_2 = -1500	3385.2	3996.9	-3491.9
Q_3 = 300	x_3 = 1000	y_3 = 1000	1402.5	3994.3	1902.6
Q_4 = 300	x_4 = 1000	y_4 = 2500	2567.9	3989.9	3490.5

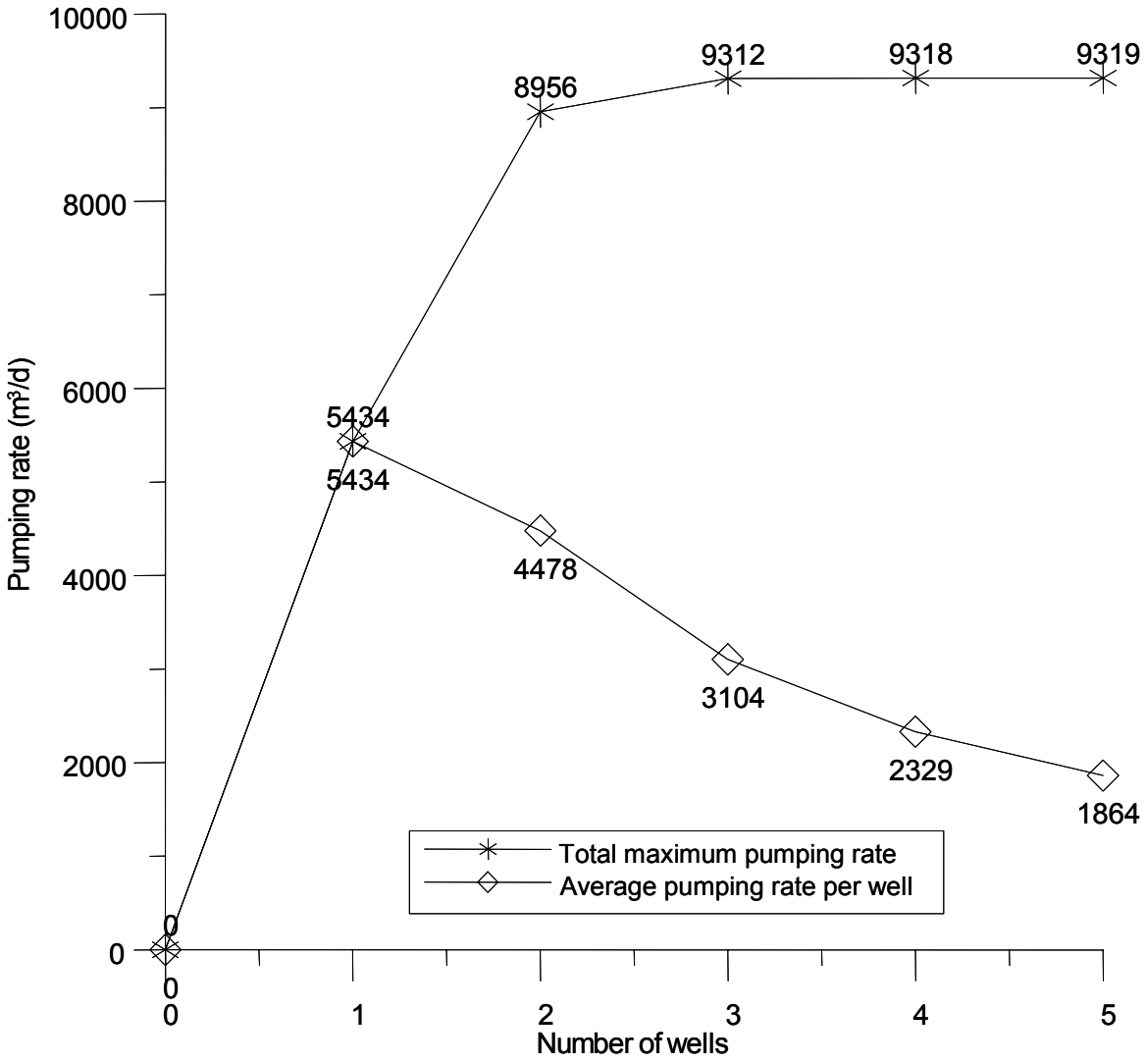

Figure 3.6 The relationship between the number of wells and the maximum pumping rates and the average pumping rate per well

indicates that the same optimal pumping rate from three pumping wells can be obtained from four pumping wells by formulating a similar pattern of toe delineation. Since Figure 3.5d is an intermediate solution, continuing the simulation will lead to the results shown in Figure 3.5b. Obviously, the improvement achieved is minimal as shown in Figure 3.6, since the four pumping wells are already more than the critical number of wells for this case.

Example 3: Another practical application of the procedure developed in this study is the solution to the saltwater intrusion problem for fixed well locations. In a sequential approach, the model developed can first be used to optimize the pumping rates for the existing wells to prevent the saltwater intrusion. In such a case, the independent variable vector consists of only the pumping rates of each well. With the current model, this situation can be simulated very easily by not allowing perturbations for well locations.

To test the current model for fixed well location case, a comparison between Cheng et al.'s work [2000] and the model developed in this study is presented for two cases. Table 3.3 provides the physical parameters of the aquifer and all other related pumping well information. After the evaluation on the physical parameters used by Cheng et al., their fresh water discharge of 40 m^2/d is evaluated to be a typing error since this fresh water discharge is too large. Instead, for this problem, a value of 0.4015 m^2/d is used as the fresh water discharge to duplicate their results.

The first case is the Case 1 of the example problems presented in Cheng et al. [2000] which consists of eight wells. The second is Case 3 of the same work which contains seven wells. In their work, they initially started with a total of fifteen wells and

Table 3.3 Summary of modeling parameters and the comparison of results with Cheng et al. [2000] fixed well optimization example

Aquifer parameters	**Value**	**MOGA parameters**	**Value**
Aquifer type	unconfined	α	1
Saltwater density	1.025 g/cm^3	β	0
Uniform flow rate	0.4015 m^2/d	**Population size**	20
Saltwater depth	15 m	**Mating probability**	0.9
Hydraulic conductivity	40 m/d	**Mutation probability**	0.1
		Convergence	0.1

Sub-domain and bounding parameters (for all wells)

	Case 1 (eight wells)	**Case 3 (seven wells)**
$\mathbf{k_1}$	150	250
$\mathbf{k_2}$	0 (fixed-well)	150
$\mathbf{k_3}$	0 (fixed-well)	150
η	0.000001	0.000001
$\mathbf{Q_{min}, Q_{max}}$ **m^3/d**	150, 1500	100, 5000
$\boldsymbol{x_{min}, x_{max}}$ **m**	0, 4000	0, 4000
$\mathbf{y_{min}, y_{max}}$ **m**	-3500, 3500	-3500, 3500

Starting Points			**Optimal Pumping Rate**	
Q, m^3/d	***x*, m**	**y, m**	**Q, m^3/d**	
Case 1 (eight wells) fixed-well				
			Cheng et al.'s	This work
$Q_1 = 150$	$x_1 = 1000$	$y_1 = 2500$	$Q_1 = 255$	$Q_1 = 221.7$
$Q_2 = 150$	$x_2 = 1700$	$y_2 = 1100$	$Q_2 = 402$	$Q_2 = 579.8$
$Q_3 = 150$	$x_3 = 1800$	$y_3 = -300$	$Q_3 = 158$	$Q_3 = 154.4$
$Q_4 = 150$	$x_4 = 3500$	$y_4 = -500$	$Q_4 = 728$	$Q_4 = 733.2$
$Q_5 = 150$	$x_5 = 1600$	$y_5 = -800$	$Q_5 = 150$	$Q_5 = 151.1$
$Q_6 = 150$	$x_6 = 3600$	$y_6 = -2800$	$Q_6 = 1500$	$Q_6 = 1402.9$
$Q_7 = 150$	$x_7 = 1400$	$y_7 = -3000$	$Q_7 = 185$	$Q_7 = 215.9$
$Q_8 = 150$	$x_8 = 2000$	$y_8 = -2000$	$Q_8 = 232$	$Q_8 = 178.4$
			$Q_{total} = 3610$	$Q_{total} = 3637.4$
Case 3 (seven wells) fixed-well				
			Cheng et al.'s	This work
$Q_1 = 150$	$x_1 = 1000$	$y_1 = 2500$	$Q_1 = 201$	$Q_1 = 198.1$
$Q_2 = 150$	$x_2 = 1700$	$y_2 = 1100$	$Q_2 = 351$	$Q_2 = 380.0$
$Q_3 = 150$	$x_3 = 1700$	$y_3 = 200$	$Q_3 = 150$	$Q_3 = 150.1$
$Q_4 = 150$	$x_4 = 3500$	$y_4 = -500$	$Q_4 = 1497$	$Q_4 = 1462.0$
$Q_5 = 150$	$x_5 = 2000$	$y_5 = -2000$	$Q_5 = 155$	$Q_5 = 150.0$
$Q_6 = 150$	$x_6 = 3600$	$y_6 = -2800$	$Q_6 = 1387$	$Q_6 = 1406.6$
$Q_7 = 150$	$x_7 = 1400$	$y_7 = -3000$	$Q_7 = 150$	$Q_7 = 150.2$
			$Q_{total} = 3891$	$Q_{total} = 3897.0$

eventually screened down to eight and seven. Here, our results are compared with their results for only eight and seven wells cases. The pumping rates of all wells are initially set to the minimum pumping rate, 150 m^3/d, as suggested by Cheng et al. [2000].

While this solution was obtained by Cheng et al. [2000] on a Pentium 450-MHz microcomputer using about 6 hours of CPU time, less than 30 minutes of simulation time have been used on a compatible machine to obtain these results. Both runs improved upon those of Cheng et al. One of the reasons for this may be that the independent variable in this study is continuous, while in their case the independent variable, which is the pumping rate, is discretized. The continuous variable approach may provide a flexible design and lead to a better result. Comparison of the results is given in Figure 3.7 and Table 3.3.

It is noted that the optimal pumping rates are still far less than the global pumping rates that can be estimated from the moving well simulations, even though more wells are used for the fixed location case. It is obvious from this result that the locations of the wells are not optimized. Hence, the existing wells may be moved to new locations to further increase the total pumping rate, while avoiding saltwater intrusion. This, for practical purposes, means that the old wells must be abandoned and new wells must be placed at the different locations with new pumping rates. The model developed is a very useful tool to analyze such cases.

Based on the previous results, another simulation is conducted to see if optimization of the well locations can improve the solution. The model developed is capable of assigning a moving well condition to any number of wells (i.e., none, some or all of the wells), the simulation was conducted by only moving one well which is the first

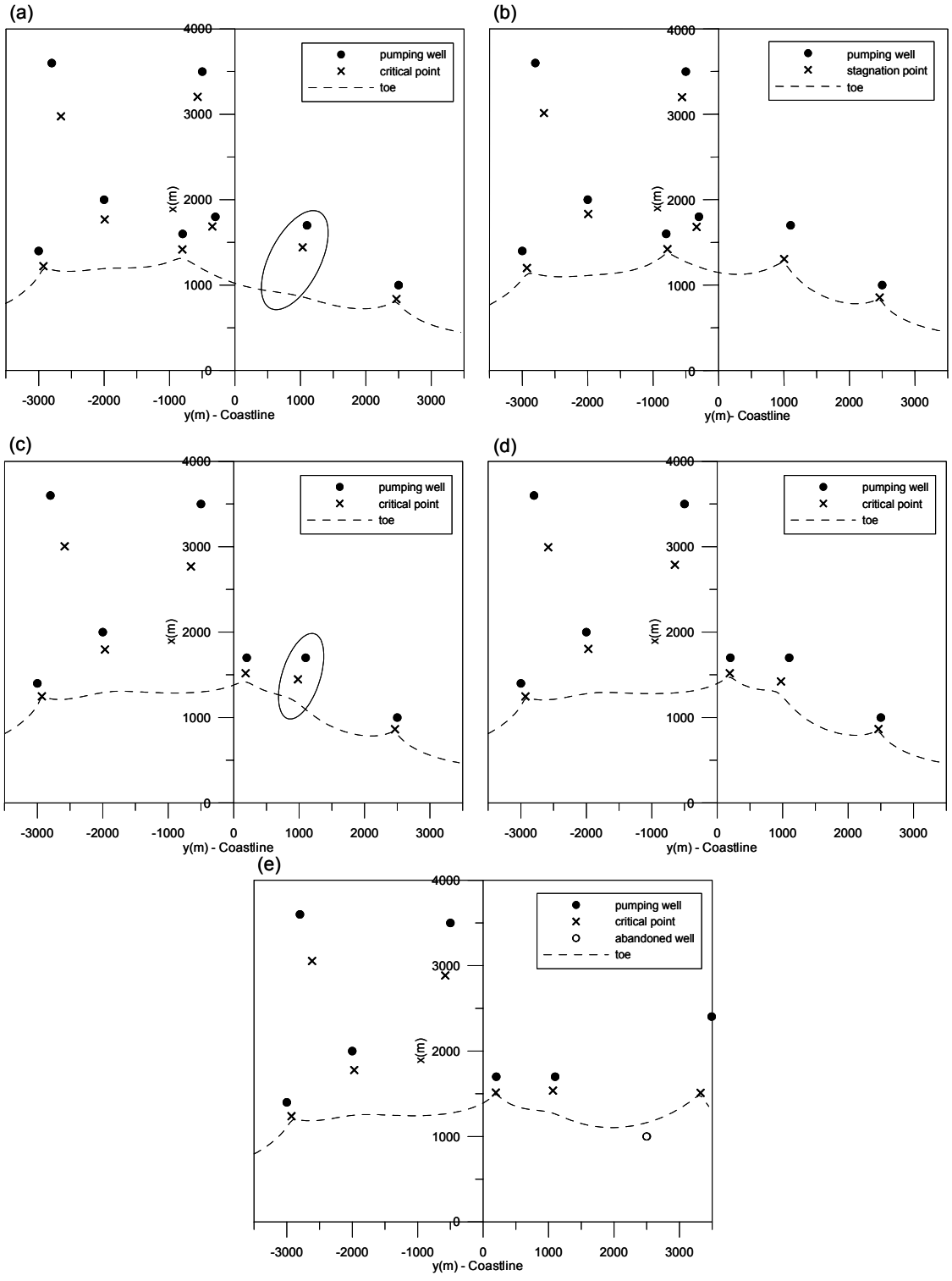

Figure 3.7 Comparison of results between Cheng et al. [2000] and MOGA application; (a) Cheng et al. Case 1 results; (b) MOGA Case 1 results; (c) Cheng et al. Case 3 results; (d) MOGA Case 3 results. (e) MOGA results obtained after abandoning one well given in Case 3

well of Case 3 in Table 3.3. In this case, the total pumping rate increased to 4600 m^3/d from 3897 m^3/d (Figure 3.7e and Table 3.4). This suggests that optimization of the well locations together with the pumping rates improves the results significantly.

Example 4: Separate simulations of the two-well case, each with one component of the multi-objective criteria were conducted, before experimenting with a full multi-objective problem. The results for these cases are given in Figures 3.8a and 3.8b. As shown in Figure 3.8a and 3.8b, each objective successfully forces the solution in opposite but expected directions. The first objective forces the wells to be placed farther inland, while the second objective forces them to move closer to the coastline. As seen in Figure 3.8b, the optimal solution is obtained when the pumping rates of both wells are decreased to the minimum pumping rate, so that the distance between the stagnation point and the reference location is minimized.

To demonstrate the use of the model for the multi-objective formulation, an simulation starts with the parameter set, given in Table 3.5 ($\beta = 0$, to maximize pumping rate only), and as the pumping rate reaches the maximum allowable pumping, the pumping wells stay around the location identified by the circles in Figure 3.8c. Then, the second objective is turned on ($\beta = 1$, to minimize the distance between the stagnation point and the reference location together with maximizing the pumping rate). The objective weighting coefficient was determined from previously conducted numerical experiments. When the model works with the multi-objective criteria, the wells position themselves in a way to minimize the distance between their stagnation points and the

Table 3.4 Summary of modeling parameters and the results of pumping well placement - Case 3 of Cheng et al. [2000]

Aquifer parameters	**Value**	**MOGA parameters**	**Value**
Same with Table 3.3			
Sub-domain and bounding parameters – Case 3 Well #1 moving			
Same as Table 3.3 except for well number 1 k_1= 150, k_2 = 75, k_3 = 75.			

Starting Points			**Optimal Pumping Rate**		
Q, m^3/d	***x*, m**	**y, m**	**Q, m^3/d**		
Q_1 = 150	x_1 = 1000	y_1 = 2500	Q_1 = 1477.4	x_1 = 2403.4	y_1 = 3492
Q_2 = 150	x_2 = 1700	y_2 = 1100	Q_2 = 166.4		
Q_3 = 150	x_3 = 1800	y_3 = -300	Q_3 = 150.1		
Q_4 = 150	x_4 = 3500	y_4 = -500	Q_4 = 1220.7		
Q_5 = 150	x_5 = 1600	y_5 = -800	Q_5 = 186.9		
Q_6 = 150	x_6 = 3600	y_6 = -2800	Q_6 = 1275.1		
Q_7 = 150	x_7 = 1400	y_7 = -3000	Q_7 = 166.2		
			Q_{total} = 4642.8		

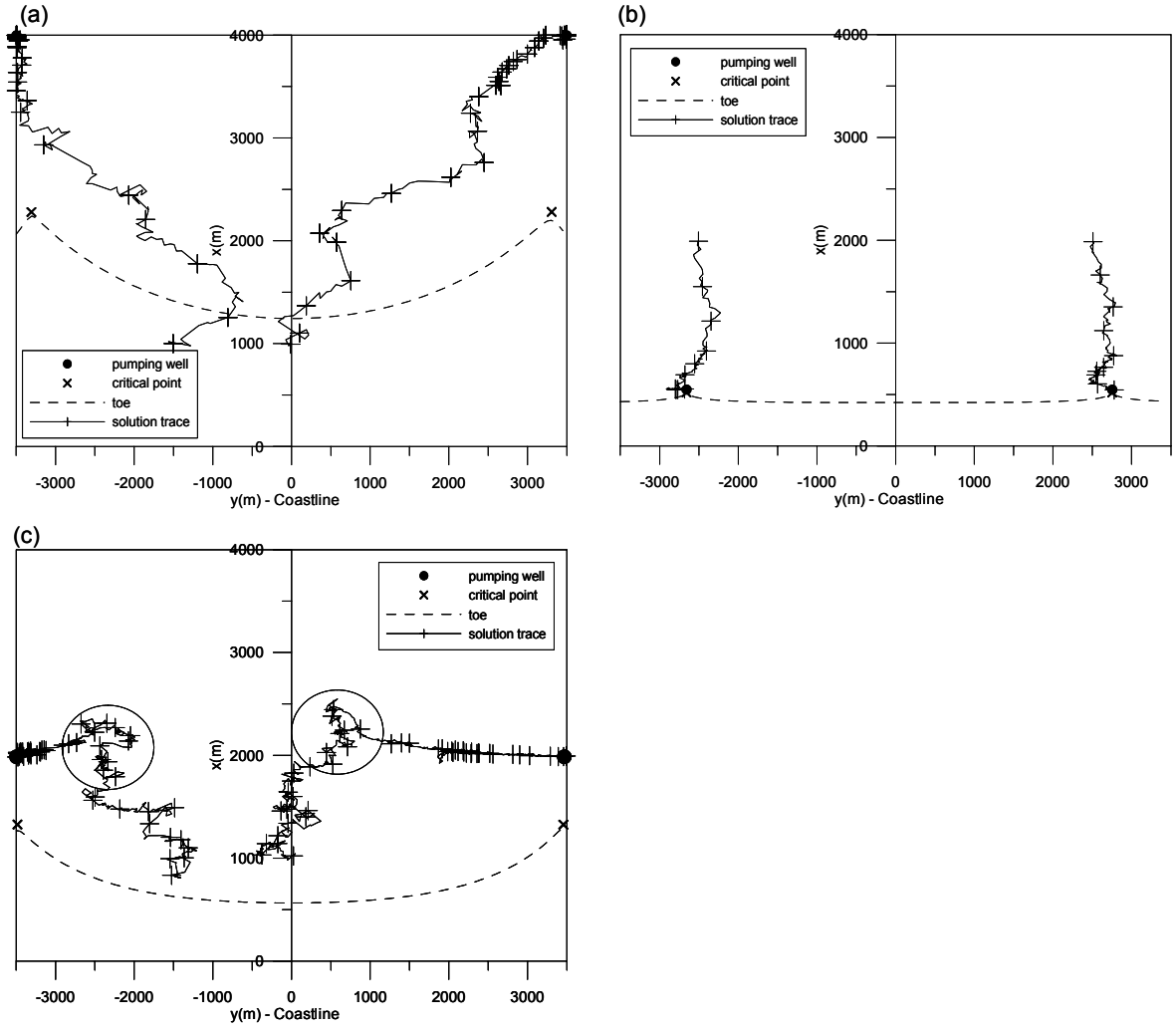

Figure 3.8 (a) The pumping rate maximization objective for two pumping well case; (b) Placement of the well as close as possible to the shoreline objective for two pumping well case; (c) Use of multi-objective criteria for two well case

Table 3.5 Summary of modeling parameters and the results of MOGA simulation

Aquifer parameters	**Value**	**MOGA parameters**	**Value**
Same as Table 1 initially. β is changed to be 1 when the pumping reaches the maximum pumping			
Sub-domain and bounding parameters (for all wells)			
		Two wells for multi-objective analysis	
$\mathbf{k_1}$		150	
$\mathbf{k_2}$		75	
$\mathbf{k_3}$		75	
η		0.00001	
$\mathbf{Q_{min}, Q_{max}}$ **m^3/d**		100, 2000	
x_{min}, x_{max} **m**		0, 4000	
$\mathbf{y_{min}, y_{max}}$ **m**		-3500, 3500	
Starting Points		**Optimal Points**	
Q, m^3/d	***x*, m**	**y, m**	**Q, m^3/d**	***x*, m**	**y, m**
Double wells					
$Q_1 = 300$	$x_1 = 1000$	$y_1 = 0$	1999.2	1986.8	3467.9
$Q_2 = 300$	$x_2 = 1000$	$y_2 = -1500$	1996.4	1986.6	-3495.8

interface location, while maintaining the maximum pumping rates. Figure 3.8c illustrates this multi-objective tendency, and the results obtained for this case. As the final solution, the two wells are located at extreme y-axis locations and at around x-axis location 2000 m.

3.8 Discussions

As for the results of the fixed-well cases, perturbation of well locations is turned off to conduct single objective optimization. The results are compared with the best solution by Cheng et al. Our model produced slightly better results than theirs, indicating that both models solve the problem of pumping rate optimization successfully. The proposed model is also run for several moving well cases. The results indicated that the total pumping rate, from a selected finite domain, can be improved significantly when well locations are introduced as independent variables. For practical purposes, being able to use well locations as independent variables is of great importance in the design stage.

In the water management problem for coastal aquifers, the two main objectives are maximizing the pumping while placing the pumping wells as close to the coast as possible. Here, the possible restriction considered is the pumping site boundaries, which may be close to the shore line. In this work, these two objectives are combined into a single scalar objective function. In order to test the proposed single objective, a hypothetical coastal aquifer is set up (see Table 3.5). First, the impact of each separate objective is demonstrated. The results for maximizing pumping rates and minimizing the distance between the stagnation points and the reference location are shown in Figures 3.8a and 3.8b respectively. Based on the heuristic point provided previously, both cases

produced expected results. The wells move apart from each other in order to maximize pumping rates and they move closer to the coastline to minimize the distance. As can be seen from Figure 3.8a and 3.8b, these two objectives conflict with each other.

In our study, to find the optimum solution for the multi-objective case, first the model is run only maximizing the pumping rates. Once the wells reach the allowed maximum pumping rates, the second objective is activated so that they can be placed close to the coastline as much as possible. This is achieved by reducing the interaction between the wells by moving them further apart from each other. However, this does not imply that the model should run on a sequential two-step process to satisfy multi-objective criteria. The proposed model is capable of performing multi-objective analysis without using the sequential approach. In such cases, the weighing of objective weighing parameters is of importance and should be determined appropriately by the user. Most of the time this process is empirical, and the choice of relative importance of the multi-objective criteria depends on the preferences of the user.

The saltwater intrusion detection algorithm works efficiently when small perturbations in independent variables are used, especially when the search continues in near optimal solutions. When the saltwater toe location moves further inland than the current pumping well location, oscillations in toe delineation start. These oscillations feed wrong information about the well intrusion to the GA resulting in failure of the optimization procedure. However, this problem can be prevented by using small sub-domains which will not let the toe location to move over the well location significantly. For instance, the model can start the simulation with a large sub-domain, in other words each perturbation can be large in the beginning of the simulation. Later the optimization

can continue with a smaller sub-domain as the solution reaches the optimal solution without feeding wrong information to the GA due to failure of well-intrusion detection.

3.9 Conclusions

The problems that were tested and presented here have shown that the proposed mathematical formulation produces an optimal solution in an efficient manner as indicated in Example 3. The formulation of the optimization problem combined with the GA is straightforward and can be applied to the homogenous coastal aquifers under steady state fresh water flow. While the previous work often focuses on indirect methods or pumping rate optimization only, in this paper a new formulation in which the perturbations of pumping rates are presented and well locations are used as continuous independent variables explicitly. This approach produces the optimal solutions not only for the fixed-well cases, but it also handles the optimization of well location cases as well. The proposed model perturbs the well location and pumping rate within the sub-domain, and the GA is applied to simultaneously find the optimal well location and pumping rate in the defined problem domain. The advantage is a significant reduction in model runs which consequently reduces the computational time and cost.

In addition, the constraint for detecting the well intrusion uses the stagnation point concept. This is a sharper constraint for the well-intrusion detection when compared to the studies which uses the well location instead. This in turn may have improved the optimal solution that was obtained in this chapter when compared to the results obtained earlier [Cheng et al., 2000].

CHAPTER 4

VARIABLE DENSITY FLOW IN A VARIABLY SATURATED POROUS MEDIUM

In this chapter, the governing equations for variable density flow in a variably saturated porous medium are provided. The finite element formulation of these governing equations is presented in Appendix C. Based on these governing equations and the Galerkin finite element formulation, a three-dimensional finite element model for variable density flow in a variably saturated porous medium, TechFlow, was developed and tested through the use of several benchmark test problems. The benchmark problems used in this chapter are: the Henry problem, the Elder problem, and the salt dome problem. These problems are used for the verification of TechFlow code. Additionally, a more detailed analysis of the Elder problem is provided in an effort to answer some of the questions that are still debated in the literature in Chapter 5.

4.1 Governing Equations

In this thesis, the governing equations used for variable density flow consist of three fundamental conservation equations: (i) continuity equation of flow; (ii) momentum equation; and, (iii) contaminant transport equation. In addition, these three equations are linked to the equations of the bulk fluid density and the hydrodynamic dispersion equations.

4.1.1 Equation of the Bulk Fluid Density

According to previous studies [Frind, 1982; Huyakorn et al., 1987; Kolditz et al., 1998], the linearized equation of the bulk fluid density under an isothermal state was formulated in terms of hydraulic head as,

$$\rho = \rho_0\left(1 + \lambda_h\left(h - h_0\right) + \lambda_c C\right) \tag{4.1}$$

where h is the hydraulic head, h_0 is the reference hydraulic head, ρ is the density of fluid, ρ_0 is the reference density of the fluid, λ_h represents the coefficient of compressibility of the fluid associated with the change of the hydraulic head at constant mass fraction of the solute, λ_C is the coefficient of expansivity resulting from the change of the mass concentration of the solute at constant hydraulic head, and C is the relative concentration.

The relationship between density and concentration can also be approximated using other representations such as an exponential function as given by Kolditz et al. [1998]. The equations describing the relationship between density and other relevant parameters are formulated based on experiments and are approximate relationships.

Another equation for describing the relationship between density and concentration (or mass fraction) is provided by Herbert at al. [1988] and used by Oldenburg and Pruess [1995]. This equation was derived from the assumption that when two liquids are well mixed, the masses or the volumes of respective components are additive. In this study, among these equations which describe the relationship between density and concentration, the linear equation obtained from the experiments is chosen to describe the relation between the bulk fluid density and concentration.

4.1.2 Continuity Equation of Flow

The macroscopic mass balance equation of the fluid averaged over a representative elementary volume (REV) in a porous medium is,

$$\frac{\partial(S\phi\rho)}{\partial t} + \nabla \cdot (\phi\rho\vec{v}) = \rho Q_\rho \tag{4.2}$$

where S is the saturation ratio, ϕ is the porosity, t is the time, $\vec{v}$ is the fluid velocity vector, and ρQ_ρ is the source term of the fluid mass in an aquifer. Based on Equation (4.2), the flow equation for a variably saturated porous medium can be written in terms of hydraulic head and mass concentration,

$$\phi \frac{\partial S}{\partial t} + S S_0^h \frac{\partial h}{\partial t} + S\phi\lambda_C \frac{\partial C}{\partial t} + \nabla \cdot \vec{q} + \lambda_c \vec{q} \cdot \nabla C = Q_\rho \tag{4.3}$$

where S_0^h is the specific storativity of a porous medium with respect to hydraulic head change and $\vec{q}$ is the Darcy velocity vector. The derivation for Equation (4.3) is provided in Appendix B.1. The head-based flow equation, Equation (4.3), has the advantage over pressure-based flow equations because numerically large static pressures may dominate the dynamic pressure differences that cause motion. The resulting pressure-based numerical scheme may therefore operate at less than optimum numerical efficiency. A more efficient way is to write the flow equation in terms of a quantity that can be directly related to the driving forces. Such a quantity is the equivalent freshwater hydraulic head, defined as $h = \frac{p}{\rho_0 g} + z$ [Frind, 1982].

4.1.3 Momentum Equation of Flow (the Darcy Equation) and Dispersive Flux

The momentum balance equation for variable-density fluid flow in a porous medium in terms of hydraulic head can be given as,

$$\vec{q} = \phi\vec{v} = -\frac{\hat{k}\rho_0\vec{g}}{\mu}\left(\nabla h + \left(\frac{\rho - \rho_0}{\rho_0}\right)\vec{e}\right) \tag{4.4}$$

where $\hat{k}$ is the tensor of permeability of a porous medium and $\vec{e}$ is the unit vector in the gravitational direction. The dispersion tensor can be written as Bear [1979],

$$\hat{D} = \gamma D_m\hat{\delta} + \alpha_T|v|\hat{\delta} + (\alpha_L - \alpha_T)\frac{\vec{v}_i\vec{v}_j}{|v|} \tag{4.5}$$

where γ is the tortuosity, D_m is the coefficient of molecular diffusion, $\hat{\delta}$ is the Kronecker-delta (unit tensor), α_T is the transverse dispersivity, v is the characteristic value of macroscopic velocity, α_L is the longitudinal dispersivity, and, $\vec{v}_i$ and $\vec{v}_j$ are the velocities in i and j directions respectively.

4.1.4 Contaminant Transport Equation

The solute transport with a source is governed by the following advection-dispersion equation,

$$\frac{\partial(\phi C)}{\partial t} + \nabla\cdot(\phi\vec{v}C) - \nabla\cdot\left(\phi\hat{D}\cdot\nabla C\right) = Q_C \tag{4.6}$$

where Q_C is the source term of the solute in terms of mass concentration. Ignoring the expansivity resulting from the change of mass concentration λ_C, Equation (4.6) can be written as follows,

$$\phi \frac{\partial C}{\partial t} + (1-\phi)\lambda_h C \frac{\partial h}{\partial t} + \phi \vec{v} \cdot \nabla C - \nabla \cdot \left(\phi \hat{D} \cdot \nabla C\right) + C Q_\rho = Q_C \qquad (4.7)$$

Kolditz et al. [1998] defined approximation level of density variations in the mass equations when Equation (4.2) and (4.6) are expanded. Based on the levels that they defined, Equation (4.3) results in Level 3 while Equation (4.7) is Level 2. As for the numerical approximation, the Galerkin finite element method is used to solve Equations (4.3), (4.4), and (4.7). In this numerical solution, TechFlow utilizes two methods to integrate the governing equations numerically. For regular elements that have analytical solutions for integrals (i.e., trilinear brick elements in which local axis are parallel to the corresponding global axis), TechFlow uses analytical solutions. For irregular elements, numerical integration is inevitable. Thus, according to these criteria, TechFlow integrates trilinear brick elements utilizing the following methods: (i) an analytical integration method that reduces numerical errors for regular elements; and, (ii) numerical integration using 27 point Gauss quadrature for irregular elements.

As for time marching schemes, TechFlow can utilize several time marching schemes. In the finite element formulation, the time derivative term is handled using a finite difference method. Depending on the choice of the time weight factor, the time approximation scheme can become a forward difference (or Euler) scheme, the Crank-Nicholson scheme, and the backward difference scheme. These numerical schemes are presented in Appendix C.5.

In solving the advection-dispersion equation numerically, it is well known that difficulties may arise when the advective component is large such as the case of the Elder problem. When convection-dominated flow is solved on a coarse grid numerically, the resulting outcome often causes numerical oscillations, and the solution becomes invalid.

This relationship between advection component and grid size, thus grid density, can be described by the grid Peclet number. For stability of numerical solutions the grid Peclet number should satisfy certain criteria, thus a grid Peclet number is closely associated with grid density and thus convergent grid density concept. In general, a satisfactory grid Peclet number stability criteria (i.e., Kolditz et al. [1998] suggested this grid Peclet number to be smaller than 5 for the Elder problem) requires dense grid densities. In an effort to retain the concept of local mass conservation in these difficulties, Frolkovič and Schepper [2001] provided upwind algorithms. The algorithm does not work with a direct approximation of the exact mass balance in Equation (4.7). Instead, the algorithm works with another approximation of $\widetilde{C}$ and $\widetilde{h}$ that can be approximated by the choice of several functions provided by Frolkovič and Schepper [2001]. Note that this upwind algorithm is still at local level of mass conservation and is intended to come up with reasonable solutions through this algorithm even in cases that dense grid densities are required. A direct application of the Galerkin finite element approximation to Equation (4.3) and (4.7) does not estimate the velocity at the nodes. Rather, the independent variables of hydraulic head and concentration (therefore density by Equation (4.1)) are solved on a nodal basis, and the discharge (velocity) is calculated from these values. Several approaches have been introduced to calculate the velocity field. One is the local smoothing schemes proposed by Diersch and Kolditz [1998]. In this method the velocity is calculated at the center of element by Equation (4.4) with given hydraulic head and densities one nodal basis.

Another method is consistent velocity approximation [Voss and Souza, 1987; Frolkovic, 1998]. Voss and Souza [1987] directly solved Equations (4.3) and (4.6) and

interpolate velocity at the elemental Gauss points. The authors recognized the inherent problem of interpolating velocity using both pressure (or hydraulic head) and density that are based on nodal values of these parameters. Their linear basis functions require that pressure varies linearly in any direction. Yet pressure can only vary linearly in the vertical direction when density is constant. Therefore, if density differs in the vertical direction between nodes, the pressure must vary quadratically. This paradox can be resolved several ways, including the use of nonlinear weighting functions for the pressure, or eliminating the vertical component of density variability. The authors chose to retain the linear weighting functions and assigned a constant (volume average) density value for each element. Benson et al. [1998] suggested that the result of this consistent velocity approximation is velocity truncation that is limited by the order of the pressure interpolation, which is first-order. Conversely, one can consider the velocity truncation error in terms of the density gradient, which is the information that is lost by assuming a constant density. Later, Frolkovič [1998] generalized consistent velocity approximation by Voss and Souza [1987] so that it can be used for different types of finite elements and discretizations. Note that this consistent velocity method is still an elemental velocity estimation which is not a satisfactory resolution of the problem.

The other method is the one suggested by Yeh [1981]. This method applies an additional Galerkin finite element method to Equation (4.4), and solves the velocity at each node. Unlike the first two methods, this method guarantees velocity field to be globally continuous just as hydraulic heads and concentrations are.

In TechFlow, an adaptive method such as the upwind algorithm is not implemented in the numerical solution. This is based on the idea that certain grid density criteria (i.e., a

convergent grid) must be met for solving convection-dominated flow so that a unique solution can be obtained from this approach. The findings and discussions of this issue, specifically in the Elder problem case are provided in Chapter 5. As for the method of estimating velocity fields, TechFlow utilizes the method of Yeh [1981] to obtain a globally continuous velocity distribution, thus reducing the error of mass balance. The formulation of these governing equations and the globally continuous velocity formulation are provided in Appendix C.2.

4.2 The Henry Problem

The Henry problem [Henry, 1964] has been one of the most popular benchmarking problems in variable density flow. Although none of the numerical solutions provided in the literature matches the analytical solution presented by Henry, several researchers have solved the problem numerically and reached the point that the numerical solution is more or less in agreement with the analytical solution.

The boundary conditions of the Henry problem, defined in terms of hydraulic head are depicted in Figure 4.1. The parameters used in Henry's problem are given in Table 4.1. With these boundary conditions and parameters, the numerical solution of the Henry problem obtained from TechFlow is provided in Figure 4.2. The results indicate good agreement with that of SUTRA provided by Voss and Souza [1987] and showed a better match when compared with the recent numerical results obtained from TOUGH2, FEFLOW and ROCKFLOW [Oldenburg and Pruess, 1995; Kolditz et al., 1998] (Figure 4.3). Especially, the comparison with FEFLOW and ROCKFLOW indicates that all of the results are almost identical.

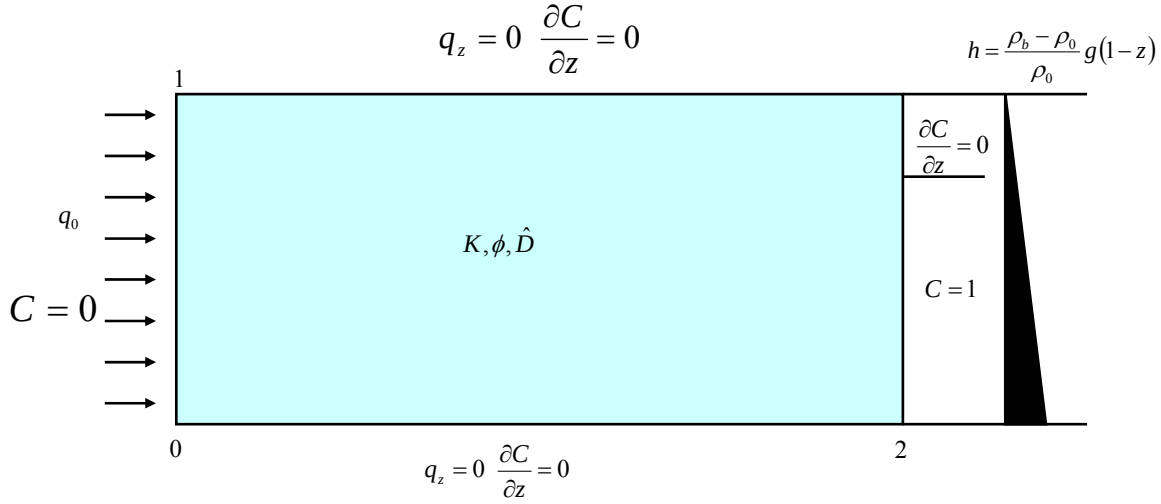

Figure 4.1 Boundary conditions of the Henry problem

Table 4.1 Parameters for the Henry problem

Symbol	Quantity	Value	Unit
D_m	Molecular diffusion coefficient	6.6×10^{-6}	m^2s^{-1}
k	Permeability	1.019368×10^{-9}	m^2
μ	Dynamic viscosity	10^{-3}	$kgm^{-1}s^{-1}$
g	Gravitational coefficient	9.81	ms^{-2}
α_L, α_T	Transverse and longitudinal dispersivity	0, 0	m
ϕ	Porosity	0.35	-
ρ_0, ρ_s	Density of water and saltwater	$(1,1.0245)\times10^3$	kgm^{-3}
q_0	Freshwater recharge	6.6×10^{-5}	ms^{-1}

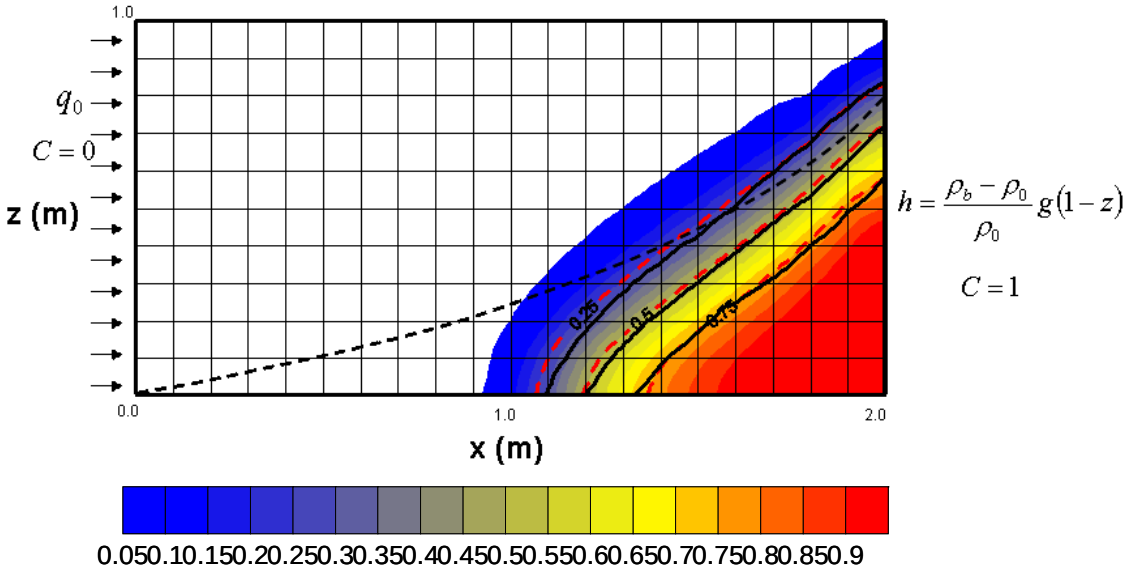

Figure 4.2 Isochlor contours of steady state concentrations for the Henry problem: SUTRA [1987] (black solid line), the Ghyben-Herzberg interface (black dotted line), and TechFlow (red dotted line)

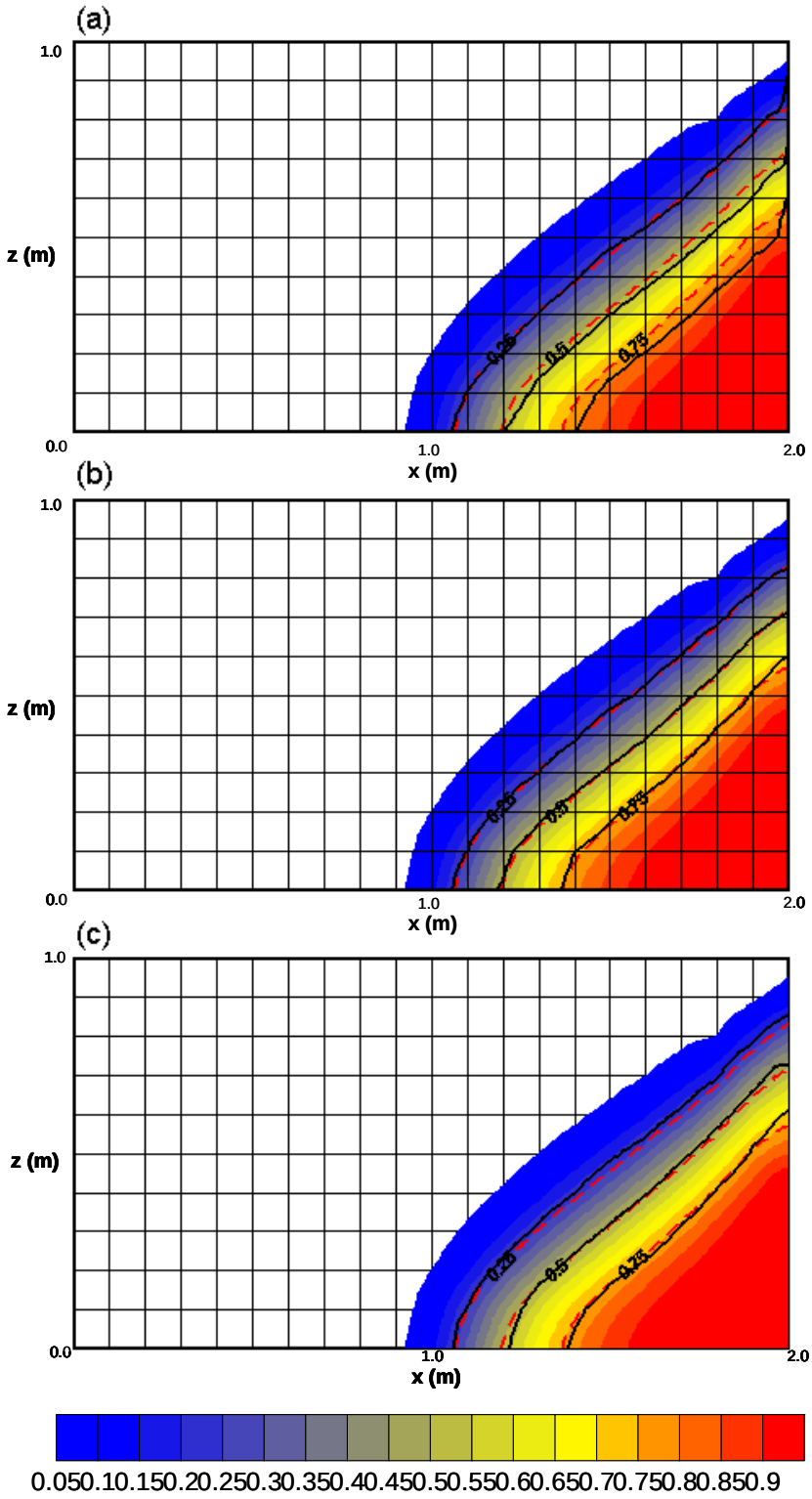

Figure 4.3 Isochlor contours of steady state results for the Henry problem: (a) TOUGH2 [1995] (solid line), TechFlow (red dotted line); (b) FEFLOW [1998] (solid line), TechFlow (red dotted line); (c) ROCKFLOW [1998] (solid line), TechFlow (red dotted line)

4.3 The Elder Problem

Simpson and Clement [2003] analyzed the Elder problem in two different ways: (i) an approach to solve flow and solute-transport equations separately without coupling; and, (ii) an approach to solve coupled flow and solute-transport equations through updates between flow and transport equations. They provided a comparison of these coupled and uncoupled solutions of the Henry problem to separate the density-dependent effect from the boundary effects that may impact the solution. In other words, if two solutions are similar to each other, the density-dependent effects are not dominant. Thus, the solution mostly depends on the boundary conditions imposed regardless of density difference (i.e., no need to couple the two models because density effects are minimal). In fact, the solution obtained from the uncoupled simulation looks similar to the correct solution (the coupled solution). Therefore, the concentration distribution in Henry's problem is primarily determined by the boundary forcing imposed on the problem, and not necessarily the result of density coupled flow and transport processes. On the other hand, the Elder problem is a good example of free convection phenomena, where the fluid flow is driven purely by the density differences of the fluids.

Figure 4.4 illustrates the boundary conditions of the Elder problem. Table 4.2 presents the specific parameters for the Elder problem used in this application. For comparison, the result obtained by Frolkovič and Schepper [2001] was used and is provided in Figure 4.5 where the dimensionless isochlor lines C = 0.2, 0.4, 0.6 and 0.8 are shown (numerical values are not included in the figures for clarity). The isochlor is defined as a ratio of a density difference to the maximum density difference. Figure 4.6 shows the numerical results obtained from TechFlow as the solution of the Elder problem.

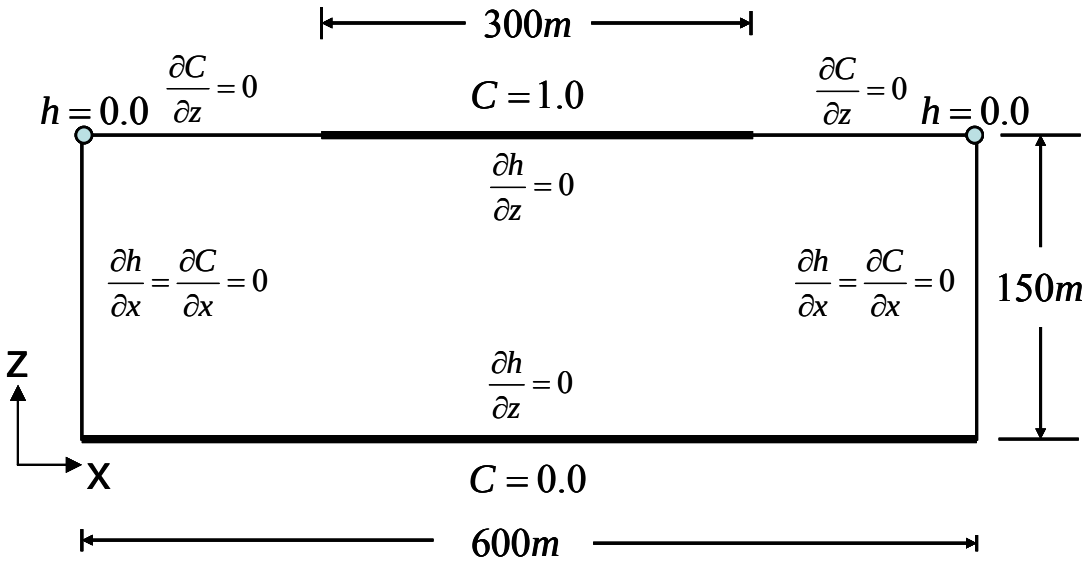

Figure 4.4 Boundary conditions of the Elder problem

Table 4.2 Parameters for the Elder problem

Symbol	Quantity	Value	Unit
D_m	Molecular diffusion coefficient	3.565×10^{-6}	m^2s^{-1}
k	Permeability	4.845×10^{-13}	m^2
μ	Dynamic viscosity	10^{-3}	$kgm^{-1}s^{-1}$
g	Gravitational coefficient	9.81	ms^{-2}
α_L, α_T	Transverse and longitudinal dispersivity	0, 0	m
ϕ	Porosity	0.1	-
ρ_0, ρ_s	Density of water and saltwater	$(1,1.2)\times10^3$	kgm^{-3}

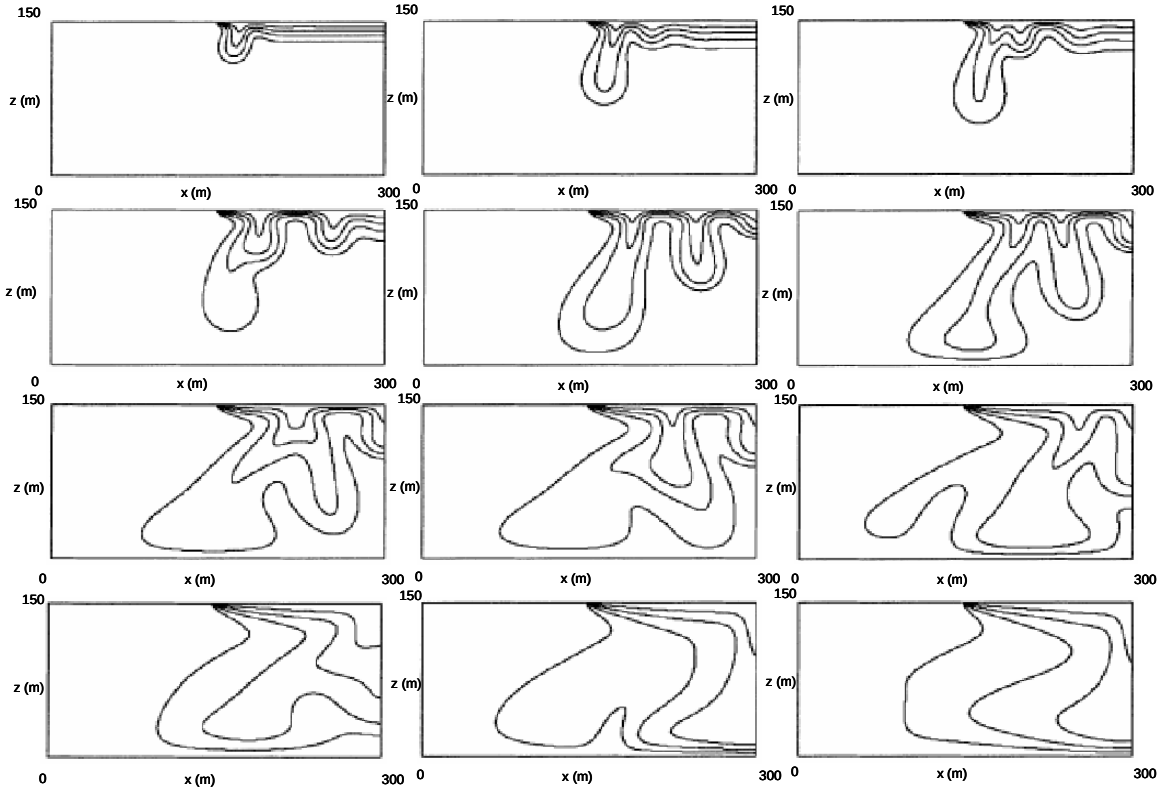

Figure 4.5 Results for t = 1, 2, 2.5, 3, 4, 5, 6, 7, 10, 12, 15 and 20 yr at grid level 7 from Frolkovič and Schepper [2001]

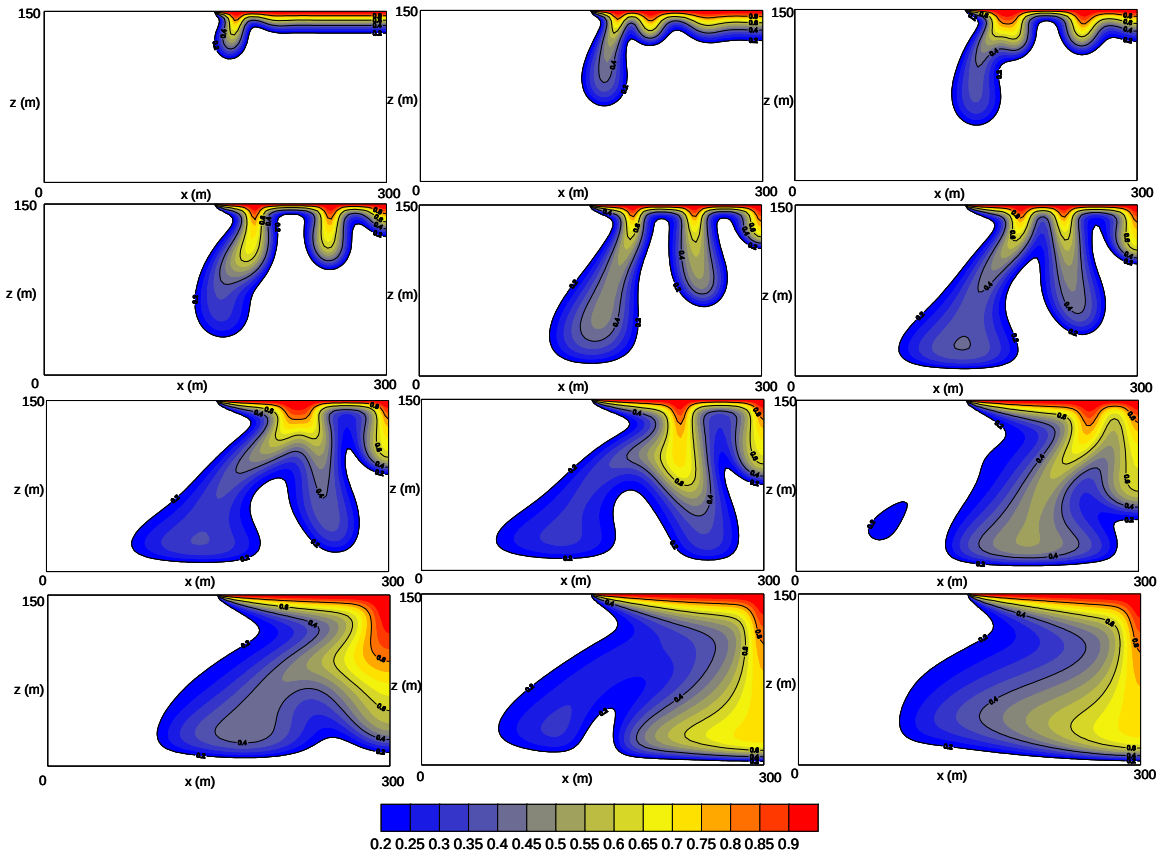

Figure 4.6 Results of the Elder problem for 1, 2, 2.5, 3, 4, 5, 6, 7, 10, 12, 15 and 20 year at regular grid of level 7 from TechFlow

In this solution, a level 7 grid idealization was utilized. The level of grid is defined as the *l*th level that consists of 2^{2l+1} identical square elements. Since the Elder problem is a symmetrical problem, the solutions are provided only for a half of the problem domain. Although there is slight difference between the two solutions for the 0.4 isochlor for the 5th year and 0.2 isochlor for the 10th year, TechFlow results are in very good agreement with the results of Frolkovič and Schepper [2001] (Figure 4.5). This outcome confirms their result that is produced on a regular mesh at level 7. Chapter 5 analyzes the Elder problem in detail.

4.4 The Salt Dome Problem (HYDROCOIN Level 1 Case 5)

The next benchmark test problem is HYDROCOIN level 1 Case 5. The Hydrologic Code Intercomparison (HYDROCOIN) project was started in 1984 as an international cooperative effort for studying groundwater modeling in the context of radioactive waste disposal site evaluation. The stated objective of HYDROCOIN level 1 studies was to "verify the accuracy of groundwater flow codes" for a variety of hydrogeological problems [1987]. Among several problems, Case 5 problem is known as the salt dome problem, which was designed to evaluate a system in which groundwater flow is influenced by significant density variations caused by variability in the concentration of dissolved salt (Figure 4.7). More specifically, the problem was designed to simulate groundwater flow and solute transport in a two-dimensional vertical plane in which fluid density depends on the dissolved-solids concentration and was developed to represent a rough approximation of the subsurface geologic conditions existing at the Gorleben salt dome in Germany. The assumptions and framework of the problem are described by

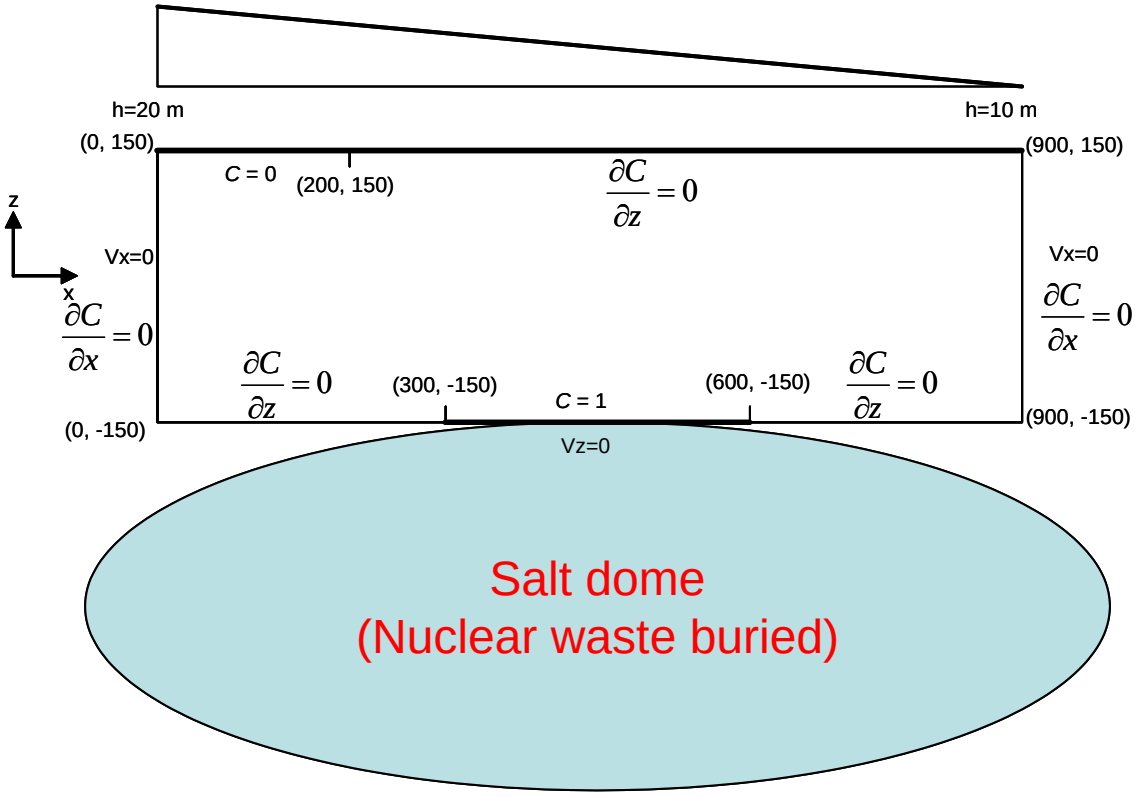

Figure 4.7 Boundary conditions and the problem domain for the salt dome problem

OECD [1988; 1992] and in the several reports that present results of HYDROCOIN participants (e.g., Herbert and Jackson, [1986]; Herbert et al., [1988]; Leijnse and Hassanizadeh, [1989]; U.S. Nuclear Regulatory Commission, [1988]; Yabusaki et al., [1988]). The OECD report [1988] also presents and compares the results by six project teams that simulated the problem using six different models. Further, particular results of several other research teams are also presented in separate reports of the HYDROCOIN project participating teams.

As shown in Figure 4.7, Case 5 considers groundwater flow over a salt dome. The basic geometry and boundary conditions are illustrated in Figure 4.7. The problem is simplified to a 900-m-long × 300-m-deep two-dimensional cross section. The aquifer is assumed to be homogeneous, isotropic, and recharged by fresh water at the surface. The lateral and bottom boundaries are no-flow conditions.

The problem is formulated based on the assumption that the top of the salt dome (i.e., the bottom of the problem domain in Figure 4.7) is exposed to circulating groundwater in the overlying aquifer, slowly releasing saturated brine (i.e., radioactive waste dissolved in water) by a diffusive/dispersive process. Thus, in the original definition and evaluation of this problem, salt is assumed to enter the flow system by transverse dispersion only along the central third of the bottom boundary [OECD, 1988]. Thus, molecular diffusivity and mechanical dispersivity are actively discussed in various studies [Herbert et al., 1988; Oldenburg and Pruess, 1995; Kolditz et al., 1998].

Recently, Oldenburg and Pruess [1996] reanalyzed the problem using the TOUGH2 code and provided a numerical solution different from the solution provided by Herbert et al. [1988]. While Herbert et al. provided the solution that shows recirculating

flow patterns in the region above the bottom boundary of the system, Oldenburg and Pruess suggested the solution does not have concentration in the upstream section of the salt dome and only the other two thirds of the region overlying the bottom boundary has salt concentrations. They called this flow pattern as a "swept-forward" pattern and claimed that this swept-forward solution is related to the magnitude of molecular diffusion. They claim that the molecular diffusion coefficients larger than $D > 10^{-7}\ m^2 / s$ produces the swept forward solution. The work by Oldenburg and Pruess was discussed by Johns and Rivera [1996] in support of the original Herbert et al's solution (i.e., the recirculating pattern). This discussion was followed by reply from Oldenburg, Pruess and Travis in support of a swept-forward solution.

Later, Konikow et al. [1997] showed that if a constant-concentration boundary condition is applied at a node in an active flow field that is the central third of the bottom boundary in a solute-transport model, a solute flux can occur by both advective and dispersive processes. Thus, the constant-concentration boundary is modified to allow solute transport by dispersion only and significantly less salt from the salt dome is released into the flow field. Thus, in a finite element model, the constant-concentration boundary condition that is modified to prohibit advective transport along the specified constant-concentration boundary produces a solution with a swept-forward flow pattern while the model with no modification of this boundary handling produces a solution of a recirculating flow pattern. Therefore, the result of the salt dome problem depends very little on which numerical model is used as long as the selected model uses the proper boundary conditions and equations.

Table 4.3 summarizes the physical parameters of the salt dome problem. Figure 4.8 presents three previous results and only the result of a recirculating flow pattern by TechFlow. The result of TechFlow is in very good agreement with the other recirculating flow pattern solutions by Herbert et al. [1988] and Kolditz et al. [1998]. Although TechFlow is not modified to obtain a swept-forward solution as Konikow et al. [1997] suggested, code verification is confirmed through code comparison with the other results of a recirculating flow pattern for the salt dome problem.

4.5 Discussions

Three benchmarking problems are tested for the verification of TechFlow code developed in this study. Although these test problems are good applications in variable density flow, the physics of the problem in each test are very different. The Henry problem is intended to describe the saltwater intrusion. A density difference by mass of about 2.5 % is not a strongly density-driven flow system. In fact, this problem is a hypothetical problem in which the boundary condition forces the broad dispersive transition area as Simpson and Clement [2003] mentioned. In addition, the flow is more oriented in the horizontal direction where the significance of the density coupling diminishes.

Unlike Henry's problem, the Elder problem is of importance to test the density coupling because the problem is purely density-driven flow due to the unstable condition set by the boundary conditions such that the heavier fluid stays on the top of the lighter fluid. In addition to the unstable condition, the density difference by mass is also approximately an order of magnitude greater than the one in Henry's problem.

Table 4.3 Parameters for the salt dome problem

Symbol	Quantity	Value	Unit
D_m	Molecular diffusion coefficient	1.39×10^{-8}	m^2s^{-1}
k	Permeability	1.0×10^{-12}	m^2
μ	Dynamic viscosity	8.9×10^{-4}	$kgm^{-1}s^{-1}$
g	Gravitational coefficient	9.80665	ms^{-2}
α_L, α_T	Transverse and longitudinal dispersivity	20, 2	m
ϕ	Porosity	0.2	-
ρ_0, ρ_s	Density of water and saltwater	$(0.997,1.2)\times10^3$	kgm^{-3}
Δp	Pressure difference at the top	10^{-5}	Pa

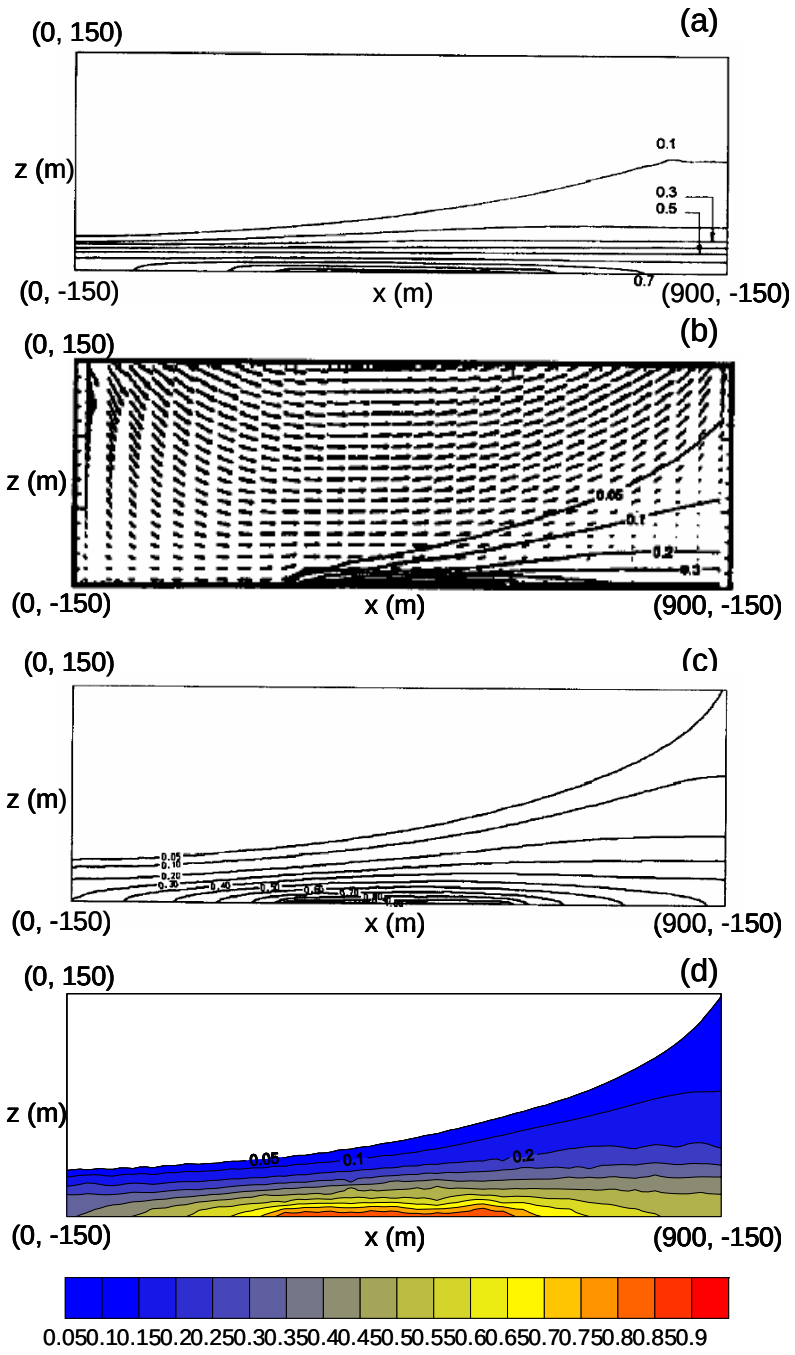

Figure 4.8 Results for the salt dome problem: steady-state solutions (a) NAMMU by Herbert et al. [1988] – recirculating flow pattern; (b) TOUGH2 by Oldenburg and Pruess [1995] – swept-forward flow pattern; (c) FEFLOW by Kolditz et al. [1998] – recirculating flow pattern; (d) TechFlow in this study – recirculating flow pattern

The physics of the fluid flow produces fingers as the plume advances. The occurrence of the fingers is a complicated problem in which most of the times the fingers are associated with the physical instability. This instability increases as the difference in densities of the two fluids gets larger. This is one of the main reasons why the Elder problem is very sensitive to several kinds of perturbations which are investigated in Chapter 5. The result of TechFlow in this chapter is referred to the most recently published result by Frolkovič and Schepper [2001] for the benchmarking purpose. Both of the results are in good agreement.

Lastly, HYDROCOIN Level 1 Cast 5, the salt dome problem is used for another benchmark test problem. This problem is designed to understand the physics of variable density flow above the salt dome through an international cooperative effort. There have not been any cases where nuclear wastes are buried in a salt dome for storage. Considering the extremely long half time of decay of radioactive materials, the importance of the project will deserve the significant consideration for proper and safe handling of these wastes. Modeling was chosen as a first step of the project to understand the physics of variable density flow specific to the salt dome problem. The main difference between the Elder and salt dome problems lies in the physical instability [Park and Aral, 2004]. Unlike the Elder problem, there is no physical instability occurring in the problem domain in the salt dome problem. This makes a difference in terms of modeling difficulties. This problem in fact has a solution that is in agreement by several researchers as in the case of the Henry problem. The key question to be answered on the salt dome problem is that given the hydraulic gradient on top of the problem domain, will the salt solution which contains radioactive materials reach to the upper boundary when

salt at the bottom is transported by transverse dispersion only. Due to the different ways of handling the constant-concentration boundary condition in a solute-transport model as pointed out by Konikow et al. [1997], inconsistent results are found in the literature. Rectification of the constant-concentration boundary condition resolves this inconsistency. Thus, although there is a significant density difference, the salt dome problem can be solved relatively easily because of the fact that no physical instability exists in this problem. The physical instability seems to play an important role in variable density flow because the instability pushes the models to the limit, yielding numerical solutions prone to errors. This makes this field still challenging and motivates many researchers and scientists. An in-depth analysis of this problem is provided in Chapter 5 where the physical instability due to density differences as well as other numerical perturbations associated with the way the flow velocity is estimated are discussed.

4.6 Conclusions

The governing equations of variable density flow are provided in this chapter. Based on these governing equations, TechFlow, a three-dimensional Galerkin finite element model of variable density flow in a variably saturated porous medium is developed for further studies that will be covered in the rest of the thesis. TechFlow was vigorously tested through three popular benchmark problems and produced the results which are in good agreement with the ones obtained by other researchers.

Due to the lack of analytical solutions for variable density flow and experimental data, the benchmark test problems are required for the verification of variable density flow model. Limited to the code comparison, TechFlow developed in this study passed

the code verification that has been widely used for the existing models. In addition to code comparison, the verification of TechFlow is expanded to the experimental data that are recently published by Osward and Kinzelbach [2004]. This work is provided in Chapter 7.

CHAPTER 5

SENSITIVITY OF THE SOLUTION OF ELDER PROBLEM TO DENSITY, VELOCITY AND OTHER NUMERICAL PERTURBATIONS

The numerical solution of the Elder problem has attracted the attention of researchers for the past decade. Unique solution of the problem is still under debate. In this chapter, a study are provided where instability issues associated with the numerical solution of the Elder problem is investigated from the following perspectives: (i) physical instability issues associated with density differences used in the numerical solution; (ii) sensitivity of the solution to idealization irregularity; and, (iii) the importance of accurate estimation of the velocity field and its association to the grid density levels that is necessary to solve the problem accurately.

5.1 Introduction

Modeling of variable density flow in subsurface hydrology has been emphasized during the past decades. This is not only because this problem is related to many mission-critical problems such as disposal of nuclear waste, saltwater intrusion, and fate and transport of contaminants but it also describes an important physical phenomenon in groundwater flow. Compared to other well-known knowledge in unison for groundwater flow and/or solute transport modeling in the subsurface hydrology field, the modeling of variable density flow is a complex application and is still at a conceptual and hypothetical level [Bear 1979;Javandel et al. 1984;Herbert et al. 1988;Oldenburg and Pruess 1995;Kolditz et al. 1998]. This implies that this field of science still requires

detailed experimental and numerical studies just to establish the criteria for developing reliable modeling tools that may be accepted by researchers. In the literature, there have been several benchmark studies associated with variable density flow. These include Henry's problem, the Elder problem, HYDROCOIN Level 1 Case 5 problem, and the salt lake problem [Henry 1964;Elder 1967;Swedish Nuclear Power Inspectorate 1984;Wooding et al. 1997a;Wooding et al. 1997b]. Among these, it seems obvious that the Elder problem is one of the most popular and also the most difficult problem to solve in a consistent manner.

The Elder problem has a history for its believed correct solution being associated with the number of fingers or the direction of flow that it produces at the center of the domain as a stationary solution. The controversy starts with Elder [1967] who provided a single-finger and downward-flow solution at the center and Voss and Suoza [1987] who reproduced it using the SUTRA model. The SUTRA solution in fact gave credibility to the single-finger solution until Oldenburg and Pruess [1995] demonstrated a two-finger and upward fresh water flow solution at the center of the problem domain. They associated their solution with what they termed to be a "convergent grid." In their study they claimed that the two-finger solution is closer to the original photograph taken by Elder during his experimental work. This two-finger solution has been considered to be the correct solution and other researchers have confirmed it using various other models [Kolditz et al. 1998;Prasad and Simmons 2003].

Lately, Frolkovič and Schepper [2001] came back with a single-finger solution obtained from a finer grid (Level 7) than the one used by Oldenburg and Pruess [1995]. The level of the grid is defined as the l^{th} level which consists of 2^{2l+1} identical square or

rectangular elements. In addition to this single-finger solution, Frolkovič and Schepper also showed a new three-finger solution obtained after using several different consecutive levels of grid density (i.e., computation of the stationary solution using adaptive grid method from grid level 4 to 7). The fact of not identifying a unique solution to the Elder problem motivated other researchers to work on this problem with different approaches. Woods et al. [2003] investigated possible numerical errors of variable density flow using SUTRA and suggested that the Elder problem is prone to error and is extremely sensitive to the methods used in simulation, such as mass lumping and time marching schemes. Unfortunately they could not perform their simulation on grid level 7 although they showed a Peclet (*Pe)* number analysis in association with grid density to justify their simulation at lower levels of grid density. A fine grid that consisted of 16000 triangle elements was also used by Boufadel et al. [1999] for the Elder problem. However this solution did not match with Frolkovič and Schepper's [2001] level 7 solution and Boufadel's solution yielded asymmetric two-finger solution. Thus at this point, it seems that there is no single solution of the Elder problem on which the researchers can fully agree. More work is required to understand why this problem is yielding different numerical solutions.

Similar to the Elder problem, HYDROCOIN Level 1 Case 5 problem also involves density differences up to 20%. This problem has been studied extensively as well [Herbert et al. 1988;Oldenburg and Pruess 1995;Johns and Rivera 1996;Oldenburg et al. 1996;Kolditz et al. 1998]. For this application the conclusion reached by Konikow et al. [1997] is that the differences in results are associated with the way constant-concentration boundary condition at nodes are handled rather than which model was

used to solve the problem. The difference between the HYDROCOIN and the Elder problem is the physical instability associated with the Elder problem. Unlike the HYDROCOIN problem, the Elder problem starts with the instability from the beginning since the heavier fluid is placed on top of the lighter fluid. This instability pushes the models to the limit, yielding numerical solutions prone to perturbation effects.

In this chapter, the effect of various perturbations on the numerical solution of the Elder problem is investigated. This analysis is accomplished by introducing perturbations to the solution which can be categorized in two groups: (i) perturbations in physical parameters of the problem; and, (ii) effects of global and local irregularities in idealization and also the effect of the numerical solution of the velocity field in these idealizations. The first perturbation is associated with various density differences that can be used in the Elder problem. In this chapter, the density difference perturbation is used to identify the boundary where the solution to the Elder problem becomes independent of grid density effects. This analysis yielded a vertical grid Peclet number criterion that needs to be satisfied to obtain consistent results. The analysis based on grid Peclet number will provide the necessary criteria for forming convergent grids that may be applied to physically unstable problems similar to the Elder problem. The second perturbation is associated with the detailed analysis of the Elder problem in reference to numerical perturbations (i.e., grid irregularity, grid density and accuracy of numerical methods to estimate the velocity field). The answers to these effects are very important in answering the question: “Is there a consistent solution to the Elder problem?” The three-dimensional variable density flow model (TechFlow) developed in this thesis is used for this analysis.

5.2 Sensitivity of the Elder Problem to Density Difference

In this section, the contribution of physical parameters used in the Elder problem to the instability issues observed in numerical solutions is first investigated. For this purpose various density differences are carefully selected to obtain grid density independency to achieve a unique and stable solution to the Elder problem. This is accomplished by searching for a stationary solution obtained from the selected grid densities while associating this with the density differences used in the Elder problem. The density differences tested are 15 %, 20%, and 25 %, respectively.

As mentioned previously many times, the Elder problem is notorious in yielding different solutions based on the grid levels used. Thus, the selection of a grid level as the "convergent grid" is of importance before conducting the simulations on the instability analysis based on density differences. Thus, the question of different solutions obtained for different grid densities used in the numerical solution need to be addressed first. There have been three reported solutions depending on the density of grid used and the adaptive grid solutions chosen [Frolkovic and De Schepper 2001]. Since the concept of "convergent grid" is not well understood or well defined in the Elder problem case, in this study three different grid densities, which can be found in the previous works, were initially considered for the analysis of physical instability issue in association with density differences. These include the most coarse mesh (22×25 rectangular elements compatible with level 4 mesh) used by Voss and Souza [1987], the medium mesh (44×50 rectangular elements compatible with level 5) used by Kolditz [1998], and the most dense mesh (240×140 rectangular elements compatible with level 7) used by Frolkovič and Schepper [2001]. Considering only the half of the problem domain, half-

finger solution seems to be developed at 20 years of simulation on the most coarse and dense meshes while a single finger solution is generated on the medium mesh. The grid selection has been a hot discussion topic in evaluating the results of the Elder problem [Oldenburg and Pruess 1995]. Thus, as stated above, identifying a convergent grid level before performing density perturbation simulations is the first priority for the analysis. Although some researchers mentioned "grid convergence" in their studies, there seems to be no quantitative criterion except the one given in Kolditz et al. [1998] that can be applied to the Elder problem. In their study, Kolditz et al [1998] developed a mesh analysis based on the vertical grid Peclet number. The vertical grid Peclet number is defined as,

$$Pe = \frac{q}{\phi D_m}\Delta z \approx \frac{\left| K\left(\frac{\Delta h}{H} - \lambda_C \Delta C\right)\right|}{\phi D_m}\Delta z = \\ = \left|\frac{K\Delta h}{\phi D_m} - \frac{KH\lambda_C \Delta C}{\phi D_m}\right| = \left|\frac{K\Delta h}{\phi D_m} - Ra\right|\frac{\Delta z}{H} \tag{5.1}$$

where ΔC is the maximum difference of mass concentration, Δh is the maximum difference of hydraulic head, Δz is the characteristic vertical element length, and R_a is the Rayleigh number. Their study revealed that a grid convergent numerical solution can be obtained for the vertical grid Peclet numbers smaller than five for the Elder problem. However, none of grid Peclet numbers obtained from their various grids satisfies the theoretical stability criterion of linear advection-diffusion problems. Theoretical stability criterion requires grid Peclet number to be less than two for the numerical solution to be stable and virtually exact when compared with the analytical solution [Daus et al. 1985;Frind 1988]. Thus, based on our confirmation of Frolkovič and Schepper [2001]

results as shown earlier in Chapter 4, we conclude that grid level 7 can be considered to be a convergent grid in analyzing density difference effects since it is the only grid that satisfies the theoretical stability criterion and confirmed solutions by various researchers which include the present work.

In the investigation of physical instability analysis, which is conducted by varying the density difference used in the Elder problem, the use of the coarsest mesh is excluded to rule out the possibility of numerical errors associated with grid density effects so that we can focus our attention to the physical instability itself. Simulations of density dependent instability analysis on the medium (level 5) and most dense (level 7) grids for density differences of 15, 20 and 25 percent are conducted. The computed vertical grid Peclet numbers for the chosen medium (level 5) and most dense (level 7) grid range between 4.4 and 1.4 respectively. These grids satisfy the criterion of vertical Peclet numbers that is reported in Kolditz et al. [1998]. Vertical grid Peclet number in fact changes with the density difference used. The vertical grid Peclet numbers for each chosen density difference and grid density are provided in Table 5.1.

Table 5.1 Simulation schemes for physical instability on regular grids

Density difference $(\rho_s - \rho_0)/\rho_0$	Rayleigh Number	Grid density	The Vertical Grid Peclet number	Solution pattern (number of finger in a half domain)
0.15	300	Level 5	2.9	One and half
0.15	300	Level 7	1.04	One and half
0.20	400	Level 5	4	One
0.20	400	Level 7	1.42	Half
0.25	500	Level 5	4.4	Half
0.25	500	Level 7	1.57	One

Once grid independency of the numerical solution at lower density differences is demonstrated, the density difference will be increased up to 25 % to investigate the pattern of the solution obtained at higher density differences. In all the grids used in these simulations, structured, uniform, regular, trilinear brick elements are used. Thus, numerical perturbation associated with the use of irregular elements is not introduced in this analysis. Instability in numerical solution associated with mesh irregularity will be discussed later.

The numerical results obtained for the Elder problem for the medium and most dense grids (Figure 5.1) confirms the previous works [Oldenburg and Pruess 1995;Kolditz et al. 1998;Frolkovic and De Schepper 2001]. This in turn adds to the credibility of the use of TechFlow for the solution of the Elder problem as well as the other benchmark problems as shown in Chapter 4. In summary, at 20 % density difference, which is the standard density difference used in Elder problem applications, the result of TechFlow successfully reproduced two different solution types obtained when two different grid densities are used. This was also observed in other studies [Oldenburg and Pruess 1995;Kolditz et al. 1998;Frolkovic and De Schepper 2001].

The simulations at 15 % density difference in fact yielded the criteria for the independency of stable solution from grid density. For this density difference the two results from two different grids are almost same. Interestingly, at this density difference level, the third kind of one and half finger solution was obtained for both these simulations as reported by Frolkovič and Schepper [2001]. Note that smaller density difference reduces the physical instability and the model produces the same solution independent of grid density while the solution at 25% density difference is not at all as

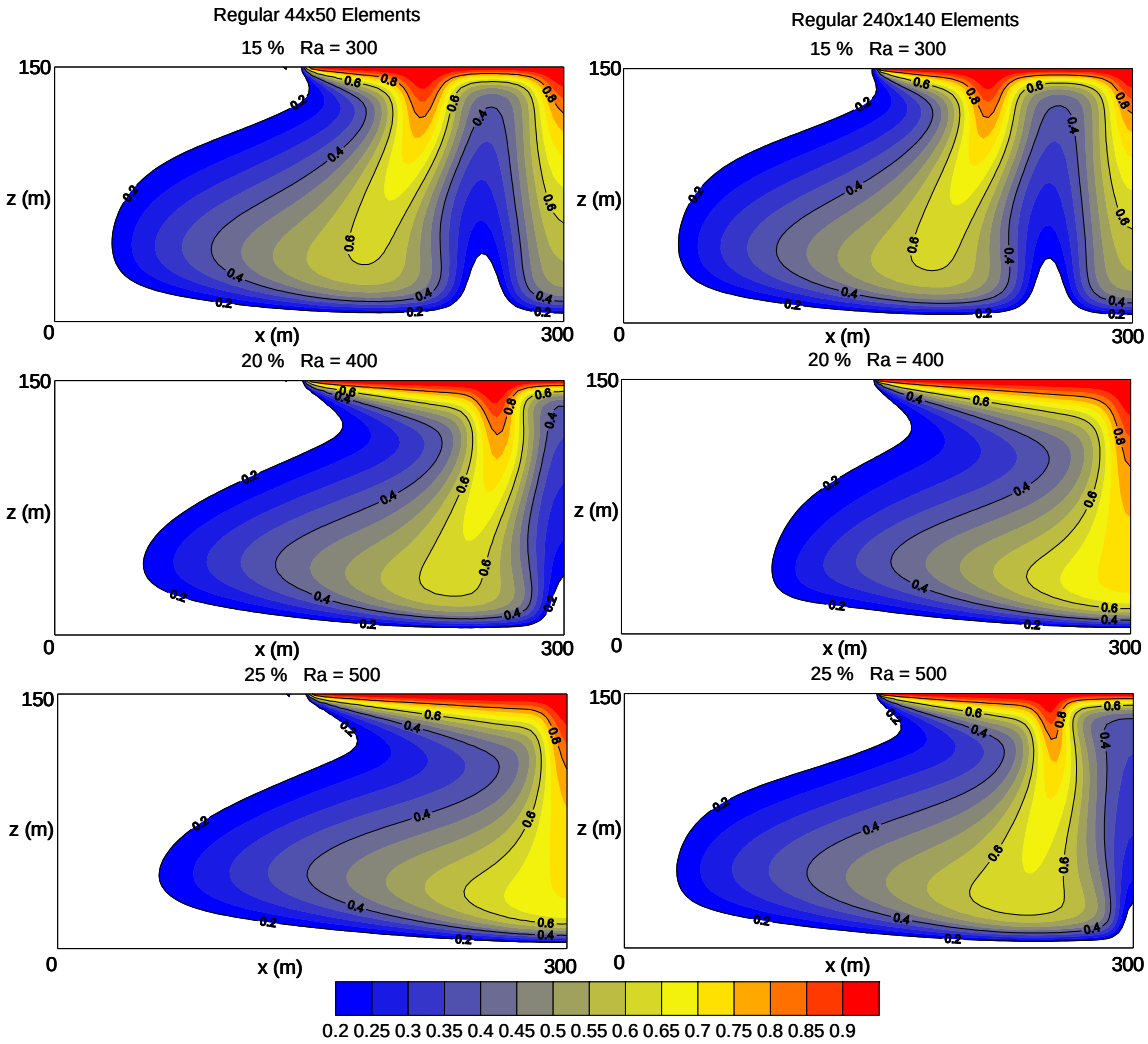

Figure 5.1 Stationary results obtained from various density differences on two different grids.

expected (Figure 5.1). In fact, for the high density difference case, nonlinear (non-Fickian) dispersion effect was shown to be important by other researchers [Hassanizadeh and Leijnse 1995;Schotting et al. 1999]. However, in this study, nonlinear dispersion effect was not taken into consideration. The simulations were conducted with the pure interest of finding out the boundary of grid density independence in association with the density difference effects. The boundary for the model to produce two different solutions due to the density difference level lies in between 15 % and 20 % density difference or Rayleigh numbers between 300 and 400 for the chosen regular grid densities. However the Rayleigh numbers do not necessarily represent the physical instability because the characteristic length scale is ambiguous. For the condition defined in the Elder problem, the source of physical instability (i.e., the heavier fluid is on top of the lighter fluid) is what makes the Elder problem difficult to solve. A good example of a high Rayleigh number solution for 20 % density difference that is independent of grid density is the case of HYDROCOIN Level 1 Case 5 problem where the Rayleigh number is extremely high but the results are confirmed stable results at lower grid densities [Konikow et al. 1997].

Although Kolditz et al. [1998] indicated that a grid convergent numerical solution can be obtained for grid Peclet numbers smaller than 5 for the Elder problem, stricter grid Peclet number criterion seems to be required to obtain consistent results. In this work, the grid independency achieved at 15 % density difference requires the vertical grid Peclet number to be smaller than 3 which is very close to the theoretical criterion (Table 5.1). All the simulations conducted for analysis of density difference effects were done using the global velocity approximation [Yeh 1981].

It is also noted here that the advantage of the use of the head-based equation mentioned previously is in the estimation of the vertical grid Peclet number in Equation (5.1) compared to the pressure-based equation. The computed maximum hydraulic head differences for 15 %, 20%, and 25 % density difference are about 12 *m*, 15 *m*, and 21 *m* respectively. The maximum head differences were obtained from all the head differences in the problem domain at each time step of each simulation of 15 %, 20%, and 25 % density difference. In general, it is observed that the head differences increase as time progreses in the Elder problem.

5.3 Sensitivity of the Elder Problem Solution to Numerical Perturbations

Most of the simulations for the Elder problem, except Boufadel [1999], were performed using a regular grid. Boufadel provided the solution obtained at 16,000 triangle elements which show a single finger solution. This contradicts the solutions obtained by Frolkovič and Schepper [2001] and as well as the ones obtained in this paper. To understand the differences in simulation results one has to also understand the differences associated with the idealization irregularity, especially when there are various solutions to the same problem as is the case with the Elder problem.

As Frolkovič and Schepper [2001] mentioned, when the grid is not aligned to the boundaries of the solution domain, the interpolation of the initial conditions can cause perturbations which, eventually, may determine the nature of the numerical solution for inherently unstable problems. The uniform and aligned grid with square elements is expected to be free of this type of perturbation. Nevertheless, the sensitivity of the Elder problem to the perturbations that may be generated due to the presence of irregular

elements is important since for problems with complex domains and boundaries the aligned grids are not feasible. To study grid irregularity effect, an irregular grid was created to see how this affects the solution of the Elder problem. For the generation of an irregular grid, Argus ONE, a commercial mesh generator, was used to create a grid whose density is compatible with the medium grid density (level 5). The 2-D mesh generated through Argus ONE is extended to a 3-D mesh for the application. For this case 27 point Gauss quadrature integration was used in the numerical integration. To evaluate the error that may be introduced to the numerical solution through the use of numerical integration, a simulation was first conducted on the regular 2200 element grid with numerical integration used for the computation instead of analytical integration. The detail of analytical integration that is used in TechFlow is provided in Appendix C.4. For regular grids, TechFlow automatically uses an analytical solution of element integration to reduce the computational burden. But for this simulation this function was turned off and the code was forced to use the numerical integration. This, in fact, increases the computational burden. However, it is worthwhile to conduct this analysis to observe the numerical errors that may be introduced to the solution. The two numerical results obtained from analytic integration and numerical integration for the 2200 element grid was identical and agrees with the single-finger solution. These results are the same kind with the case of 20 % density difference with Rayleigh number 400 in Figure 5.1. This gives credibility to the numerical integration procedures used for the irregular element analysis in TechFlow. It should be also observed that the mesh generated by Argus ONE has some directional tendency and this is a limitation of this mesh generator

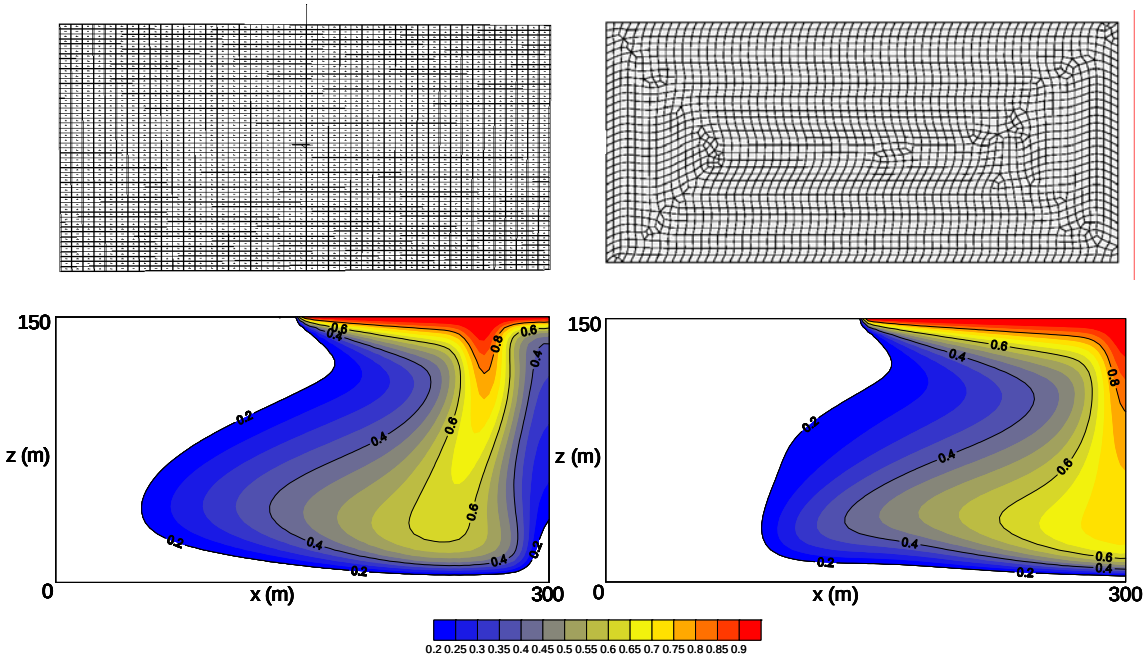

Figure 5.2 Comparison for 20 years between regular and irregular grid with density of the medium mesh (i.e. 2200 elements)

(Figure 5.2). The single-finger solution obtained on the regular medium density grid is shown in column (a) of Figure 5.2. This result is in agreement with previous work [Oldenburg and Pruess 1995;Kolditz et al. 1998]. The irregular mesh solution using the medium density grid is shown in column (b) of Figure 5.2. Note that the result for this case is a half-finger solution although the density of the grid is same. This indicates that regularity of element does make a difference in obtaining a stationary solution to the Elder problem. This implies that additional complication will be introduced to the solution of density dependent flows since the complex domain solutions are always in favor of the use of irregular grids.

To better understand the perturbation effects introduced by the use of an irregular grid in the Elder problem, additional simulations were conducted with the use of three different irregularities that may appear in grid generation which was artificially introduced in our case. These mesh irregularities are: (i) Half of the horizontal layer of the grid is zigzagged in the top area of the medium regular grid; (ii) One vertical column of the grid three elements to the left of the center of the medium regular grid is zigzagged vertically downward; and, (iii) Two elements are zigzagged in the top center area of the medium regular grid. The numerical results obtained are compared with the results obtained from medium regular grid (level 5). In Figure 5.3, the various grid irregularities are shown and the stationary results obtained for each case are shown in Figure 5.4. In general, the introduction of irregular elements does affect the solution significantly at the initial stages of plume development. Although the results in column (b) and (c) are similar at year 2, they are clearly different from the regular grid results shown in (a) in the number of fingers developed at the same year. However, these two perturbations were

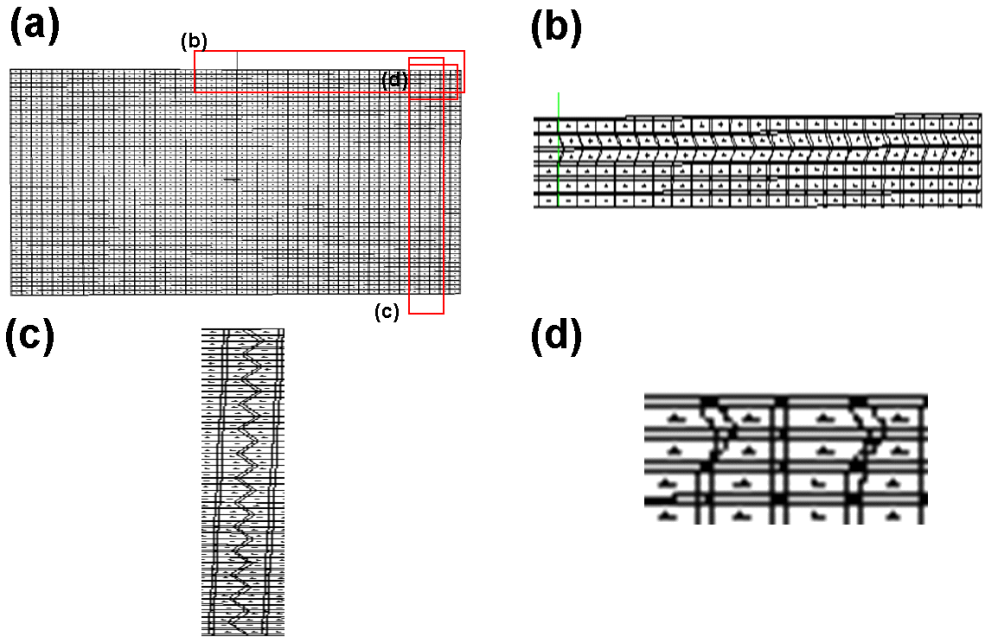

Figure 5.3 Various grids: (a) the medium regular grid, (b) half of the horizontal layer of the grid zigzagged in the top area, (c) One vertical column of the grid three elements away from the center zigzagged, (d) two zigzagged in the top center area

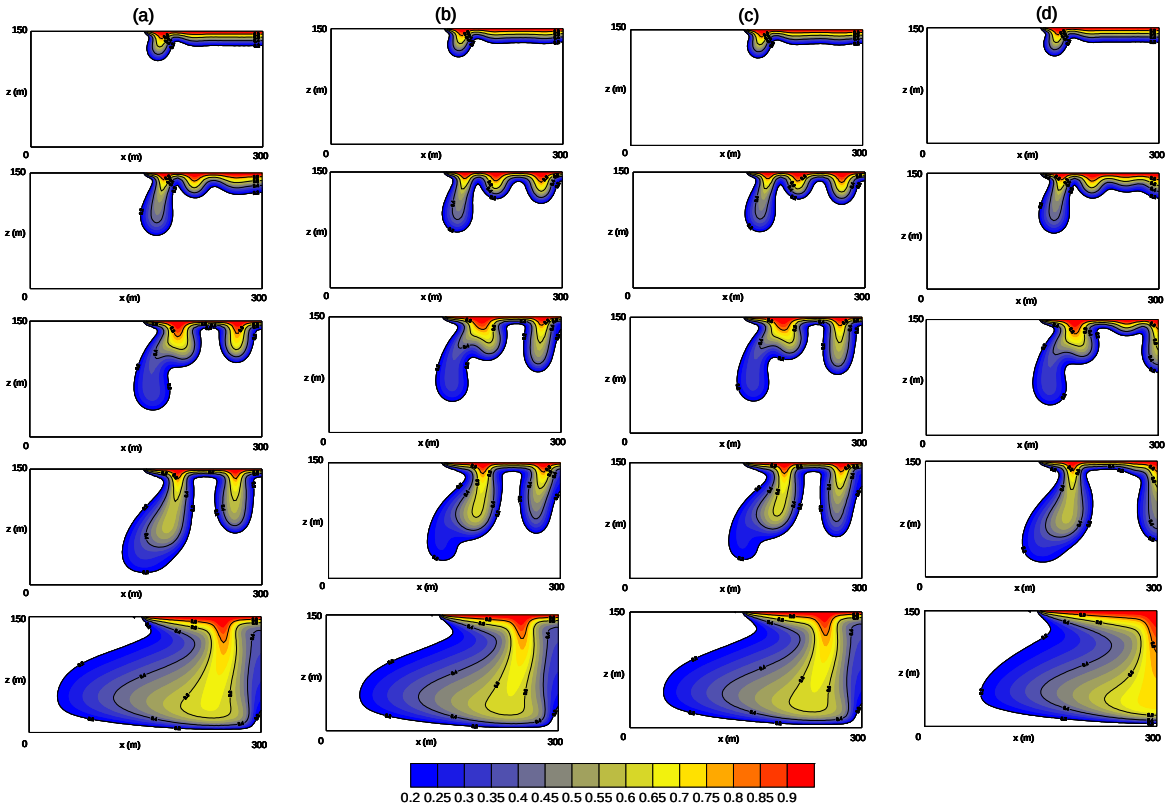

Figure 5.4 Results for year 1, 2, 3, 4, and 30 at the medium level grid with various combinations of regular and irregular elements: (a) the medium regular grid, (b) half of the horizontal layer of the grid zigzagged in the top area, (c) One vertical column of the grid three elements away from the center zigzagged, (d) two zigzagged in the top center area

not non uniform or large enough to change the pattern of the stationary result obtained from the medium grid density simulations. The solution is a single-finger solution obtained after 30 years. Therefore the grid perturbation introduced by zigzagging the grid both horizontally and vertically does affect the initial plume development but does not cause any change in the stationary solution. From the experience gained from grid (b) and (c), a zigzagged element grid (d) was carefully chosen to find one irregular element pattern that changes the pattern of the stationary solution. Note that the irregularity introduced in case (b) and (c) were uniform across the solution domain albeit being in one direction. When an idealization with a zigzag in only two elements (local irregularity) is implemented, the results change significantly as shown in Figure 5.4d. The location selected to place the irregular elements is important as they affect the beginning of the plume development. This indeed makes a difference in the final stationary solution. Interestingly, the final solution for this case falls in half-finger category which can be obtained from regular level 7 grid. Therefore, it is concluded that a local numerical perturbation associated with grid irregularity is sensitive enough for the Elder problem to reach to two different stationary solutions.

Another extremely important variable that affects the Elder problem solution is the way the velocity field is calculated. In the literature, two methods are used in variable density flow modeling: finite difference or finite element models. Both methods are supposed to yield compatible results as long as the degree of accuracy used in the two numerical solution schemes is compatible. Before the discussion on the method used in velocity field calculation, note the results produced by TechFlow at level 6 grid (Figure 5.5). These results are almost identical with the one obtained by Frolkovič and Schepper

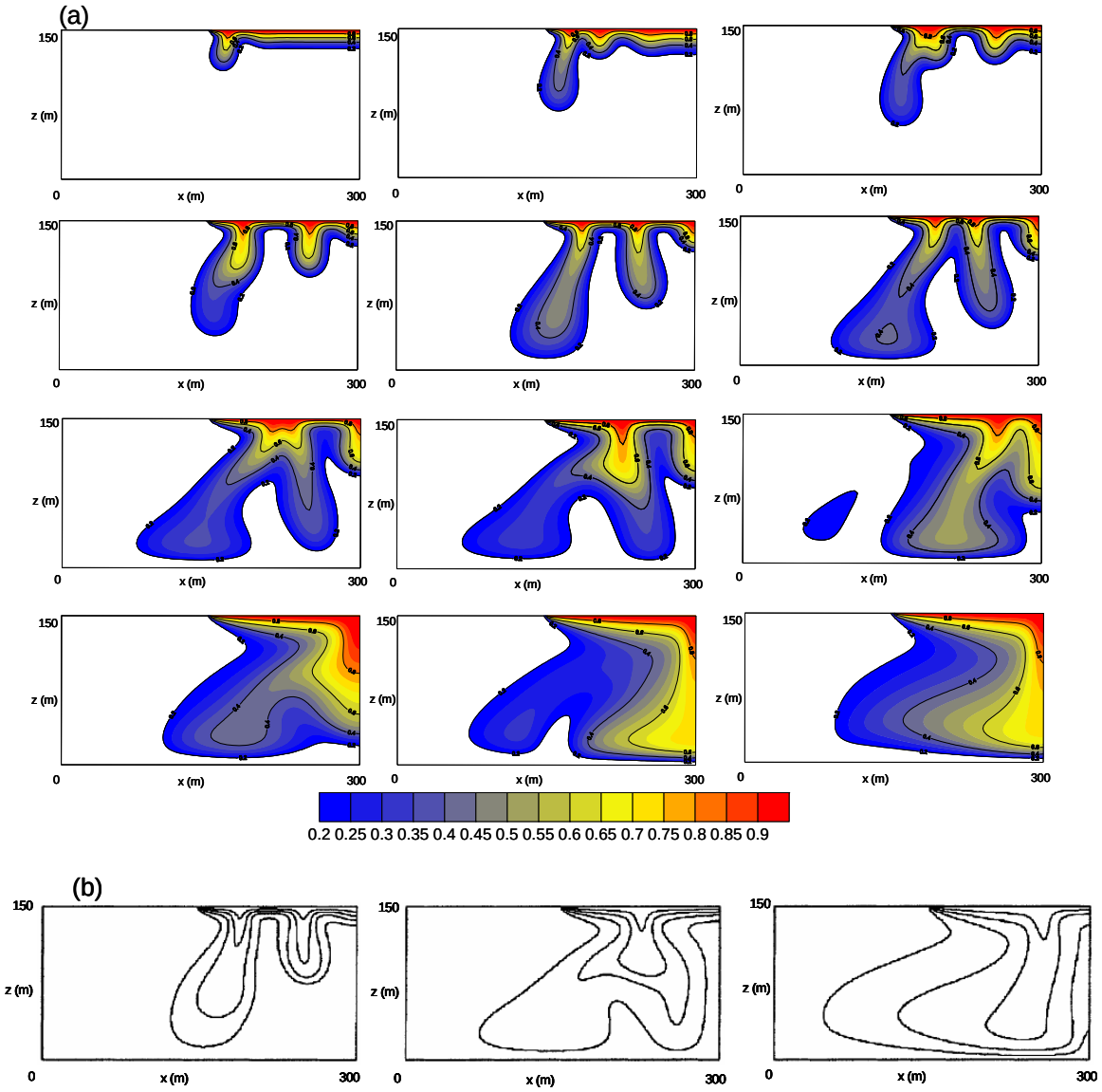

Figure 5.5 (a) TechFlow results of the Elder problem for 1, 2, 2.5, 3, 4, 5, 6, 7, 10, 12, 15 and 20 year at regular grid of level 6, (b) Results for 4, 7, and 20 year at grid Level 6 from Frolkovič and Schepper [2001]

[2001] which was obtained from level 7 grid. As noted earlier, this solution was confirmed using TechFlow with the same grid density. Thus, using TechFlow, their grid 7 results were also confirmed with grid level 6 idealization. However, this outcome is contradicting the stationary result they have obtained from their level 6 grid. Specially, the result at year 4 differs not only from the one obtained by SUTRA from level 6 grid without mass lumping [Woods et al. 2003] but also from the ones by Oldenburg and Pruess [1995] and Kolditz et al. [1998]. This obviously indicates that either TechFlow may be fairly inaccurate or it uses different methods in some aspects of the simulation. In velocity field calculations, TechFlow uses the method proposed by Yeh [1981] which guarantees the velocity to be continuous across the elements. To obtain continuity of velocity, the nodal gradient must also be treated as an unknown [Segol 1976]. Obviously, this increases computational burden depending on the dimension of the problem solved. However, the use of continuous velocity fields is essential and requires additional application of Galerkin method to the Darcy equation to solve the velocity field. In this way, the error in mass balance can be reduced [Yeh 1981]. Thus, with computed hydraulic head and density distribution, the momentum equation discussed in Equation (4.27) was reformulated in the form of Galerkin finite element method, velocity component in each direction was solved at every node.

The finite difference models do not have an alternative method to compute globally continuous velocity fields as can be done in the finite element method, unless they make use of the methods of finite element analysis separately for the velocity calculations. Thus, this implicitly assumes that velocity fields which are obtained from either through the consistent velocity approximation as defined by Voss and Souza [1987] or a more

extended consistent velocity approximation obtained by Frolkovič [1998] are still discontinuous velocity fields across the element boundaries. Voss and Souza [1987] in the SUTRA model interpolates velocity at the elemental Gauss points by retaining the linear weighting functions and assigns a constant density value for each element. Benson et al. [1998] showed that this leads to velocity truncation error in terms of the density gradient, which is the information that is lost by assuming a constant density. Among the finite element models referenced in this study, only Kolditz et al. [1998] used two finite element models (FEFLOW and ROCKFLOW) which have both global continuous and local discontinuous velocity estimation. Which method was used to produce the result of grid level 6 in their application is unknown. Nevertheless, the estimation of velocity is of great importance especially in convection-dominated flow problems such as the Elder problem. A speculation can be made such that this may be one of the reasons as to why there exist various solutions of the Elder problem in the literature. The results of TechFlow at grid level 6 indicate that continuous velocity estimation is of importance in determining the grid density to obtain consistent result of the Elder problem. To test this and understand if this tendency occurs in the lower level grids (lower than level 6), the simulations were done on grid level 4 using continuous and discontinuous velocity calculations. It is obvious from Figure 5.6 that TechFlow has a similar trend of producing one level of higher grid result than those obtained from other models with locally discontinuous velocity estimation because of the implementation of globally continuous velocity method. This may be why Frolkovič and Schepper [2001] require level 7 grid to produce the half-finger solution presumably with less accurate velocity estimation. As the grid density increases, the loss of mass conservation due to discontinuity of velocity

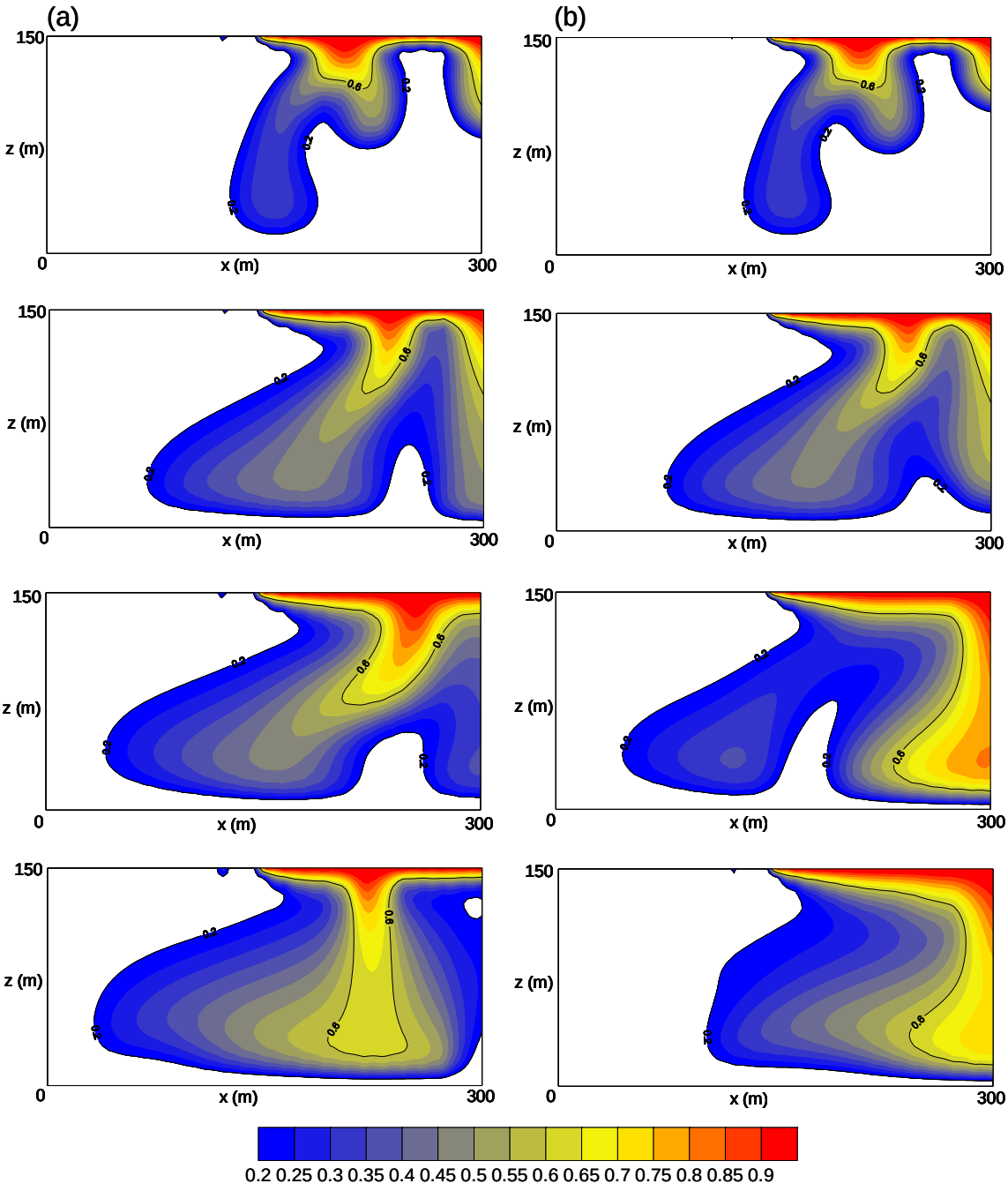

Figure 5.6 TechFlow results of the Elder problem for year 4, 10, 15, and 20 at regular grid of level 4 (a) with continuous velocity method, (b) with discontinuous velocity method

reduces. Yeh [1981] indicated that when spatial distribution of the velocity is significant, inputting this discontinuous flow field to the contaminant transport computation could conceivably produce large errors. Since the results from Figure 5.5 and 5.6 indicate that the global continuous velocity method requires less dense grid to obtain the same pattern for the Elder problem, the statement by Yeh [1981] is again demonstrated in this study.

5.4 Discussions

The fact that there exist various solutions of the Elder Problem in the literature is an obstacle to establishing the Elder problem as a benchmark test for variable density flow modeling. On the other hand, the simplicity associated with the definition of the Elder problem, indicates that this problem is still an excellent choice for benchmark testing. Thus, the analysis that is directed toward "physical instability", "idealization instabilities" and "accurate velocity field computation" issues, as discussed in this chapter is another step toward establishing the Elder problem as a benchmark test problem. There are several other sources of numerical errors that maybe the origin of instabilities. These are spatial and temporal approximation used in choice of elements and time marching methods employed in the solution. Assuming they are all taken care of at the same level of accuracy, the grid density, irregularity, and the approximations of nonlinear terms (velocity related computations) are the ones that need to be addressed carefully to arrive at unique solutions. As long as there is a satisfactory grid Peclet number for grid convergence, the awareness of choice with time marching approximation, satisfactory Curant number condition for the time step, and the procedure to approximate nonlinear terms such as at element level or node level or global or local level are handled properly,.

there should not be significant differences in numerical results among various variable density flow models. Otherwise, it is inappropriate to compare the numerical results. One good example can be found at the misconception of HYDROCOIN problem as indicated by Konikow et al.[1997] previously. As reported in this study, the accurate computation of the velocity field is a key component of the solution. Various simulations provided in this chapter show that the differences in velocity estimations lead to significantly different results associated with the grid density.

The numerical simulations performed in this chapter indicate that stricter vertical grid Peclet number criterion together with global continuous velocity approximation method at grid level 6 is required to confirm the most recently obtained Elder problem results given by Frolkovič and Schepper [2001], which was obtained at grid level 7. Grid Peclet number is a ratio of numerical dispersion to the real dispersion. Satisfying this criterion at conservative level can significantly reduce numerical dispersions. Although numerical dispersions are welcomed in some cases, they are still fictitious and should be ruled out when the cause of differences among models are not clearly identified. Global continuous velocity estimation reduces the grid density approximately by factor of 1/4. Conversely, locally obtained velocity requires denser grid by a factor of 4. In other words, one level of higher grid density is required when discontinuous velocity fields are used in solution. Although globally continuous velocity estimation increases the computational burden, this is still more economical compared to increase in number of nodes to compensate the loss of mass balance caused by locally estimated velocity fields.

Most analysis using the modified equivalent partial differential equation (MEPDE) approach can not be applied to finite element model with irregular elements due to

vagueness of handling dimensions which are not parallel to the axis selected. However, the numerical error analysis using MEPDE is still useful for qualitative purposes. Sensitivity to element regularity brings a question about variable density flow being in favor of aligned as opposed to unaligned elements. Further, small physical or numerical perturbations are observed to make a difference in the stationary solution of the Elder problem. As also shown by Frolkovič and Schepper [2001], small perturbation in initial condition may affect the solutions. All of these applications should be complemented with conservative vertical grid Peclet and Curant number as well as global continuous velocity estimation to arrive at unique solutions.

5.5 Concluding Remarks

Numerical experiments for physical instability indicate that the physical instability is what makes the Elder problem difficult to solve. At a 15 % density difference, the grid level 5 and 7 produced a one-and-half finger plume as the stationary solution. The solution obtained at grid level 7 in this study is identical to the one obtained by Frolkovič and Schepper [2001]. With global continuous velocity estimation, this solution can be obtained from grid level 6 idealization as demonstrated in this study.

Irregular grids do affect the pattern of the solution especially in the early stages of the plume development. The pattern of two irregular elements in an otherwise the regular grid idealization can alter the stationary solution indicating the Elder problem is sensitive to local grid regularity. Stricter vertical grid Peclet number criterion is required to rule out possible numerical errors associated with grid size and similarly numerical dispersion. Compared to the importance of the use of accurate velocity fields in the Elder problem

and the way it affects the nonlinear terms are extremely important. The numerical methods used to estimate velocity field seems to be overlooked in the models that use finite difference method. Even for finite element models, for example SUTRA, one of the most commonly used model in the literature, does not handle velocity according to the level of accuracy required in the Elder problem.

Establishing the Elder problem as a benchmark test problem for variable density flow model is extremely helpful for the modelers in verifying their codes. Among the three most popular benchmark tests that include, the Henry problem, the Elder problem, and HYDROCOIN Level 1 Case 5, the Elder problem solution is the only one that is still producing multiple solutions. The work in this study sets more strict numerical guidelines for the solution of convection-dominated flow such as the Elder problem. Various cases discussed in this study in reference to physical instability, numerical perturbations and the use of globally continuous velocity fields are another step toward the acceptance of the Elder problem as a benchmark problem in this challenging area of convection-dominated flows.

CHAPTER 6

SALTWATER INTRUSION HYDRODYNAMICS IN A BEACH

In this chapter, the focus is on the saltwater intrusion hydrodynamics in a beach under the influence of tidal effects. Up until Boufadel [Boufadel 2000], most work that has been done to investigate saltwater intrusion hydrodynamics in a beach under tidal effects were conducted based on the Dupuit assumption, which implies horizontal flow in a beach. As discussed in Chapter 2, this is an important assumption to reduce a three-dimensional representation to a two-dimensional representation. But, in reality, there are problems where the Dupuit assumption is no longer valid. One of these problems is the saltwater intrusion hydrodynamics in a beach because flow in some regions of the solution domain in a beach cannot be approximated as horizontal flow. Given this consideration, the tidal effects problem at a beach is studied in detail in this chapter. In addition, this chapter also contains results and discussions on the effects of different types of boundary conditions that can be used for the analysis of saltwater intrusion hydrodynamics problem. This is a finite domain problem which necessitates the proper handling of the boundary conditions. Furthermore, in this chapter the sensitivity of numerical solution of saltwater intrusion hydrodynamics in a beach under the influence of tidal effects is studied with respect to variations in density differences.

6.1 Introduction

Hydrodynamics in a beach consists of complex physical processes that include mixing in a porous medium, water flow in both unsaturated and saturated zones, and the

effects of tidal wave on the overall saltwater intrusion problem. With the exclusion of complexity associated with variable density flow, unlike the Henry, Elder, and salt dome problems, the hydrodynamics of a beach is the first problem that includes unsaturated and saturated porous medium together in this thesis. In addition to the presence of a variably saturated porous medium, saltwater intrusion hydrodynamics in a beach is a problem where transient solution is necessary as a result of the periodic nature of tidal rise and fall. Another difficulty comes from the geometry of the problem domain. Because beaches have a mild slope, the problem domain is no longer ideal such as a rectangular domain as was considered in the Elder, Henry and Salt Dome problems. This geometry requires irregular elements in the idealization of the solution domain that leads to additional computational burden in the numerical integration associated with the irregular elements.

Another factor that complicates the beach problem is the variable boundary condition that needs to be considered at the tidal beach slope. This variable boundary condition is considered as a function of time in this study. This is again associated with the tidal effects that are normally described as a periodic function. As a result of this variable boundary condition that leads to the periodic change of flow directions, Boufadel [2000] noted that beach hydraulics are highly two dimensional with water entering the beach at a near-vertical angle and leaving it at a near-horizontal angle, which casts doubts on analyses of beach hydraulics based on the Dupuit assumption.

Meanwhile, the scale of the problem domain is small compared to other regional groundwater flow and transport problems that are based on the “aquifer” approach which are mostly large-scale (kilometers) applications. The scale in the vicinity of the tidal

effect zone can be measured meters, which is associated with the height of tide that is in most cases less than several meters.

To investigate hydrodynamics at a beach under the influence of tidal effects, the problem that Boufadel [2000] used in his experiment and simulation is selected as a case study. Since the verification of TechFlow in unsaturated zone is not provided previously, first a code verification of flow in unsaturated zone is provided by comparing the results of TechFlow with the ones from Celia et al. [1990] and Forsyth et al. [1995]. After the code verification, the description of boundary and initial conditions of Case 2 of Boufadel's problems are followed to study the saltwater intrusion problem in a beach under tidal effects. Three types of solute-transport boundary conditions are formulated to investigate the effect of these boundary conditions on the numerical solution of the problem. Then, sensitivity of the numerical solution to a slightly increased density difference is conducted based on the three types of the boundary conditions that can be used in the solute-transport equation. Based on the results obtained from two different density differences and the three types of boundary conditions used in the solute-transport equation, an important recommendation is made in the proper choice of boundary condition that can be used in the solution of this finite domain problem.

6.2 Verification of Flow in a Variably Saturated Porous Medium

As explained in Chapter 4, the governing equations used in TechFlow are developed for variably saturated flow condition in which the van Genuchten empirical equation is used to characterize unsaturated flow hydraulic conductivity parameters. Numerical approximations based on different forms of the governing partial differential

equation can lead to significantly different results for unsaturated flow problems. Numerical solutions based on the standard h-based form of Richards equation [Hillel 1980] generally yield poor results, characterized by large mass balance errors and erroneous estimates of infiltration depth. Conversely, numerical solutions based on the mixed form of Richards equation can be shown to possess the conservative property, so that mass is perfectly conserved [Celia et al. 1990].

In an effort to resolve this issue on the h-based form of Richards equation, Celia et al. [1990] proposed the approach based on a fully implicit (backward Euler) time approximation applied to the mixed form of the unsaturated flow equation in the finite difference approximations. Later, Rathfelder and Abriola [1994] provided the numerical formulation for this mixed form for a finite element method. Appendix C provides the details for this formulation. This method is used in TechFlow. For the verification of TechFlow, two test problems for flow in unsaturated zone are presented: (i) a sample problem solved by Celia et al. [1990]; and, (ii) a sample problem solved by Forsyth et al. [1995].

6.2.1 Celia et al.'s Problem

This problem is a one-dimensional flow problem for freshwater in an unsaturated soil column. The description of the column with initial and boundary conditions is provided in Figure 6.1. Table 6.1 summarizes the physical parameters of the problem. As seen in Figure 6.2, the result of TechFlow is in very good agreement with Rathfelder and Abriola [1994]'s result. The solution is almost identical with true solution.

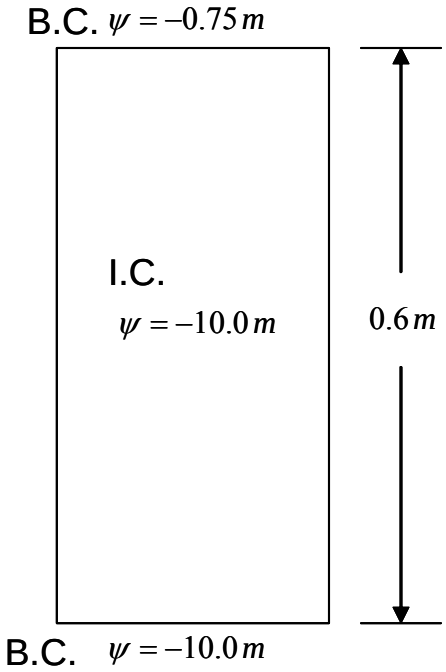

Figure 6.1 The description of Celia et al.'s [1990] problem with initial and boundary conditions. Note ψ is a pressure head

Table 6.1 Physical parameters for Celia et al.'s problem

Symbol	Quantity	Value	Unit
k	Intrinsic permeability	9.35247×10^{-12}	m^2
K	Hydraulic conductivity	9.22×10^{-5}	ms^{-1}
ρ	Water density	998.2	kgm^{-3}
g	Gravitational coefficient	9.807	ms^{-2}
μ	Dynamic viscosity	993×10^{-6}	$kgm^{-1}s^{-1}$
ϕ	Porosity	0.368	-
S_r	Residual soil saturation ratio	0.2772	-
n	Parameters of the van Genuchten model	2	-
m		0.5	-
α		3.35	m^{-1}

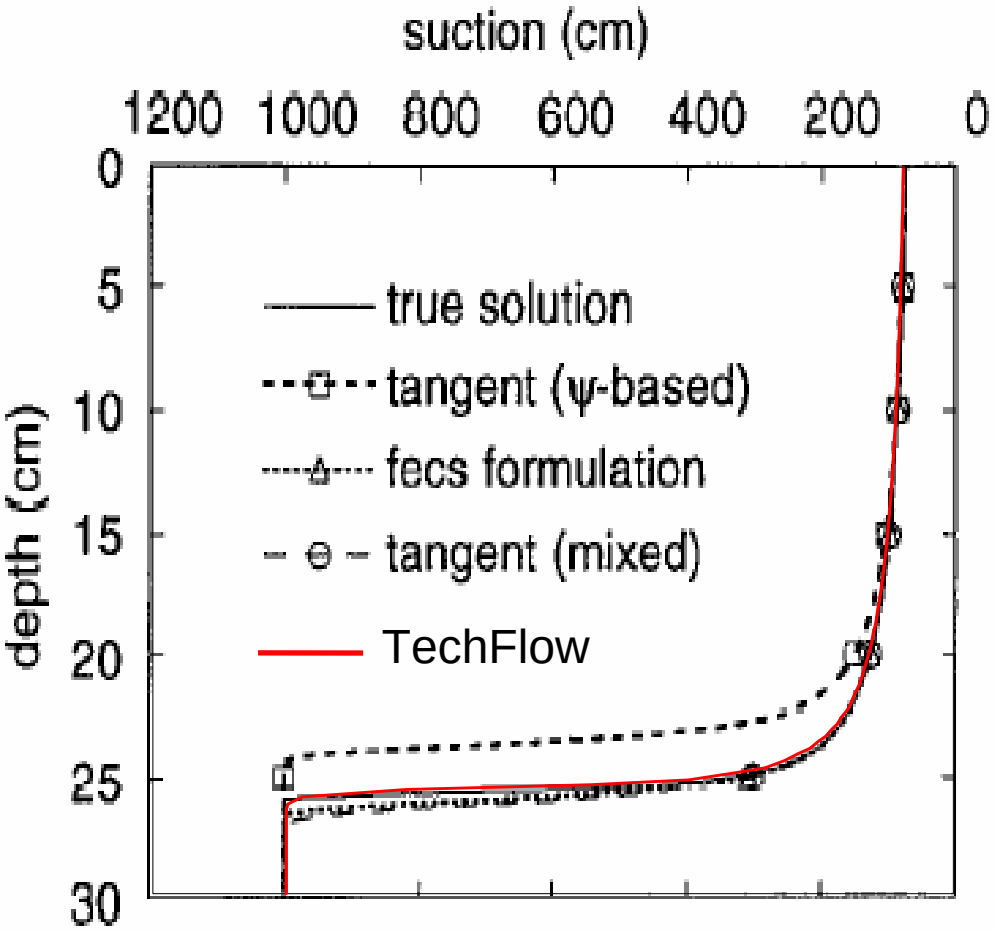

Figure 6.2 Comparison of the result of TechFlow (red solid line) with the results by Rathfelder and Abriola [1994] at time 6 hrs

6.2.2 Forsyth et al.'s Problem

The second problem used to verify TechFlow is the one solved by Forsyth et al. [1995]. Figure 6.3 shows the description of the problem. This time, the boundary condition on the top uses infiltration rather than pressure head. Similar to Celia's problem, the result of TechFlow matches very well with the ones obtained by Forsyth et al. [1995]. The numerical results obtained for this problem are given in Figure 6.4.

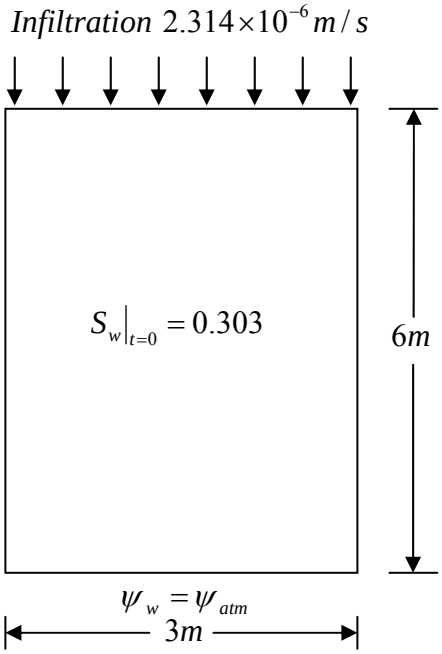

Figure 6.3 The description of Forsyth et al.'s [1995] problem with initial and boundary conditions

Table 6.2 Physical parameters for Forsyth et al.'s problem

Symbol	Quantity	Value	Unit
k	Intrinsic permeability	2.95×10^{-13}	m^2
ρ	Water density	998.2	kgm^{-3}
g	Gravitational coefficient	9.807	ms^{-2}
μ	Dynamic viscosity	993×10^{-6}	$kgm^{-1}s^{-1}$
ϕ	Porosity	0.33	-
S_r	Residual soil saturation ratio	0	-
n	Parameters of the van Genuchten model	1.506	-
m		0.336	-
α		1.43	m^{-1}

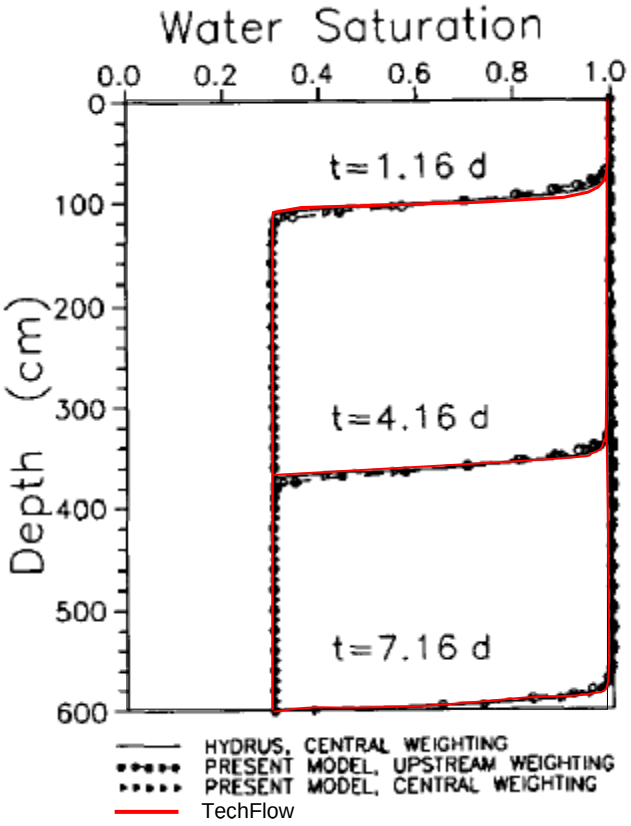

Figure 6.4 Comparison of the result of TechFlow (red solid line) with the results by Forsyth et al.[1995] at times 1.16 d, 4.16 d, and 7.16 d.

6.3 Description of Saltwater Intrusion Problem at a Beach under Tidal Effects

Based on the experiment conducted by Boufadel [2000], a problem for saltwater intrusion hydrodynamics at a beach is formulated under tidal effects. Boufadel have performed Case 1 and 2 of the experiments with density difference of 0.2 % and 2.4 %, respectively. Because of small density difference, he did not solve the coupled equation of flow and transport equations for Case 1. On the other hand, he solved the coupled equation for Case 2 with a limited number of iterations between these equations (i.e., the number of iterations he chose is one). Note that even for Case 2, the density difference based on the density difference between fresh water and seawater is one order lower when compared to the density differences used in the Elder problem and HYDROCOIN Level 1 Case 5. In this chapter, Case 2 is chosen for simulation of saltwater intrusion hydrodynamics in a beach under tidal effects.

The problem domain consists of an 8 *m* long $\times$ 2 *m* high $\times$ 0.6 *m* wide carbon steel tank filled with the sand. Figure 6.5 shows the schematic of the beach area considered and flow boundary conditions. A slope of 10% from a height of 115 to 65 *cm* and another 50 % slope from 65 to zero *cm* are graded as shown in Figure 6.5. The sand covers 630 *cm* at the bottom. According to the tidal conditions, hydraulic head boundary conditions on seaside vary. These variable boundary conditions are set to have the intertidal zone on the beach surface to range from 200 *cm* to 450 *cm* (Figure 6.5). Figure 6.6 shows the periodic function of pressure head representing the tidal effects. This pressure head is used to form variable hydraulic head Type I boundary condition at the sea side. The tidal period is set to be 1,320 seconds (22 minutes) obtained from the experiment conducted by Boufadel [2000]. This short period is due to the small problem domain that is

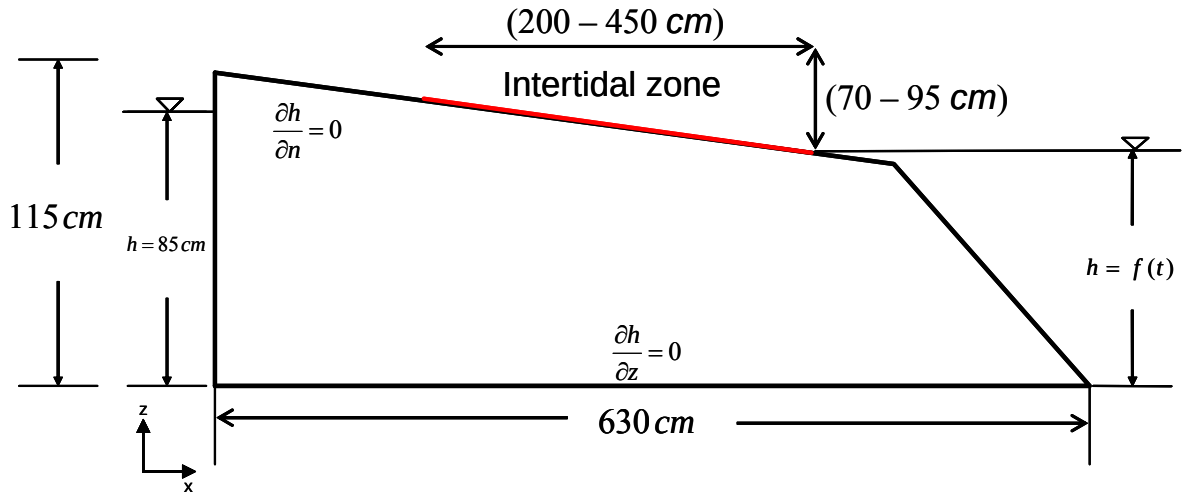

Figure 6.5 Schematic of the beach and flow boundary condition. Red line is the intertidal zone

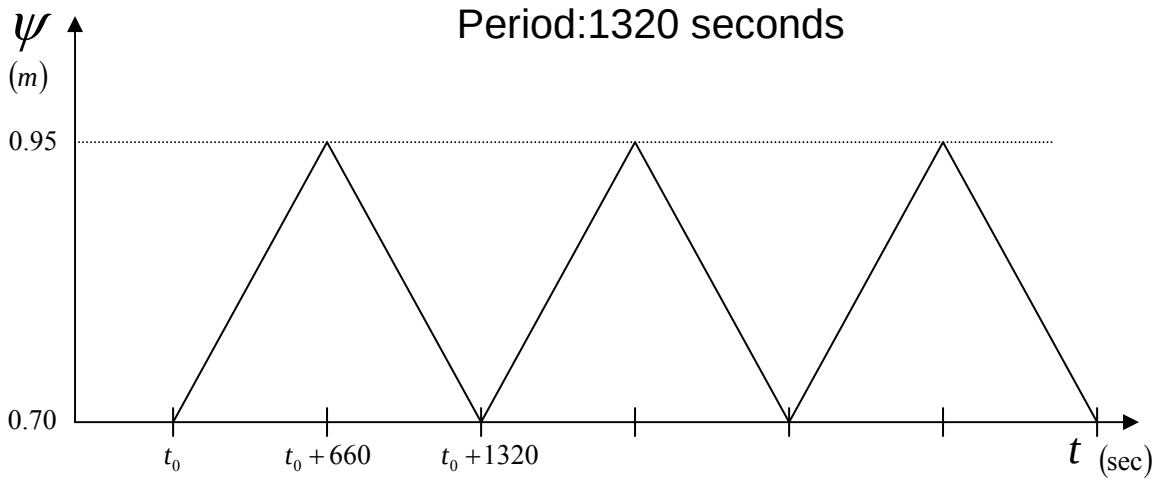

Figure 6.6 Tidal effect (pressure head) represented by a linear relation with a period of 1320 seconds

set specific to the experiment.

One important material property of a porous medium is permeability. Based on permeability, hydraulic conductivity can be estimated with the parameters of the van Genuchten model for unsaturated zone as well as fluid properties. Unlike this general approach, Boufadel [2000] did not use permeability to compute saturated hydraulic conductivity. Instead of starting from permeability, he seems to measure different saturated hydraulic conductivities for his two experiments. Since there is no permeability presented based on his experiments, saturated hydraulic conductivity together with the parameters of the van Genuchten model that Boufadel [2000] provided were used for the simulation. Table 6.3 presents this saturated hydraulic conductivity of Case 2 and the parameters of the van Genuchten model.

Table 6.3 Modeling parameters associated with porous medium and fluid

Parameter	Value	Units
$K_{x0} = K_{z0}$	0.75	$cm\,s^{-1}$
α	0.125	cm^{-1}
n	3.50	dimensionless
S_r	0.01	dimensionless
α_L	0.75	cm
α_T	0.25	cm
γD_m	10^{-6}	$cm^2 s^{-1}$

The problem domain for hydrodynamics in a beach was discretized in two different grids. The first grid consists of 1,942 trilinear brick elements that are a combination of regular and irregular elements as shown in Figure 6.7. This grid is intended to reduce element-geometry-associated computation by reducing a number of irregular elements that require numerical integration. The other grid consists of 2,413 trilinear irregular brick elements only set to obtain more accurate results by assigning a denser grid of irregular elements on unsaturated zone while a less dense grid is placed on saturated zone. This preferential grid placement is to account for the nonlinearity associated with the unsaturated zone equations along with a reasonable computational burden. However, the computational burden is expected to be increased significantly due to numerical integration, which is in this problem 27-point Gauss quadrature integration for all finite element integrals of flow and transport equation.

Although an effort is made to make the problem as close to Case 2 of Boufadel's experiment as possible, some subtle differences are inevitable in the numerical simulations. One of these differences is originated from the handling of nonlinearity (coupling) between flow and transport equation. While TechFlow iterates on solutions until hydraulic head and concentration corresponding to each node satisfy the convergence criterion (within a preset tolerance), MARUN (Boufadel's model) limited this iteration to one cycle. Another one of these differences is associated with the boundary conditions that were obtained from the Boufadel's experiment. TechFlow uses hydraulic head boundary conditions, and these hydraulic head boundary conditions are estimated from the pressure heads obtained from the schematic of Boufadel's work.

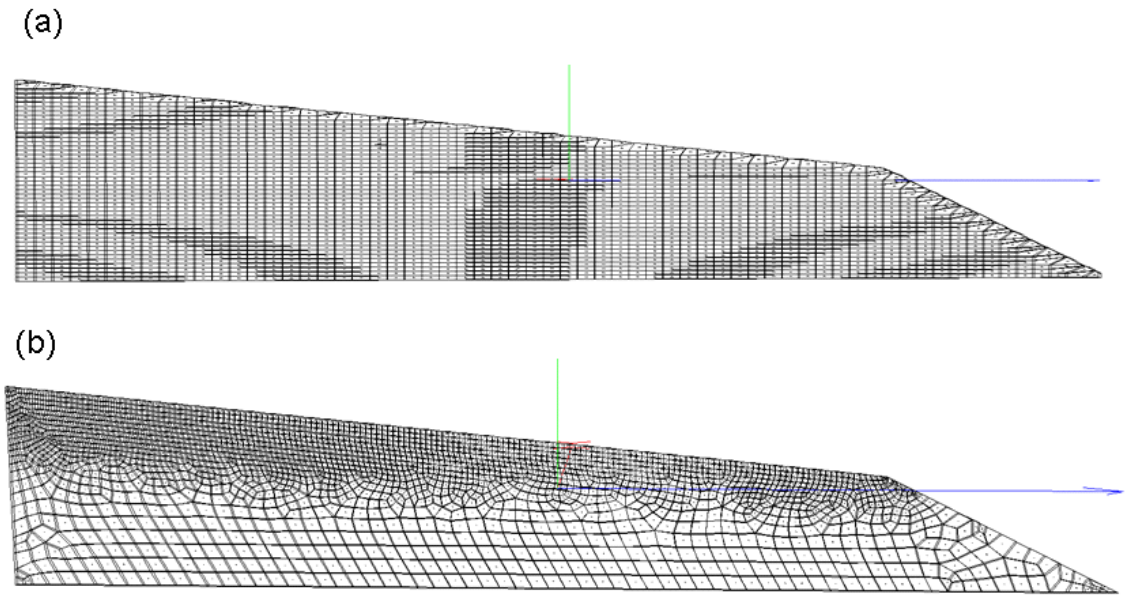

Figure 6.7 Two grids; (a) Grid 1: 1942 combinational regular and irregular elements, (b) Grid 2: 2413 irregular elements

The initial hydraulic head and concentration distribution were obtained by running TechFlow until it reaches steady state with the pressure heads at inland and seaside set equal to be 85 and 70 cm, respectively, and with a Dirichlet boundary condition of transport equation at the inland boundary set to be $C = 1$. The initial concentration to obtain this initial condition for the simulation was $C(x, z, t = 0) = 1$. Based on this initial state the tidal cycle was started at $t = 1.67\, hours$ as used by Boufadel for case 2 simulations. A time step of 30 seconds was used throughout the numerical simulation.

As for the boundary conditions of the transport equation, different types of boundary conditions including the one that Boufadel [2000] used are introduced. In the next section a discussion on the use of these boundary conditions is presented. The conditions for selecting the appropriate boundary condition to better represent the complicated hydrodynamics problem in a beach are discussed in detail.

6.3.1 Boundary Conditions

Because of the periodic nature of saltwater intrusion hydrodynamics in a beach under tidal effects, the boundary conditions for flow and transport equations need to be selected carefully. Compared to boundary conditions for transport equations, the ones for the flow equation are simpler. This is because boundary conditions of the transport equation are dependent on the flow direction in and out of the boundary, which depends on the tidal cycle. Unlike solving a hydraulic head (i.e., scalar), the seepage face boundary conditions of the transport equation are associated with flow velocity (i.e., a vector). Considering the periodic change of flow directions at the seepage face boundary

due to the tidal effects, this change of flow directions should be considered in the transport model to better represent this periodic phenomenon.

For the flow equation at the inland side, Type I constant boundary condition of hydraulic head, is assigned below the water level. This represents hydrostatic condition for positive pressure head $\psi(0,z) \geq 0$. For the boundary above the water table where $\psi(0,z) < 0$, Type II boundary condition, was assigned as $\partial h/\partial x = 0$. Similarly at the seaside, Type I variable boundary condition is assigned for the boundary below the sea level ($\psi(0,z) \geq 0$). The variable boundary condition is defined as $h(0,z) = f(t) + z$ where $f(t)$ is described in Figure 6.6. For the boundary above the sea level ($\psi(0,z) < 0$), a seepage face boundary condition was applied, and the method to introduce the seepage face boundary condition was adopted from Pinder and Gray [1977].

As for the boundary conditions of the transport equation, three kinds of boundary conditions at both inland and seaside are used for the simulation. These boundary conditions are identified as Case 1, 2, and 3. In this notation, the complexity increases as the case number increases. Table 6.4 presents these three types of the boundary conditions for the transport equation. While Case 1 is simplest to consider, Case 1 does not account for the direction of flow because it only uses Type I boundary conditions to represent the concentrations regardless of flow directions. Therefore, this can be interpreted as the case where the boundary conditions for the transport equation is considered to be independent of the flow conditions. In fact, these boundary conditions are valid and frequently used in the cases where there are no tidal effects as Henry's problem.

Table 6.4 Various boundary conditions for transport equation

	Inland boundary	**Seaside boundary**
Case 1	$C = 0$ when $\psi(z) \geq 0$ $\frac{\partial C}{\partial n} = 0$ when $\psi(z) < 0$	$C = 1$ when $\psi(z) \geq 0$ $\frac{\partial C}{\partial n} = 0$ when $\psi(z) < 0$
Case 2	If water is entering the domain $C = 0$ when $\psi(z) \geq 0$ $\frac{\partial C}{\partial n} = 0$ when $\psi(z) < 0$ If water is leaving the domain $\frac{\partial C}{\partial n} = 0$ regardless of the sign of ψ	If water is entering the domain $C = 1$ when $\psi(z) \geq 0$ $\frac{\partial C}{\partial n} = 0$ when $\psi(z) < 0$ If water is leaving the domain $\frac{\partial C}{\partial n} = 0$ regardless of the sign of ψ
Case 3	If water is entering the domain $C = 0$ when $\psi(z) \geq 0$ $\frac{\partial C}{\partial n} = 0$ when $\psi(z) < 0$ If water is leaving the domain Free exit BC when $\psi(z) \geq 0$ $\frac{\partial C}{\partial n} = 0$ when $\psi(z) < 0$	If water is entering the domain $C = 1$ when $\psi(z) \geq 0$ $\frac{\partial C}{\partial n} = 0$ when $\psi(z) < 0$ If water is leaving the domain Free exit BC when $\psi(z) \geq 0$ $\frac{\partial C}{\partial n} = 0$ when $\psi(z) < 0$

Among these three cases, Case 2 is the boundary conditions that is closest to the one used by Boufadel [2000]. To represent the flow direction in the simulation, Boufadel used a Neuman boundary condition, $\partial C/\partial n = 0$, which represents the so-called "outflow boundary condition" where water leaves the porous medium without a change in concentration. This boundary condition is in fact valid if the advective component of transport does not affect the boundary concentrations. Thus, the boundaries, which are far away from the source concentration are well-explained by this boundary condition. However, this boundary condition has a limitation on any boundary affected by both advective and dispersive transport where water leaves or enters the porous domain. These boundaries are well-observed from his experiments and coincide with the zones that violate the Dupuit assumption.

To account for the boundaries that are affected by advective and dispersive transport and also to guarantee no concentration change when water leaves, Frind [1988] proposed the use of "free exit boundary condition" of the advection-dispersion equation to compensate this inconsistency. In his study, he showed in one- and two-dimensional finite element applications where the free exit boundary condition can in fact be applied whenever there is a non-zero advective component with a concentration gradient at the boundary. In two-dimensional finite element method, he used triangular elements and provided the boundary matrix that makes use of free exit boundary conditions. In addition, he showed the numerical solution in a finite domain with a free exit boundary condition, using a correctly proportioned spatial discretization, where the solution behaves like an infinite-domain solution.

In the simulations conducted in this chapter, free exit boundary conditions are included in transport model. The boundary conditions that include the free exit boundary condition are identified as Case 3 (Table 6.4). Since this boundary condition requires a non-zero advective component, it is only applied to saturated zone. This is because advective component in unsaturated zone is very small when compared to that in saturated zone. Considering that TechFlow uses three-dimensional elements (trilinear brick element), free exit boundary conditions for this three-dimensional element are derived in this chapter.

In the Galerkin finite element formulation, when the Gauss theorem is applied to the second order derivative terms, the transformation provides a natural boundary integral term. This natural boundary integral term for the transport equation in three dimensions is expanded as,

$$\int_{\Gamma} D_n^* \hat{C}_j \frac{\partial w_j}{\partial n} w_i d\Gamma = \hat{C}_j \int_{\Gamma} \left(D_{xx} \frac{\partial w_j}{\partial x} n_x + D_{xy} \frac{\partial w_j}{\partial y} n_x + D_{xz} \frac{\partial w_j}{\partial z} n_x + D_{yx} \frac{\partial w_j}{\partial x} n_y + D_{yy} \frac{\partial w_j}{\partial y} n_y + D_{zz} \frac{\partial w_j}{\partial z} n_y + D_{zx} \frac{\partial w_j}{\partial x} n_z + D_{zy} \frac{\partial w_j}{\partial y} n_z + D_{zz} \frac{\partial w_j}{\partial z} n_z \right) w_i d\Gamma \tag{6.1}$$

where D is the coefficient of hydrodynamic dispersion tensor, $\hat{C}_j$ is the approximate solution of concentration, w_i is the basis function, and n_x, n_y, and n_z are the directional component of normal inward vector of the plane where the free exit boundary is located. To apply a free exit boundary condition, each term in Equation (6.1) needs to be integrated over the nodes that are associated with the boundary of the element. Likewise, irregular elements require numerical integrations. A description of free exit boundary

conditions is provided in Figure 6.8. The details of handling of free exit boundary conditions on trilinear brick element are given in Appendix C.6.

As in the case of TechFlow, the free exit boundary condition for three-dimensional trilinear brick element regardless of element geometry is implemented. The verification of the free exit boundary condition was conducted by comparing the analytical solution of one-dimensional solution with the numerical result as Frind [1988] did. The analytical solution for a one-dimensional semi-infinite medium with Type III source boundary condition ($\frac{vC_0}{\phi} = vC - D\frac{\partial C}{\partial x}$) is

$$\frac{C(x,t)}{C_0} = \frac{1}{2}\left[erfc\left(\frac{x-vt}{2\sqrt{Dt}}\right) - \exp\left(\frac{xv}{D}\right) erfc\left(\frac{x+vt}{2\sqrt{Dt}}\right)\left(1+\frac{v(x+vt)}{D}\right)\right] + \frac{v\sqrt{t}}{\sqrt{\pi D}}\exp\left(-\frac{(x-vt)^2}{4Dt}\right) \tag{6.2}$$

where C_0 is the concentration of the source fluid, v is the velocity, ϕ is the porosity, and D is the dispersion coefficient. The numerical solution has a finite domain length, L.

Starting from the base parameters, six different cases of Peclet number (Pe) were compared with the analytical solution. The base parameters are

$$v = 0.1 \quad D = 0.1 \quad L = 40 \quad \Delta x = 2 \quad \Delta t = 20$$

Different Peclet numbers are obtained by varying the dispersion coefficient that was in the range of $0.8 \geq D \geq 0.025$. For the time-marching scheme, Crank-Nicolson scheme was used to increase the accuracy. Figure 6.9 shows the results of concentration profiles at 80, 160, 240, 320, 400, and 480 time units. As shown in Figure 6.9, the numerical solution is in good agreement with the analytical solution. In general, as the transport equation becomes more dispersion dominated (i.e., Pe = 0.25 and 0.5), the need for a

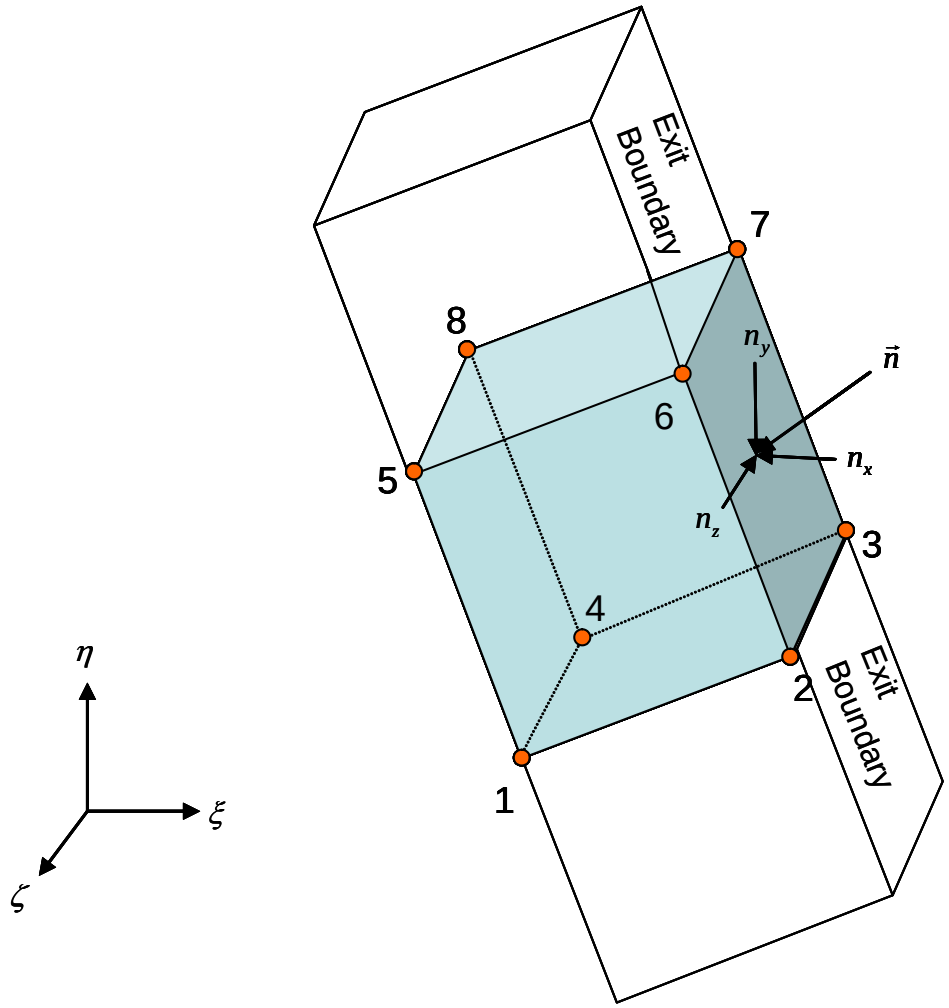

Figure 6.8 Trilinear brick elements on exit boundary

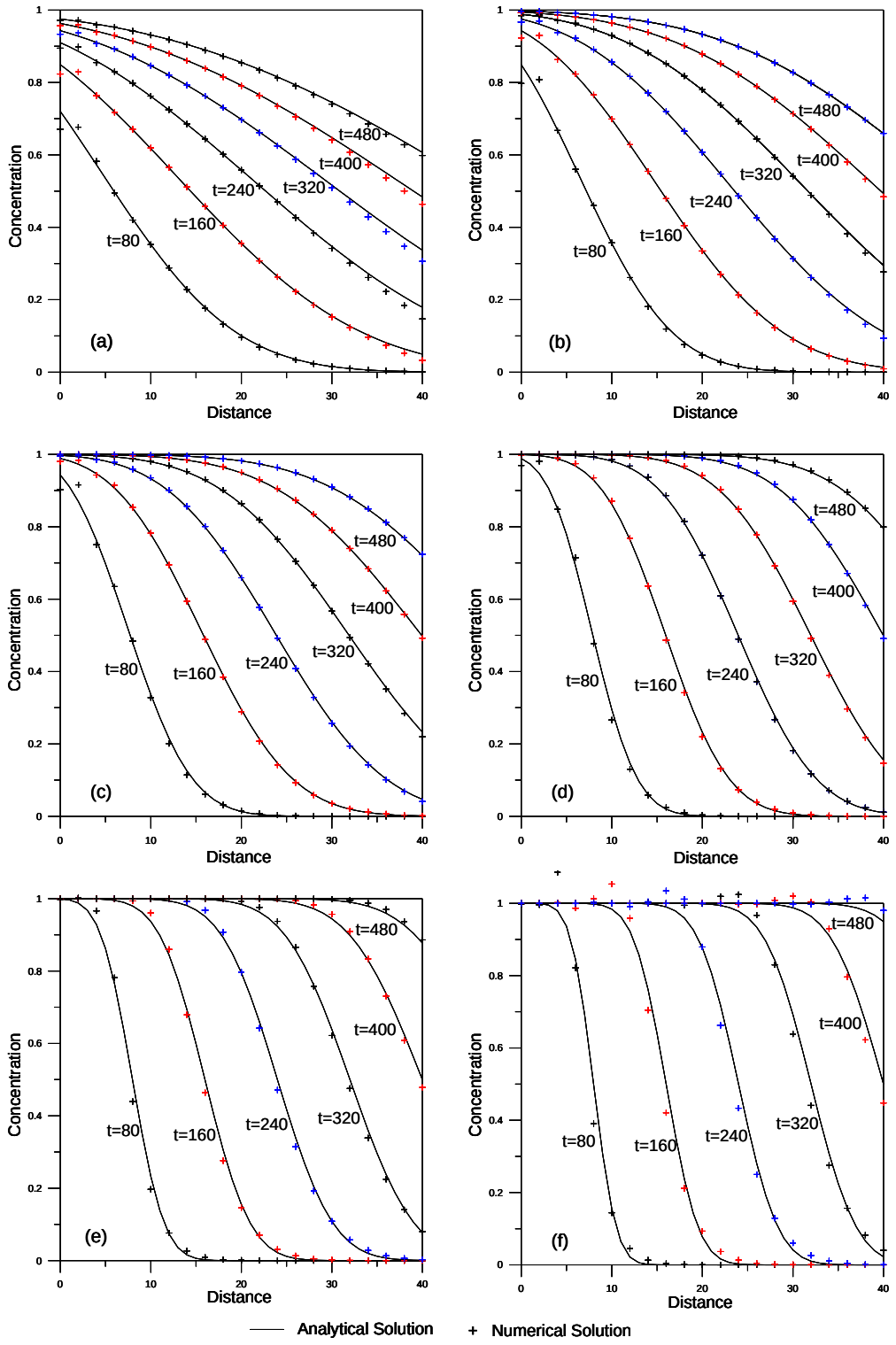

Figure 6.9 Concentration profiles at 80, 160, 240, 320, 400, and 480 time units, free exit boundary condition: (a) Pe=0.25, (b) Pe=0.5, (c) Pe=1.0, (d) Pe=2.0, (e) Pe=4.0, and (f) Pe=8.0

proper downstream exit boundary condition increases. Since this downstream boundary condition is in general unknown, this drift in the numerical solution is difficult to be handled with the free exit boundary condition. However, at the other end of the range, i.e. with larger *Pe*, the free exit boundary is valid as long as the advective component is dominant. Overall, the results show that the free exit boundary condition produces accurate results for about $Pe \geq 1.0$.

Note that this free exit boundary condition is only active Equation (6.1), when the natural boundary term does not become zero. This natural boundary term is not zero when there is concentration gradient at the boundary. Thus, the free exit boundary condition becomes active only when there is concentration gradient at the boundary. This occurs in each case of Figure 6.9 at the exit boundary where there is a concentration gradient at the boundary. Conversely, the concentration lines that did not reach to the exit boundary are not affected by the free exit boundary condition because there are no concentration gradients. However, the significance of the free exit boundary increases with increasing advective component as explained previously.

6.4 Results

Although Case 2 in this study is the closest boundary condition to Case 2 of Boufadel's experiment, there are several differences in the numerical application. The first difference originates from the level of approximation on the governing equation. While Boufadel's model implicitly uses the Boussinesq approximation in the flow equation, TechFlow does not have this assumption. Instead, TechFlow includes the nonlinear terms, which are introduced because the Boussinesq approximation is not used,

in the flow equation to use full density approximations. Accordingly, the level of approximation for TechFlow lies between Level 2 and 3 while MARUN (Boufadel's model) is based on Level 1. These levels are based on the level of approximation for variable density flow as Kolditz et al. [1998] used in their work. They categorized this level of approximation into three levels depending on the selection of the expanded form of governing equations for both flow and transport models obtained from the general close form of each equation. The second difference is associated with the level of nonlinear coupling, TechFlow iterates between flow and transport model until a convergent solution is achieved while MARUN limited the number of iterations to one iteration (i.e., updating) between flow and transport model. This produces significant differences in terms of computational burden and accuracy. Third, MARUN uses pressures measured from experimental devices directly while TechFlow uses the hydraulic head deduced from the heights of water both inland and seaside obtained from his experimental setup. Lastly, although Boufadel [2000] indicated the period of tidal rise and fall and the starting time of this tidal effect in the simulation, this study found inconsistency in the time of the highest and lowest tide in Boufadel's simulation against given information of tidal conditions. Thus, the time of the highest and lowest tides does not necessarily coincide between the results obtained by MARUN and TechFlow.

Figure 6.10 shows the modeling results documented by Boufadel at times 1.725, 1.883, 8.842, and 8.975 hours. Although Boufadel mentioned that these analysis times were selected to show the behavior of the dependent variables in the beach just before the tidal cycle, at the first high tide, at the last low tide, and at the last high tide, this study found that these times are not consistent with the tide as defined in Figure 6.6. However,

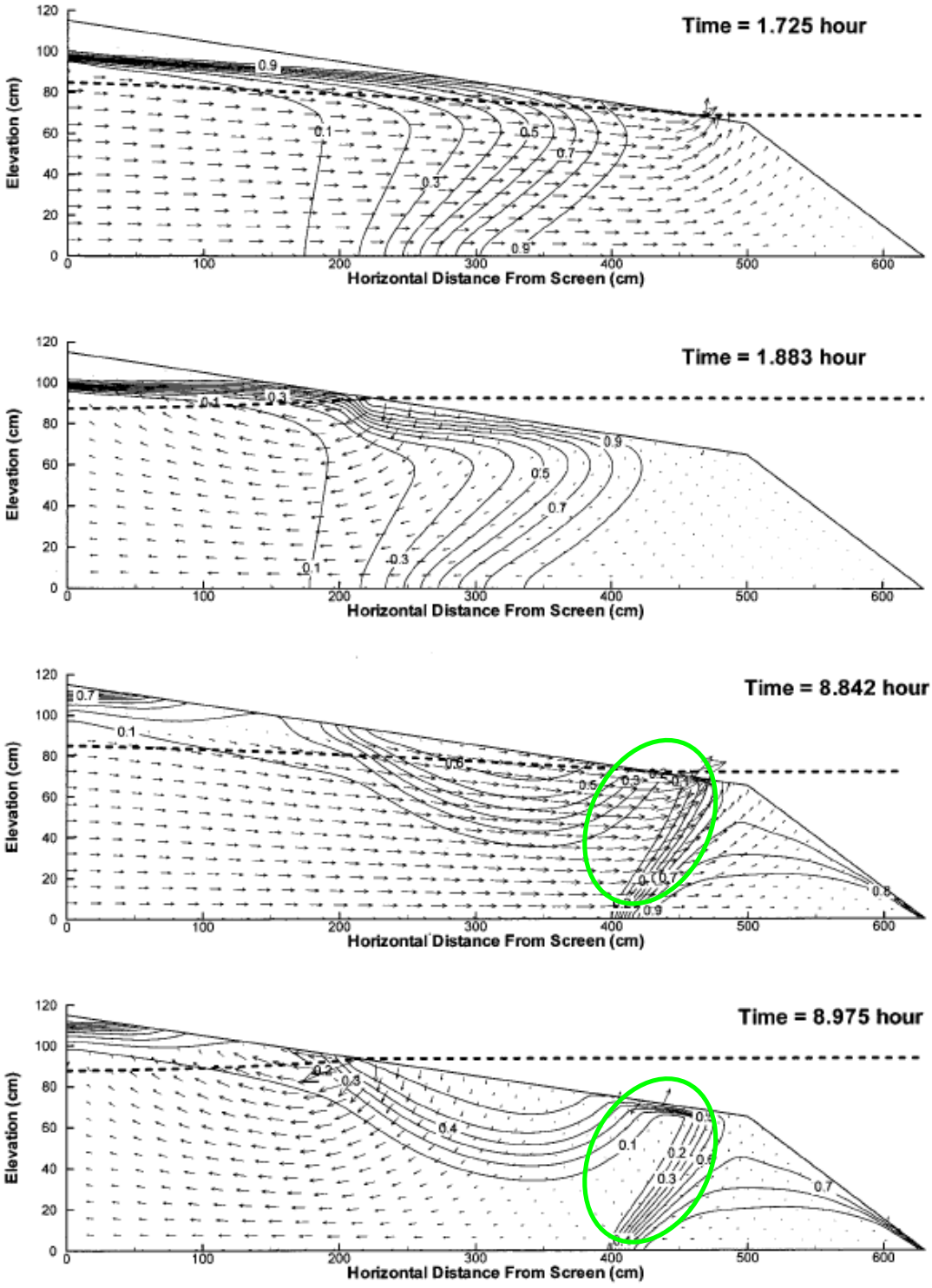

Figure 6.10 Concentration and Darcy flux distribution at four different times. The dashed lines represent the beach water table and the sea water level [Boufadel 2000]

for the analysis of the tidal effect, it is still reasonable to refer to his figure. The results clearly show that there exists a quasi-steady state distribution (cyclic) of salinity in the intertidal zone of the beach. The dynamic hydraulics and hydrodynamics are observed underneath the intertidal zone. Note that the magnitude of velocity in a lower part of the intertidal zone is large at lower tide and this determines the shape of the plume in the region indicating solute mass exits through the lower part of the intertidal zone and divides the region into two plumes, one in seaside and the other under the intertidal zone. From the last figure of Boufadel's result, there is a clear gap between these two plumes as shown in the green circle.

The results of TechFlow from Grid 1 and 2 for three cases depending on the different types of solute-transport boundary conditions used can be found in Figure 6.11, 12, 13, and 14. Despite of several differences in the simulation as mentioned previously, overall all of the results are in good agreement with Boufadel's experiment. Similar to the one in Boufadel's results, all of the results in all cases obtained at the lowest tide after five cycles from TechFlow have the gap identified in Boufadel's results.

In addition to the comparison of the numerical results obtained from TechFlow with the results obtained from MARUN, additional simulations were conducted to find the critical parameter in this saltwater intrusion hydrodynamics in a beach under tidal effects. This is because the results from Figure 6.11 to 14 show little differences regardless of different types of boundary conditions used in the solute-transport model. Thus, among the physical parameters in the system, the density difference was carefully chosen to perform a sensitivity analysis in an effort to see how the system is sensitive to this physical parameter. As mentioned previously, the density difference between fresh

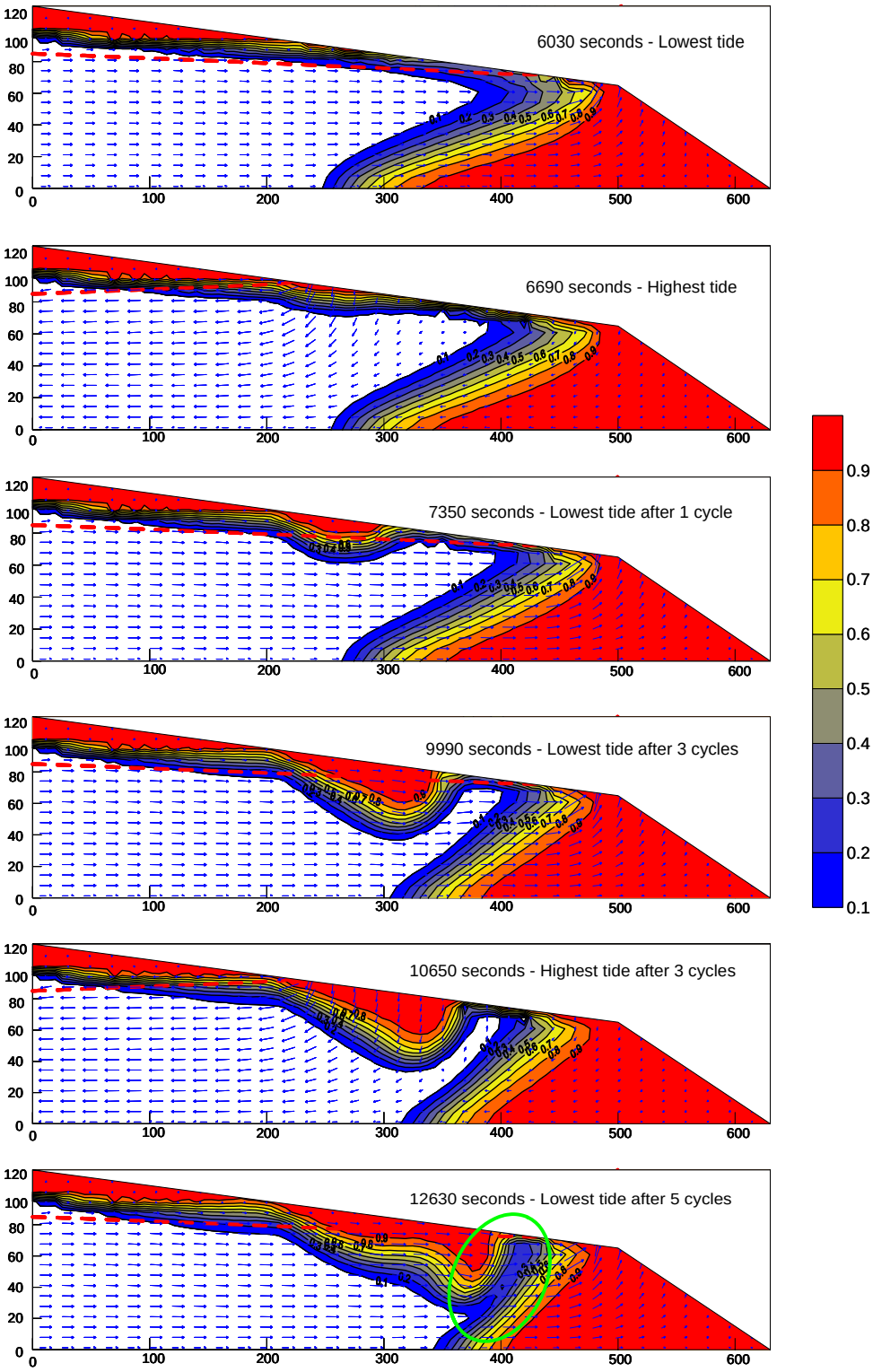

Figure 6.11 Concentration and Darcy flux distribution at six different times from Grid 1. The red dashed lines represent the beach water table for Case 1 of boundary conditions

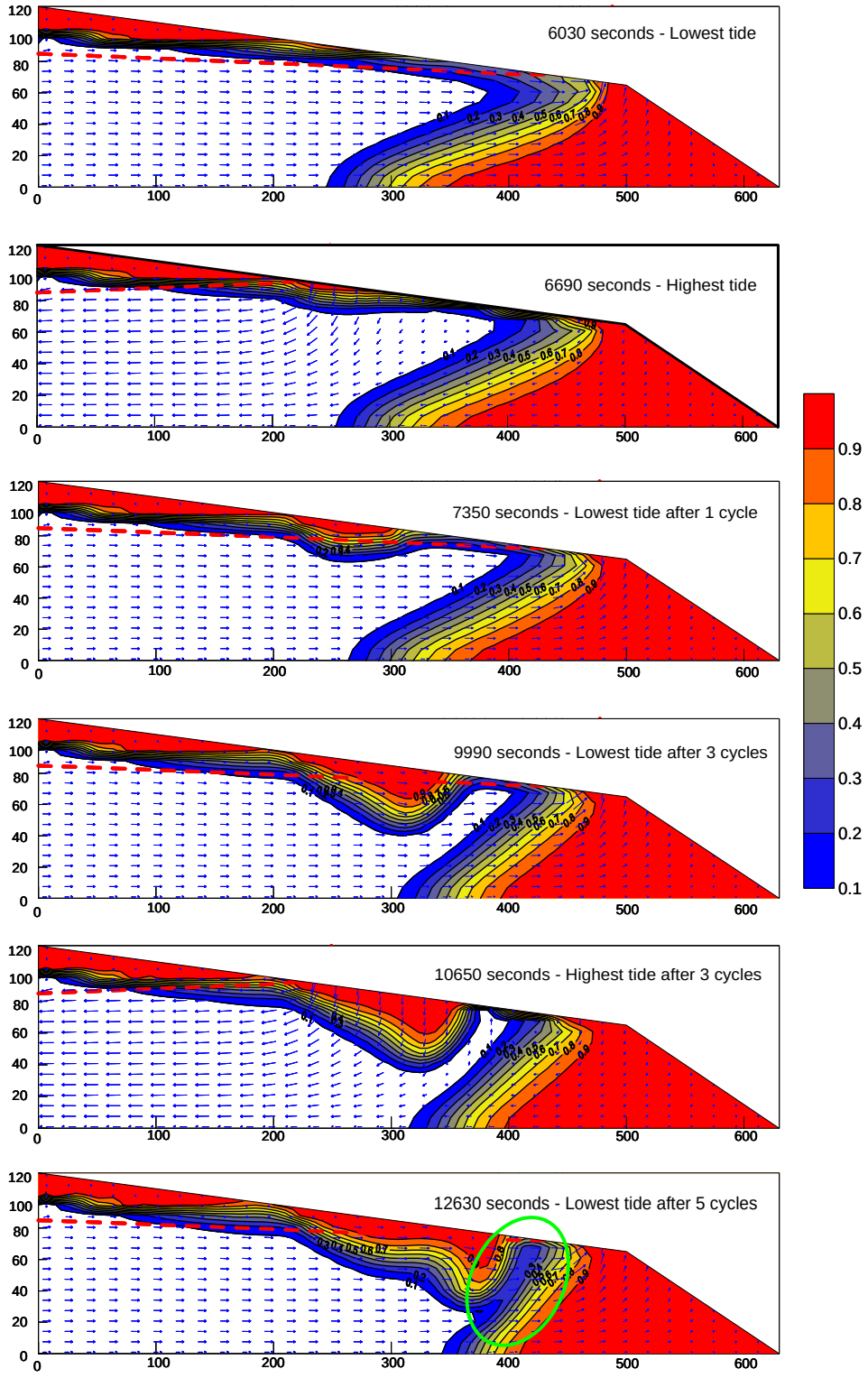

Figure 6.12 Concentration and Darcy flux distribution at six different times from Grid 2. The red dashed lines represent the beach water table for Case 1 of boundary conditions

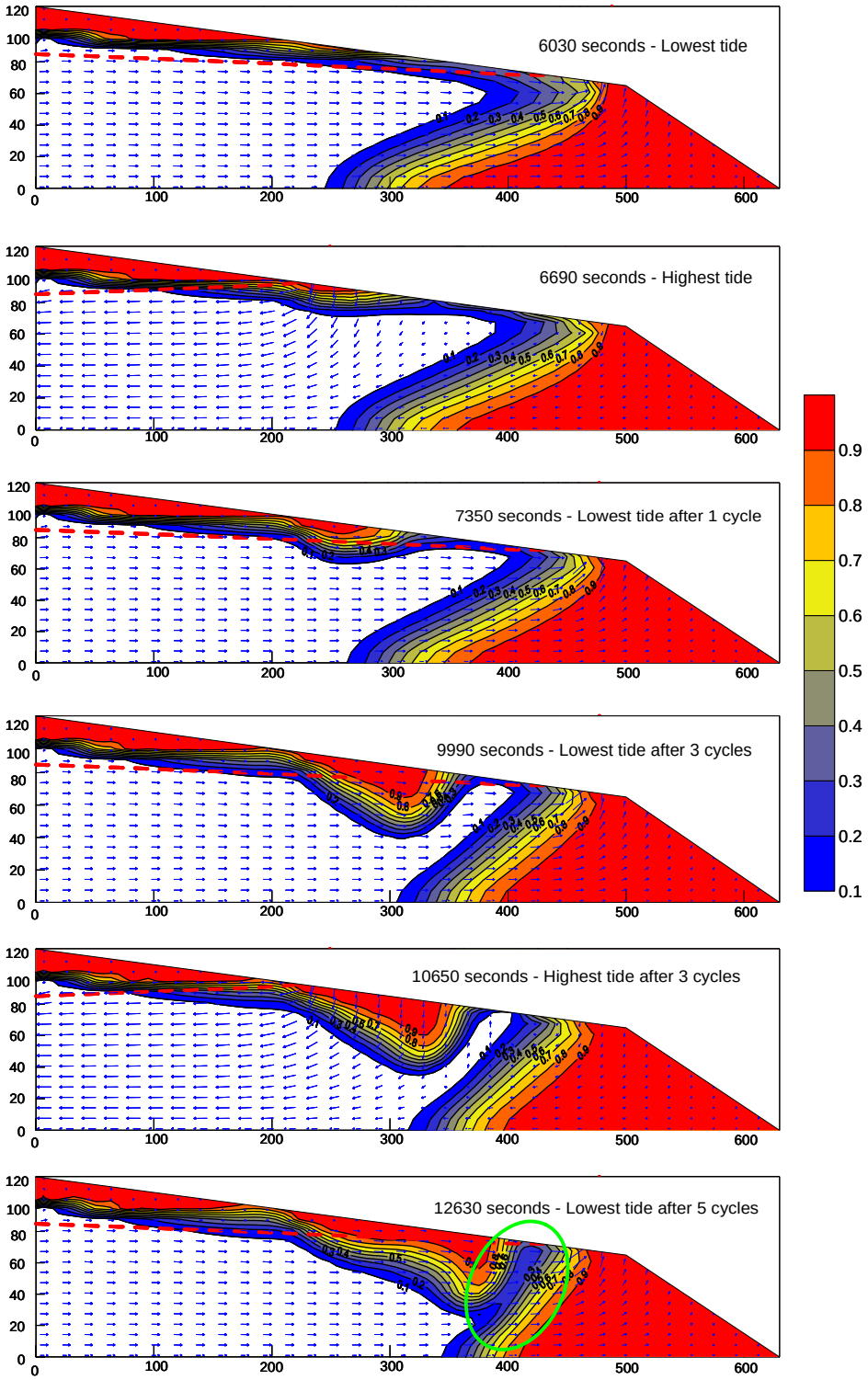

Figure 6.13 Concentration and Darcy flux distribution at six different times from Grid 2. The red dashed lines represent the beach water table for Case 2 of boundary conditions

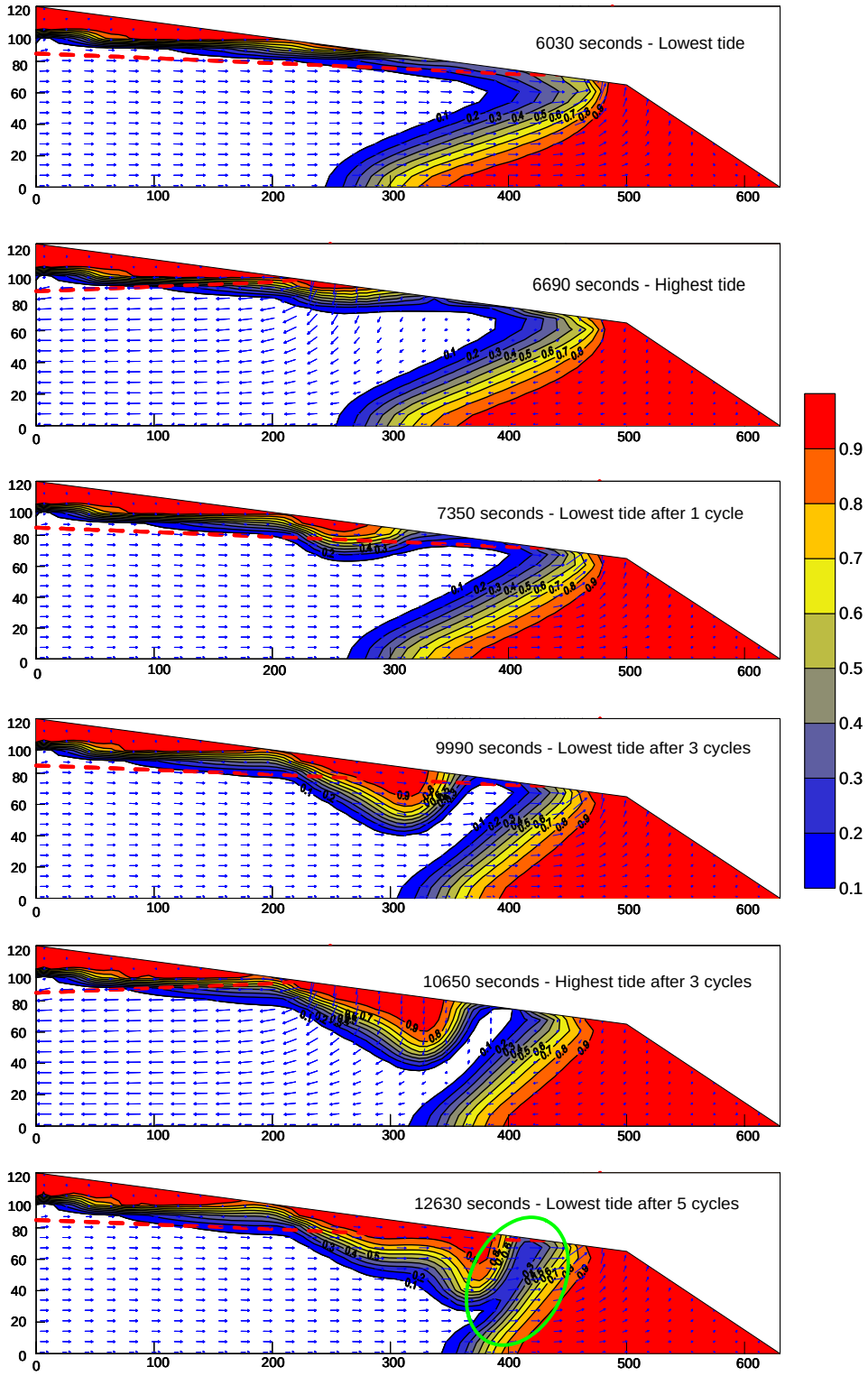

Figure 6.14 Concentration and Darcy flux distribution at six different times from Grid 2. The red dashed lines represent the beach water table for Case 3 of boundary conditions

water and seawater is 2.4 % by mass which is small compared to the Elder and salt dome problem. Thus, the density difference was increased to 3.0 % by mass, the simulations based on the different boundary conditions defined earlier were conducted. Figure 6.15 shows the results of lowest tide after five cycles at this 3.0 % density difference based on the use of the three different boundary conditions in solute-transport model.

Unlike the results from the 2.4 % density difference, the results from the 3.0 % density difference are significantly different in two ways. One is the tendency that the results of the 3.0 % density difference show more significant fingering phenomena than those of the 2.4 % density difference. In fact, the 2.4 % density difference results only show moderate fingering effect in the upper part from the gap. This wide plume under the intertidal zone moves up and down according to the tidal period, and fingering in this region is not fully developed. Since most of times the head on the inland is larger than that in the seaside, the flow direction is mainly towards the seaside. The second is the difference between the results depending on the different types of boundary conditions imposed to solute-transport equation. While there is little difference among the 2.4 % density difference results, Case 3 of the 3.0 % density difference is significantly different from the former two cases. This difference is interesting because there is a significant change in the profiles based on a slight increase of the density difference. This indicates that the solution is very sensitive to density differences. Another important point to note is that in the results of 3.0 % density difference case, none of the results shows the gab observed in the 2.4 % density difference. In general, the results between Case 1 and 2 show a similar pattern of concentration distribution, and the result for Case 3 is less prone to fingering compared to the former two results.

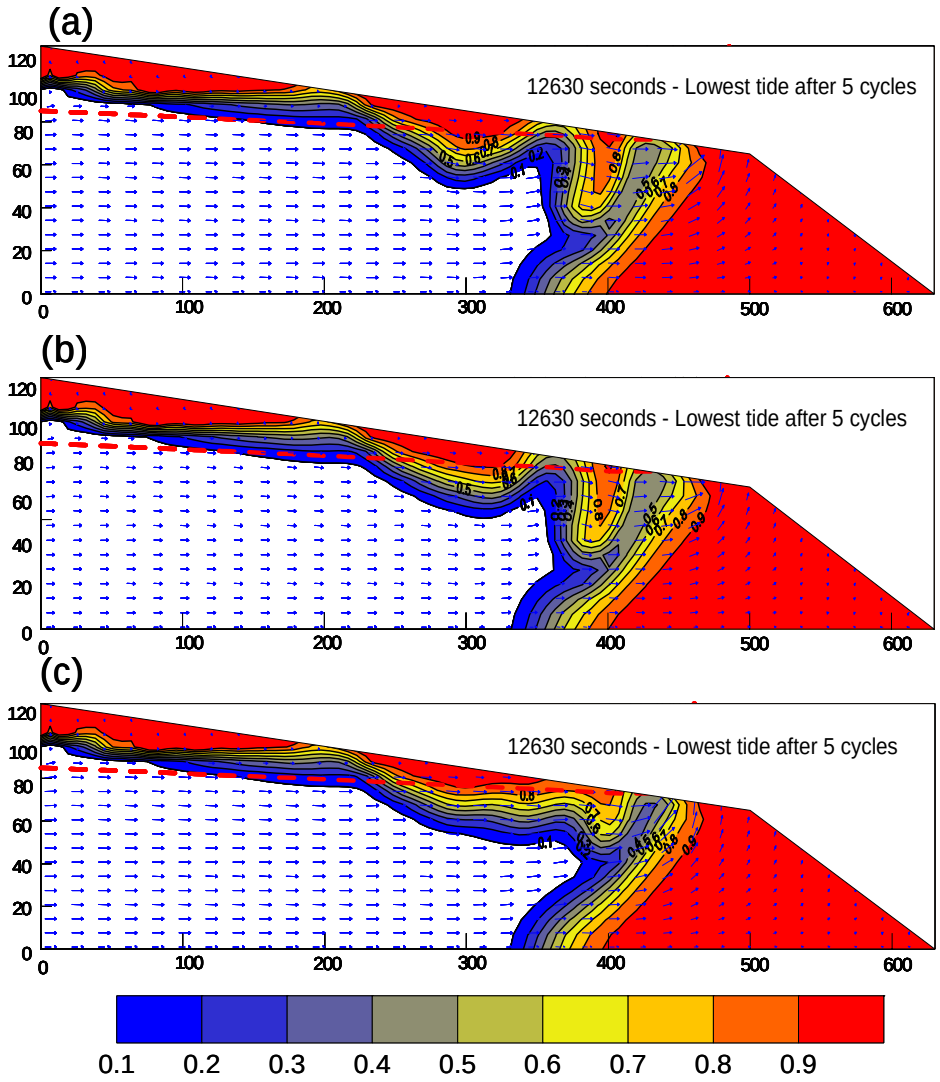

Figure 6.15 Concentration and Darcy flux distribution at 3.0 % density difference. The red dashed lines represent the beach water table for (a) Case 1, (b) Case 2, and (C) Case 3 boundary conditions

6.5 Discussions

This discussion section includes the comparison with Boufadel's simulation, the effects of using two different grids, the effects of the different types of boundary conditions in solute-transport model, sensitivity analysis of density difference associated with the different types of boundary conditions in solute-transport model and submarine groundwater discharge (SGD) along the intertidal zone and saltwater wedge.

6.5.1 Comparison with Boufadel's Result

First, when compared to Boufadel's result (Figure 6.10), the result of TechFlow shows that the transition zone between freshwater and saltwater (i.e., only by direct contact between freshwater and saltwater with no tidal effects) is more skewed than that of Case 2 from Boufadel's experiment. This indicates the result from Boufadel is closer to the case when there is no density coupling effect where the flow of constant density (i.e., no density difference between fluids) is horizontal. This generates vertical transition zone between saltwater and freshwater. The reason that the transition zone is skewed and not orthogonal to horizontal plane is that the heavier fluid (saltwater) goes under the lighter fluid (freshwater) at the transition zone while mixing between theses fluids occurs. In fact, Case 1 of Boufadel's result (not provided in the thesis) obtained without density coupling clearly shows this vertical transition zone in his result. As for the slope of the transition zone between Boufadel's results and those from this study, the incomplete iteration of coupling between flow and transport equation from Boufadel's simulation to represent density coupling effects may contribute this difference. In contrast to the

incomplete iteration, TechFlow iterates the solutions of hydraulic head and concentration until the preset convergence criteria are met.

Secondly, from the numerical results obtained at 8.975 hours (Figure 6.10), the Darcy flux in the upper part of water table in the left shows upward movement even above the water table. This does not make sense at all because the direction of flow is against the direction of gravity. In addition to the direction of flow, the other discrepancy can be also found in the magnitude of the Darcy flux in the same region compared to the magnitude in saturated zone. Generally, the magnitude of velocity in unsaturated zone is significantly smaller than that in saturated zone. However, the Darcy flux in unsaturated zone at 8.975 hours in Figure 6.10 is considerably large. Nonetheless, TechFlow does not show these phenomena.

Lastly, both of the results show the gap as discussed previously. This gap is created because the flow velocity (i.e., advective transport) is large such that solute mass in the gap exits through the boundary and results in a thin plume in the region. However, in general, the plume especially under the intertidal zone in this study is more curved than that in Boufadel's results.

6.5.2 Effects of Using Two Different Grids

The simulation is conducted on two different grids as shown in Figure 6.7. Grid 1 was intended to reduce the computational burden by making most of elements regular so that numerical integration is avoided as many times as possible. However, because of geometrical and physical constraint, Grid 1 has disadvantages that can be summarized as follows. First, irregular elements are not healthy due to violation of angles to fit the

geometry. To reduce element-geometry-associated error, FEM requires healthy elements that are not acute and extreme shape of the element. (i.e., trilinear brick element that looks like six-node linear wedge, bilinear element that looks like equilateral triangle, etc). In addition, Grid 1 also has physical limitation such that all regular elements are uniform regardless to saturation ratios of the porous medium. Due to high non-linearity of the van Genuchten empirical equation, denser grids are required in unsaturated zones than saturated zones. This uniform grid density in fact did create an eddy of negative concentration in the unsaturated zone because improper grid density is applied to the zone. Unlike Grid 1, Grid 2 does not have these two restrictions. However it requires more intensive computation because of numerical integration over added irregular elements. As indicated, Grid 2 has denser grid in the unsaturated zone and coarser grid in the saturated zone. In addition, Grid 2 fits sloping beach domain nicely.

Although there are some disadvantages in Grid 1, the results from Grid 1 and 2 for Case 1 in Table 6.4 are in good agreement. Little difference is observed between these two grids. This may mean high level of numerical integration (i.e., 27-point Gauss quadrature integration) accounts for some of unhealthy elements along the beach line, and the concern of the nonlinear effect in unsaturated zone is observed to be within a manageable limit to the grid density. These can be advantages especially when this problem needs to be scaled up to the regional scale of groundwater flow and transport model. In fact, several works found in the literature do not meet strict grid density decades ago in modeling of saltwater intrusion and saltwater upconing [Diersch et al. 1984;Reilly and Goodman 1987;Voss and Souza 1987;Panday et al. 1993]. However, validity of these results still needs to be investigated in this variable density flow. Thus,

the work to find out what kinds of the applications in variable density flow can be tackled at regional scales with reasonable grid density is another study that is of great importance. The details of the scale issue associated with the grid density will be provided in Chapter 7 and 8.

6.5.3 Effects of the Different Types of Boundary Conditions in Solute-transport Model

One of the goals in conducting the simulation with various types of boundary conditions is to investigate the most appropriate boundary condition that describes saltwater intrusion hydrodynamics in a beach. Once a problem domain is determined, the boundary condition to govern the boundary of the problem domain should be selected to represent the hydrodynamics of the system as close as possible to real situations. Generally, three types of boundary conditions are well-known and widely used in solving partial differential equations either analytically or numerically. In this chapter, the selection of boundary conditions for transport equation consists of three collections of boundary conditions as described in Table 6.2. Case 1 in Table 6.2 is fixed boundary conditions. This is in fact the simplest collection of the boundary conditions in solving hydrodynamics in a beach. Unlike Case 1, Case 2 and 3 are adaptive boundary conditions. The adaptive boundary conditions are required to describe the change of flow directions into the transport model because the change of flow directions keeps switching the boundary to be an entry boundary or an exit boundary. This boundary switching can not be appropriately handled by the fixed boundary condition. Thus, Case 2 and 3 use adaptive boundary conditions that represent this entry or exit boundary. When water is

entering the system, the corresponding boundary becomes an entry boundary. When water is leaving the system, the boundary becomes an exit boundary. In short, Case 1 is the collection of the boundary conditions that only represent the entry boundary regardless of the flow direction while Case 2 and 3 have two different boundary conditions for the entry and exit boundaries depending on the flow direction.

Regardless of the type of boundary conditions used in the solute-transport model, the cases of the simulations show little difference. From all the results at 2.4 % density difference, the gap, which occurs due to significant advective component, is clearly shown in all the cases and has small concentration. Further, the upper part under the intertidal zone next to the gap is wide and shows little fingering effect. Concentration gradients of this plume near the intertidal zone are almost zero. These are important factors when the comparison between the result at 2.4 % density difference and the result at 3.0 % density difference is made.

Unlike the similarity among all the cases at 2.4 % density difference, the results at 3.0 % density difference are significantly different. Related to the significant advective component zone (i.e., the gap), this gap is no longer shown in all the cases of boundary conditions. This is because the increased density difference forces the plume along the intertidal zone down, narrows the gap, and eventually fills the gap with the concentration from the plume. This triggers effects of different types of boundary conditions when the water leaves the system. Because there is significant advective zone in the gap, it pushes the concentration out of the system, now the boundary, especially in the lower part of the intertidal zone becomes an exit boundary. However, the handling of this exit boundary is different according to the cases defined. In this handling of the exit boundary, Case 1 and

2 show little difference that is supposed to allow the solute mass to exit the system through the exit boundary. Different from Case 1 and 2, Case 3 allows the solute mass to exit significantly because the lower part of the intertidal zone is the exit boundary with significant advective component and this significant advective component with the free exit boundary condition in Case 3 tries to have the thin gap by allowing the solute mass out of the system. Thus, the significant fingering observed in Case 1 and 2 may not be real fingerings but the resulting effects generated by improper handling of the free exit boundary conditions. In fact, the fingerings in Case 1 and 2 are not created by downward movement of the plume but created by upward movement of the plume. Therefore, Case 3 shows the least fingering effect because the solute mass properly exits the system. The gap becomes thinner as the solute mass exited the system decreases. Figure 6.16 provides the result obtained at the lowest tide after six cycles and shows this thinning effect in the gap. As shown, compared to the last result at the lowest tide after five cycles, the gap has clearly become thinner than that at one cycle earlier.

6.5.4 Sensitivity Analysis of Density Difference Associated with the Different Types of Boundary Conditions in Solute-transport model

Additional simulation with higher density difference, 3.0 % by mass, was conducted to investigate the sensitivity of solution to the density difference. This density difference is one of the physical parameters and is selected similar to the case of the Elder problem sensitivity analysis. To identify the parameters or conditions that reflect sensitivity of solution to the density difference in the saltwater intrusion hydrodynamics in a beach under tidal effects is a difficult problem. Deciding quantitative indicator is

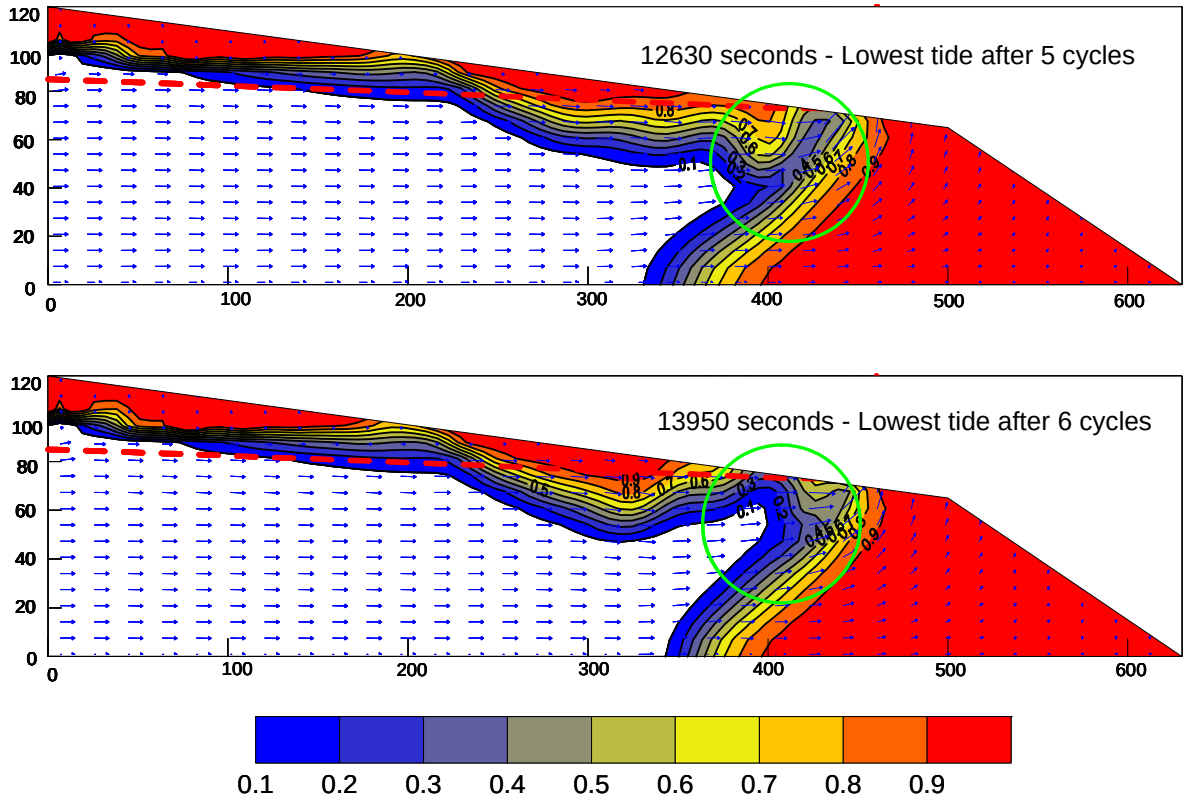

Figure 6.16 Concentration and Darcy flux distribution for Case 3 boundary conditions at 3.0 % density difference. The red dashed lines represent the beach water table.

difficult unless the goals are clearly defined. Thus, in this sensitivity analysis to the density difference, fingerings are chosen as the indicator. These fingerings are very moderate in all the cases of the simulation with density difference, 2.4 %. In addition to the selection of fingerings as an indicator, note that these fingerings themselves are based on the qualitative analysis rather than the quantitative one.

The numerical results from Case 1 and 2 of the 3.0 % density difference simulation are almost the same while Case 3 is significantly different from the others in terms of the fingerings (Figure 6.15). However, Case 1 is more prone to fingering than Case 2 indicating that Case 2 lost more solute mass out of the system through the intertidal zone than Case 1 did. In fact, the difference of the boundary conditions for Case 1 and 2 occurs only when the water is leaving the boundary. However, the amount of the mass transported by advective component is minimal resulting little difference between Case 1 and 2.

In addition to the extent of the fingering between Case 1 and 2, the fingering observed in both cases is particular. In general, fingerings are generated by density differences in physically unstable systems. This leads the fingering as the plume goes down in the gravitational direction. But, the fingering in Case 1 and 2 is generated by vertical upward movement of the plume directed to avoid the thick plume that filled the gap observed at 2.4 % density difference. Thus, this fingering is closely associated with local significant advective component at low tides.

Interestingly, Case 3 of the 3.0 % density difference shows significant difference from Case 1 and 2. Especially, the concentration profile in the gap right underneath the lower part of the intertidal zone is significantly shallow, which leads to less fingering

effect. This clearly indicates that the free exit boundary condition defined previously uses the significant advective component in the gap to allow significant solute mass to exit the system through the exit boundary. In fact, the matrix formulation of free exit boundary conditions in one-dimensional application, the velocity in the advective component must have some magnitude relative to the dispersive component so that the free exit boundary can be valid indefinitely. This unique zone (the gap) in this saltwater intrusion hydrodynamics in a beach under tidal effects is extremely important because the zone has a significant advective component that triggers the free exit boundary condition to allow the solute mass to exit the system. Thus, the system becomes less prone to fingerings. In other words, the fingering observed in Case 1 and 2 at the 3.0 density difference is artificially generated due to improper handling of the exit boundary condition.

6.5.5 Submarine Groundwater Discharge (SGD) along the Intertidal Zone and Saltwater Wedge

To better understand the hydrodynamics along the intertidal zone and saltwater wedge, six quasi-steady state solutions after five cycles with two different density differences and three different types of boundary conditions are evaluated with respect to the SGD. In general, at the lowest tide seawater is flushed out and there is no circulation in the saltwater wedge zone. At the highest tide, there is no external freshwater influx from inland because the main flow direction is changed to the inland.

In addition to the change of the flow direction, the local convective circulation at the lowest and highest tides occurs underneath the intertidal zone but with different characteristics. Table 6.5 summarized the discharge contribution along the intertidal zone

Table 6.5 Discharge contribution along the intertidal zone and the saltwater wedge zone and the local circulation rate under the intertidal zone for six pseudo-steady state solutions

Type A		Type B		Type C	
The 2.4 % density difference					
Intertidal zone	14.5 %	Intertidal zone	13.7 %	Intertidal zone	14.1 %
Seabed	85.5 %	Seabed	86.3 %	Seabed	85.9 %
Percent ratio of outflow to inflow along the intertidal zone $\left(\left(Q_{out}^{IT}/Q_{in}^{IT}\right)\times 100\right)$					
293 %		188 %		356 %	
The 3.0 % density difference					
Intertidal zone	4.9 %	Intertidal zone	2.2 %	Intertidal zone	59.4 %
Seabed	95.1 %	Seabed	97.8 %	Seabed	40.6 %
Percent ratio of outflow to inflow along the intertidal zone $\left(\left(Q_{out}^{IT}/Q_{in}^{IT}\right)\times 100\right)$					
193 %		53 %		1100 %	

and the saltwater wedge zone and the local circulation rate under the intertidal zone for six quasi-steady state solutions at the lowest tide. In this estimation, the discharge contribution is calculated across the two segments (i.e., the intertidal zone and saltwater edge) while the local circulation rate is computed only along the intertidal zone boundary. Except for Case 3 at the 3.0 % density difference, the discharge contribution from the intertidal zone decreases as the density difference increases. The discharge from the intertidal zone at the lowest tide is mostly determined by velocity direction relative to the slope of the beach and the external freshwater inflow.

Interestingly, at the highest tide discharge from the lower portion of the intertidal zone is also observed as shown in Figure 6.17 while most of flow directions head to inland. This implies local convective circulation occurring under the intertidal zone. But, the SGD in this zone is not purely contributed by seawater but by the complicated hydrodynamics due to the change of the flow direction caused by tidal fluctuation. This outflowing portion of the lower intertidal zone is clearly related to the development of the plume underneath. The plume development is significantly affected by density

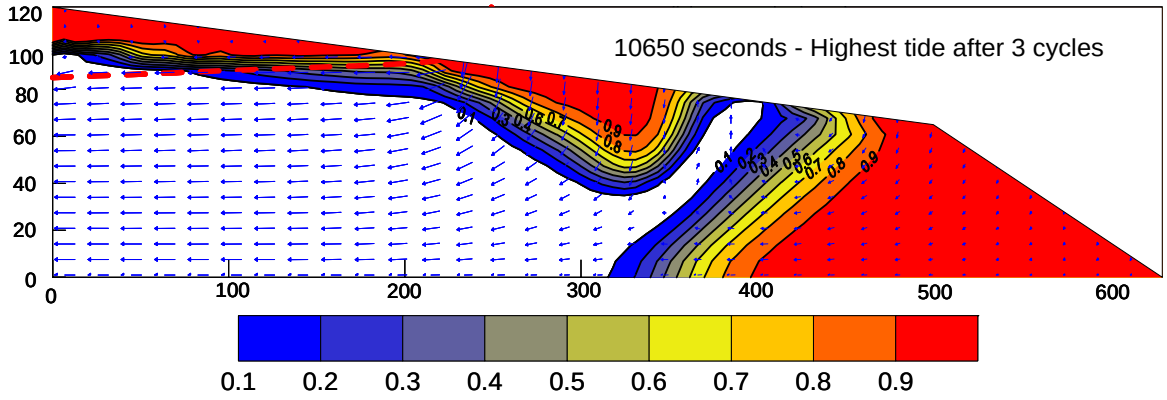

Figure 6.17 Concentration and Darcy flux distribution at the highest tide after three cycles for the 2.4 % density differences obtained with Type A boundary conditions. The red dashed line represents the water table

differences and the choice of the boundary conditions. Since the hydraulic head at the highest tide is higher than the head inland, the seawater recharge contribution along the intertidal zone and the saltwater wedge zone and the local circulation rate under the intertidal zone for six quasi-steady state solutions at the highest tide is summarized in Table 6.6. The percent ratio of outflow to inflow along this submerged intertidal zone at the highest tide is obviously much less than those at the lowest tide because of the entire change of the flow direction. The recharge contribution is mostly from the intertidal zone due to the mild slope that makes physically instable condition (i.e., the saltwater stays on top of the freshwater) as opposed to the discharge contribution at the lowest tide.

6.6 Conclusions

Saltwater intrusion hydrodynamics in a beach under the influence of tidal effects are investigated by solving Boufadel's problem. Hydrodynamics in a beach is a complex problem that includes variable density flow in a variably saturated porous medium with

Table 6.6 Seawater recharge contribution along the intertidal zone and the saltwater wedge zone and the local circulation rate under the intertidal zone for six pseudo-steady state solutions

Type A		**Type B**		**Type C**	
The 2.4 % density difference					
Intertidal zone	88.8 %	Intertidal zone	87.4 %	Intertidal zone	87.5 %
Seabed	11.2 %	Seabed	12.6 %	Seabed	12.5 %
Percent ratio of outflow to inflow along the intertidal zone $\left(\left(Q_{out}^{IT}/Q_{in}^{IT}\right)\times 100\right)$					
11.2 %		14.6 %		15.3 %	
The 3.0 % density difference					
Intertidal zone	86.3 %	Intertidal zone	85.8 %	Intertidal zone	84.1 %
Seabed	13.7 %	Seabed	14.2 %	Seabed	15.9 %
Percent ratio of outflow to inflow along the intertidal zone $\left(\left(Q_{out}^{IT}/Q_{in}^{IT}\right)\times 100\right)$					
10.7 %		14.6 %		12.3 %	

seepage flow and under the influence of tidal effects. In addition, it is also geometrically unique because of a mild slope of beach within a finite solution domain. This mild slope together with tidal effects changes the flow direction along the intertidal zone and creates instable conditions periodically such that the heavier fluid stays on top of the lighter fluid as in the case of the Elder problem. Obviously, this instable condition vertically affecting the system hardly holds the Dupuit assumption valid.

Based on the results of TechFlow on two different grids with the use of various boundary conditions for the transport equation, the saltwater intrusion hydrodynamics in a beach under the influence of tidal effects shows unique dynamics. These solutions are primarily affected by density differences, tidal effects on a mild slope, variably saturated porous medium and finite domain solution condition. As Boufadel [2000] and this study showed in the results, the advective component in the gap is significant at lower tides. This significant advective component as well as the periodic change of the flow direction makes the saltwater intrusion hydrodynamics unique and indicates that traditional

boundary conditions in solute-transport equation is hardly valid. The improper handling of the exit boundary condition leads to the artificial fingerings because the solute mass is kept and accumulated in the system. However, the free exit boundary effectively allows the solute mass exit through the exit boundary especially in the gap area.

The gap in the system is an important region because two plumes are divided by the gap. The thickness of the gap changes as the density difference changes. For the 2.4 % density difference, the gap is so thin that the effects of the different types of boundary conditions in solute-transport model are minimal. However, at slightly increased density difference, 3.0 %, the corresponding gap is filled with concentration as the plumes are developed. This gap located in the high advective zone that occurs due to tidal effects, a unique geometry of the system and hydraulic heads triggers the free exit boundary condition and allows the solute mass out of the system. Thus, the system becomes less prone to fingerings. Therefore, saltwater intrusion hydrodynamics in a beach under tidal effects is one of the good examples that the traditional boundary condition has a limitation on describing the exit boundary of the solute-transport model caused by the change of the flow direction.

CHAPTER 7

SALTWATER UPCONING BENEATH PUMPING WELLS

As discussed in Chapter 2, saltwater upconing can be analyzed using three different approaches: (i) the analytical solution assuming the steady state condition; (ii) the use of numerical model based on the sharp interface between fresh water and saltwater; and, (iii) the use of a numerical model for variable density flow. The first two methods have been widely used until 90's. In the last method, the study was recently emphasized to investigate grid densities in which the result of variable density flow can be made reliable. In this chapter, the variable density model developed is applied to problems such as the application Reilly and Goodman [1987] provided in 80's and the most recent experiment (the saltpool problem) Oswald and Kinzelbach [2004] conducted. Although these two problems are related to the topic of saltwater upconing, there is a significant difference of importance in testing the accuracy and reliability of the numerical results because the recent studies show that variable density flow models including this saltpool problem often require extremely dense grids to assure accuracy in the numerical results [Diersch and Kolditz 2002;Johannsen et al. 2002;Park and Aral 2004]. Thus, in this chapter, two applications for the saltwater upconing were selected as follows: (i) the application that was used with no thorough grid density consideration; and (ii) the saltpool problem obtained from the extremely high grid density. Based on the comparison between the results from the previous work and this study, discussions, results, and recommendations are provided in this chapter.

7.1 Introduction

The validation of variable density flow model is of great importance before the model is applied to field cases. Due to difficulties associated with measuring three-dimensional concentration distributions temporally in a porous medium, the experiments themselves have been limited to one- or two- dimensional experiments. These difficulties led researchers and scientists in variable density flow to the previous benchmark test problems that are either two-dimensional or hypothetical problems. Thus, the comparison between codes in these benchmark test problems is of limited significance. In fact, until recently there was no three-dimensional temporal experimental data that can be used for the verification of the existing models. Being aware of the fact that the models of variable density flow are yet in the process of validation or verification, the researchers have struggled to find application to test their models through well documented complex applications and thus establish the benchmark test problems. Recently, thanks to the new state-of-art technology, a Nuclear Magnetic Resonance Imaging technique (NMRI), Oswald and Kinzelbach [2004] performed a series of laboratory experiments with well-defined experimental parameters for typical variable-density flow problems and provided data for the three-dimensional salt concentration distribution in a porous medium temporally. Two experiments were conducted with 1 and 10 % density differences of two fluids. They also performed numerical simulations with a variable density flow code and compared their results with the laboratory experiments. Although the simulations are conducted on various grid densities rainging from 25,848 to 315,120 nodes, they concluded that the code used did not pass the tests that consist of a breakthrough curve and a two-dimensional concentration distribution of diagonal cross-section obtained from

the experiment. Though the agreement for the experiment of 1% salt mass fraction was satisfactory, the result of the 10% density difference differs significantly from the experimental results. The main reason for this difference, as they indicated in their study, is the artificial widening of the interface by non-consistent local flow velocities.

Later, Johannsen et al. [2002] (note: although this reference appeared in the literature at an earlier date, it uses the experimental data of Oswald and Kinzelbach [2004]) also carried out detailed numerical investigations and obtained reference solutions within a reasonable accuracy. They indicated that for the high concentration case a very high spatial grid resolution using up to 16 million grid points is necessary to solve this problem accurately. This is very unfortunate because the computation for even this experimental benchmark test problem is very costly and the question for selecting proper grid densities for real problems is still not answered.

In this chapter, two applications for the saltwater upconing problems are selected to study saltwater upconing beneath pumping wells. Starting from the result of Reilly and Goodman [1987] to the saltpool experiment by Osward and Kinzelbach [2004], the results of TechFlow are compared with theses previous work, and the discussions associated with grid density especially on the saltwater upconing application are provided in this chapter.

7.2 Reilly and Goodman [1987] – Saltwater Upconing Problem

Apart from the methodology used, saltwater upconing problems have been known widely. Starting from the analytical solution based on the sharp interface assumption to variable density flow and transport, the saltwater upconing problems are tackled in three

methods introduced previously. Although the relevant assumptions depend on the method used and each method produces output, it is of great importance to understand how these results are different from each other. It was Reilly and Goodman [1987] that first did comparisons of the two methods and indicated: (i) for low to moderate pumpages the 50 % isochlor and sharp interface correlate well; (ii) the well can discharge significant concentrations of saltwater, even though a stable cone (according to the sharp-interface method) exists below the well screen; (iii) there is an almost linear relationship between the well discharge rate and the concentration of the discharge at low pumping rates that maintain a stable cone; and, (iv) upconing is sensitive to transverse dispersivity, whereas it is insensitive to longitudinal dispersivity. In addition, they also suggested that a simulation of upconing at Test Site No. 4, Truso, Cape Cod, Massachusetts, indicates that the appropriate field value of transverse dispersivity is very small, and this supports the validity of the sharp-interface assumption for analyzing the behavior of systems with thin saltwater-freshwater transition zones.

Figure 7.1 describes a schematic of saltwater upconing beneath a pumping well. The figure shows the change in location of steady-state saltwater cones using a sharp-interface perspective. The figure also illustrates that at some distance below the well, a critical rise of the cone exists which is the maximum equilibrium position the cone can attain. The reason that this maximum exists is that for discharge rates greater than the critical pumping rate the vertical freshwater gradient is too steep in this area just below the well to allow the saltwater to remain static. In reality, a transition zone between the two fluids exists instead of idealized sharp interface. Thus, low concentrations of

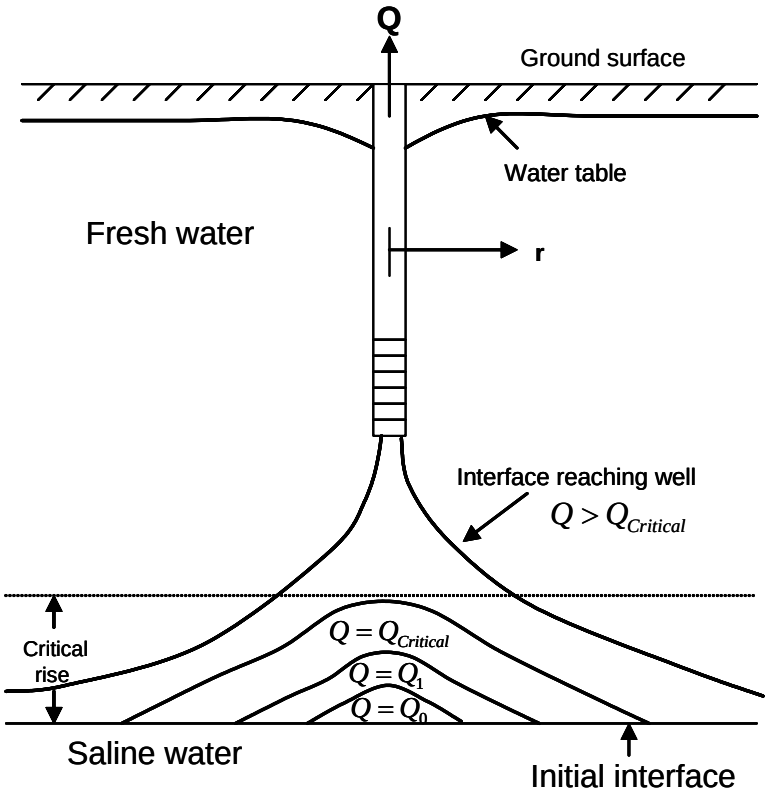

Figure 7.1 A schematic of saltwater upconing beneath a pumping well

saltwater are expected to move with the fresh water along the fringes of the transition zone and be discharged by the well, even at pumping rates less than the critical rate.

Reilly and Goodman [1987] solved the saltwater upconing beneath a pumping well in radial coordinates using their variable density flow model as well as the sharp interface model. Because the physics of the system are different, the selection of appropriate boundary conditions is not straightforward in performing comparisons between the two methods. While Reilly and Goodman [1987] choose a initial transition zone in their physical diagram, the study in this chapter makes a use of the simplest initial condition only for the purpose of the comparison of the results obtained by them. This is in part because in the next problem, the saltpool problem, the most recent well-defined problem with boundary conditions is covered. Thus, a comparison with the results of the saltpool problem is emphasized in order to verify TechFlow with respect to the applications of saltwater upconing. Figure 7.2 describes diagram of physical systems simulated in variable-density solute-transport system approach. The problem follows the same physical parameters of Comparison 1 that Reilly and Goodman [1987] conducted. The same problem in fact reappears in the work of Voss and Souza [1987] with metric unit system while Reilly and Goodman [1987] used imperial unit system. Figure 7.2 follows the former unit system. A 20-m long partially penetrating well is centered 15 m below the aquifer (Figure 7.2). Recharge is distributed along the top of the section. Significant system parameters are given in Table 7.1.

Since the problem is formulated in a radial coordinate system, a conversion of the application in a radial coordinate system into a Cartesian coordinate system is required because TechFlow is developed in the Cartesian coordinate system. In this conversion,

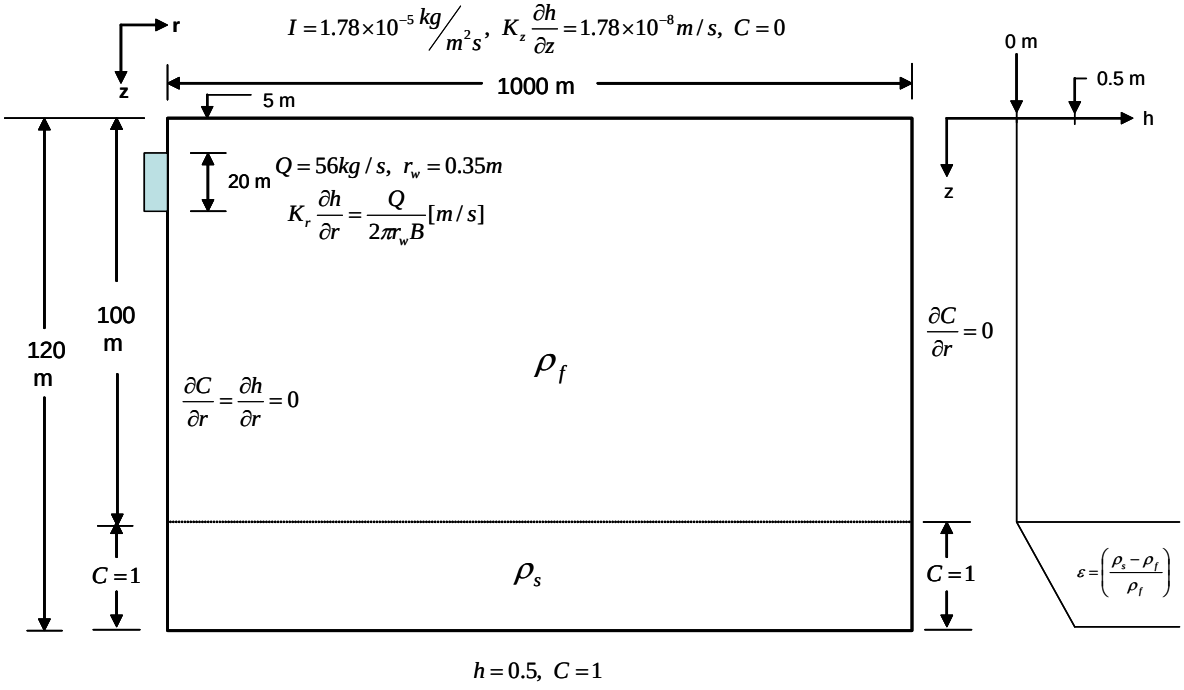

Figure 7.2 Diagram of physical systems simulated in variable-density solute-transport system approach.

Table 7.1 Physical parameters for Comparison 1 from Reilly and Goodman [1987]

Symbol	Quantity	Value	Unit
k_h	Horizontal intrinsic permeability	2.56×10^{-11}	m^2
k_v	Vertical intrinsic permeability	1.00×10^{-11}	m^2
ρ_f	Fresh water density	1000	kgm^{-3}
ρ_s	Saltwater density	1024.99	kgm^{-3}
g	Gravitational coefficient	9.81	ms^{-2}
μ	Dynamic viscosity	1000×10^{-6}	$kgm^{-1}s^{-1}$
ϕ	Porosity	0.2	-
α_L	Longitudinal dispersivity	1.0	m
α_T	Transverse dispersivity	0.5	m
Q	Pumping rate	56	kgs^{-1}
I	Recharge rate	1.78×10^{-5}	$kgs^{-1}m^{-2}$
r_w	Well radius	0.35	m

the application becomes three-dimensional, so the conversion in turn leads to the increased number of elements in discretization. Thus, compatible grids are accordingly created by increasing the size of each element as the elements are located farther away from the center in radial coordinate system. Originally, Reilly and Goodman [1987] performed the simulation on two different grid densities. Compatible grids of the densities in the Cartesian coordinate system with those of the original densities in the radial coordinate system are created in an effort to solve the problem of Comparison 1.

Table 7.2 provides the grid parameters of two grids while Figure 7.3 illustrates the two grids created in the Cartesian coordinate system. As shown in Figure 7.3, the grids generated do not have curvy arch in the edge of the element at the outer boundary. This elimination may cause possible errors that may occur at the outer boundary. However, these errors should be minimal.

As for discretization errors, the results from the two different grids are nearly the same in each case. The comparison with the result from Reilly and Goodman [1987] and the solution obtained from the sharp interface model are provided in Figure 7.4. The result of TechFlow is in good agreement with a little oscillation towards the outer boundary where large elements are used. As can be seen, this oscillation is growing as it reaches to the outer boundary indicating the grid density in the outer boundary is not dense enough to eliminate the oscillation. However, concentration isochlors beneath the penetrated well are in good agreement not showing any oscillation because of denser grid density beneath the well. Note that in Comparison 1 the discharge simulated is the maximum permissible discharge for the sharp-interface method such that the critical rise is achieved at this discharge. In this case, the sharp interface is near the 50 % saltwater

Table 7.2 Grid parameters for two compatible grids with the ones from Reilly and Goodman [1987]

Grid 1	
X: 1000 m	Number of element in X direction: 29
Y: 4 m	Number of element in Y direction: 1
Z: 120 m	Number of element in Z direction: 30
Grid 2	
X: 1000 m	Number of element in X direction: 59
Y: 2 m	Number of element in Y direction: 1
Z: 120 m	Number of element in Z direction: 60

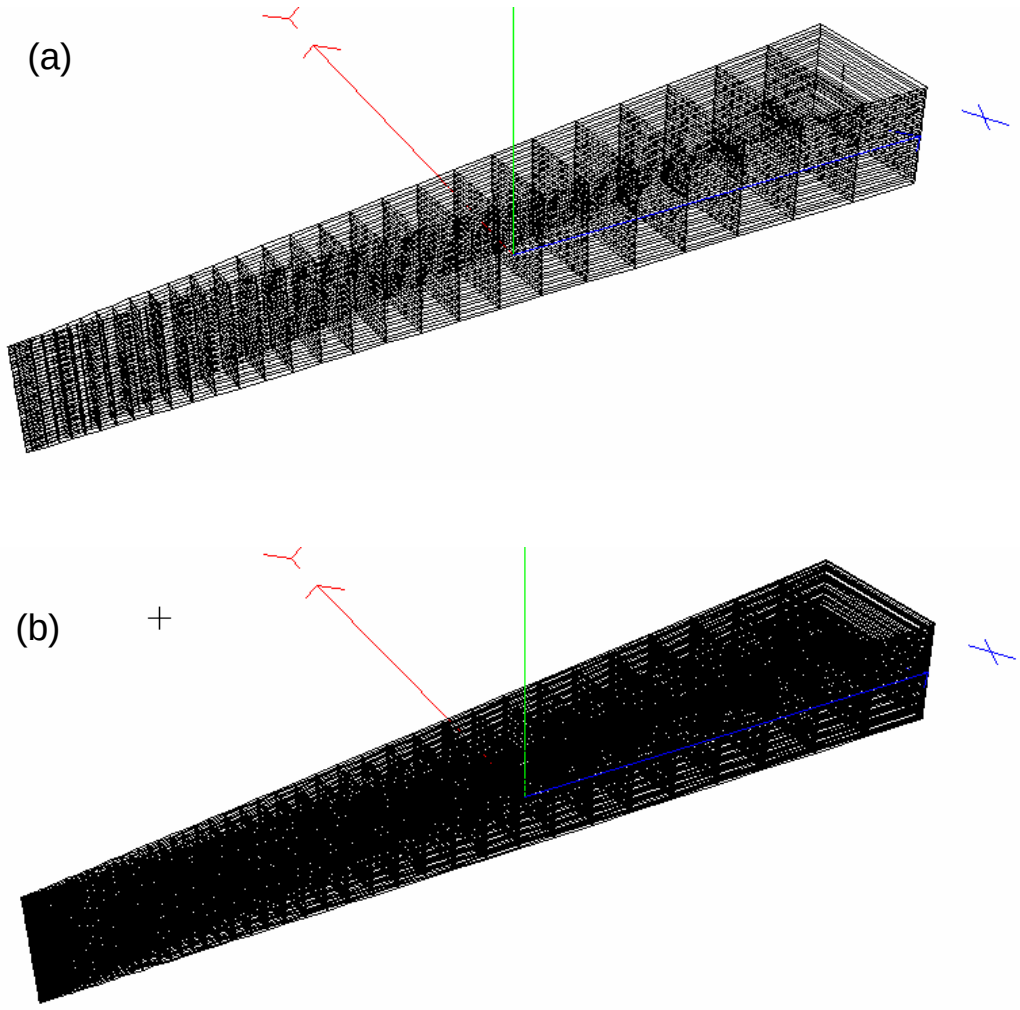

Figure 7.3 Two different grids of densities in Cartesian coordinate system used for TechFlow

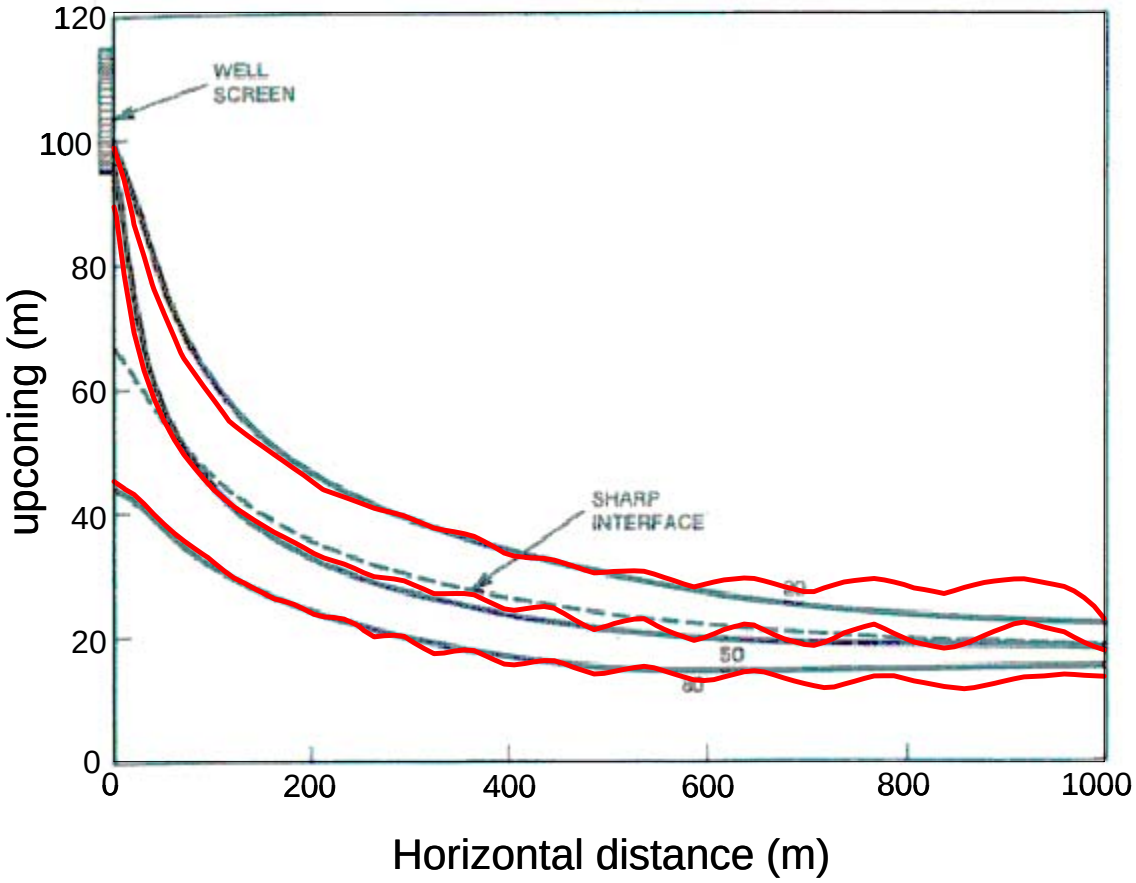

Figure 7.4 Comparison of the results by TechFlow (red solid line) with the results from Reilly and Goodman [1987] (black solid line) and the results from the sharp interface model (black dotted line).

isochlor, except directly beneath the pumping well. The zone of dispersion is not symmetric about the 50 % isochlor and the well in variable-density solute-transport model in fact discharges a significant mount of salt. Thus, this indicates that critical pumping rate estimated from the sharp interface model should not be allowed in the case as Comparison 1 to prevent saltwater from degrading water qualities.

7.3 The Saltpool Problem by Oswald and Kinzelbach [2004]

Oswald and Kinzelbach [2004] provided time-dependent experimental data for a three-dimensional dispersive variable-density problem, especially suited for comparison with results from numerical modeling. This experiment is carried out in a 20 cm cubic box of acrylic plastic filled with glassy beads of spherical shape (average diameter 1.2 mm, varying between 1.0 and 1.3 mm). Once the box was fully filled with this homogeneous and isotropic saturated porous medium, an elastic plastic cover was fitted on its top. Inflow and outflow were then possible only via small holes in the four corners of the plastic cover and a central hole in the bottom plate. The box was sealed tightly with screws along the four edges. Figure 1 illustrates a schematic of the experiment. The experiment carried out at two different density differences. Case 1 is 1 % and Case 2 is 10 %. In the first phase, the box, initially filled with freshwater, is recharged by saltwater at the specified density difference through the whole in the bottom while freshwater discharges through the four holes in the top cover. In the second phase, all the holes are closed until stable horizontal layers of two fluids are established with a very small mixing zone. In the third phase, the box is recharged with freshwater through the single hole while discharge occurs through the diagonally opposite hole in the cover as indicated in Figure 7.5. They defined two reference solutions for comparison with numerical results.

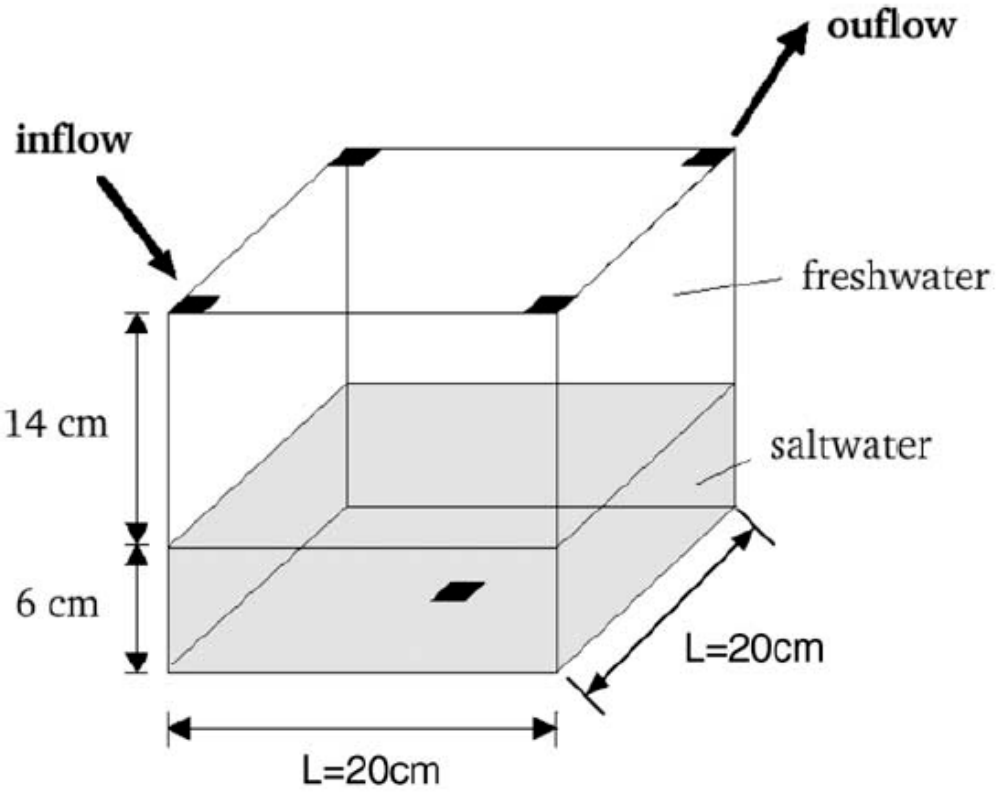

Figure 7.5 A schematic of the experiment [Oswald and Kinzelbach 2004]

One is the breakthrough curve measured from the outflow and the other is the concentration distribution in the diagonal vertical cross-section.

Later Johannsen et al. [2002] provided initial conditions they used in their simulation, which allows direct simulations from the third phase of the experiment. In this initial condition, they chose the initial conditions for the salt-mass fraction to be the continuous, piecewise linear one-dimensional profile. The initial conditions are provided in Equation 7.1.

$$C(x,y,z,0)=\begin{cases} 1 & if\ \ z \le z_m - \dfrac{\omega}{2} \\ \dfrac{1}{2} - \dfrac{(z - z_m)}{\omega} & if\ \ z_m - \dfrac{\omega}{2} < z < z_m + \dfrac{\omega}{2} \\ 0 & if\ \ z_m + \dfrac{\omega}{2} \le z \end{cases} \tag{7.1}$$

where $z_m = \dfrac{V_s}{\phi L^2}$ is the vertical position of the initial mixing zone, V_s is the volume of saltwater recharged during phase 1, ϕ is the porosity, L is the side length of the cube, ω is the width of the transition zone (i.e., the value $\omega = 8\,mm$ in both cases. This value is derived from the experimental results).

Neglecting the very low fluid compressibility, the initial hydraulic conductivity is assumed to be zero. The inflow and outflow are modeled by inserting point sinks and sources at the corresponding corners of the cube. No flow boundary condition for flow equations is assigned to all the boundaries. Boundary conditions for two nodes, not assigned source or sink at the corners of the top plate, are Type I ($h = 1$) such that the matrix formulated from the flow equation is not singular. As for the transport model, no flux boundary condition is assigned to all the boundaries. The concentration of the node,

assigned as a inflow source, is assigned to be zero (i.e., $C = 0$). Table 7.3 provides the significant parameters of the experiment.

Figure 7.6 presents two numerical results of the breakthrough curves, obtained by Oswald and Kinzelbach [2004] and by Johannsen et al. [2002] in the reference solutions. The result obtained by Oswald and Kinzelbach [2004] is from a grid that consists of 50,978 nodes while the one obtained by Johannsen et al. [2002] is from the grid that consists of 16,974,593 nodes. Although the breakthrough curve for Case 1 obtained by Oswald and Kinzelbach [2004] is good agreement with the measured one, the one for Case 2 differs significantly from the measured one. The model for Case 2 is clearly prone to overestimate the concentration in the breakthrough curve. They mentioned that a grid refinement could improve the result only to some extent. Nonetheless, the numerical result did not pass this breakthrough curve test. In contrast, the breakthrough curves for both cases, obtained by Johannsen et al. [2002] later, are in good agreement with the measured data. Note that although huge number of nodes were used (i.e., nearly 17 million nodes) in discretization, their results still overestimated the experimental results.

Unlike these two overestimated results, Kolditz et al. [1998] provided their results that underestimate the concentration compared to the measured data. Their results are provided in Figure 7.7. They used two different meshes, mesh A and mesh B. Mesh A, in which hexahedral (i.e., block element) elements are used, consists of 274,625 nodes while mesh B, in which pentahedral elements are used for only the symmetric half of the box, consists of 140,010. Thus, the levels of grid densities are compatible each other but with different elements and sizes of the problem domain. Both results for Cases 1 and 2 are in good agreement with the measured data. The result from mesh A shows a slightly

Table 7.3 Parameters of the saltpool experiment

Symbol	Quantity	Case 1	Case 2	Units
γ	Density difference ratio	1 %	10 %	-
V_s	Volume of the saltwater recharge	8.64	8.9964	$10^{-4} m^3$
t_3	Time period of Phase 3	8412	9594	s
L	Side length of the cube	0.2	0.2	m
Q_3	Outflow rate	1.89	1.83	$10^{-6} m^3 s^{-1}$
ϕ	Porosity	0.372	0.372	-
D_m	Molecular diffusion coefficient	10	10	$10^{-10} m^2 s^{-1}$
k	Permeability	10	10	$10^{-10} m^2$
α_L	Longitudinal dispersivity	1.2	1.2	$10^{-3} m$
α_T	Transverse dispersivity	0.12	0.12	$10^{-3} m$
ρ_f	Fresh water density	998.23	998.23	kgm^{-3}
ρ_s	Saline water density	1005.82	1071.60	kgm^{-3}
μ_f	Freshwater dynamic viscosity	1.002	1.002	$10^{-3} kgm^{-1} s^{-1}$

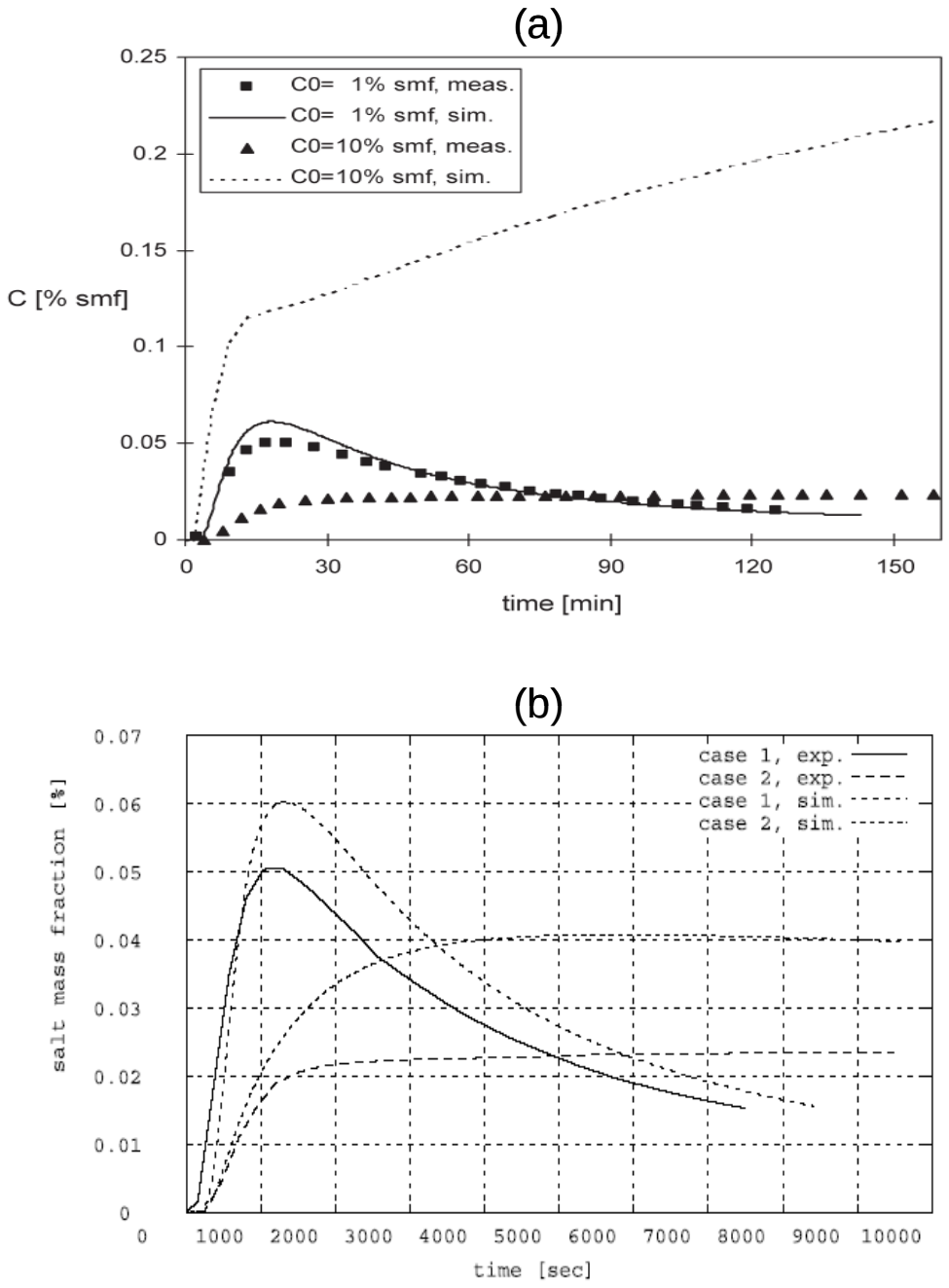

Figure 7.6 Caparison of measured and simulated breakthrough curves for Cases 1 and 2. (a) Oswald and Kinzelbach [2004], (b) Johannsen et al. [2002]

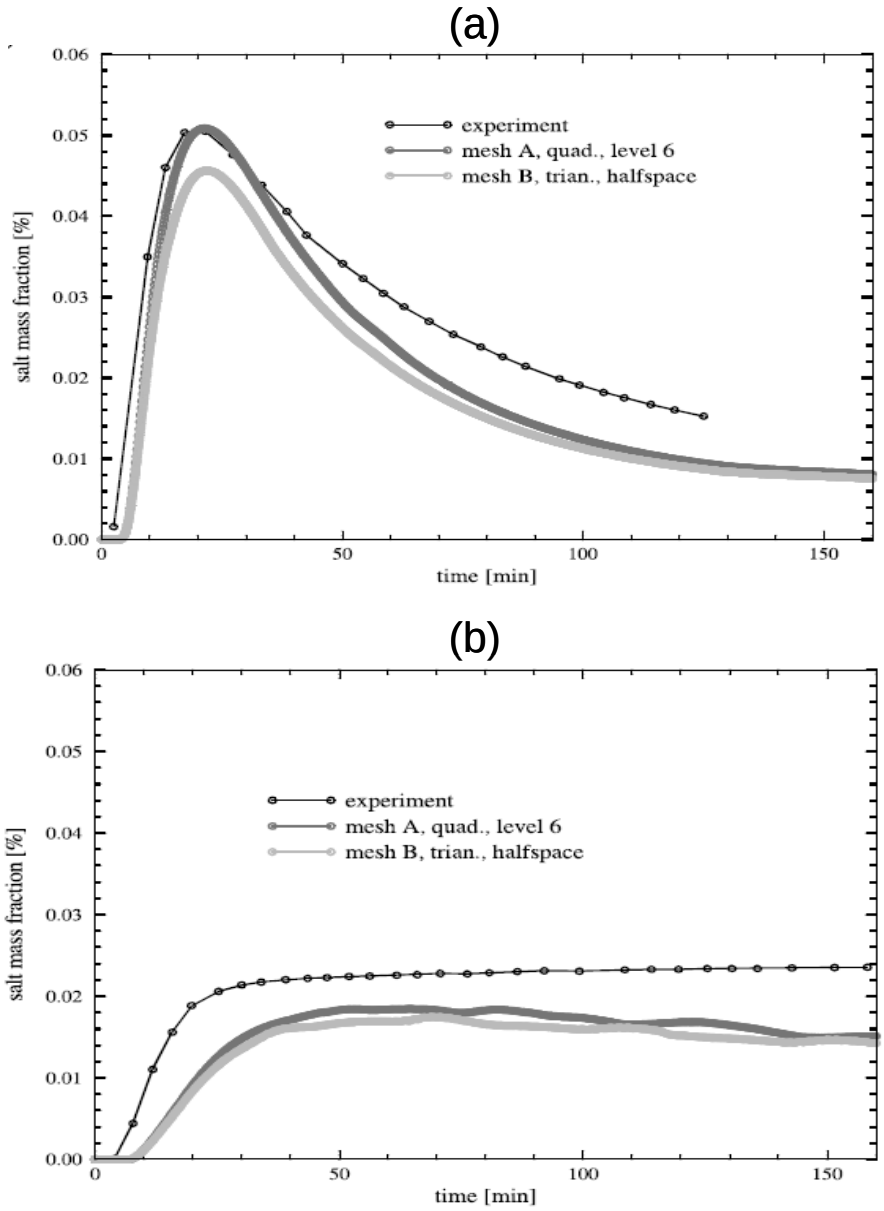

Figure 7.7 Caparison of measured and simulated breakthrough curves for (a) Case 1 and (b) Case 2 from Kolditz et al. [1998]

better agreement than that from mesh B. Obviously, these results are in better agreement than those from Oswald and Kinzelbach [2004] and Johannsen et al. [2002]. The grid density used is level 6. The grid level in this three-dimensional application is defined as shown in Table 7.4.

Discretization for TechFlow was not exactly followed by the level of grid in Table 7.4. The number of nodes used in the grid is 35,937 and the total number of hexahedra (i.e., block elements) is 32,768 composed to be a form of $16 \times 16 \times 128$ rather than that of $32 \times 32 \times 32$. Thus, the compatible level is five while Johannsen et al. [2002] used level eight and Kolditz et al. used six. As can be seen in Table 7.4, the number of nodes significantly increases as the level increases. Figure 7.8 provides the breakthrough curves obtained from TechFlow. In the simulation, two different velocity estimations are used. As expected from Chapter 5, the global continuous velocity method leads to better solution in each case than the discontinuous velocity method. Although the grid density is considerably lower than those used in the previous works, the results for both cases obtained with the global continuous velocity method are in better agreement with the measured ones than any of the previous results provided in this chapter.

As for the other reference solution that is concentration distribution in diagonal vertical cross-section, this reference solution is to test the model both spatially and temporally in three dimensions. Since the concentration distribution is gradual in the mixing zone, isolines of 10 % and 50 % are selected for the comparison. Figure 7.9 presents the results for both cases from Oswald and Kinzelbach [2004] and TechFlow. In this reference solution, both Oswald and Kinzelbach [2004] and TechFlow produce the results that are in good agreement with the measured concentration distribution for Case

Table 7.4 The hierarchy of grids

Level i	**Length (** *mm*)	**# of hexahedra**	**# of grid points**
0	200	1	8
1	100	8	27
2	50	64	125
3	25	512	729
4	12.5	4,096	4,913
5	6.25	32,768	35,937
6	3.125	262,144	274,625
7	1.5625	2,097,152	2,146,689
8	0.78125	16,777,216	16,974,593

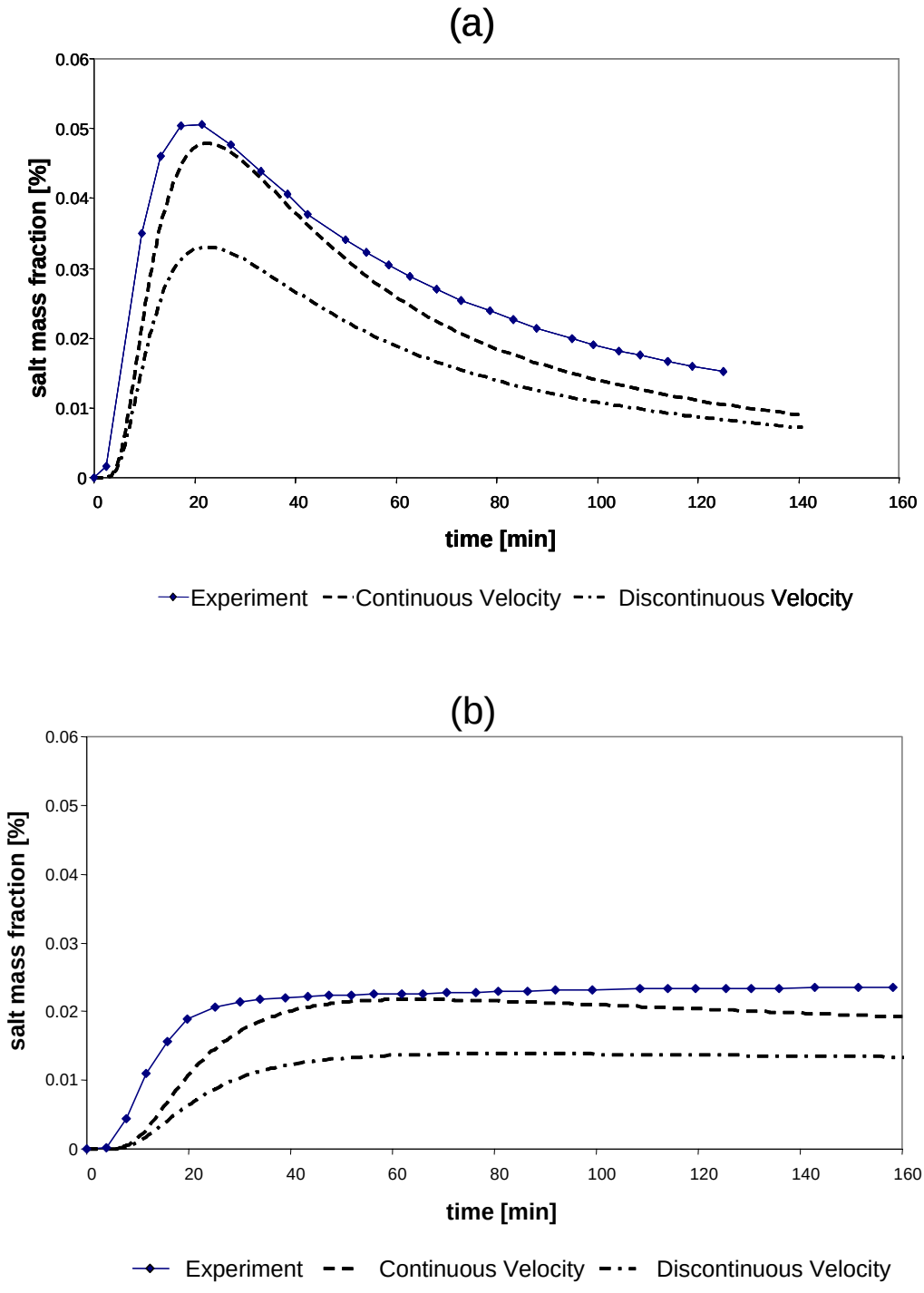

Figure 7.8 Caparison of measured and simulated breakthrough curves for (a) Case 1 and (b) Case 2 from TechFlow

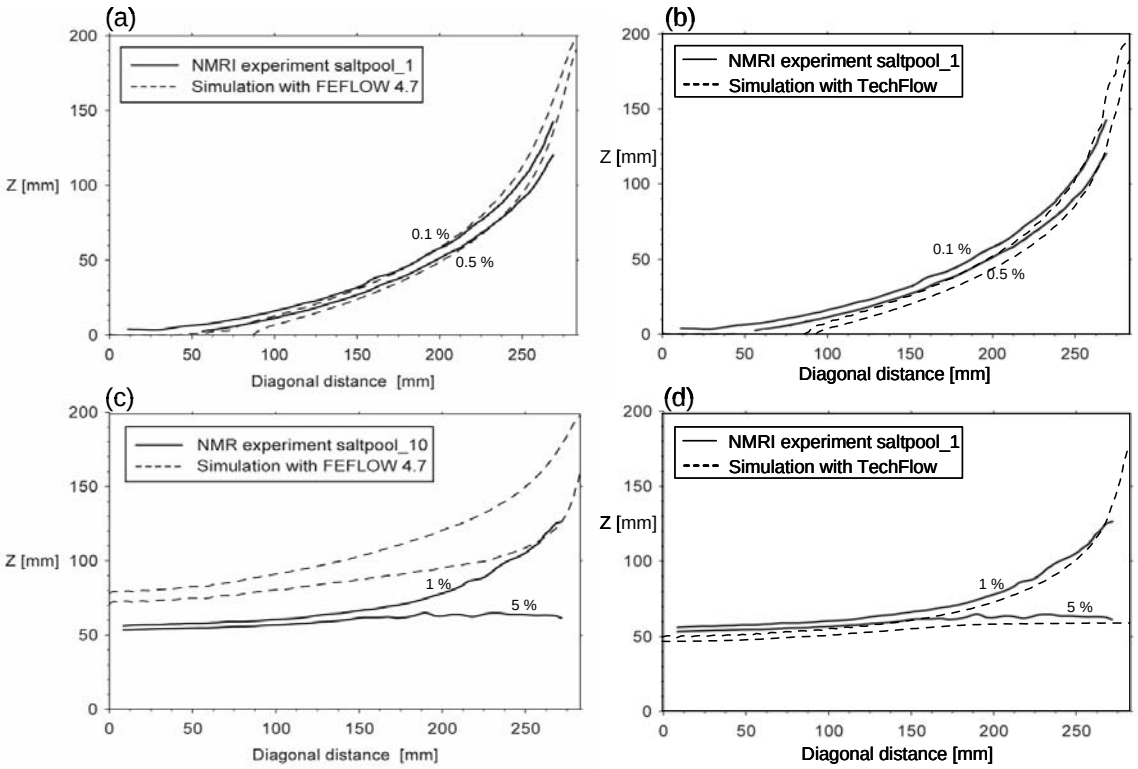

Figure 7.9 Caparison of measured and simulated concentration distributions in diagonal vertical cross-section for Cases 1 and 2: (a) Case 1 from Oswald and Kinzelbach [2004], (b) Case 1 from TechFlow, (c) Case 2 from Oswald and Kinzelbach [2004], and (d) Case 2 from TechFlow

1. However, the result for Case 2 from Oswald and Kinzelbach [2004] overestimates concentration considerably while that from TechFlow is still in good agreement with the measured concentration distribution.

Later, Johannsen et al. [2002], who produced the breakthrough curve of (b) in Figure 7.6, adjusted parameters within measurement errors that can be introduced in the experiment. Replacing K, ϕ, and α_T by

$$K^{(2)} = 1.194K, \qquad \phi^{(2)} = 0.962\phi, \qquad \alpha_T^{(2)} = 0.360\alpha_T \qquad (7.2),$$

their model produces both reference solutions in Figure 7.10. This time, both reference solutions are in very good agreement with the corresponding measured data. In this parameter adjustment from Equation 7.2, the hydraulic conductivity increases while the porosity and the transversal dispersivity decrease. This parameter adjustment is based on the result from (b) in Figure 7.6, which produces overestimation of concentration. Thus, this adjustment can hardly be applied to the results that underestimate the concentration.

7.4 Discussions

This chapter introduced two applications in saltwater upconing problems. The first application is solved on the significantly sparse grid compared to those used in the second application. Although the first application lacks validity of the numerical result due to the fact that the application was solved before the benchmark test problems were established, the saltwater upconing especially underneath the pumping well appears to be well-described in the simulation. On the other hand, the second application, which is the saltpool problem, is known to require a huge number of nodes in the discretization. Johannsen et al. [2002] indicated that for Case 2, which is the 10 % density difference

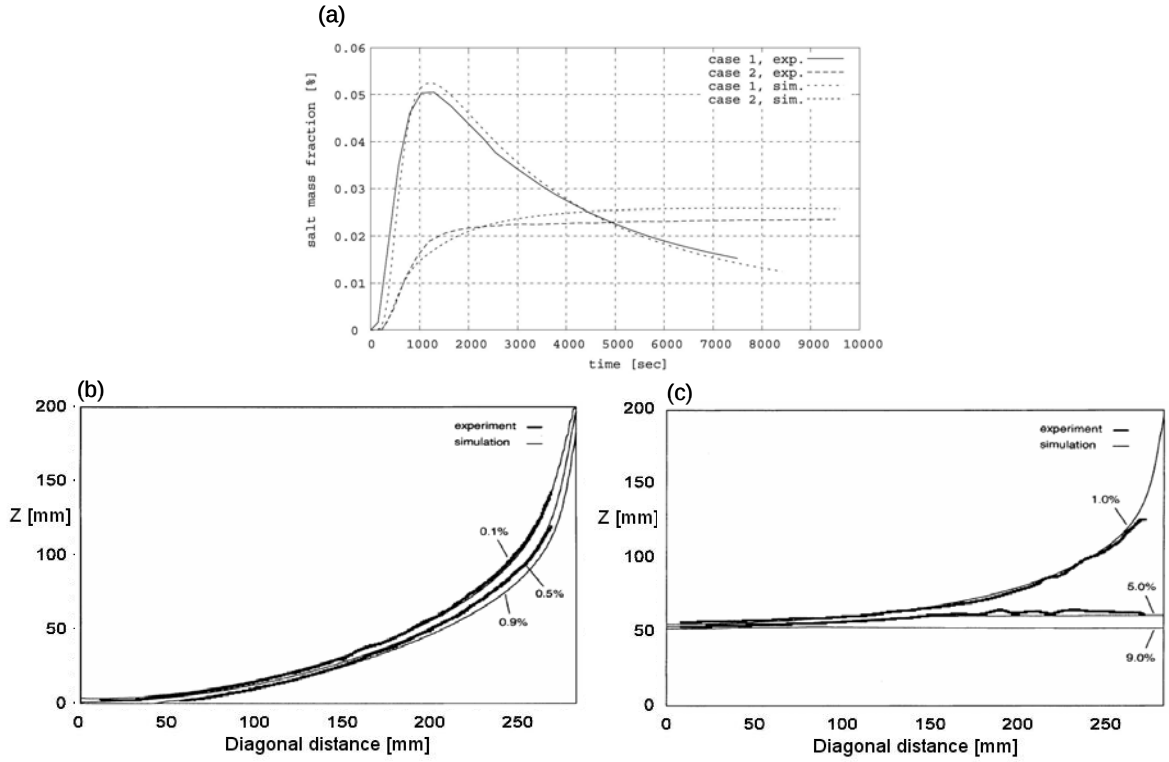

Figure 7.10 Reference solutions obtained from Johannsen et al. [2002] (a) the breakthrough curve for both cases, concentration distribution in diagonal cross-section for (b) Case 1 and (c) Case 2

between two fluids, a very high spatial grid resolution, consisted of up to 16 million grid points, is necessary. Diersch and Kolditz [2002] later, based on this recommendation, used about a little more than quarter million grid points for solving the saltpool problem. Considering the small box of the problem domain, this requirement is unfortunate because the use of the high performance computing (HPC) is necessary at these grid resolutions and the problem is still one of the benchmark test problems. In fact, Johannsen et al. [2002] solved Case 2 on 128 processors and reported the simulation of 240 time-steps took 22 days. This indicates why variable density flow and transport in porous media is still the challenging area and requires considerable work for improving numerical models associated with the grid density and further applying them to the field scale problems.

In the numerical solution of the Elder problem in Chapter 5, as demonstrated, using TechFlow it was possible to obtain reliable results at one lower level of density grid. The key in the study of the Elder problem is that velocity calculations play an important role in the reduction of the grid density. Motivated by this finding, the saltpool problem is solved on a considerably less dense grid (i.e., Level 5) by TechFlow with the global continuous velocity estimation. Two reference solutions obtained from TechFlow are provided in the previous section. Both results without the parameter adjustment are in good agreement with the measured data. This may indicate that the grid density recommended by Johannsen et al. [2002] can be reduced significantly with the global continuous velocity estimation.

To investigate the grid density requirement in the saltpool problem, attempts to solve the saltpool problem using TechFlow with the global continuous velocity

estimation were done at much lower grid densities such as Level 4 in Table 7.4. Although transient solutions appear to be fine in the beginning of the simulation at lower levels, the numerical solution could not pass over the certain time period because of an abrupt local negative concentration indicting the certain grid density must be met for the problem. None of the attempts at grid levels lower than five was succeeded. However, the level 5 grid is still one level lower grid than the minimum grid level (Level 6) shown in the grid convergence study by Johannsen et al. [2002]. As shown in Table 7.4, one grid level produces about one order-of-magnitude difference in the number of grid points. Computationally, this makes a big difference. For example, the grid level 5 problem can be solved on single decent computer within a reasonable time. In contrast, any grid level higher than five requires the HPC, thus the code itself to be rewritten for utilizing the HPC.

In addition to the velocity estimation associated with grid densities for solving the saltpool problem, the results obtained from TechFlow for the two reference solutions with no adjustment of the parameters are more accurate than all other results provided in this chapter. This may indicates that TechFlow with the global continuous velocity estimation not only requires less grid densities but also produces more accurate results for the problem even at the lower grid levels. In other words, the grid density can be significantly reduced with the global continuous velocity estimation in the saltpool problem as well as the Elder problem shown in Chapter 5.

7.5 Conclusions

In this chapter, two applications of the saltwater upconing problem are solved. The results obtained by TechFlow are in good agreement with those results obtained from the other researchers in the first application and the experimental data in the saltpool problem. Especially two reference solutions from TechFlow in the saltpool problem are significantly important because the solutions are in good agreement with the measured data than those from the others and obtained from much less dense grid than those used by the others. This indicates that the grid density can be reduced significantly with the global continuous velocity estimation. The difference can be either about one order-of-magnitude less number of grid points or one level lower grid density defined in Table 7.4. Although the computation for the global continuous velocity estimation is a bit heavier than those for other velocity estimations, the reduction of the grid density considerably pays this additional computation off.

In addition to the grid density reduction with the velocity estimation, the parameter adjustment, recommended by Johannsen et al. [2002] for their overestimated concentration, can not be applicable to this study because the results from this study and from Diersch and Kolditz [2002] tend to underestimate concentrations. Having TechFlow tested through the benchmark test problems and this three-dimensional experiment, TechFlow will be further used to solve three-dimensional problems of saltwater upconing due to pumping under tidal effects at the field-scale in Chapter 8.

CHAPTER 8

SALTWATER UPCONING DUE TO PUMPING UNDER TIDAL EFFECTS

In continuation with the saltwater upconing beneath pumping wells topic, which was discussed in Chapter 7, in this chapter saltwater upconing due to pumping under tidal effects is covered. As provided in Chapter 6, saltwater intrusion hydrodynamics in a beach under the influence of tidal effects consists of complex physical processes that include mixing in porous medium, water flow in both unsaturated and saturated zones, and the effects of tidal wave on the overall saltwater intrusion problem. This problem also includes all the complexities that are discussed in the salt dome problem as well as the Henry problem that was discussed in this thesis earlier. In those cases, the application discussed was for a two-dimensional case in Chapter 6 and the discussion was limited to the physical processes without a pumping well. On the other hand, the two or three dimensional applications discussed in Chapter 7 do not consider tidal effects although the pumping wells were introduced. Thus, this chapter presents the application that describes saltwater intrusion and/or upconing due to pumping under tidal effects. In addition to the added complexity in physical processes of the saltwater intrusion, the results of the application are extended by providing generalized interpretation of results using dimensional analysis.

8.1 Introduction

Saltwater upconing due to pumping requires three-dimensional approach in Cartesian coordinates. Two dimensional vertically averaged solutions for pumping wells

have been undertaken in groundwater flow for constant density flows. In this approach, the problem domain is normally horizontal and pumping is vertically averaged. This averaged pumping is based on the analytical solution which is introduced in Chapter 3. Because of the vertically averaged conditions, this solution loses the dimensional freedom in the vertical direction and saltwater upconing can not be described in this two-dimensional application. On the other hand, two-dimensional application in radial coordinates can describe the saltwater upconing but this introduces other restriction such as the problem should be axis-symmetric. This restriction makes the analysis of nonhomogeneous medium not possible. Therefore, saltwater upconing problem can only be analyzed properly when the approach is truly three-dimensional.

In addition to the three-dimensional requirement for simulating saltwater upconing, the saltwater upconing applications in Chapter 7 use ideal initial or boundary conditions such as horizontal layers of fresh water and saltwater. Although the findings of saltwater upconing beneath pumping wells in Chapter 7 are significant, the ideal conditions make these applications of limited usefulness for practical purpose. In most cases in coastal aquifers, possible initial conditions themselves are steady-state conditions of the saltwater intrusion uniquely determined by aquifer properties, geometry of the problem domain, fresh water recharge such as precipitation or fresh water influx from inland, and tidal conditions. This initial status thus needs to be solved from these aquifer conditions. If pumping wells are introduced, then this saltwater intrusion as an initial condition should be accounted for.

As studied in Chapter 6, the saltwater intrusion is much more complicated when tidal effects are introduced. Fortunately, the saltwater intrusion hydrodynamics under

tidal effects, as described in Chapter 6, reaches the pseudo-steady state in which concentration profile under the intertidal zone is vertically periodic. The complication of the tidal effects due to pumping originates from the locations of well screens in the vertical direction. Thus, in this case the Dupuit assumption hardly holds in the system. For example, if the well screen reaches to the bottom of the aquifer, the saltwater upconing would not occur while lateral saltwater encroachment is emphasized. However, the saltwater upconing after lateral saltwater encroachment due to pumping can occur with partially penetrating wells although the well screen is still in the saturated zone. These scenarios of the saltwater upconing under tidal effects have never been solved.

Saltwater intrusion in large-scale aquifers are solved by researchers [Huyakorn et al., 1987; Ma et al., 1997; Essink, 2001; Voss and Koch, 2001]. If problems become large scale, unsaturated zones are incorporated into boundary conditions so that the problem domain only covers a saturated zone. This is a reasonable approximation specially when the aquifer is large and most of the flow is assumed to be horizontal. The inclusion of a unsaturated zone into this large scale problem makes it almost impossible to handle the boundary between the unsaturated zone and the saturated zone based on the van Genuchten model [van Genuchten, 1980]. Because physical processes governed by the van Genuchten model are developed at micro scale, this micro-scale can hardly be distinctively represented at a large-scale approximation due to the increased size of element or block that is used in idealization of the solution domain.

Similar to saltwater intrusion hydrodynamics in a beach that is discussed in Chapter 6, the application made in this chapter has a mild slope intended to represent distinctive tidal effects along the intertidal zone. Thus, the problem domain is a variably saturated

porous medium. The physical parameters associated with the van Genuchten model are mostly same but the problem domain is extended in y-direction to represent a three-dimensional domain. To provide generalized results, a dimensional analysis is conducted primarily based on the work from Boufadel [Boufadel et al., 1997,1998,1999b; Boufadel, 2000]. The dimensionless number defined as the ratio of capillary force to gravity force is used in the analysis. Characteristic time obtained from the defined characteristic length divided by hydraulic conductivity is used to estimate the period of tide in the simulation. The advantage and disadvantage of this dimensional analysis is provided in a separate section in this chapter.

To investigate the saltwater intrusion or upconing hydrodynamics due to pumping under tidal effects, a three-dimensional application is developed for three scenarios of saltwater intrusion for demonstrative purposes. They are saltwater intrusion due to pumping with no tidal effects, saltwater intrusion due to pumping under tidal effects, and saltwater upconing due to pumping under tidal effects for a partially penetrating well.

8.2 The Application of Saltwater Intrusion/Upconing Due to Pumping under Tidal Effects

A three dimensional problem is formulated to investigate the saltwater intrusion or upconing hydrodynamics due to pumping under tidal effects. The problem is solved with pumping locations of well screens varied to describe saltwater intrusion or upconing either under no tidal effects or under tidal effects.

8.2.1 Preparation of the Application

The problem consists of 500 $cm \times 250\ cm \times 115\ cm$ of a porous medium. A slope of 10% from a height of 115 to 67.5 cm is created along z axis. According to the tidal conditions, hydraulic head boundary conditions on seaside vary. These variable boundary conditions are set to have the intertidal zone on the beach surface to range from $325 cm$ to $450 cm$. The periodic function of pressure head, similar to that used in Chapter 6, represents the tidal effects. In this application the amplitude is different. The range of the corresponding periodic hydraulic head based on the periodic pressure head is from 72.5 cm to 82.5 cm. This pressure head is used to form variable hydraulic head Type I boundary condition at the seaside. The tidal period is set to be 1,320 seconds (22 minutes). This short period is due to the small problem domain that is set specific to the experiment by Boufadel [Boufadel et al., 1998]. The assertion of this tidal period associated with large scale applications will be discussed later in this chapter through the use of dimensional analysis. A pumping well is assigned at the center of the horizontal plane (x,y-plane). The location of the well screen varies depending on the problem focus. That is either saltwater encroachment or saltwater upconing. Figure 8.1 provides the problem description for three-dimensional saltwater intrusion in a phreatic aquifer subject to well pumping under tidal effects.

Material properties of the porous medium are set to be the same as in Chapter 6 except the fact that the problem is extended to y-direction to have the width of 250 cm. Table 8.1 presents important material properties. The discussion on the choice of these material properties associated with dimensional analysis is also provided later in this chapter.

The problem domain for saltwater intrusion or upconing due to pumping under tidal effects was discretized to have a reasonable number of nodes. From the experience learned from Chapter 6, a grid that consists of 19,560 brick elements that are a combination of regular and irregular elements is created as shown in Figure 8.2. The grid consists of two different grid densities. Denser grid density is assigned on the unsaturated zone while less dense grid density is placed on the saturated zone. Spacing between nodes along x and y axis is 12.5 *cm* . Vertical spacing is 2.5 *cm* in the unsaturated zone and 5.0 *cm* in the saturated zone. The time step for the numerical simulation was set to

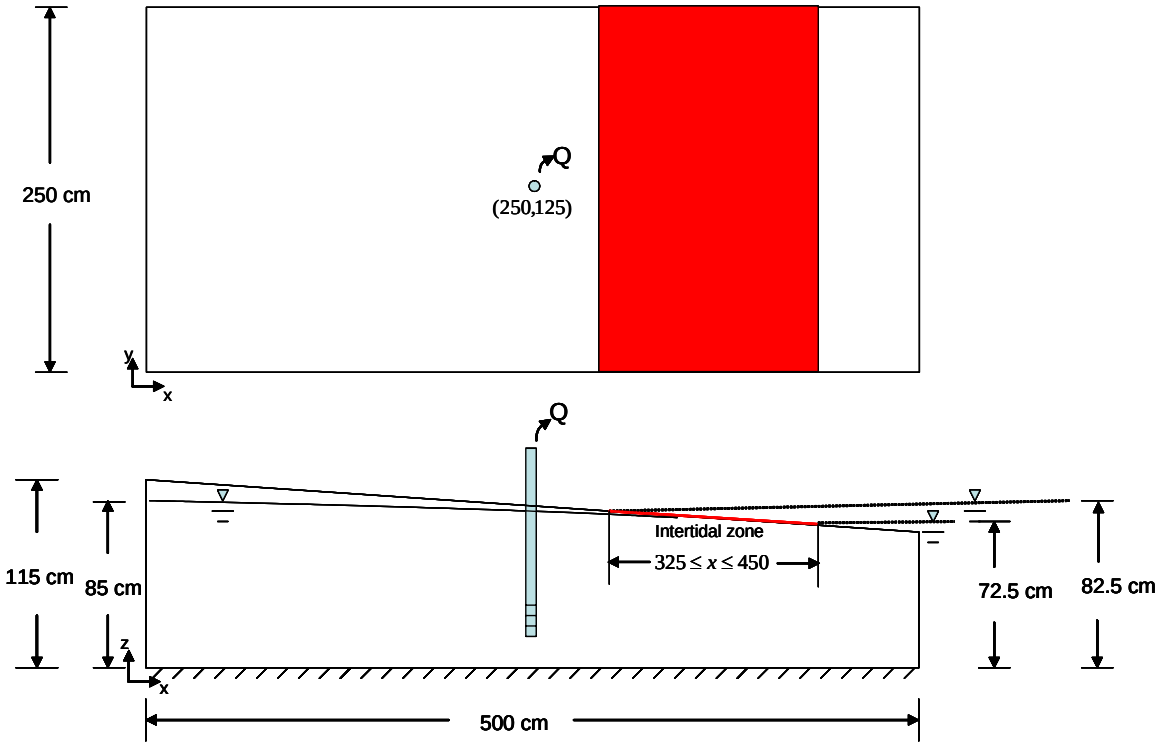

Figure 8.1 Problem description for three-dimensional saltwater intrusion in a phreatic aquifer subject to well pumping under tidal effects.

Table 8.1 Modeling parameters associated with porous medium and fluid

Parameter	Value	Units
$K_{x0} = K_{y0} = K_{z0}$	0.75	$cm\,s^{-1}$
α	0.125	cm^{-1}
n	3.50	dimensionless
S_r	0.01	dimensionless
α_L	0.75	cm
α_T	0.25	cm
γD_m	10^{-6}	$cm^2 s^{-1}$

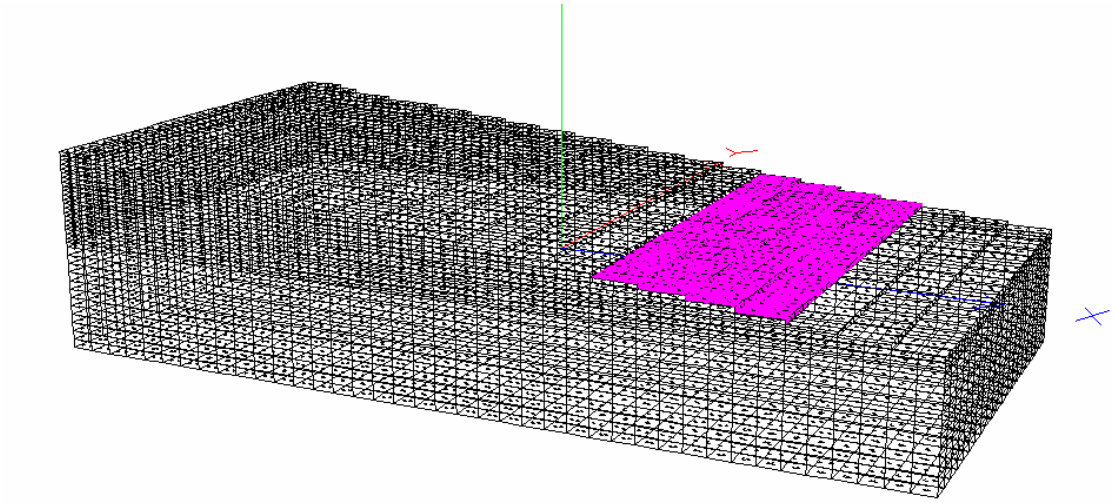

Figure 8.2 Idealization of the problem for three-dimensional saltwater intrusion in a phreatic aquifer subject to well pumping under tidal effects. Purpled surface indicates the intertidal zone.

be 30 seconds. This time step is chosen to be small enough to represent variable hydraulic heads at the seaside under tidal effects.

Boundary conditions for flow and solute transport model are assigned similar to Case 1 in Table 6.4 of Chapter 6. The boundary conditions on two newly created surfaces along y direction are set to be no flow and no flux condition. The initial hydraulic head and concentration conditions for the problems are obtained through the following steps. First, the hydraulic head distribution is obtained by solving the problem with two constant hydraulic head boundary condition both at the inland and at the seaside until the solution reaches steady state. The head boundary condition at the inland is assigned to be 85 *cm* while the head boundary condition at the seaside is 77.5 *cm* which is the mid point of tide. Note that this problem is a constant density problem to delineate water table in the case of fresh water only. To validate the numerical result of the water table, the analytical solution for unsaturated flow in one dimension is used. Figure 8.3 shows these two water table lines. Second, this hydraulic head distribution from unsaturated flow together with zero initial concentration distribution is used to solve a steady state solution of saltwater intrusion similar to the Henry problem. In this solution, the seaside head boundary condition has a linear relation in which the slope of the linearity is determined by density differences. The corresponding boundary condition similar to the Henry problem for solute-transport equation is also assigned. This steady state solution is used as initial hydraulic head and concentration for the pumping situation with no tidal effects. On the other hand, the pseudo-steady state solution is also obtained from the same previous initial conditions from unsaturated flow with tidal effects included. Then, this

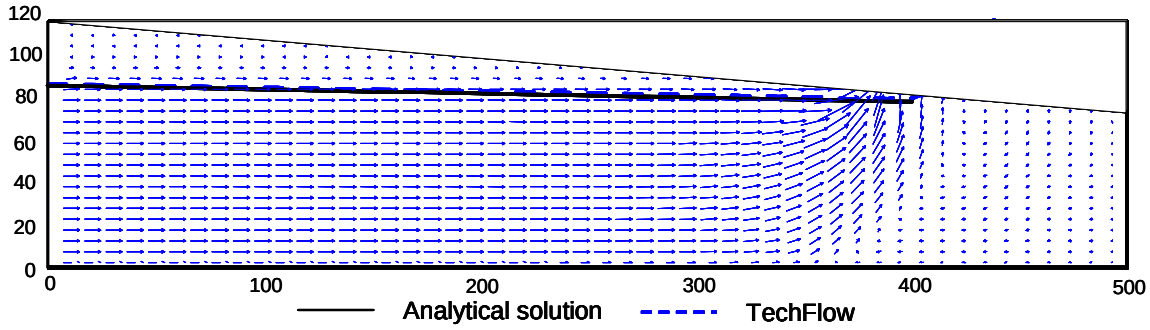

Figure 8.3 Water tables delineated from the one-dimensional analytical solution and from TechFlow. Blue dotted line is obtained from the cross-section of the result at the center of the three-dimensional problem domain.

steady state solution is used as initial hydraulic head and concentration for the pumping situation with tidal effects. Two initial conditions are generated in steps mentioned previously. Figure 8.4 depicts cross-sectional concentration and Darcy flux distribution of each initial condition. The solid line in (a) of Figure 8.4 is the sharp interface obtained from the analytical solution derived from the Ghyben-Herzberg assumption. As in Figure 4.2, the difference is shown between the result from TechFlow and the analytical solution and this difference is expected.

8.2.2 Saltwater Intrusion Due to Pumping with no Tidal Effects

For the given problem domain, the analytical solution of one-dimensional unsaturated flow with given hydraulic freshwater heads both in the inland and the seaside is used to estimate the total freshwater recharge from the inland. The computed total inland recharge rate is $Q_{Tin} = 2.85 \times 10^{-4} m^3 / s$. Considering saltwater flux from the

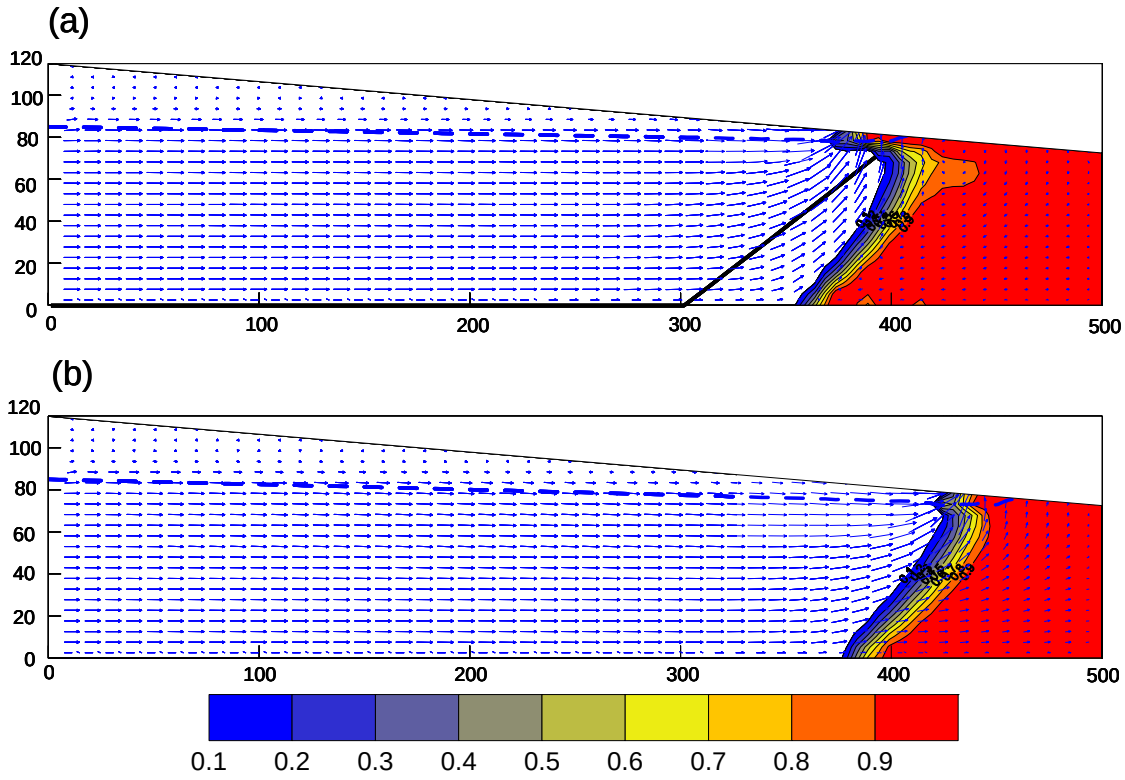

Figure 8.4 Cross-sectional concentration and Darcy flux distribution used as initial conditions for the simulation of saltwater intrusion or upconing (a) seawater level set at the mid point of tide used in the case of no tidal effects; (b) the lowest tide under tidal effects used in the case of tidal effects. Solid line in (a) is the analytical solution of the sharp interface between fresh water and saltwater

seaside and no flow boundary condition for the flow equation assigned onto both sides of the problem domain, the pumping rate assigned to the well is chosen to be about 19 % of the total inland recharge rate, which is $Q = 5.372 \times 10^{-5} m^3 / s$. This pumping rate is still considerably large because of the narrow width of the problem domain. The reason for assigning this large pumping rate is to investigate dynamic saltwater intrusion and further upconing after lateral saltwater encroachment occurs. Because of violation of the assumptions that the flow is horizontal in the fresh water region, which means that equipotentials are vertical lines or surfaces, and the flow rates in the saltwater region are assumed to be negligible in relation to the flow rates in the freshwater region, the analytical solution provided in Chapter 2 has a limitation when wells are intruded. In addition, the well location is chosen to be at the center of the problem domain in the xy-plane close to the seaside to generate these extreme cases. Thus, the distinction between lateral saltwater encroachment and saltwater upconing can be made with the location of the well screen varied vertically.

Figure 8.5 depicts transient solutions of lateral saltwater encroachment due to pumping under no tidal effects. The well screen is placed as depicted in Figure 8.5. Water is pumped through the screen that covers from the bottom of the aquifer to about a half depth from the water table. As pumping starts, saltwater including the transition zone encroaches inland. By the time reaches about 3,330 seconds, the bottom part of the well is intruded by saltwater water indicating that water quality is degraded and the pumping exceeded the allowable pumping rate that leads to guarantee water quality under steady state solution. This pumping scenario may occur when the aquifer conditions are not completely understood such that well is placed too close to the transition zone. However,

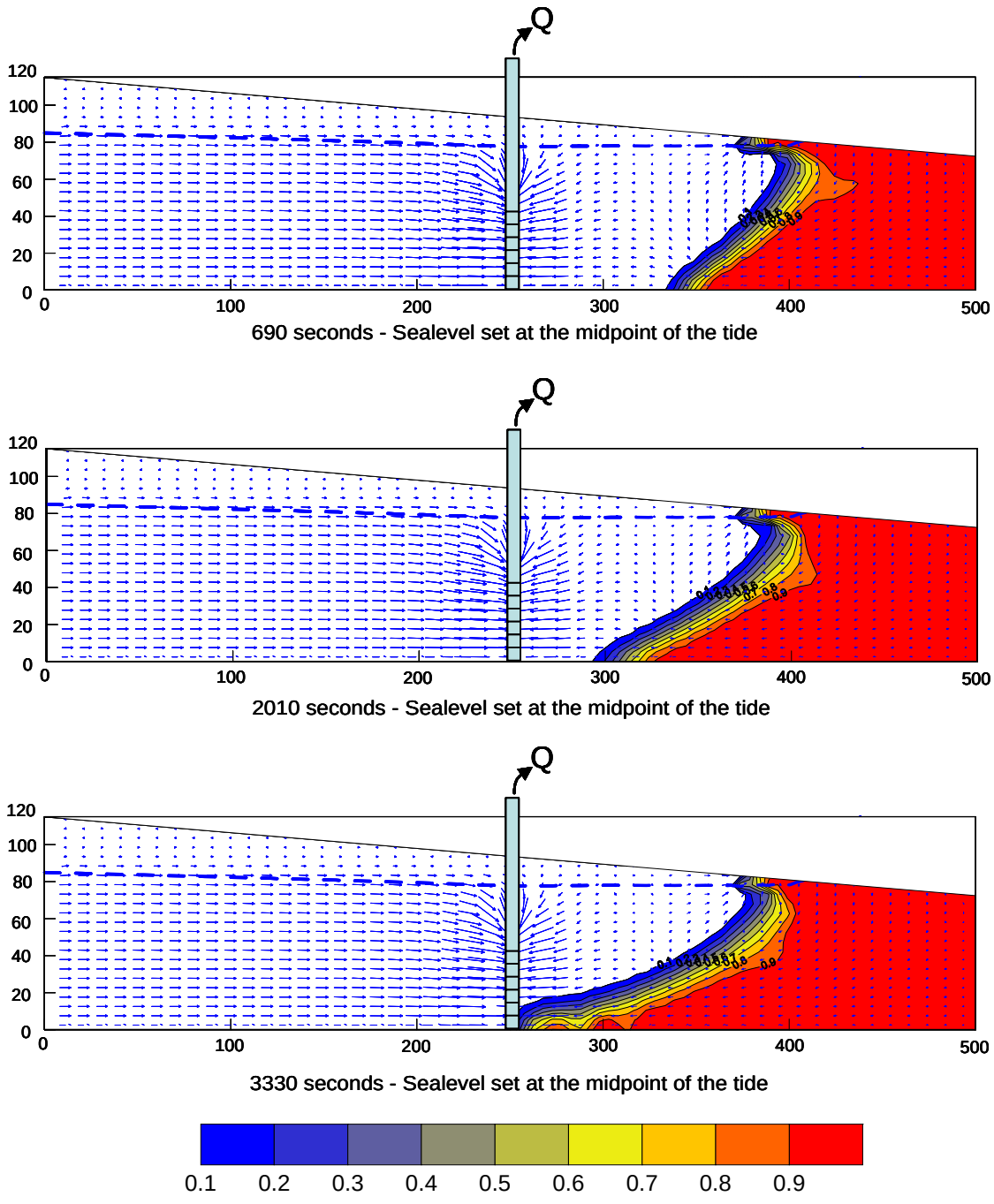

Figure 8.5 Cross-sectional concentration and Darcy flux distribution of transient solutions for no tidal effect

this is intended for extreme cases. In general, the lower part of the transition zone is encroached more than the upper part. This is different from overall encroachment occurring in the case of confined aquifers [Huyakorn et al., 1987].

With respect to the assigned pumping rate, toe line is estimated from analytical solution as in Chapter 3. The corresponding toe line assigned as 0.5 isochlor of the bottom of the aquifer in x,y-plane is also delineated in Figure 8.6. As shown in (a) of Figure 8.6, both results are significantly different. In fact, both solutions of toe line are contradicting because the assigned pumping rate is allowable based on the analytical solution while the result from TechFlow shows that the assigned pumping rate is not allowable since salt water intrusion occurs. There are several possible reasons for this difference. Most significantly, the analytical solution has no outlet open for the fresh water flow to the sea while the formulated application allows significant amount of the fresh water to exit to the sea, which is clearly shown in Figure 8.4. This in fact means that much less fresh water recharge is introduced in the numerical solution, thus much lower pumping rate can endanger the aquifer. Based on the assumptions that the analytical solution is derived from, horizontal flow assumed in the analytical solution which is only valid when the aquifer is very thin and the region of interests is far away from the seaside thus equipotential lines or surfaces are vertical. However, the region of interests in the application is very close to the transition zone and most of Darcy flux in the region is not horizontal. In addition to the first two differences, the pumping in the analytical solution is vertically averaged while the application provided in this chapter has an option to locate the screen of the well in the vertical direction. Placing the well screen along the saturated zone vertically to represent the averaged pumping rate is almost impossible

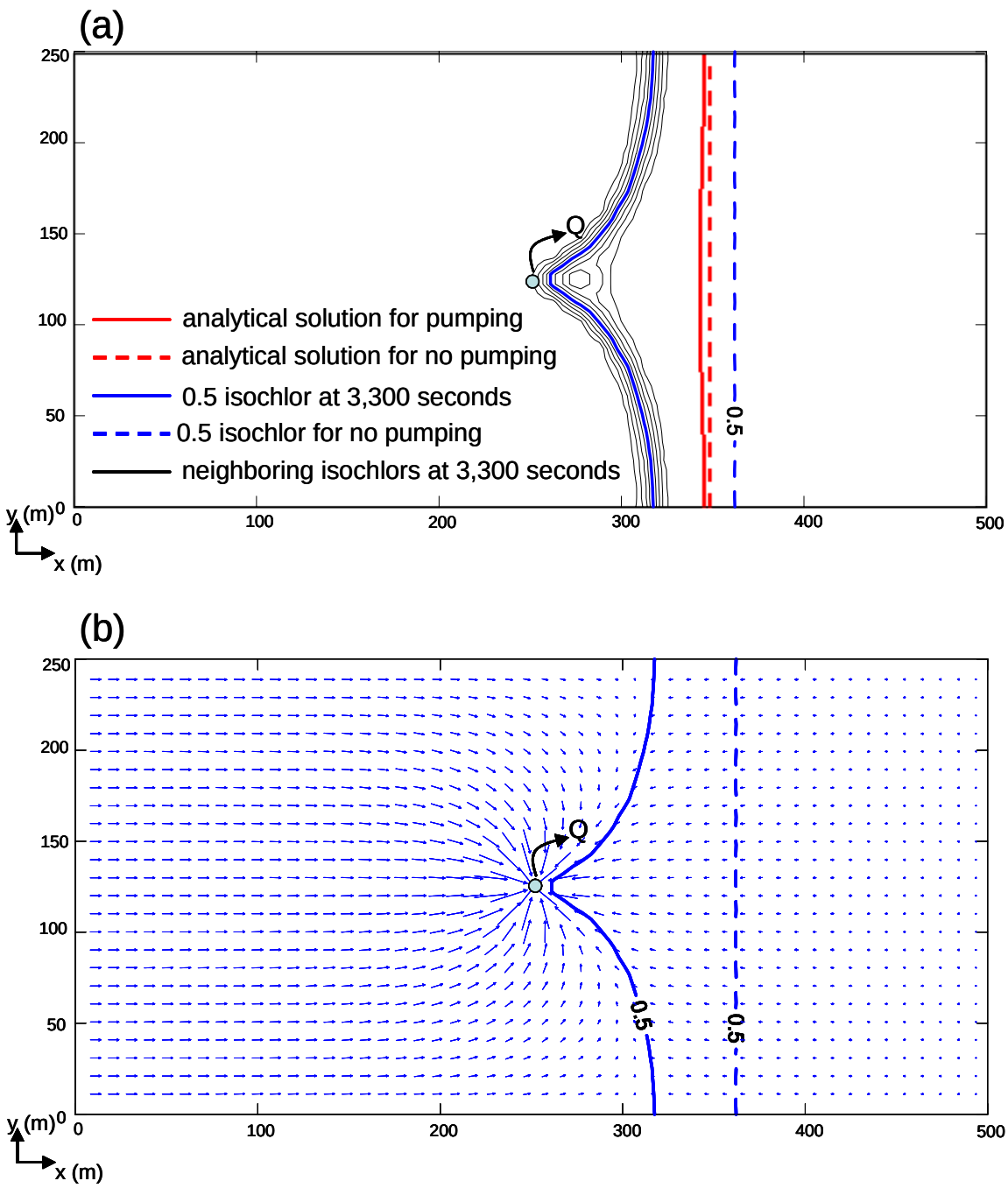

Figure 8.6 (a) Comparison of the result of TechFlow with that from analytical solution (b) 0.5 isochlor line at the bottom of the aquifer: a blue solid line and Darcy flux are taken at time = 3330 seconds while a blue dotted line is taken with no pumping rate.

because it makes the top portion of the well screen pump in unsaturated zone. If pumping in unsaturated zone occurs, the assumption of constant pressure of the air used in the numerical solution is no longer valid. Obviously, the analytical does not consider any vertical change of pressure head around the pumping well. Thus, any well screen not placed along the saturated zone creates non-horizontal flow more of the water is pumped from the bottom of the aquifer. Another reason is that the sharp interface assumption in the analytical solution makes the interface movement tight while the transition zone in the numerical solution is flexible to be wide. This can be seen that 0.5 isochlor does not coincide with the mid-point line of the transition zone in (a) of Figure 8.6 similar to the first application of saltwater upconing in Chapter 7. In fact, 0.5 isochlor at the center of y-axis is much closer to the inland while higher values of neighboring isochlors are closer to the seaside. The sharp interface solution does not have this flexibility. As shown in Chapter 7, this asymmetric condition in saltwater upconing indicates the critical pumping that the sharp interface solution allows is improper water quality management. This did occur at the much lower pumping rate. Lastly, from the comparison of the toe location encroached at time 3,300 seconds with that in no pumping case in (b) of Figure 8.6, the chosen width of the problem domain is relatively too short to represent an infinite width along y-direction assumed in the analytical solution in Chapter 3. In fact, this infinity assumption in the analytical solution hardly holds due to complex geometry of coastline in general.

8.2.3 Saltwater Intrusion Due to Pumping under Tidal Effects

While the first pumping scenario is intended to describe saltwater intrusion hydrodynamics due to pumping in a variably saturated porous medium, the pumping scenario in this section is designed to represent the same physics but under tidal effects. In order to make a comparison, the same location of the well screen and pumping rate are initially assigned. Figure 8.7 depicts cross-sectional concentration and Darcy flux distribution of transient solutions under tidal effects taken at the center of y-axis. Four transient solutions at the highest tide are provided. To obtain the results, the initial condition as in (b) of Figure 8.4 was used for this simulation. Although the steady state solution is obtained and becomes the initial condition of this simulation under tidal effects with no pumping, the initial condition does not have a concentration profile underneath the intertidal zone for the given conditions. However, the solutions in Figure 8.7 clearly show concentration profile developing underneath the intertidal zone due to pumping. This plume development is distinctive compared to the result of no tidal effects.

Similar to the first scenario, the toe location of 0.5 isochlor in the bottom of the aquifer at time of 4,650 seconds is presented in Figure 8.8. The transition zone is encroached laterally not showing much difference from that with no tidal effects. However, three-dimensional representation in Figure 8.9 depicts much more complicated concentration profile in the upper part of the aquifer. Thus, the concentration profile underneath the intertidal zone itself is truly three-dimensional. Since the location of the well screen is placed from the bottom of the aquifer, the extent of lateral encroachment is emphasized in the lower part of the transition zone of the saltwater rather than in the

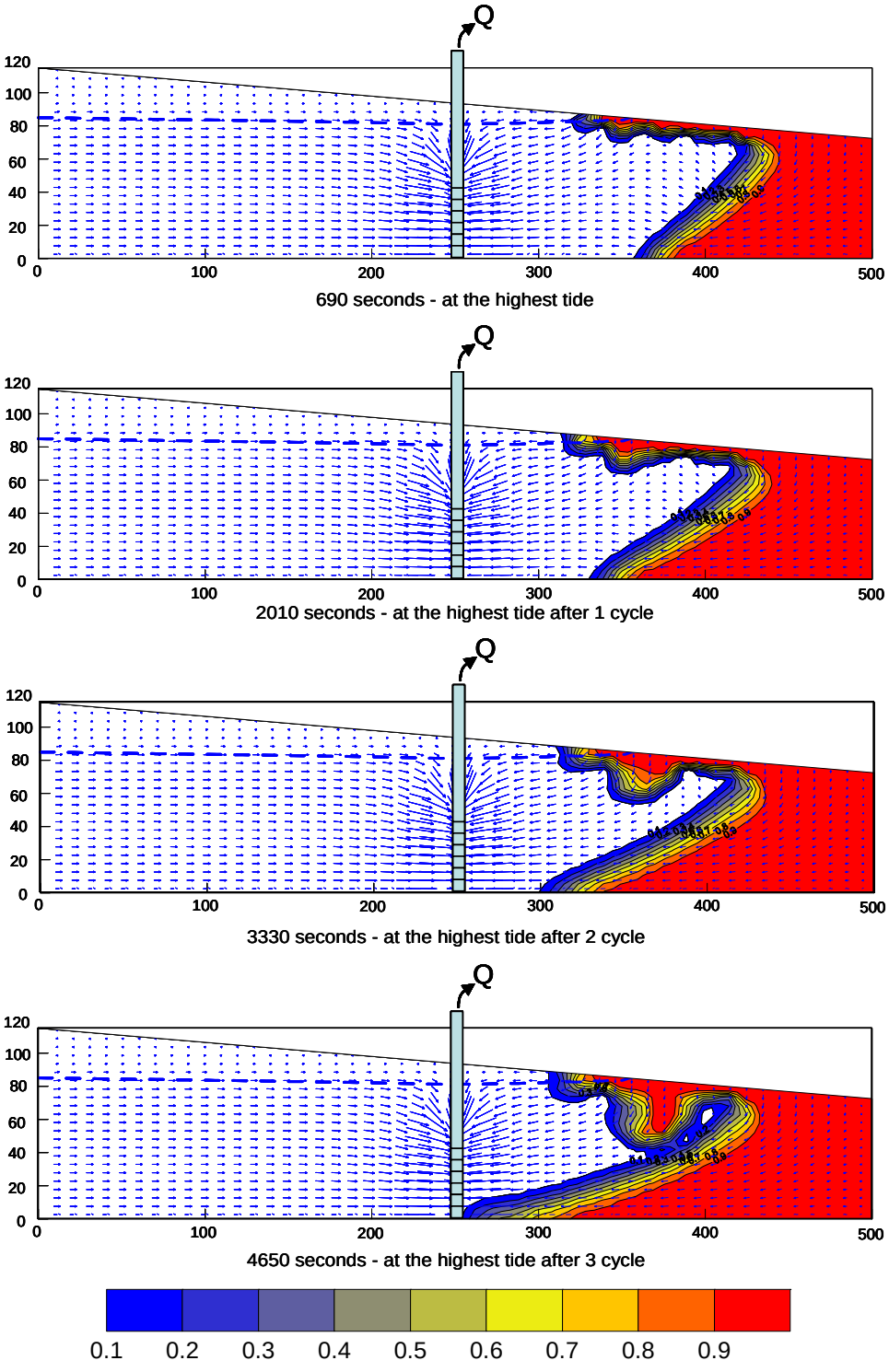

Figure 8.7 Cross-sectional concentration and Darcy flux distribution of transient solutions under tidal effects

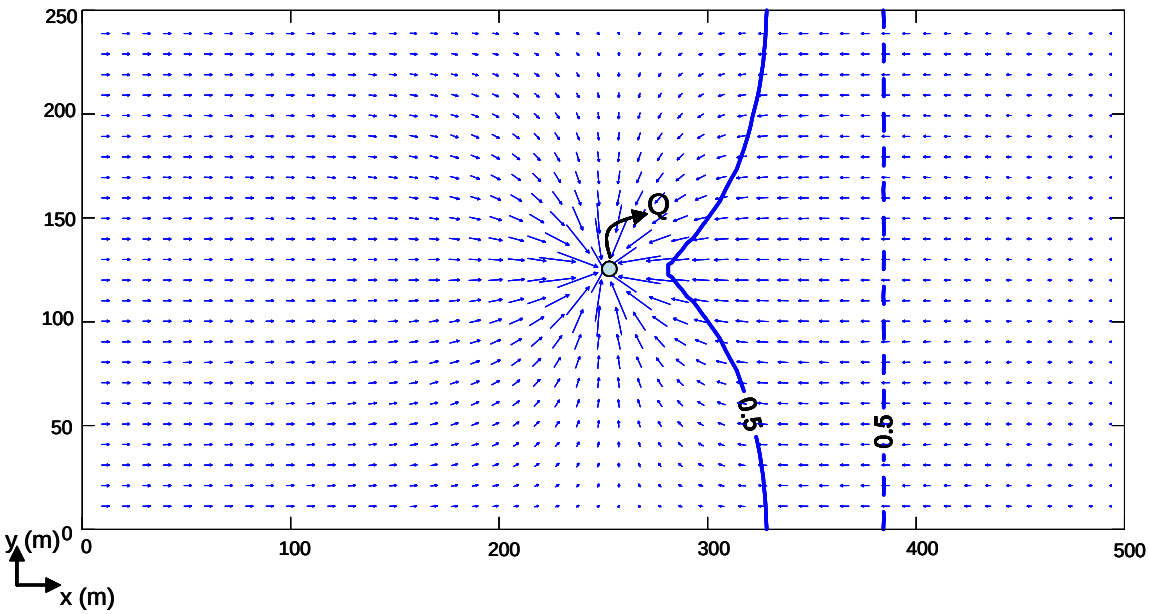

Figure 8.8 0.5 isochlor line at the bottom of the aquifer: a blue solid line and Darcy flux are taken at time = 4,650 seconds while a blue dotted line is taken from the steady-state solution of the lowest tide under tidal effects with no pumping rate

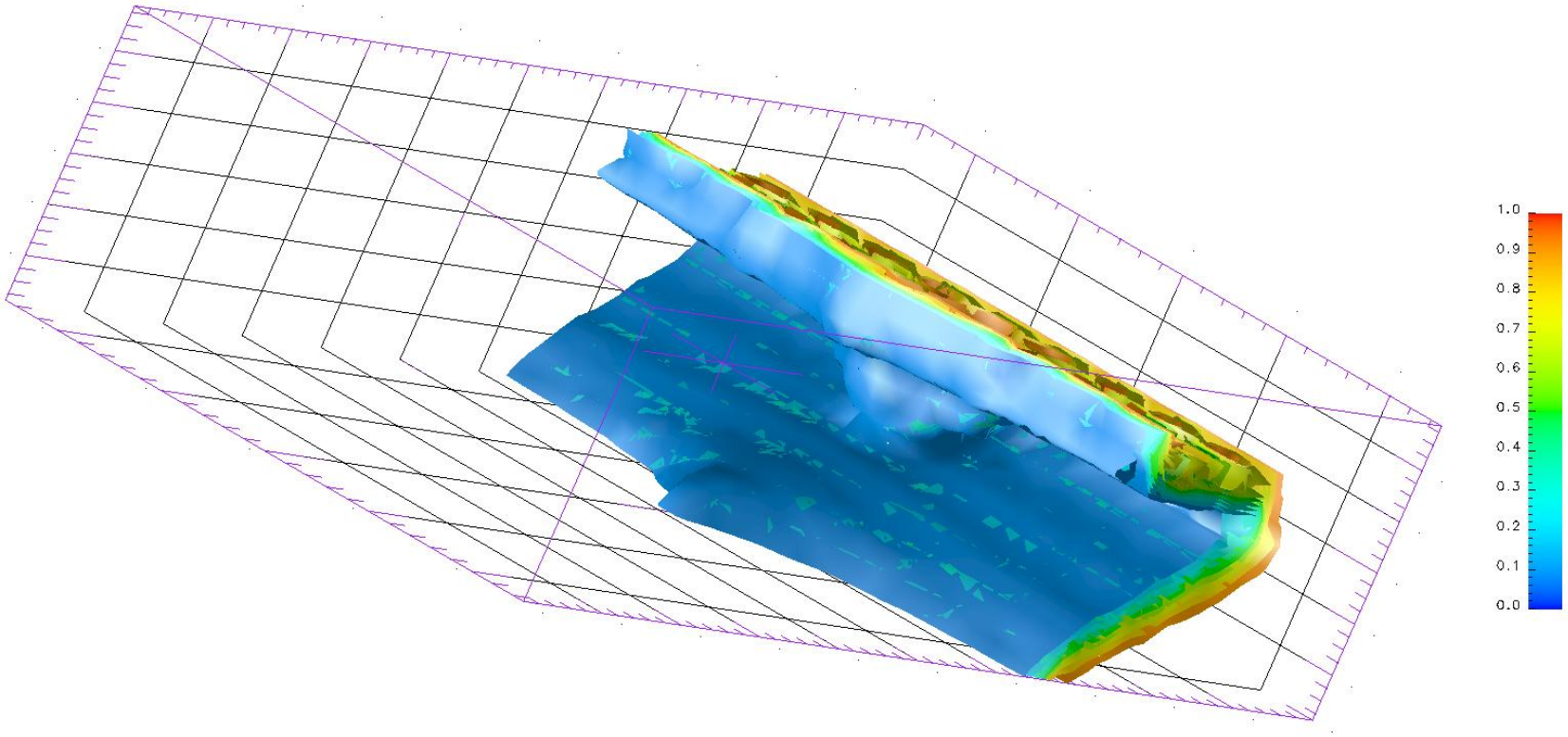

Figure 8.9 Saltwater Intrusion due to pumping under tidal effects

upper part and the saltwater upconing is prohibited because of the lower location of the well screen.

8.2.4 Saltwater Upconing Due to Pumping under Tidal Effects for a Partially Penetrating Well

The location of the well screen is adjusted to be in an upper part of the saturated zone to simulate saltwater upconing after lateral saltwater encroachment. Since the tide keeps changing, the well screen can not be placed close to the water table. After several simulations, the well screen is placed as shown in Figure 8.10. Figure 8.10 depicts cross-sectional concentration and Darcy flux distribution of transient solutions under tidal effects taken at the center of y-axis. Five transient solutions taken only at the highest tide are provided. In general, the concentration profile is similar to that in the second scenario. In this case, more encroachment from the upper part of the concentration profile is observed. When the transition zone reaches close to the well position, the upconing of the saltwater concentration occurs underneath the well indicating three-dimensional nature of the pumping in the aquifer. Figure 8.11 depicts the toe location of 0.5 isochlor in the bottom of the aquifer at time of 5,970 seconds. The well location is marked in a circle which represents the well location in xy-plane but the well screen is not covered at the bottom. Unlike the previous two pumping scenarios, there is no direct well screen at the bottom of the problem domain, thus generates saltwater upconing near above this circle. From the result obtained at time of 5,970 seconds in Figure 8.10, the edge of the concentration profile underneath the pumping well is vertical. Considering the dissolved concentration at the edge of the transition zone, this upright direction can be justified due

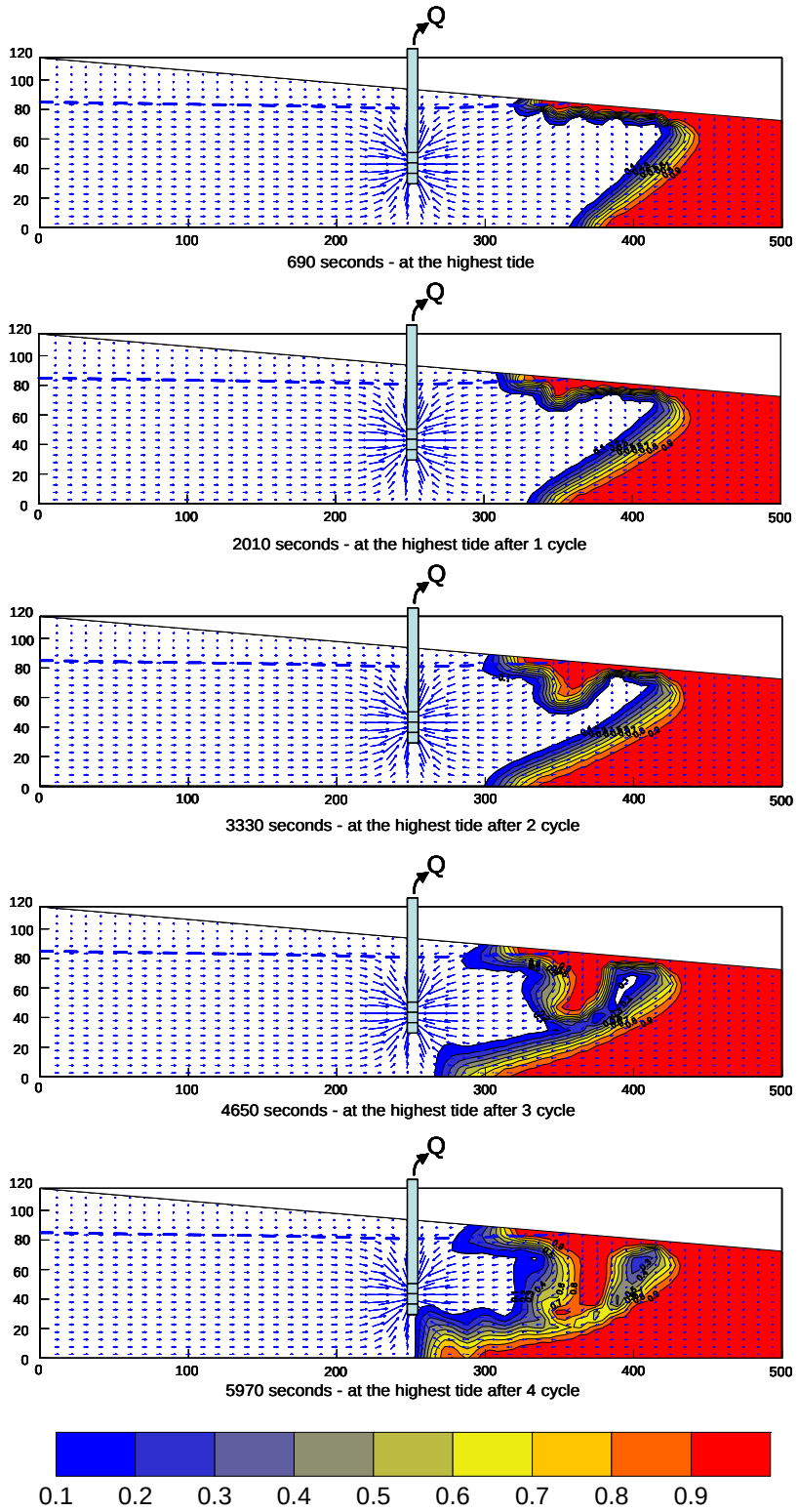

Figure 8.10 Cross-sectional concentration and Darcy flux distribution of transient solutions under tidal effects

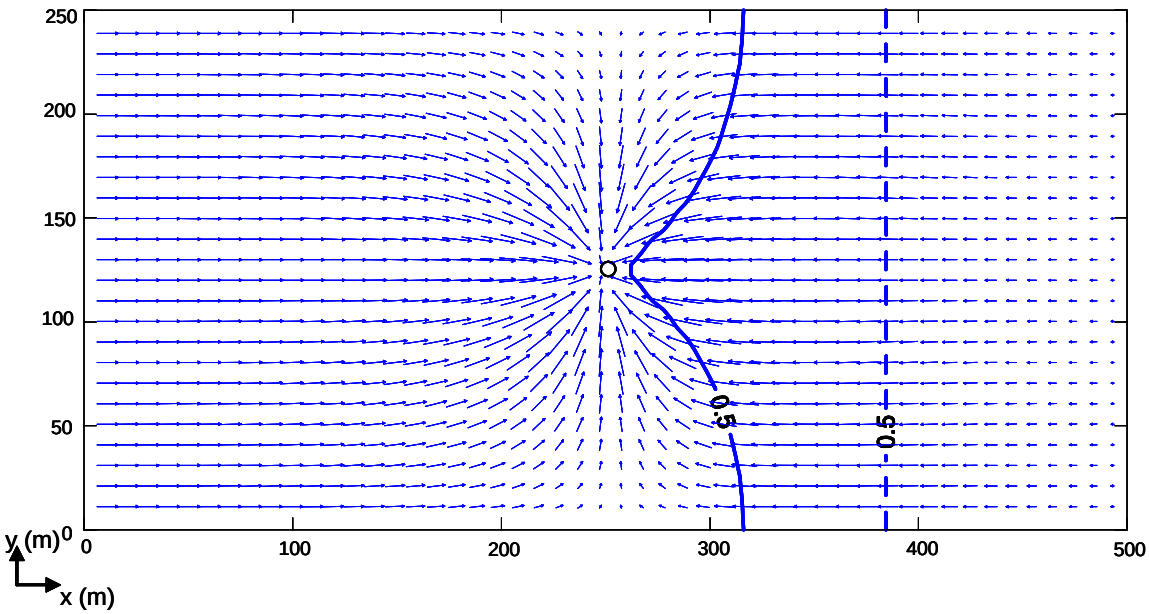

Figure 8.11 0.5 isochlor line at the bottom of the aquifer: a red solid line and Darcy flux are taken at time = 5,970 seconds while a black dotted line is taken from the steady-state solution of the lowest tide under tidal effects with no pumping rate

to less concentration gradient. Because of this less concentration gradient at the edge, the direction of the edge is almost coincide with the direction of the fresh water flux as shown in Figure 8.10. The three dimensional representation of the concentration distribution in Figure 8.12 shows subtle difference of concentration profiles in the upper zone and upconing effect in the lower zone. This saltwater upconing did occur because of the placement of the well screen in the upper part of the saturated zone. Although the pattern of solute development in the upper zone is similar to that in the second scenario, Figure 8.10 clearly shows a difference of concentration distribution in the extent of lateral encroachment in the upper zone at the central cross-section.

8.3 Dimensional Analysis and Scaling up

To conduct a dimensional analysis on solute transport in a variably saturated porous media, variables that are important in solute transport in variably saturated porous media must be selected. Among the selected variables, a dependent variable is expressed as a function of the other independent variables. In the variable selection process, the important physics of interests should be considered. Considering the application provided in this chapter, one of important variables in groundwater flow and transport is hydraulic conductivity which is highly dependent on the saturation ratio of porous media. Thus, three important variables associated with hydraulic conductivity are taken from the work by van Genuchten [1980] to represent hydraulic conductivity in variably saturated porous media. If only a saturated porous medium is considered, then, simple saturated hydraulic conductivity can replace the van Genuchten parameters. In fact, Smith [2004] took advantage of the use of hydraulic conductivity instead of the van Genuchten parameters

in his dimensional analysis on mixed convection and density-dependent seawater circulation in coastal aquifers. This is because the aquifer is fully saturated.

As for a dependent variable in the application in this chapter, density (ε) that can be represented by concentration is chosen. The other independent variables that compose the function to represent the chosen dependent variable are selected as $\{n, \alpha, S_r, \alpha_L (= \alpha_T), D_m, \phi, L, Q_f\}$ where Q_f is an external terrestrial groundwater inflow (uniform freshwater inflow) subtracted by outflow (pumped freshwater only) $\left[L^3 T^{-1}\right]$ and L is a characteristic length. These independent variables are carefully chosen to describe two transport components, aquifer properties, exerting force and pressure (i.e., n, α, S_r, and ϕ are for advection and aquifer properties, $\alpha_L (= \alpha_T)$ and D_m are for hydrodynamic dispersion, and L and q_f are for an exerting force and pressure). For the purpose of simplicity, aspect ratios in geometry, hydraulic conductivity, and dispersivities are not considered in the dimensional analysis. From Buckingham's Pi Theorem [Buckingham, 1914], the number of the independent dimensionless groups can be formulated to be seven (9 minus 2). These dimensionless groups are listed and described in Table 8.2.

Seven dimensionless groups shown in Table 8.2 have their own physical meaning. Among them, the principle dimensionless number is chosen and defined as the ratio of capillary force to gravity force. This is to consider importance of fluid flow in a variably saturated porous medium. Capillary force can be represented by the inverse of α while gravity force can be represented by L as hydraulic head or pressure head can be represented by length. The ratio can also be interpreted as a ratio of the height of the capillary fringe to the domain height.

Based on the dimensional analysis, the previous results can be generalized and scaled up using dimensionless formulation primarily following the work from Boufadel [Boufadel et al., 1997,1998,1999b; Boufadel, 2000]. The approach consists of conducting nondimensionalization as $x^* = x/L$, $y^* = y/L$, $z^* = z/L$, $K = K_{xo}/K_0 = K_{yo}/K_0 = K_{zo}/K_0$, $t^* = t/T_0$, where $T^0 = L/K_0$, $\alpha_L^* = \alpha_L/L$, $\alpha_T^* = \alpha_T/L$, and $\alpha^* = \alpha/L$, where starred quantities are dimensionless and T^0 is a characteristic time. By rewriting the governing equations in Chapter 4, Boufadel et al. [Boufadel et al., 1999b; 1999a] showed that the hydraulics and hydrodynamics in two domains of different sizes (but geometrically similar) are the same provided the dimensionless quantities above are conserved along with n, S_r, and ϕ. Based on this dimensional analysis, an advantage in the modeling-scale system (i.e., small-scale system) requires a coarser porous medium in small-scale system than that in prototype-

Table 8.2 Dimensionless groups and physical meanings

Dimensionless group	Physical meaning
$\varepsilon = \dfrac{\rho_S - \rho_f}{\rho_f}$	Fluid density difference
n	The uniformity of the pores
S_r	Residual soil saturation ratio
ϕ	Porosity
$\dfrac{\alpha^{-1}}{L}$	The ratio of capillary force to gravity force
$\dfrac{L}{\alpha_L (or\ \alpha_T)}$	Dispersion parameter
$\dfrac{q_f L}{D_m}$	The seepage Peclet number described by Lee and Cheng [1974]

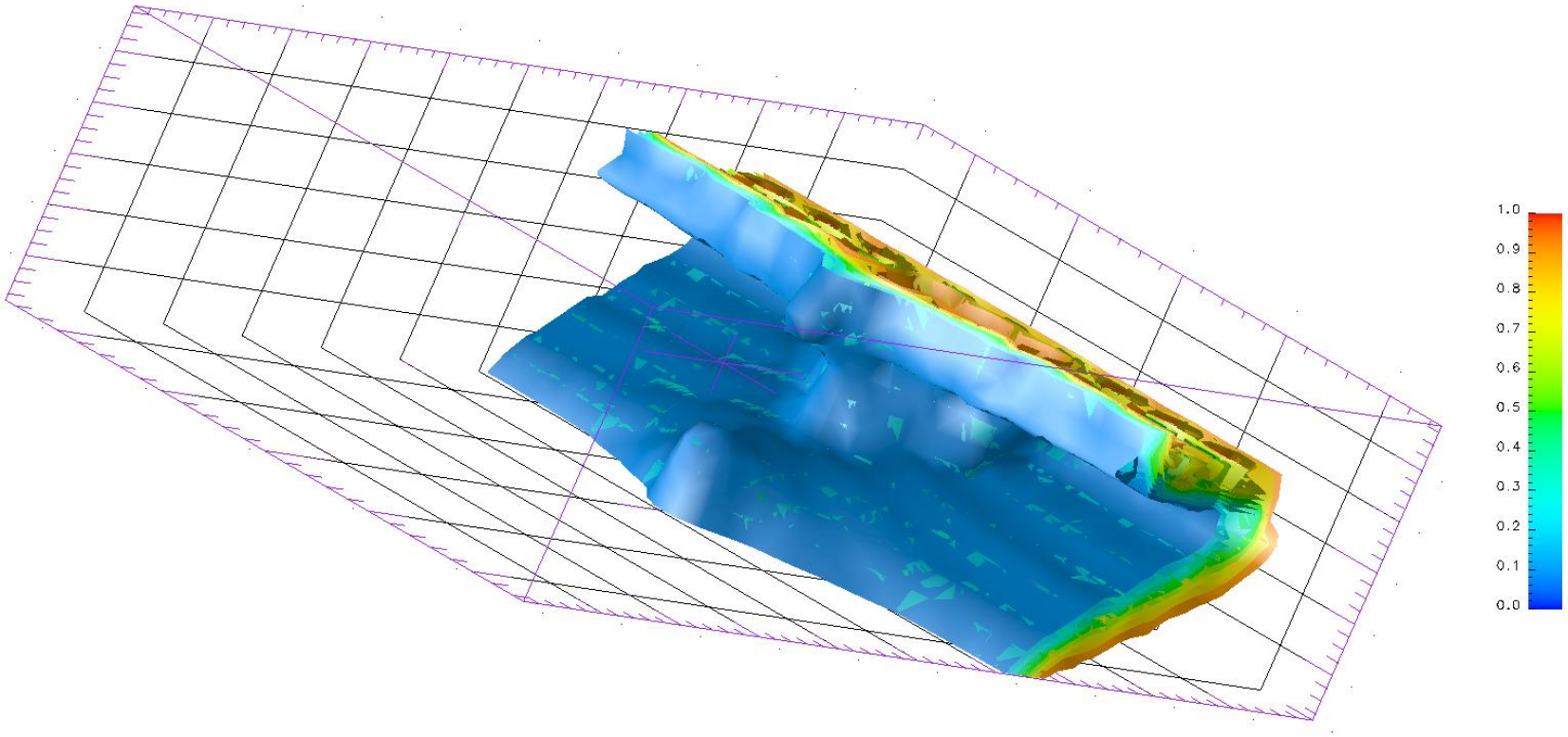

Figure 8.12 Saltwater Upconing after lateral saltwater encroachment due to pumping under tidal effects

scale system. This makes it easy to choose laboratory sand that conserves the value of α because it is always possible to find sand coarser than one found in a natural beach. Then, the saturated freshwater hydraulic conductivity of the laboratory sand is measured to compute the tidal period in the laboratory setup. An example of the properties of a natural beach scaled up five times is provided in Table 8.3.

As for other properties, the dispersivity value is known to increase with both the degree of heterogeneity and the travel distance from source. Since the principle dimensionless number is of interests in the boundary between unsaturated zone and saturated zone, the importance of the dispersivity is associated with the intertidal zone of the beach. Considering high degree of homogeneity in sandy beaches and the small travel time of water flow and solute transport in the intertidal zone, the longitudinal dispersivity is probably only a bit larger than the scaled-up value. For other values such as the van Genuchten parameters except α , Boufadel [1998] showed that S_r and ϕ of sandy beaches do not significantly affect water flow unless they are extreme values. Thus, based on the principle dimensionless number provided and considering the unique situations of beaches with respect to the dispersivity, the dimensionless formulation is flexible for a wide application of the previous results.

As an example of an application of the previous results in the case of Table 8.2, the pumping rate scaled up to a natural beach with the computed characteristic length and time scale based on the provided dimensional analysis is computed to be 201 cm^3/s while the pumping rate that is assigned as about 19% of the total fresh water recharge computed from the analytical solution of one-dimensional unsaturated flow with scaled-up hydraulic freshwater heads is 227 cm^3/s . With the former pumping rate in the

Table 8.3 Scale-up of the application parameters

Parameter	Application	Natural Beach
$Dimension, cm \times cm \times cm$	$500 \times 250 \times 115$	$2500 \times 1250 \times 575$
$K_0,\ cm/s$	0.75	0.127
$K_{x0} = K_{y0} = K_{z0},\ cm/s$	0.75	0.127
$\alpha^{-1},\ cm$	8	40
$\alpha_L,\ cm$	0.75	3.75
$\alpha_T,\ cm$	0.25	1.25
Tidal Amplitude A, cm	10	50
Tidal Period T	22 min	12.25 hours
$Q, cm^3/s$	5.372×10	2.01×10^2
ϕ	0.36	0.36
n	3.5	3.5
S_r	0.01	0.01

example of the natural beach and the geometrically projected length and location of the well screen as in the third scenario, saltwater upconing would occur and the well would be intruded about at the highest tide after four cycles as in Figure 8.10. Similar interpretation about the first and second scenarios for the example can also be conducted. Since the dimension of the screen is a length, the corresponding screen length and location in the example can simply be five times scaled up. For an example of the third scenario, 30 cm of the screen length located from 30 to 55 cm in the vertical direction at the center of xy-plane in the small scale corresponds to 1.5 m of the screen length located from 1.5 to 2.75 m in the vertical direction in the example of the natural beach.

8.4 Discussions and Concluding Remarks

In this chapter, three scenarios of the saltwater intrusion due to pumping under no tidal effects or under tidal effects are solved and investigated. The large pumping rate is intentionally assigned to induce extreme cases of saltwater intrusion. Tidal effects produce distinctive plume development especially under the intertidal zone due to pumping. The developed plume under the intertidal zone is significantly influenced by pumping according to the location of the well screen. Due to three dimensional nature of the application, the location of the well screen does make a difference in lateral saltwater encroachment between the upper zone and the lower zone. Specially, saltwater upconing after lateral saltwater encroachment can only occur when the location of the well screen is placed in relatively high position. This difference can be simulated when the application is solved in three-dimension.

For practical usefulness of the results in this chapter, a dimensional analysis is provided. In this analysis, the principle dimensionless number is chosen as a ratio of capillary force to gravity force. Thus, the analysis is focused on the physics of water flow between the unsaturated zone and the saturated zone. This choice is based on the following considerations. Considering a small density difference between fresh water and saltwater, the physical instability is thought to be small, thus the Rayleigh number is ruled out. Considering high degree of homogeneity in sandy beaches and the small travel time of water flow and solute transport in the intertidal zone, the dispersivity is assumed to be constant. In addition, the difficulties to quantify dispersive effects that include velocity, dispersivity, and molecular diffusion coefficient, the Peclet number was ruled out as an important dimensionless number. Hence, the proposed dimensional analysis has a limitation when saltwater intrusion hydrodynamics of interests requires further physical considerations as approached through the other important dimensionless numbers discussed. Nonetheless, the results obtained from the application in this chapter can be used for interpretation of practical applications in which the principle dimensionless number is of interest.

CHAPTER 9

CONCLUSIONS AND FURTHER RESEARCH CONSIDERATION

9.1 Conclusions

From the chapters provided in this thesis, the following findings and conclusions can be summarized for saltwater intrusion in coastal aquifers.

1. The proposed optimization problem uses a progressive genetic algorithm technique and the method developed is applied to the previous work of Cheng et al. [2000].Through this analysis, several other applications are provided to demonstrate the use of the model in practical applications. This work is the first to optimize pumping rates as well as well locations simultaneously in coastal aquifer management.
2. A three-dimensional finite element model (TechFlow) of variable density flow in a variably saturated porous medium is developed in this study and tested through various benchmark test problems such as the Henry problem, the Elder problem, and HYDROCOIN Level 1 Case 5 (i.e., the salt dome problem) for comparison between codes and the saltpool problem for comparison between the developed model and the three-dimensional temporal experimental measurement.
3. From the numerical experiments in the Elder problem, the following conclusions are reached: (i) the physical instability is what makes the Elder problem difficult to solve; (ii) the Elder problem is sensitive to local grid regularity; (iii) Stricter vertical grid Peclet number criterion is required to rule out possible numerical

errors associated with grid size and similarly numerical dispersion; and, (iv) globally continuous velocity estimation can help reduce the grid density while obtaining convergent solutions to saltwater intrusion problems.

4. In saltwater intrusion hydrodynamics in a beach under the influence of tidal effects, the advective component in the gap between the plume underneath the intertidal zone and the saltwater wedge as well as the periodic change of the flow direction indicate that traditional boundary conditions in solute-transport equation is hardly valid. The improper handling of the exit boundary condition leads to the artificial fingerings because the solute mass is kept and accumulated in the system. However, the free exit boundary effectively allows the solute mass exit through the exit boundary especially in the gap area. The thickness of the gap changes as the density difference changes.
5. As for the saltpool experiment, two reference solutions obtained from TechFlow are in good agreement with the measured data than those from the others and obtained from much less dense grid than those used by the others indicating that the grid density can be reduced significantly with the global continuous velocity estimation. In addition to the grid density reduction with the velocity estimation, the parameter adjustment, recommended by Johannsen et al. (2002) for their overestimated concentration, can not be applicable to this study because the results from this study and from Diersch and Kolditz (2002) tend to underestimate concentrations.
6. In the application for saltwater upconing due to pumping under tidal effects, the developed plume under the intertidal zone is significantly influenced by pumping

according to the location of the well screen. Due to three dimensional nature of the application, the location of the well screen does make a difference in lateral saltwater encroachment between the upper zone and the lower zone. In the dimensional analysis, the principle dimensionless number is chosen as a ratio of capillary force to gravity force. Thus, the analysis is focused on the physics of water flow between the unsaturated zone and the saturated zone. The results obtained from the application can be used for interpretation of scaled-up applications in which the principle dimensionless number is of interest.

9.2 Further Research Consideration

Based on the study of saltwater intrusion in coastal aquifers in this thesis, further research consideration can be recommended as following:.

1. Physical instability investigation of coastal aquifer periodically submerged by tide and the choice of proper boundary conditions.
2. Optimization of well screen locations to prevent saltwater intrusion near coastal aquifers.
3. Saltwater intrusion in islands associated with the influence on ecosystem.
4. Submarine groundwater discharge analysis in mild sloping seabed under tidal influence.

APPENDIX A

MULTI-OBJECTIVE OPTIMIZATION OF PUMPING RATES AND WELL LOCATIONS IN COASTAL AQUIFERS

Appendix A includes an example problem that is used in the solution of Laplace equation utilizing the single potential theory and a detailed derivation of the equation used to solve for the toe location in the analytical solution.

A.1 An Example Problem of the Laplace Equation using Single Potential Theory with Appropriate Boundary Conditions

As an example, a vertical cross-section of an unconfined aquifer with a constant surface recharge I is selected as shown in Figure A.1. The governing equation is

$$\frac{d^2\phi}{dx^2} = -\frac{w}{K} \tag{A.1}$$

where ϕ is the single potential defined by Strack [1976] and K is the hydraulic conductivity of a saturated porous medium.

The boundary conditions are

$$\begin{aligned} &\phi = 0 \qquad at\ x = 0 \\ &\frac{d\phi}{dx} = \frac{q}{K} \quad at\ x = L \end{aligned} \tag{A.2}$$

where q is the fresh water volume outflow rate per unit length of coastline. Solution obtained from Equation (A.1) with the boundary conditions of Equation (A.2) is

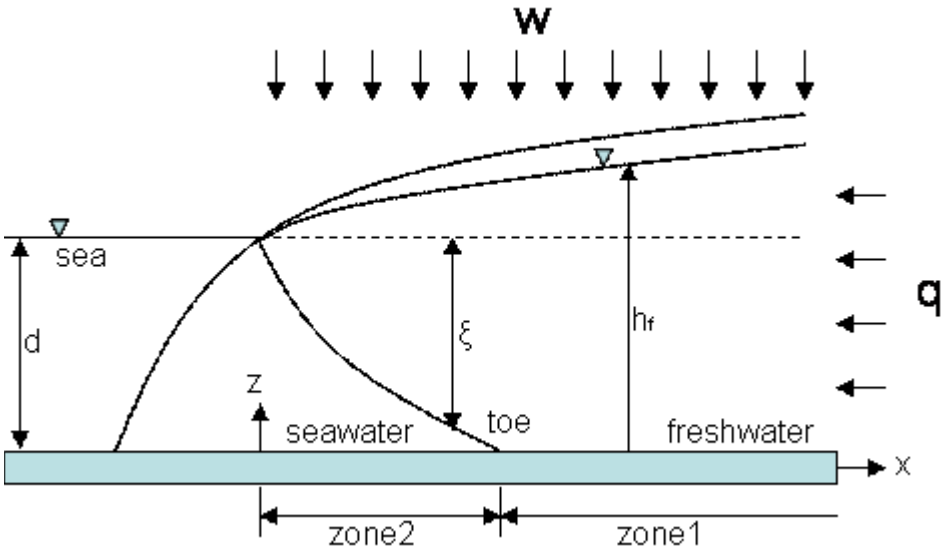

Figure A.1 Tracking saltwater toe in a one-dimensional problem.

$$\phi = -\frac{w}{2K}x^2 + \left(\frac{q}{K} + \frac{wL}{K}\right)x \tag{A.3}$$

Substituting the potential value defined in Equation (3.15) into Equation (A.3), the toe location can be solved

$$x_{toe} = \frac{q}{w} + L - \sqrt{\left(\frac{q}{w} + L\right)^2 - 2\frac{\phi_{toe}K}{w}} \tag{A.4}$$

where ϕ_{toe} is as defined in Equation (3.15).

A.2 Derivatives of Equation 3.18 and 3.19

A typical way to solve a set of nonlinear equations is the Newton-Raphson method. The advantage of this method is that it is fast and easy to use. However, it requires the derivatives of a nonlinear equation and this makes it tricky since in most cases it is difficult or impossible to obtain these derivatives. For the analytical solution of the

saltwater intrusion problem, there are two nonlinear equations to solve for the stagnation point. These equations are the following:

$$\begin{bmatrix} \dfrac{\partial \phi}{\partial x} = 0 \\ \dfrac{\partial \phi}{\partial y} = 0 \end{bmatrix} \Rightarrow \begin{bmatrix} F_1(x,y) = 0 \\ F_2(x,y) = 0 \end{bmatrix} \tag{A.5}$$

Taking only the first two terms from the Taylor series expansion of Equation (A.5) and simplifying it for x and y, the rearranged equation can be written as,

$$\begin{Bmatrix} x^{k+1} \\ y^{k+1} \end{Bmatrix} = \begin{Bmatrix} x^{k} \\ y^{k} \end{Bmatrix} - \frac{1}{D} \begin{bmatrix} \dfrac{\partial F_2}{\partial y} & -\dfrac{\partial F_1}{\partial y} \\ -\dfrac{\partial F_2}{\partial x} & \dfrac{\partial F_1}{\partial x} \end{bmatrix} \begin{bmatrix} F_1\left(x^k, y^k\right) \\ F_2\left(x^k, y^k\right) \end{bmatrix} \tag{A.6}$$

where $D = \begin{vmatrix} \dfrac{\partial F_1}{\partial x} & \dfrac{\partial F_1}{\partial y} \\ \dfrac{\partial F_2}{\partial x} & \dfrac{\partial F_2}{\partial y} \end{vmatrix}$ is the determinant.

The corresponding derivatives for multiple wells of the saltwater intrusion problem can now be evaluated from Equation (3.18) and (3.19). These are given below,

$$\frac{\partial F_1}{\partial x} = \sum_{i=1}^{n} \frac{Q_i}{4\pi K} \left[T_1 + 4 \left\{ \frac{(x+x_i)}{R_2} - (x-x_i)\frac{R_1}{R_2^2} \right\} \left\{ \frac{(x-x_i)}{R_1} - (x+x_i)\frac{R_2}{R_1^2} \right\} \right] \tag{A.7a}$$

$$\frac{\partial F_1}{\partial y} = \sum_{i=1}^{n} \frac{Q_i}{4\pi K} \left[T_2 - 4(y-y_i) \left\{ \frac{R_1}{R_2^2} - \frac{1}{R_2} \right\} \left\{ \frac{(x-x_i)}{R_1} - (x+x_i)\frac{R_2}{R_1^2} \right\} \right] \tag{A.7b}$$

$$\frac{\partial F_2}{\partial x} = \sum_{i=1}^{n} \frac{Q_i}{4\pi K} \left[T_2 - 4 \left\{ (x-x_i)\frac{R_1}{R_2^2} - \frac{(x+x_i)}{R_2} \right\} \left\{ \frac{(y-y_i)}{R_1} - (y-y_i)\frac{R_2}{R_1^2} \right\} \right] \tag{A.7c}$$

$$\frac{\partial F_2}{\partial y} = \sum_{i=1}^{n} \frac{Q_i}{4\pi K} \left[T_3 - 4(y-y_i) \left\{ \frac{R_1}{R_2^2} - \frac{1}{R_2} \right\} \left\{ \frac{(y-y_i)}{R_1} - (y-y_i)\frac{R_2}{R_1^2} \right\} \right] \tag{A.7d}$$

where

$$R_1 = (x + x_i)^2 + (y - y_i)^2 \tag{A.7e}$$

$$R_2 = (x - x_i)^2 + (y - y_i)^2 \tag{A.7f}$$

$$T_1 = \frac{R_1}{R_2}\left\{\frac{2}{R_1} - 8\frac{(x + x_i)(x - x_i)}{R_1^2} + 8(x + x_i)^2\frac{R_2}{R_1^3} - 2\frac{R_2}{R_1^2}\right\} \tag{A.7g}$$

$$T_2 = \frac{R_1}{R_2}\left[8\frac{R_2}{R_1^3}(x + x_1)(y - y_1) - \frac{4}{R_1^2}\{(x - x_i)(y - y_i) + (x + x_i)(y - y_i)\}\right] \tag{A7h}$$

$$T_3 = \frac{R_1}{R_2}\left\{\frac{2}{R_1} - 8\frac{(y - y_i)^2}{R_1^2} + 8(y - y_i)^2\frac{R_2}{R_1^3} - 2\frac{R_2}{R_1^2}\right\} \tag{A.7i}$$

With these derivatives used in Equation (A.6), the toe location can be obtained.

APPENDIX B

VARIABLE DENSITY FLOW IN A VARIABLY SATURATED POROUS MEDIUM

Appendix B includes a full development of the flow equation for variable density flow in a variably saturated porous medium.

B.1 Derivation of the Flow Equation for Variable Density Flow in a Variably Saturated Porous Medium

The derivation of the continuity equation in a porous medium is based on the average parameters defined in a representative elementary volume (REV) [Hassanizadeh and Gray, 1979a, b; Bear and Bachmat, 1990]. The macroscopic mass balance equation of the fluid in a variably saturated porous medium is

$$\frac{\partial(S\phi\rho)}{\partial t} + \nabla \cdot (\phi\rho\vec{v}) = \rho Q_\rho \tag{B.1}$$

where S is the saturation ratio, ϕ is the porosity, t is the time, $\vec{v}$ is the fluid velocity vector, and ρQ_ρ is the source term of the fluid mass.

The soil moisture and the freshwater hydraulic conductivity are correlated by the model of van Genuchten [1980]:

$$\text{For } \psi = h - z \geq 0.0,\ S = 1.0 \text{ and } \hat{K} = \hat{K}_0 \tag{B.2}$$

where $\hat{K}_0$ is the tensor of the saturated hydraulic conductivity. For $\psi = h - z \leq 0.0$, the effective saturation ratio, S_e, is given by:

$$S_e = \frac{S - S_r}{1 - S_r} = \left[\frac{1}{1 + (\alpha|\psi|)^n}\right]^m \; or \; \left[\frac{1}{1 + (\alpha|h - z|)^n}\right]^m \tag{B.3}$$

and $\hat{K}$ is given by:

$$\hat{K} = \hat{K}_0 S_e^{1/2}\left[1 - \left(1 - S_e^{1/m}\right)^m\right]^2 \tag{B.4}$$

where $m = 1 - (1/n)$, S_r is the residual saturation ratio. The parameter α represents a characteristic pore size and higher α values imply a coarser material. The inverse of α provides an estimate of the capillary fringe. The term n represents the uniformity of the pores and higher values of n imply a more uniform pore-size distribution [van Genuchten, 1980; Boufadel et al., 1998].

The flow equation can be expanded as

$$\phi\rho\frac{\partial S}{\partial t} + S\rho\frac{\partial \phi}{\partial t} + S\phi\frac{\partial \rho}{\partial t} + \rho\nabla\cdot(\phi\vec{v}) + \phi\vec{v}\cdot\nabla\rho = \rho Q_\rho \tag{B.5}$$

Then, the temporal derivative term in (B.5) can be written as

$$\phi\rho\frac{\partial S}{\partial t} + S\rho\frac{\partial \phi}{\partial t} + S\phi\frac{\partial \rho}{\partial t} = \rho\lambda_{CA}\frac{\partial h}{\partial t} + S\rho\left(S_0^h\frac{\partial h}{\partial t} + \phi\lambda_C\frac{\partial C}{\partial t}\right) \tag{B.6}$$

where $\lambda_{CA} = \phi\dfrac{\partial S}{\partial \psi}$ is the specific moisture capacity, $S_0^h = (1-\phi)\alpha_h + \phi\lambda_h$ is the specific storativity of a porous medium with respect to hydraulic head change, $\alpha_h = \dfrac{1}{(1-\phi)}\dfrac{\partial \phi}{\partial h}$ is the elastic property of the solid matrix due to the change of the hydraulic head, $\lambda_h = \dfrac{1}{\rho}\dfrac{\partial \rho}{\partial h}\bigg|_c$ is the coefficient of compressibility of the fluid resulting from the change of the hydraulic head at constant mass fraction of the solute, and $\lambda_c = \dfrac{1}{\rho}\dfrac{\partial \rho}{\partial C}\bigg|_h$ is the

coefficient of expansivity resulting from the change of the mass concentration of the solute at constant hydraulic head.

The mass flux term can be written as,

$$\rho\nabla\cdot\left(\phi\vec{v}\right)+\phi\vec{v}\cdot\nabla\rho=\rho\nabla\cdot\vec{q}+\rho\lambda_c\vec{q}\cdot\nabla C \tag{B.7}$$

Dividing by ρ, the resulting equation of the flow equation can be arranged in the form:

$$\lambda_{CA}\frac{\partial h}{\partial t}+SS_0^h\frac{\partial h}{\partial t}+S\phi\lambda_C\frac{\partial C}{\partial t}+\nabla\cdot\vec{q}+\lambda_c\vec{q}\cdot\nabla C=Q_\rho \tag{B.8}$$

Following the work of Celia et al. [1990], the mixed form of the Richards equation is used for modeling flow in the unsaturated zone. The mixed form of the Richards equation in one dimension can be expressed by retaining moisture content in the storage term as follows

$$\frac{\partial\theta}{\partial t}-\frac{\partial}{\partial z}\left[K(h)\left(\frac{\partial h}{\partial z}\right)\right]=0 \tag{B.9}$$

where θ is the moisture content. This form eliminates the mass balance error associated with the classical head-based form of the Richards equation, which is (B.8) in this study [Celia et al., 1990]. The flow equation of (B.8) can now be in written the mixed form as

$$\frac{\partial\theta}{\partial t}+SS_0^h\frac{\partial h}{\partial t}+S\phi\lambda_C\frac{\partial C}{\partial t}+\nabla\cdot\vec{q}+\lambda_c\vec{q}\cdot\nabla C=Q_\rho \tag{B.10}$$

Originally, Celia et al.[1990] proposed the numerical solution of Equation (B.9) in finite difference method using modified Picard method. Rathfelder and Abriola [1994] proposed the equivalent form of the modified Picard method in finite element method. With respect to the saturation ratio instead of the moisture content, the flow equation derived become the same form as Equation (4.3) given in Chapter 4.

$$\phi \frac{\partial S}{\partial t} + SS_0^h \frac{\partial h}{\partial t} + S\phi\lambda_C \frac{\partial C}{\partial t} + \nabla \cdot \vec{q} + \lambda_c \vec{q} \cdot \nabla C = Q_\rho \tag{4.3}$$

where $\theta = \phi S$. This flow equation is fully developed by using the equation of state for the bulk fluid density. The equation describes variable-density flow in a variably saturated non-deformable porous medium with no assumption of the Boussinesq approximation that implies that the contour of the equipotential hydraulic head is not orthogonal to the velocity vectors.

APPENDIX C

THE GALERKIN FINITE ELEMENT FORMULATION OF VARIABLE DENSITY FLOW IN A VARIABLY SATURATED POROUS MEDIUM

Appendix C includes the Galerkin formulations of the flow equation, the Darcy equation, and the contaminant transport equation and methods used in analytical integration, time marching schemes, and the free exit boundary condition.

C.1 The Flow Equation

The flow equation from equation (4.3) can be expanded to yield

$$\phi\frac{\partial S}{\partial t}+SS_0^h\frac{\partial h}{\partial t}+S\phi\lambda_C\frac{\partial C}{\partial t}+\frac{\partial q_x}{\partial x}+\frac{\partial q_y}{\partial y}+\frac{\partial q_z}{\partial c}+\lambda_c\left(q_x\frac{\partial C}{\partial x}+q_y\frac{\partial C}{\partial y}+q_z\frac{\partial C}{\partial z}\right)=Q_\rho \quad \text{(C.1)}$$

Ignoring the compressibility of the fluid resulting from the change of the hydraulic head, the Darcy equation of (4.4) becomes

$$q_x=K_{xx}\frac{\partial h}{\partial x}+K_{xy}\frac{\partial h}{\partial y}+K_{xz}\left(\frac{\partial h}{\partial z}+\lambda_C C\right) \quad \text{(C.2a)}$$

$$q_y=K_{yx}\frac{\partial h}{\partial x}+K_{yy}\frac{\partial h}{\partial y}+K_{yz}\left(\frac{\partial h}{\partial z}+\lambda_C C\right) \quad \text{(C.2b)}$$

$$q_z=K_{zx}\frac{\partial h}{\partial x}+K_{zy}\frac{\partial h}{\partial y}+K_{zz}\left(\frac{\partial h}{\partial z}+\lambda_C C\right) \quad \text{(C.2c)}$$

Note that when the principal direction of hydraulic conductivity is matched with the coordinates, Equations (C.1) and (C.2) become simpler because $K_{xy}=K_{xz}=K_{yx}=K_{yz}=K_{zx}=K_{zy}=0$. In the case where the principal direction of hydraulic conductivity varies spatially, the individual element axes can be rotated to the

principle directions; two rotations would be required for each element in the three-dimensional case. The six cross-derivative terms that appear in the governing equation are thereby eliminated. Thus, the residual form of the flow equation in simpler form yields

$$R(\hat{h}) = \phi \frac{\partial \hat{S}}{\partial t} + SS_0^h \frac{\partial \hat{h}}{\partial t} + S\phi\lambda_C \frac{\partial \hat{C}}{\partial t} + \frac{\partial}{\partial x}\left(K_{xx} \frac{\partial \hat{h}}{\partial x} \right) + \frac{\partial}{\partial y}\left(K_{yy} \frac{\partial \hat{h}}{\partial y} \right) + \frac{\partial}{\partial z}\left\{ K_{zz}\left(\frac{\partial \hat{h}}{\partial z} + \lambda_C \hat{C} \right) \right\} + \lambda_c \left[\left(K_{xx} \frac{\partial \hat{h}}{\partial x} \right) \frac{\partial \hat{C}}{\partial x} + \left(K_{yy} \frac{\partial \hat{h}}{\partial y} \right) \frac{\partial \hat{C}}{\partial y} + \left\{ K_{zz}\left(\frac{\partial \hat{h}}{\partial z} + \lambda_C \hat{C} \right) \right\} \frac{\partial \hat{C}}{\partial z} \right] - Q_\rho \tag{C.3}$$

To apply the Galerkin finite element method, the weighted residual equation of the general form is

$$\int_\Omega R(\hat{h}) w_i(x, y, z) d\Omega = 0 \tag{C.4}$$

where the Ω is a three-dimensional domain. Substitution for the residual R yields

$$\int_\Omega \left[\phi \frac{\partial \hat{S}}{\partial t} + SS_0^h \frac{\partial \hat{h}}{\partial t} + S\phi\lambda_C \frac{\partial \hat{C}}{\partial t} + \frac{\partial}{\partial x}\left(K_{xx} \frac{\partial \hat{h}}{\partial x} \right) + \frac{\partial}{\partial y}\left(K_{yy} \frac{\partial \hat{h}}{\partial y} \right) + \frac{\partial}{\partial z}\left\{ K_{zz}\left(\frac{\partial \hat{h}}{\partial z} + \lambda_C \hat{C} \right) \right\} + \lambda_c \left[\left(K_{xx} \frac{\partial \hat{h}}{\partial x} \right) \frac{\partial \hat{C}}{\partial x} + \left(K_{yy} \frac{\partial \hat{h}}{\partial y} \right) \frac{\partial \hat{C}}{\partial y} + \left\{ K_{zz}\left(\frac{\partial \hat{h}}{\partial z} + \lambda_C \hat{C} \right) \right\} \frac{\partial \hat{C}}{\partial z} \right] - Q_\rho \right] w_i(x, y, z) d\Omega = 0 \tag{C.5}$$

When applying Gauss's theorem, the equation will be expanded as

$$\int_{\Omega}\Bigg[-\phi\frac{\partial\hat{S}}{\partial t}w_i - SS_0^h\frac{\partial\hat{h}}{\partial t}w_i - S\phi\lambda_C\frac{\partial\hat{C}}{\partial t}w_i + K_{xx}\frac{\partial\hat{h}}{\partial x}\frac{\partial w_i}{\partial x} + K_{yy}\frac{\partial\hat{h}}{\partial y}\frac{\partial w_i}{\partial y}$$
$$+\left\{K_{zz}\left(\frac{\partial\hat{h}}{\partial z}+\lambda_C\hat{C}\right)\right\}\frac{\partial w_i}{\partial z} -$$
$$\lambda_c\left[\left(K_{xx}\frac{\partial\hat{h}}{\partial x}\right)\frac{\partial\hat{C}}{\partial x}+\left(K_{yy}\frac{\partial\hat{h}}{\partial y}\right)\frac{\partial\hat{C}}{\partial y}+\left\{K_{zz}\left(\frac{\partial\hat{h}}{\partial z}+\lambda_C\hat{C}\right)\right\}\frac{\partial\hat{C}}{\partial z}\right]w_i + Q_\rho w_i\Bigg]d\Omega \qquad \text{(C.6)}$$
$$+\int_{\Gamma}\left[K_{xx}\frac{\partial\hat{h}}{\partial x}n_x + K_{yy}\frac{\partial\hat{h}}{\partial y}n_y + \left\{K_{zz}\left(\frac{\partial\hat{h}}{\partial z}+\lambda_C\hat{C}\right)\right\}n_z\right]w_i d\Gamma = 0$$

where n_x, n_y, and n_z are the components of the inward normal at the boundary. In making the substitution, it was multiplied by -1.

We can now substitute the interpolation function of a regular cubic in three dimensions such as $\hat{h}=\sum_{j=1}^{8}\hat{h}_j w_j$, $\hat{C}=\sum_{j=1}^{8}\hat{C}_j w_j$, and $\hat{S}=\sum_{j=1}^{8}\hat{S}_j w_j$ for the variable $\hat{h}$, $\hat{C}$, and $\hat{S}$. Then, Equation (C.6) becomes

$$\int_{\Omega}\Bigg[-\phi\hat{S}_j\frac{\partial w_j}{\partial t}w_i - SS_0^h\hat{h}_j\frac{\partial w_j}{\partial t}w_i - S\phi\lambda_C\hat{C}_j\frac{\partial w_j}{\partial t}w_i + K_{xx}\hat{h}_j\frac{\partial w_j}{\partial x}\frac{\partial w_i}{\partial x} + K_{yy}\hat{h}_j\frac{\partial w_j}{\partial y}\frac{\partial w_i}{\partial y}$$
$$+\left\{K_{zz}\left(\hat{h}_j\frac{\partial w_j}{\partial z}+\lambda_C\hat{C}_j w_j\right)\right\}\frac{\partial w_i}{\partial z} -$$
$$\lambda_c\left[\begin{array}{l}\left(K_{xx}\hat{h}_j\frac{\partial w_j}{\partial x}\right)\hat{C}_j\frac{\partial w_j}{\partial x}+\left(K_{yy}\hat{h}_j\frac{\partial w_j}{\partial y}\right)\hat{C}_j\frac{\partial w_j}{\partial y}+\\ \left\{K_{zz}\left(\hat{h}_j\frac{\partial w_j}{\partial z}+\lambda_C\hat{C}_j w_j\right)\right\}\hat{C}_j\frac{\partial w_j}{\partial z}\end{array}\right]w_i - Q_\rho w_i\Bigg]d\Omega + \qquad \text{(C.7)}$$
$$\int_{\Gamma}\left[K_{xx}\hat{h}_j\frac{\partial w_j}{\partial x}n_x + K_{yy}\hat{h}_j\frac{\partial w_j}{\partial y}n_y + \left\{K_{zz}\left(\hat{h}_j\frac{\partial w_j}{\partial z}+\lambda_C\hat{C}_j w_j\right)\right\}n_z\right]w_i d\Gamma = 0$$

In Equation (C.7), the unknown variables, $\hat{C}$ and $\hat{S}$, are required to be computed at the previous iteration to solve for $\hat{h}$. The approximation of nonlinear terms, $\hat{C}_j\frac{\partial w_j}{\partial x}$,

$\hat{C}_j \frac{\partial w_j}{\partial y}$, and $\hat{C}_j \frac{\partial w_j}{\partial z}$, is evaluated at the local center of each element. They are obtained as follows

$$\begin{aligned}
\hat{C}_j \frac{\partial w_j}{\partial x} &= \sum_{k=1}^{8} \frac{\hat{C}_j}{8a} \xi_j (1+\eta_j \eta)(1+\zeta_j \zeta) = \sum_{k=1}^{8} \frac{\hat{C}_j}{8a} \xi_j \\
\hat{C}_j \frac{\partial w_j}{\partial y} &= \sum_{k=1}^{8} \frac{\hat{C}_j}{8b} (1+\xi_j \xi) \eta_j (1+\zeta_j \zeta) = \sum_{k=1}^{8} \frac{\hat{C}_j}{8b} \eta_j \\
\hat{C}_j \frac{\partial w_j}{\partial z} &= \sum_{k=1}^{8} \frac{\hat{C}_j}{8c} (1+\xi_j \xi)(1+\eta_j \eta) \zeta_j = \sum_{k=1}^{8} \frac{\hat{C}_j}{8c} \zeta_j
\end{aligned} \tag{C.8}$$

Similarly, the term, $\hat{C}_j w_j$, can be approximated at the center of the element:

$$\sum_{j=1}^{8} \hat{C}_j w_j = \sum_{j=1}^{8} \frac{\hat{C}_j}{8} (1+\xi_j \xi)(1+\eta_j \eta)(1+\zeta_j \zeta) = \sum_{j=1}^{8} \frac{\hat{C}_j}{8} \tag{C.9}$$

Lastly, the term $\hat{S}_j \frac{\partial w_j}{\partial t}$ is estimated based on the method proposed by Rathfelder and Abriola [1994].

C.2 The Darcy Equation (Momentum Equation)

After solving the hydraulic heads at nodal points, the Darcy equation is used to determine velocities. Conventionally, these velocities are obtained by taking the derivative of the approximate hydraulic head field. In this method, the partial derivatives of the hydraulic head in the Darcy equation are numerically evaluated for all nodes within an element (i.e., Local smoothing of velocity fields by Kolditz et al. [1998]). Thus, different values of velocities are obtained at a node due to the nodal connectivity. This approach naturally yields a discontinuity in velocities at nodal points and element boundaries. If continuity is to be achieved, the nodal gradient must be treated as an

unknown, which increases computational burden. An alternative technique by Yeh [1981] to compute the continuous velocities without significantly increasing computational cost is to implement the same finite element method to solve the Darcy equation.

Substitution of the known approximate hydraulic head field and concentration field in Equation (4.4) yields

$$q_x = -K_{xx}\frac{\partial}{\partial x}\left(\sum_{k=1}^{N}\hat{h}_k w_k\right) - K_{xy}\frac{\partial}{\partial y}\left(\sum_{k=1}^{N}\hat{h}_k w_k\right) - K_{xz}\left[\frac{\partial}{\partial z}\left(\sum_{k=1}^{N}\hat{h}_k w_k\right) + \lambda_C\left(\sum_{k=1}^{N}\hat{C}_k w_k\right)\right] \tag{C.10a}$$

$$q_y = -K_{yx}\frac{\partial}{\partial x}\left(\sum_{k=1}^{N}\hat{h}_k w_k\right) - K_{yy}\frac{\partial}{\partial y}\left(\sum_{k=1}^{N}\hat{h}_k w_k\right) - K_{yz}\left[\frac{\partial}{\partial z}\left(\sum_{k=1}^{N}\hat{h}_k w_k\right) + \lambda_C\left(\sum_{k=1}^{N}\hat{C}_k w_k\right)\right] \tag{C.10b}$$

$$q_z = -K_{zx}\frac{\partial}{\partial x}\left(\sum_{k=1}^{N}\hat{h}_k w_k\right) - K_{zy}\frac{\partial}{\partial y}\left(\sum_{k=1}^{N}\hat{h}_k w_k\right) - K_{zz}\left[\frac{\partial}{\partial z}\left(\sum_{k=1}^{N}\hat{h}_k w_k\right) + \lambda_C\left(\sum_{k=1}^{N}\hat{C}_k w_k\right)\right] \tag{C.10c}$$

The residual function for Equation (C.10), which is the same for y and z direction, can be written as,

$$\begin{aligned} R(x,y,z,t) = q_x &+ K_{xx}\frac{\partial}{\partial x}\left(\sum_{k=1}^{N}\hat{h}_k w_k\right) + K_{xy}\frac{\partial}{\partial y}\left(\sum_{k=1}^{N}\hat{h}_k w_k\right) \\ &+ K_{xz}\left[\frac{\partial}{\partial z}\left(\sum_{k=1}^{N}\hat{h}_k w_k\right) + \lambda_C\left(\sum_{k=1}^{N}\hat{C}_k w_k\right)\right] \end{aligned} \tag{C.11}$$

The Galerkin method weighs this residual over the whole domain using basis functions as the weighing function to yield

$$\int_{\Omega}\left[V_x + K_{xx}\frac{\partial}{\partial x}\left(\sum_{k=1}^{N}\hat{h}_k w_k\right) + K_{xy}\frac{\partial}{\partial y}\left(\sum_{k=1}^{N}\hat{h}_k w_k\right) + K_{xz}\left[\frac{\partial}{\partial z}\left(\sum_{k=1}^{N}\hat{h}_k w_k\right) + \lambda_C\left(\sum_{k=1}^{N}\hat{C}_k w_k\right)\right]\right] w_i d\Omega = 0 \tag{C.12}$$

When the approximate solution of each velocity is substituted in the velocity term, the equation yields the following form:

$$\int_{\Omega}\left(\sum_{j=1}^{N}\hat{V}_x w_j\right) w_i d\Omega + \int_{\Omega}\left[K_{xx}\frac{\partial}{\partial x}\left(\sum_{k=1}^{N}\hat{h}_k w_k\right) + K_{xy}\frac{\partial}{\partial y}\left(\sum_{k=1}^{N}\hat{h}_k w_k\right) + K_{xz}\left[\frac{\partial}{\partial z}\left(\sum_{k=1}^{N}\hat{h}_k w_k\right) + \lambda_C\left(\sum_{k=1}^{N}\hat{C}_k w_k\right)\right] w_i d\Omega = 0 \tag{C.13}$$

The element matrix of integrals can be written in the following form:

$$\left[A^e\right]\left\{\hat{V}_x\right\} = \left\{B^e\right\} \tag{C.14}$$

where

$$\left[\hat{A}^e\right] = \int_{\Omega^e} w_j w_i d\Omega^e \tag{C.15}$$

$$\left\{B^e\right\} = -\int_{\Omega^e}\left[K_{xx}\frac{\partial}{\partial x}\left(\sum_{k=1}^{N}\hat{h}_k w_k\right) + K_{xy}\frac{\partial}{\partial y}\left(\sum_{k=1}^{N}\hat{h}_k w_k\right) + K_{xz}\left[\frac{\partial}{\partial z}\left(\sum_{k=1}^{N}\hat{h}_k w_k\right) + \lambda_C\left(\sum_{k=1}^{N}\hat{C}_k w_k\right)\right]\right] w_i d\Omega^e = 0 \tag{C.16}$$

C.3 Contaminant Transport Equation

The transport equation from Equation (4.7) can be expanded to yield

$$\begin{aligned}
&\phi\frac{\partial C}{\partial t}+(1-\phi)\alpha_h C\frac{\partial h}{\partial t}+q_x\frac{\partial C}{\partial x}+q_y\frac{\partial C}{\partial y}+q_z\frac{\partial C}{\partial z}\\
&-\frac{\partial}{\partial x}\left(D^*_{xx}\frac{\partial C}{\partial x}+D^*_{xy}\frac{\partial C}{\partial y}D^*_{xz}\frac{\partial C}{\partial z}\right)-\frac{\partial}{\partial y}\left(D^*_{yx}\frac{\partial C}{\partial x}+D^*_{yy}\frac{\partial C}{\partial y}D^*_{yz}\frac{\partial C}{\partial z}\right)\\
&-\frac{\partial}{\partial z}\left(D^*_{zx}\frac{\partial C}{\partial x}+D^*_{zy}\frac{\partial C}{\partial y}D^*_{zz}\frac{\partial C}{\partial z}\right)+CQ_\rho=Q_C
\end{aligned}\qquad \text{(C.17)}$$

where $D^*_{ij}=\phi D_{ij}$ and $q_i=\phi V_i$ is the Darcy velocity.

The interpolation function is defined as

$$C(t,x,y,z)\approx\hat{C}=\sum_{j=1}^{n}C_j(t)w_j(x,y,z)\qquad \text{(C.18)}$$

Substituting the interpolation function into Equation (C.17) yields the residual function in the form as

$$\begin{aligned}
R\left(\hat{C}\right)&=\phi\frac{\partial\hat{C}}{\partial t}+(1-\phi)\alpha_h\hat{C}\frac{\partial h}{\partial t}+q_x\frac{\partial\hat{C}}{\partial x}+q_y\frac{\partial\hat{C}}{\partial y}+q_z\frac{\partial\hat{C}}{\partial z}\\
&-\frac{\partial}{\partial x}\left(D^*_{xx}\frac{\partial\hat{C}}{\partial x}+D^*_{xy}\frac{\partial\hat{C}}{\partial y}D^*_{xz}\frac{\partial\hat{C}}{\partial z}\right)-\frac{\partial}{\partial y}\left(D^*_{yx}\frac{\partial\hat{C}}{\partial x}+D^*_{yy}\frac{\partial\hat{C}}{\partial y}D^*_{yz}\frac{\partial\hat{C}}{\partial z}\right)\\
&-\frac{\partial}{\partial z}\left(D^*_{zx}\frac{\partial\hat{C}}{\partial x}+D^*_{zy}\frac{\partial\hat{C}}{\partial y}D^*_{zz}\frac{\partial\hat{C}}{\partial z}\right)+\hat{C}Q_\rho=Q_C
\end{aligned}\qquad \text{(C.19)}$$

The weighted residual equation of the general form for the Galerkin finite element method is

$$\int_\Omega R(\hat{C})w_i(x,y,z)d\Omega=0\qquad \text{(C.20)}$$

where the Ω is a three-dimensional domain. Substitution for the residual *R* yields

$$\int_{\Omega}\Bigg[\phi\frac{\partial\hat{C}}{\partial t}+(1-\phi)\alpha_h\hat{C}\frac{\partial\hat{h}}{\partial t}+q_x\frac{\partial\hat{C}}{\partial x}+q_y\frac{\partial\hat{C}}{\partial y}+q_z\frac{\partial\hat{C}}{\partial z}$$
$$-\frac{\partial}{\partial x}\left(D_{xx}^*\frac{\partial\hat{C}}{\partial x}+D_{xy}^*\frac{\partial\hat{C}}{\partial y}D_{xz}^*\frac{\partial\hat{C}}{\partial z}\right)-\frac{\partial}{\partial y}\left(D_{yx}^*\frac{\partial\hat{C}}{\partial x}+D_{yy}^*\frac{\partial\hat{C}}{\partial y}D_{yz}^*\frac{\partial\hat{C}}{\partial z}\right) \qquad (C.21)$$
$$-\frac{\partial}{\partial z}\left(D_{zx}^*\frac{\partial\hat{C}}{\partial x}+D_{zy}^*\frac{\partial\hat{C}}{\partial y}D_{zz}^*\frac{\partial\hat{C}}{\partial z}\right)+\hat{C}Q_\rho-Q_C\Bigg]w_i d\Omega=0$$

Applying the Gauss theorem, the equation is expanded as

$$\int_{\Omega}\Bigg[-\phi\frac{\partial\hat{C}}{\partial t}w_i-(1-\phi)\alpha_h\hat{C}\frac{\partial\hat{h}}{\partial t}w_i-q_x\frac{\partial\hat{C}}{\partial x}w_i-q_y\frac{\partial\hat{C}}{\partial y}w_i-q_z\frac{\partial\hat{C}}{\partial z}w_i$$
$$+D_{xx}^*\frac{\partial\hat{C}}{\partial x}\frac{\partial w_i}{\partial x}+D_{xy}^*\frac{\partial\hat{C}}{\partial y}\frac{\partial w_i}{\partial x}+D_{xz}^*\frac{\partial\hat{C}}{\partial z}\frac{\partial w_i}{\partial x}+D_{yx}^*\frac{\partial\hat{C}}{\partial x}\frac{\partial w_i}{\partial y}+D_{yy}^*\frac{\partial\hat{C}}{\partial y}\frac{\partial w_i}{\partial y}+D_{yz}^*\frac{\partial\hat{C}}{\partial z}\frac{\partial w_i}{\partial y}$$
$$+D_{zx}^*\frac{\partial\hat{C}}{\partial x}\frac{\partial w_i}{\partial z}+D_{zy}^*\frac{\partial\hat{C}}{\partial y}\frac{\partial w_i}{\partial z}+D_{zz}^*\frac{\partial\hat{C}}{\partial z}\frac{\partial w_i}{\partial z}-\hat{C}Q_\rho w_i+Q_C w_i\Bigg]$$
$$+\int_{\Gamma}D_n^*\frac{\partial\hat{C}}{\partial n}w_i d\Gamma=0 \qquad (C.22)$$

Similar to the method provided in the flow equation, the substitution of the interpolation function produces,

$$\int_{\Omega}\Bigg[-\phi\hat{C}_j\frac{\partial w_j}{\partial t}w_i-(1-\phi)\alpha_h\hat{C}_j w_j\hat{h}_j\frac{\partial w_j}{\partial t}w_i-q_x\hat{C}_j\frac{\partial w_j}{\partial x}w_i-q_y\hat{C}_j\frac{\partial w_j}{\partial y}w_i-q_z\hat{C}_j\frac{\partial w_j}{\partial z}w_i$$
$$+D_{xx}^*\hat{C}_j\frac{\partial w_j}{\partial x}\frac{\partial w_i}{\partial x}+D_{xy}^*\hat{C}_j\frac{\partial w_j}{\partial y}\frac{\partial w_i}{\partial x}+D_{xz}^*\hat{C}_j\frac{\partial w_j}{\partial z}\frac{\partial w_i}{\partial x}+D_{yx}^*\hat{C}_j\frac{\partial w_j}{\partial x}\frac{\partial w_i}{\partial y}$$
$$+\hat{C}_j D_{yy}^*\frac{\partial w_j}{\partial y}\frac{\partial w_i}{\partial y}+D_{yz}^*\hat{C}_j\frac{\partial w_j}{\partial z}\frac{\partial w_i}{\partial y}$$
$$+\hat{C}_j D_{zx}^*\frac{\partial w_j}{\partial x}\frac{\partial w_i}{\partial z}+D_{zy}^*\hat{C}_j\frac{\partial w_j}{\partial y}\frac{\partial w_i}{\partial z}+D_{zz}^*\hat{C}_j\frac{\partial w_j}{\partial z}\frac{\partial w_i}{\partial z}-Q_\rho\hat{C}_j w_j w_i+Q_C w_i\Bigg]$$
$$+\int_{\Gamma}D_n^*\hat{C}_j\frac{\partial w_j}{\partial n}w_i d\Gamma=0 \qquad (C.23)$$

C.4 Analytical integration

Element integration after transformation to local coordinates is not generally evaluated by analytical integration because the integrands are complicated nonlinear functions of local coordinates. In these cases, the determinant of the Jacobian matrix in the transformation between global and local coordinates is not constant. However, for the brick element (tri-linear element) used in this study, analytical integration is often a handy way for element integration when both corresponding axes of two coordinates are parallel each other so that the determinant of the Jacobian matrix is constant. In other words, analytical integration can be made when numerical idealization is made only with regular brick elements. For irregular brick elements, numerical integration (i.e., Gauss quadrature) is required.

The general mapping from local (ξ,η,ζ) coordinates to Cartesian (x,y,z) coordinates is mathematically expressed by

$$\begin{aligned} x &= f_1(\xi,\eta,\zeta) \\ y &= f_2(\xi,\eta,\zeta) \\ z &= f_3(\xi,\eta,\zeta) \end{aligned} \tag{C.24}$$

Naturally, we wish a point with local coordinates(ξ,η,ζ) to have a unique set of global coordinates (x,y,z). Thus we require that throughout the element domain Ω^e, the coordinates (x,y,z) be single-valued functions of the (ξ,η,ζ). Also the (ξ,η,ζ) is required to be solvable as a single-valued functions of the (x,y,z):

$$\begin{aligned} \xi &= f_4(x,y,z) \\ \eta &= f_5(x,y,z) \\ \zeta &= f_6(x,y,z) \end{aligned} \tag{C.25}$$

The element equations contain the derivatives of the interpolation function with respect to the global coordinates system (x,y,z). However, these interpolation functions are typically written in the local coordinate system (ξ,η,ζ). Derivatives in these two coordinate systems are related through the chain rule of differentiation,

$$\begin{aligned}\frac{\partial}{\partial\xi} &= \frac{\partial}{\partial x}\frac{\partial x}{\partial\xi} + \frac{\partial}{\partial y}\frac{\partial y}{\partial\xi} + \frac{\partial}{\partial z}\frac{\partial z}{\partial\xi} \\ \frac{\partial}{\partial\eta} &= \frac{\partial}{\partial x}\frac{\partial x}{\partial\eta} + \frac{\partial}{\partial y}\frac{\partial y}{\partial\eta} + \frac{\partial}{\partial z}\frac{\partial z}{\partial\eta} \\ \frac{\partial}{\partial\zeta} &= \frac{\partial}{\partial x}\frac{\partial x}{\partial\zeta} + \frac{\partial}{\partial y}\frac{\partial y}{\partial\zeta} + \frac{\partial}{\partial z}\frac{\partial z}{\partial\zeta}\end{aligned} \tag{C.26}$$

Written in the matrix form, the equation become

$$\begin{Bmatrix}\frac{\partial}{\partial\xi} \\ \frac{\partial}{\partial\xi} \\ \frac{\partial}{\partial\xi}\end{Bmatrix} = \mathbf{J}\begin{Bmatrix}\frac{\partial}{\partial x} \\ \frac{\partial}{\partial y} \\ \frac{\partial}{\partial z}\end{Bmatrix} \tag{C.27}$$

where the Jacobian matrix for a coordinate conversion in three dimensions has the following form

$$\mathbf{J} = \begin{bmatrix}\frac{\partial x}{\partial\xi} & \frac{\partial y}{\partial\xi} & \frac{\partial z}{\partial\xi} \\ \frac{\partial x}{\partial\eta} & \frac{\partial y}{\partial\eta} & \frac{\partial z}{\partial\eta} \\ \frac{\partial x}{\partial\zeta} & \frac{\partial y}{\partial\zeta} & \frac{\partial z}{\partial\zeta}\end{bmatrix} \tag{C.28}$$

For an element of size 2*a* by 2*b* by 2*c* in the relationship that two corresponding coordinates are parallel each other as shown in Figure C.1, the relationship between two coordinates is given by

$$\begin{aligned} \xi &= (x - x_c)/a \\ \eta &= (y - y_c)/b \\ \zeta &= (z - z_c)/c \end{aligned} \tag{C.29}$$

where (x_c, y_c, z_c) are the coordinates at the center of the element.

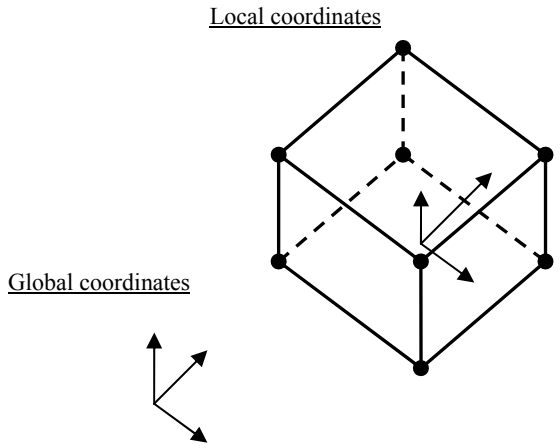

Figure C. 1 Diagram of two parallel coordinates

Thus, we have

$$\frac{d\xi}{dx} = \frac{1}{a}, \quad \frac{d\eta}{dy} = \frac{1}{b}, \quad \frac{d\zeta}{dz} = \frac{1}{c} \tag{C.30}$$

and an elemental volume of the rectangular parallelepiped element is given as

$$dxdydz = abc\, d\xi d\eta d\zeta \tag{C.31}$$

Thus, to integrate any function $f(x,y,z)$ over the element, we transform to the local coordinate system such that

$$\iiint_{\Omega^e} f(x,y,z)dxdydz = \int_{-1}^{1}\int_{-1}^{1}\int_{-1}^{1} f(\xi,\eta,\zeta)abc\, d\xi d\eta d\zeta \tag{C.32a}$$

or

$$\iiint_{\Omega^e} f(x,y,z)dxdydz = \int_{-1}^{1}\int_{-1}^{1}\int_{-1}^{1} f(\xi,\eta,\zeta)\det \mathbf{J}\, d\xi d\eta d\zeta \tag{C.32b}$$

In addition, expression for the derivatives of regular brick elements can be simplified as

$$\begin{aligned}
\frac{\partial w_i}{\partial x} &= \frac{\partial w_i}{\partial \xi}\frac{\partial \xi}{\partial x} = \frac{1}{a}\frac{\partial w_i}{\partial \xi} \\
\frac{\partial w_i}{\partial y} &= \frac{\partial w_i}{\partial \eta}\frac{\partial \eta}{\partial y} = \frac{1}{b}\frac{\partial w_i}{\partial \eta} \\
\frac{\partial w_i}{\partial z} &= \frac{\partial w_i}{\partial \zeta}\frac{\partial \zeta}{\partial z} = \frac{1}{c}\frac{\partial w_i}{\partial \zeta}
\end{aligned} \tag{C.33}$$

Using Equation (C.33), an example of analytical integration for the derivative with respect to x can be made as

$$\begin{aligned}
\iiint_{\Omega^e} \frac{\partial f(x,y,z)}{\partial x} &= \int_{-1}^{1}\int_{-1}^{1}\int_{-1}^{1}\left(\frac{1}{a}\frac{\partial f(\xi,\eta,\zeta)}{\partial \xi}\right)\det \mathbf{J}\, d\xi d\eta d\zeta \\
&= \int_{-1}^{1}\int_{-1}^{1}\int_{-1}^{1}\left(\frac{\partial f(\xi,\eta,\zeta)}{\partial \xi}\right)(bc)\, d\xi d\eta d\zeta
\end{aligned} \tag{C.34}$$

where the determinant, **J,** is *abc,* which is constant and makes the analytical integration possible.

C.5 Time Marching Schemes

As an example for time marching schemes, contaminant transport equation (i.e., parabolic equation) after the Galerkin finite element formulation can be expressed as

$$[M_{\text{conductance}}]\{C\}+[M_{mass}]\left\{\frac{dC}{dt}\right\}=\{\mathbf{F}\} \tag{C.35}$$

where the conductance matrix $[M_{\text{conductance}}]=[M_{Diffusion}]+[M_{Advection}]$ and $[M_{\text{mass}}]$ is the mass storage matrix for a time derivative.

The most commonly used method for the parabolic equation is the α family of approximations, in which a weighted average of the time derivative of a dependent variable is approximated at two consecutive time steps by linear interpolation of the values of the variable at the two steps:

$$\alpha\left\{\frac{dC}{dt}\right\}_{s+1}+(1-\alpha)\left\{\frac{dC}{dt}\right\}_{s}=\frac{\{C\}_{s+1}-\{C\}_{s}}{\Delta t_{s+1}} \qquad for\ 0\le\alpha\le 1 \tag{C.36}$$

where $\{\ \}_s$ s refers the value of the enclosed quantity at time $t=t_s=\sum_{i=1}^{s}\Delta t_i$, and $\Delta t_s=t_s-t_{s-1}$ is the sth time step. If the time interval [0, T0] is divided into equal time steps then $t_s=s\Delta t$.

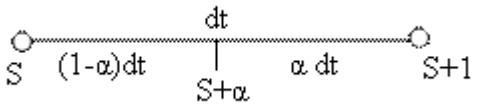

Figure C. 2 Diagram for time schemes

From Taylor's series, the evaluation of C at $S+\alpha$ in Figure C.2 can be expressed in two ways:

$$C_{S+\alpha}(t) = C_S(t_0) + (1-\alpha)\ dt\ f(t_0, C(t_0)) + \frac{((1-\alpha)\,dt)^2}{2!} f'(t_0, C(t_0)) + \ldots\ldots \quad \text{(C.37)}$$

$$C_{S+\alpha}(t) = C_{S+1}(t_1) - \alpha\ dt\ f(t_1, C(t_1)) + \frac{(-\alpha\ dt)^2}{2!} f'(t_1, C(t_1)) + \ldots\ldots \quad \text{(C.38)}$$

Ignoring higher order terms from the second order derivative in Equation (C.37) and (C.38) and subtracting Equation (C.38) by Equation (C.37), we yield

$$\alpha\ f(t_1, C(t_1)) + (1-\alpha) f(t_0, C(t_0)) = \frac{C_{S+1}(t_1) - C_S(t_0)}{dt} \quad \text{(C.39)}$$

For different values of α, we obtain the following well-known numerical integration schemes:

$$\alpha = \begin{cases} 0, & \text{the forward difference (or Euler) scheme}: \mathrm{O}(\Delta t) \\ \dfrac{1}{2}, & \text{the Crank - Nicolson scheme (stable)}: \mathrm{O}((\Delta t)^2) \\ 1, & \text{the backward difference scheme (stable)}; \mathrm{O}(\Delta t) \end{cases}$$

Equation (C.36) can be used to reduce the ordinary differential equations, Equation (C.35), to algebraic equations among the *C* at time *t*s+1. Since Equation (C.35) is valid for any $t > 0$, it is valid for $t = t$s and $t = t$s+1:

$$\left[M_{\text{conductance}}\right]_s \{C\}_s + \left[M_{mass}\right]\left\{\frac{dC}{dt}\right\}_s = \{\mathbf{F}\}_s \quad \text{at time step } t = t\text{s} \quad \text{(C.40)}$$

$$\left[M_{\text{conductance}}\right]_{s+1} \{C\}_{s+1} + \left[M_{mass}\right]\left\{\frac{dC}{dt}\right\}_{s+1} = \{\mathbf{F}\}_{s+1} \quad \text{at time step } t = t\text{s}+1 \quad \text{(C.41)}$$

where it is assumed that the mass matrix $\left[M_{\text{mass}}\right]$ is independent of time. We multiply both sides of Equation (C.35) with $\left[M_{\text{mass}}\right]$ and obtain

$$\alpha\left[M_{mass}\right]\left\{\frac{dC}{dt}\right\}_{s+1} + (1-\alpha)\left[M_{mass}\right]\left\{\frac{dC}{dt}\right\}_s = \frac{\left[M_{mass}\right]\{C\}_{s+1} - \left[M_{mass}\right]\{C\}_s}{\Delta t_{s+1}} \quad \text{(C.42)}$$

Substituting for $[M_{\text{mass}}]\left\{\frac{dC}{dt}\right\}_{s+1}$ and $[M_{\text{mass}}]\left\{\frac{dC}{dt}\right\}_{s}$ from Equation (C.40) and (C.41) into Equation (C.42), we obtain

$$\alpha\left(\{\mathbf{F}\}_{s+1}-[M_{\text{conductance}}]_{s+1}\{C\}_{s+1}\right)+(1-\alpha)\left(\{\mathbf{F}\}_{s}-[M_{\text{conductance}}]_{s}\{C\}_{s}\right)=\frac{[M_{mass}]\{C\}_{s+1}-[M_{mass}]\{C\}_{s}}{\Delta t_{s+1}} \tag{C.43}$$

Rearranging the terms into known and unknown ones, finally we obtain

$$\left(\alpha[M_{\text{conductance}}]_{s+1}+\frac{[M_{mass}]}{\Delta t_{s+1}}\right)\{C\}_{s+1}=\left((\alpha-1)[M_{\text{conductance}}]_{s}+\frac{[M_{mass}]}{\Delta t_{s+1}}\right)\{C\}_{s}+(1-\alpha)\{\mathbf{F}\}_{s}+\alpha\{\mathbf{F}\}_{s+1} \tag{C.44}$$

If $\{F\}$ and mass matrix, $[M_{\text{mass}}]$, are invariant over time and Δt is constant, we have in the simplified form as follows:

$$\left(\alpha[M_{\text{conductance}}]_{s+1}+\frac{[M_{mass}]}{\Delta t}\right)\{C\}_{s+1}=\left((\alpha-1)[M_{\text{conductance}}]_{s}+\frac{[M_{mass}]}{\Delta t}\right)\{C\}_{s}+\{\mathbf{F}\} \tag{C.45}$$

C.6 The Free Exit Boundary Condition (Type IV)

The natural boundary term generated through the Gauss theorem in transport equation is found in Equation (C.23). In three dimensions, the term is expanded as

$$\int_{\Gamma} D_n^* \hat{C}_j \frac{\partial w_j}{\partial n} w_i d\Gamma = \hat{C}_j \int_{\Gamma}\left(D_{xx}\frac{\partial w_j}{\partial x}n_x + D_{xy}\frac{\partial w_j}{\partial y}n_x + D_{xz}\frac{\partial w_j}{\partial z}n_x + D_{yx}\frac{\partial w_j}{\partial x}n_y + D_{yy}\frac{\partial w_j}{\partial y}n_y + D_{zz}\frac{\partial w_j}{\partial z}n_y + D_{zx}\frac{\partial w_j}{\partial x}n_z + D_{zy}\frac{\partial w_j}{\partial y}n_z + D_{zz}\frac{\partial w_j}{\partial z}n_z \right) w_i d\Gamma \tag{C.46}$$

We assume trilinear element with basis functions defined as

$$\sum_{j=1}^{8} w_j(\xi,\eta,\zeta) = \sum_{j=1}^{8} \frac{1}{8}(1+\xi_j\xi)(1+\eta_j\eta)(1+\zeta_j\zeta) \qquad j = 1,2,\cdots,8 \quad \text{(C.47)}$$

Letting the right hand side of Equation (C.46) without $\hat{C}_j$ to be $R^e_{E_{ij}}$ produces

$$\begin{aligned} R^e_{E_{ij}} = \int_{E^e} \Bigg(& D_{xx}\left(\frac{\partial w_j}{\partial\xi}\frac{\partial\xi}{\partial x}+\frac{\partial w_j}{\partial\eta}\frac{\partial\eta}{\partial x}+\frac{\partial w_j}{\partial\zeta}\frac{\partial\zeta}{\partial x}\right)n_x + D_{xy}\left(\frac{\partial w_j}{\partial\xi}\frac{\partial\xi}{\partial y}+\frac{\partial w_j}{\partial\eta}\frac{\partial\eta}{\partial y}+\frac{\partial w_j}{\partial\zeta}\frac{\partial\zeta}{\partial y}\right)n_x \\ & + D_{xz}\left(\frac{\partial w_j}{\partial\xi}\frac{\partial\xi}{\partial z}+\frac{\partial w_j}{\partial\eta}\frac{\partial\eta}{\partial z}+\frac{\partial w_j}{\partial\zeta}\frac{\partial\zeta}{\partial z}\right)n_x + D_{yx}\left(\frac{\partial w_j}{\partial\xi}\frac{\partial\xi}{\partial x}+\frac{\partial w_j}{\partial\eta}\frac{\partial\eta}{\partial x}+\frac{\partial w_j}{\partial\zeta}\frac{\partial\zeta}{\partial x}\right)n_y \\ & + D_{yy}\left(\frac{\partial w_j}{\partial\xi}\frac{\partial\xi}{\partial y}+\frac{\partial w_j}{\partial\eta}\frac{\partial\eta}{\partial y}+\frac{\partial w_j}{\partial\zeta}\frac{\partial\zeta}{\partial y}\right)n_y + D_{zz}\left(\frac{\partial w_j}{\partial\xi}\frac{\partial\xi}{\partial z}+\frac{\partial w_j}{\partial\eta}\frac{\partial\eta}{\partial z}+\frac{\partial w_j}{\partial\zeta}\frac{\partial\zeta}{\partial z}\right)n_y \\ & + D_{zx}\left(\frac{\partial w_j}{\partial\xi}\frac{\partial\xi}{\partial x}+\frac{\partial w_j}{\partial\eta}\frac{\partial\eta}{\partial x}+\frac{\partial w_j}{\partial\zeta}\frac{\partial\zeta}{\partial x}\right)n_z + D_{zy}\left(\frac{\partial w_j}{\partial\xi}\frac{\partial\xi}{\partial y}+\frac{\partial w_j}{\partial\eta}\frac{\partial\eta}{\partial y}+\frac{\partial w_j}{\partial\zeta}\frac{\partial\zeta}{\partial y}\right)n_z \\ & + D_{zz}\left(\frac{\partial w_j}{\partial\xi}\frac{\partial\xi}{\partial z}+\frac{\partial w_j}{\partial\eta}\frac{\partial\eta}{\partial z}+\frac{\partial w_j}{\partial\zeta}\frac{\partial\zeta}{\partial z}\right)n_z \Bigg) w_i d\Gamma \end{aligned} \quad \text{(C.48)}$$

From Figure 6.8, with the plane joining nodes 2, 3, 7, and 6 lying on the external boundary, the free exit boundary contribution becomes

$$\begin{aligned} R^e_{E_{ij}} &= 0 && when\ \ i = 2,3,7,and\ 6 \\ R^e_{E_{ij}} &= same\ as\ (C.47) && when\ i = 1,4,8,and\ 5 \end{aligned} \quad \text{(C.49)}$$

Therefore, three-dimensional derivation of the free exit boundary condition is obtained Equations from (C.47) to (C.49). In the exceptional case that the local and global axes are parallel, Equation (C.48) can greatly be simplified. Other than that, it generally requires a numerical integration. TechFlow uses Gauss quadrature for numerical integration.

REFERENCES

Aly, A. H., and P. C. Peralta. Comparison of a genetic algorithm and mathematical programming to the design of groundwater cleanup systems. Water Resources Research **35**:2415-2425, 1999.

Aral, M. M., and J. Guan. Optimal groundwater remediation system design with well locations selected as decision variables. Multimedia Environmental Simulations Laboratory **No. MESL-01-97**:Georgia Tech, Atlanta, Georgia, 1997.

Aral, M. M., J. B. Guan, and M. L. Maslia. Identification of contaminant source location and release history in aquifers. Journal of Hydrologic Engineering **6**:225-234, 2001.

Aral, M. M., M. L. Maslia, and R. C. Williams. Groundwater Remediation Using Smart Pump and Treat - Discussion. Ground Water **31**:680-681, 1993.

ASCE. Saltwater intrusion in the United States. J. Hydraulics Division **95**:no. HY5, 1651-1669, 1969.

Bastian, P., K. Birken, K. Johannsen, S. Lang, N. Neub, H. Rentz-Reichert, and C. Wieners. UG- a flexible software toolbox for solving partial differential equations. Computing and Visualization in Science **1**:27-40, 1997.

Bear, J., Dynamics of fluids in porous media. American Elsevier, New York,, 1972.

Bear, J., Hydraulics of groundwater. McGraw-Hill International Book, New York, 1979.

Bear, J., and Y. Bachmat, Introduction to modeling of transport phenomena in porous media. Kluwer Academic Publishers, Dordrecht ; Boston, 1990.

Bennett, G. D., M. J. Mundorff, and S. A. Hussain. Electric-analog studies of brine coning beneath fresh-water wells in the Punjab region. U.S. Geol. Surv. Water Supply Pap. **1608-J**:J1-J31, 1968.

Benson, D. A., A. E. Carey, and S. W. Wheatcraft. Numerical advective flux in highly variable velocity fields exemplified by saltwater intrusion. Journal of Contaminant Hydrology **34**:207-233, 1998.

Boufadel, M. C. A mechanistic study of nonlinear solute transport in a groundwater-surface water system under steady state and transient hydraulic conditions. Water Resources Research **36**:2549-2565, 2000.

Boufadel, M. C., M. T. Suidan, and A. D. Venosa. Density-dependent flow in one-dimensional variably-saturated media. Journal of Hydrology **202**:280-301, 1997.

Boufadel, M. C., M. T. Suidan, and A. D. Venosa. 2-D variably-saturated flow: Physical scaling and Bayesian estimation. Journal of Hydrologic Engineering **3**:223-231, 1998.

Boufadel, M. C., M. T. Suidan, and A. D. Venosa. A numerical model for density-and-viscosity-dependent flows in two-dimensional variably saturated porous media. Journal of Contaminant Hydrology **37**:1-20, 1999a.

Boufadel, M. C., M. T. Suidan, and A. D. Venosa. Numerical modeling of water flow below dry salt lakes: effect of capillarity and viscosity. Journal of Hydrology **221**:55-74, 1999b.

Brown, D. A., and J. Lemons. Scientific certainty and the laws that govern location of a potential high-level nuclear waste repository. Environmental Management **15**:311-319, 1991.

Buckingham, E. On physically similar systems: Illustrations of the use of dimensional equations. Phys. Rev. **4**:345-376, 1914.

Butow, E., and E. Holzbecher. Proposal for definition of HYDROCOIN level 3 case 4: sensitivity analysis for the flow over a salt dome. HYDROCOIN project:5p, 1986.

Celia, M. A., E. T. Bouloutas, and R. L. Zarba. A General Mass-Conservative Numerical-Solution for the Unsaturated Flow Equation. Water Resources Research **26**:1483-1496, 1990.

Cheng, A. H. D., D. Halhal, A. Naji, and D. Ouazar. Pumping optimization in saltwater-intruded coastal aquifers. Water Resources Research **36**:2155-2165, 2000.

Cheng, A. H. D., and D. Ouazar. Analytical solutions, in Saltwater Intrusion in Coastal Aquifers - Concepts, Methods, and Practices, edited by J. Bear et al. Kluwer Acad.:Norwell, Mass, chap. 6, pp. 163-191, 1999.

Cooper, H. H. A Hypothesis Concerning the Dynamic Balance of Fresh Water and Salt Water in a Coastal Aquifer. Journal of Geophysical Research **64**:461-467, 1959.

Dagan, G., and J. Bear. Solving the problem of local interface upconing in a coastal aquifer by the method of small perturbations. J. of Hydr. Res. **6**, 1968.

Das, A., and B. Datta. Development of management models for sustainable use of coastal aquifers. Journal of Irrigation and Drainage Engineering-Asce **125**:112-121, 1999a.

Das, A., and B. Datta. Development of multiobjective management models for coastal aquifers. Journal of Water Resources Planning and Management-Asce **125**:76-87, 1999b.

Daus, A. D., E. O. Frind, and E. A. Sudicky. Comparative Error Analysis in Finite-Element Formulations of the Advection-Dispersion Equation. Advances in Water Resources **8**:86-95, 1985.

Davis, L., Genetic algorithms and simulated annealing. Pitman ;
Morgan Kaufmann Publishers, LondonLos Altos, Calif., 1987.

Diersch, H. J., and P. Nillert. Saltwater intrusion processes in groundwater: novel computer simulations, field studies and interception techniques. Int. Symp. on Groundwater Monitoring and Management **Dresden, Complex IV**:Paper 13, 17p, 1987.

Diersch, H. J., D. Prochnow, and M. Thiele. Finite-Element Analysis of Dispersion-Affected Saltwater Upconing Below a Pumping Well. Applied Mathematical Modelling **8**:305-312, 1984.

Diersch, H. J. G., and O. Kolditz. Coupled groundwater flow and transport: 2. Thermohaline and 3D convection systems. Advances in Water Resources **21**:401-425, 1998.

Diersch, H. J. G., and O. Kolditz. Variable-density flow and transport in porous media: approaches and challenges. Advances in Water Resources **25**:899-944, 2002.

Dougherty, D. E., and R. A. Marryott. Optimal Groundwater-Management .1. Simulated Annealing. Water Resources Research **27**:2493-2508, 1991.

Elder, J. W. Transient Convection in a Porous Medium. Journal of Fluid Mechanics **27**:609-&, 1967.

Essink, G. H. P. O. Saltwater intrusion in 3D large-scale aquifers: A Dutch case. Physics and Chemistry of the Earth Part B-Hydrology Oceans and Atmosphere **26**:337-344, 2001.

Finney, B. A., Samsuhadi, and R. Willis. Quasi-3-Dimensional Optimization Model of Jakarta Basin. Journal of Water Resources Planning and Management-Asce **118**:18-31, 1992.

Fleming, P. J., and C. M. Fonseca. An overview of evolutionary algorithms in multiobjective optimization. Evolutionary Computation:3 Spring, 1995.

Fonseca, C. M., and P. J. Fleming. Genetic algorithms for multiobjective optimization: formulation, discussion and generalization. In: Forest, S., (Ed.). Genetic Algorithms, Proceedings of the Fifth International Conference:Morgan Kaufmann, Los Altos, CA, pp. 416-423, 1993.

Forsyth, P. A., Y. S. Wu, and K. Pruess. Robust Numerical-Methods for Saturated-Unsaturated Flow with Dry Initial Conditions in Heterogeneous Media. Advances in Water Resources **18**:25-38, 1995.

Frind, E. O. Simulation of long-term transient density-dependent transport in groundwater. Advances in Water Resources **5**:73-78, 1982.

Frind, E. O. Solution of the advection-dispersion equation with free exit boundary. Numerical Methods for Partial Differential Equations **4**:301-313, 1988.

Frolkovic, P. Consistent velocity approximation for density driven flow and transport. In: Van Keer R, et al., editors. ACOMEN'98. Maastricht: Shaker:603-611, 1998.

Frolkovic, P., and H. De Schepper. Numerical modelling of convection dominated transport coupled with density driven flow in porous media. Advances in Water Resources **24**:63-72, 2001.

Goldberg, D. E., Genetic algorithms in search, optimization, and machine learning. Addison-Wesley, Reading, Mass., 1989.

Gorelick, S. M. A Review of Distributed Parameter Groundwater-Management Modeling Methods. Water Resources Research **19**:305-319, 1983.

Gorelick, S. M., C. I. Voss, P. E. Gill, W. Murray, M. A. Saunders, and M. H. Wright. Aquifer Reclamation Design - the Use of Contaminant Transport Simulation Combined with Nonlinear-Programming. Water Resources Research **20**:415-427, 1984.

Guan, J., and M. M. Aral. Optimal remediation with well locations and pumping rates selected as continuous decision variables. Journal of Hydrology **221**:20-42, 1999a.

Guan, J. B., and M. M. Aral. Progressive genetic algorithm for solution of optimization problems with nonlinear equality and inequality constraints. Applied Mathematical Modelling **23**:329-343, 1999b.

Guan, J. B., and M. M. Aral. Optimal design of groundwater remediation systems using fuzzy set theory. Water Resources Research **40**:-, 2004.

Gupta, S. K., C. T. Kincaid, P. R. Meyer, C. A. Newbill, and C. R. Cole. CFEST-multi-dimensional finite-element code for the analysis of coupled fluid, energy and solute transport. Pacific Northwest Laboratory:4260, Richland, 1982.

Hallaji, K., and H. Yazicigil. Optimal management of a coastal aquifer in southern Turkey. Journal of Water Resources Planning and Management-Asce **122**:233-244, 1996.

Hassanizadeh, S. M., and W. G. Gray. General conservation equations for multi-phase systems: 1. Averaging procedure. Advances in Water Resources **2**:131-134, 1979a.

Hassanizadeh, S. M., and W. G. Gray. General conservation equations for multi-phase systems: 2. Mass, momenta, energy, and entropy equations. Advances in Water Resources **2**:191-203, 1979b.

Hassanizadeh, S. M., and A. Leijnse. A Non-Linear Theory of High-Concentration-Gradient Dispersion in Porous-Media. Advances in Water Resources **18**:203-215, 1995.

Henry, H. R. Saltwater intrusion into coastal aquifers. Intern. Ass. Of. Scient. Hydrology Publ. **2**:478-487, 1960.

Henry, H. R. Effects of dispersion on salt encroachment in coastal aquifers. U.S. Geol. Surv. Water Supply Pap. **1613-C**:C71-C84, 1964.

Herbert, A. W., and C. P. Jackson. A study of salt transport in a porous medium: The application of NAMMU to HYDROCOIN level 1 case 5. Rep. AERE **R 12147**:U.K. At. Energy Auth., Harwell Lab., Oxford, Oxfordshire, England, 1986.

Herbert, A. W., C. P. Jackson, and D. A. Lever. Coupled Groundwater-Flow and Solute Transport with Fluid Density Strongly Dependent Upon Concentration. Water Resources Research **24**:1781-1795, 1988.

Hillel, D., Fundamentals of soil physics. Academic Press, New York, 1980.

Holland, J. H., Adaptation in natural and artificial systems : an introductory analysis with applications to biology, control, and artificial intelligence, 1st MIT Press edition. MIT Press, Cambridge, Mass., 1992.

Holzbecher, E. O., Modeling density-driven flow in porous media ; principles, numerics, software. Springer ;, Berlin, 1998.

Hosokawa, T., K. Jinno, and K. Momii. Estimation of transverse dispersivity in the mixing zone of fresh-salt groundwater, in: Kovar, K. (ed.) Calibration and Reliability in Groundwater Modeling. IAHS Publ. **195**:149-158, 1990.

Huang, C. L., and A. S. Mayer. Pump-and-treat optimization using well locations and pumping rates as decision variables. Water Resources Research **33**:1001-1012, 1997.

Huisman, I. L. La formation des cones d'eau saumatre. IUGG **IAHS-Publ.**:No.37, 146-150, 1954.

Huyakorn, P. S., P. F. Andersen, J. W. Mercer, and H. O. White. Saltwater Intrusion in Aquifers - Development and Testing of a 3-Dimensional Finite-Element Model. Water Resources Research **23**:293-312, 1987.

INTERA, E. C. Revision of the documentation for a model for calculating effects of liquid waste disposal in deep saline aquifers. U.S. Geol. Surv. Water Res. Publ.:79-96 72p, 1979.

Javandel, I., C. Doughty, and C.-F. Tsang, Groundwater transport : handbook of mathematical models. American Geophysical Union, Washington, D.C., 1984.

Johannsen, K., W. Kinzelbach, S. Oswald, and G. Wittum. The saltpool benchmark problem - numerical simulation of saltwater upconing in a porous medium. Advances in Water Resources **25**:335-348, 2002.

Johns, R. T., and A. Rivera. Dispersive transport dynamics in a strongly coupled groundwater-brine flow system - Comment. Water Resources Research **32**:3405-3410, 1996.

Kastenberg, W. E., and L. J. Gratton. Hazards of managing and disposing of nuclear waste. Physics Today **50**:41-46, 1997.

Kolditz, O. Benchmarks for numerical groundwater simulations, in: Diersch H. J. FEFLOW User's Manual **Release 4.20**:WASY, Berlin, 5.1-5.129, 1994.

Kolditz, O., R. Ratke, H. J. G. Diersch, and W. Zielke. Coupled groundwater flow and transport .1. Verification of variable density flow and transport models. Advances in Water Resources **21**:27-46, 1998.

Konikow, L. F., and J. D. Bredehoeft. Computer model of two-dimensional solute transport and dispersion in groundwater. U.S. Geol. Surv. Techniques of Water-Res. Invest. **Book 7 Chapter C2**:37, 1978.

Konikow, L. F., W. E. Sanford, and P. J. Campbell. Constant-concentration boundary condition: Lessons from the HYDROCOIN variable-density groundwater benchmark problem. Water Resources Research **33**:2253-2261, 1997.

Krause, R. E., and J. S. Clarke. Coastal ground water at risk - Saltwater contamination at Brunswick, Georgia and Hilton Head island, South Carolina. U.S. Geol. Surv. Water-Res. Invest. **Report 01-4107**:poster, 2001, 2001.

Langer, M., H. Schneider, and K. Kuhn. The salt dome of Gorleben-Target site for the German radioactive waste repository, Geological Problems in Radioactive Waste Isolation, a World-Wide Review. proceedings, workshop W3B, 28th International Geological Congress, edited by P. A. Witherspoon **Rep. LBL-29703**:57-66, Lawrence Berkeley Lab., Berkeley, Calif, 1991.

Lee, C. H., and R. T. S. Cheng. Seawater Encroachment in Coastal Aquifers. Water Resources Research **10**:1039-1043, 1974.

Leijnse, A., and S. M. Hassanizadeh. Verification of the METROPOL code for density dependent flow in porous media: HYDROCOIN Project, level 1, case 5 and level 3, case 4. **Rep. 728528004**:Natl. Inst. of Public Health and Environ. Prot. (RIVM), Bilthoven, Netherlands, 1989.

Ma, T. S., M. Sophocleous, Y. S. Yu, and R. W. Buddemeier. Modeling saltwater upconing in a freshwater aquifer in south-central Kansas. Journal of Hydrology **201**:120-137, 1997.

Marryott, R. A., D. E. Dougherty, and R. L. Stollar. Optimal Groundwater-Management .2. Application of Simulated Annealing to a Field-Scale Contamination Site. Water Resources Research **29**:847-860, 1993.

Mckinney, D. C., and M. D. Lin. Genetic Algorithm Solution of Groundwater-Management Models. Water Resources Research **30**:1897-1906, 1994.

Mckinney, D. C., and M. D. Lin. Approximate Mixed-Integer Nonlinear-Programming Methods for Optimal Aquifer Remediation Design. Water Resources Research **31**:731-740, 1995.

Mendoza, C. A., and E. O. Frind. Advective-Dispersive Transport of Dense Organic Vapors in the Unsaturated Zone .1. Model Development. Water Resources Research **26**:379-387, 1990a.

Mendoza, C. A., and E. O. Frind. Advective-Dispersive Transport of Dense Organic Vapors in the Unsaturated Zone .2. Sensitivity Analysis. Water Resources Research **26**:388-398, 1990b.

Motz, L. H. Salt-Water Upconing in an Aquifer Overlain by a Leaky Confining Bed. Ground Water **30**:192-198, 1992.

Motz, L. H. A Density-Dependent Flow and Transport Analysis of the Effects of Groundwater Development in a Fresh-Water Lens of Limited Areal Extent - the Geneva Area (Florida, USA) Case-Study - Discussion. Journal of Contaminant Hydrology **18**:321-326, 1995.

Muskat, M., and R. D. Wyckoff. An approximate theory of water-coning in oil production. Transactions AIME:144-161, 1935.

Nielsen, P. Tidal Dynamics of the Water-Table in Beaches. Water Resources Research **26**:2127-2134, 1990.

Obayashi, S., T. Tsukahara, and T. Nakamura. Multiobjective genetic algorithm applied to aerodynamic design of cascade airfoils. Ieee Transactions on Industrial Electronics **47**:211-216, 2000.

OECD. The International HYDROCOIN project - Background and results.Paris, 1987.

OECD. The International HYDROCOIN project - level 1: Code verification. ReP. 71617:Paris, 1988.

OECD. The International Hydrocoin Project, level3: Uncertainty and sensitivity analysis. REP. 76319:Paris, 1992.

Oldenburg, C. M., and K. Pruess. Dispersive Transport Dynamics in a Strongly Coupled Groundwater-Brine Flow System. Water Resources Research **31**:289-302, 1995.

Oldenburg, C. M., K. Pruess, and B. J. Travis. Dispersive transport dynamics in a strongly coupled groundwater-brine flow system - Reply. Water Resources Research **32**:3411-3412, 1996.

Oswald, S. E., and W. Kinzelbach. Three-dimensional physical benchmark experiments to test variable-density flow models. Journal of Hydrology **290**:22-42, 2004.

OTA. Office of Technology Assesment, Protection the nation's groundwater from contamination, Washington D.C. **OTA-o-233,224**, 1984.

Panday, S. Mathematical-Modeling of Fresh-Water Saltwater Systems - a Density-Dependent Flow and Transport Analysis of the Effects of Groundwater Development in a Fresh-Water Lens of Limited Areal Extent - the Geneva Area (Florida, USA) Case-Study - Response. Journal of Contaminant Hydrology **18**:327-331, 1995.

Panday, S., P. S. Huyakorn, J. B. Robertson, and B. Mcgurk. A Density-Dependent Flow and Transport Analysis of the Effects of Groundwater Development in a Fresh-Water Lens of Limited Areal Extent - the Geneva Area (Florida, USA) Case-Study. Journal of Contaminant Hydrology **12**:329-354, 1993.

Park, C. H., and M. M. Aral. Multi-objective optimization of pumping rates and well placement in coastal aquifers. Journal of Hydrology **290**:80-99, 2004a.

Park, C.-H., and M. M. Aral. Sensitivity of the solution of Elder problem to density, velocity and other numerical perturbations. Journal of Contaminant Hydrology:submitted, 2004b.

Peralta, R. C., J. Solaimanian, and G. R. Musharrafich. Optimal Dispersed Groundwater Contaminant Management - Modcon Method. Journal of Water Resources Planning and Management-Asce **121**:490-498, 1995.

Philip, J. R. Periodic Nonlinear Diffusion - Integral Relation and Its Physical Consequences. Australian Journal of Physics **26**:513-519, 1973.

Pinder, G. F., and H. H. Cooper. A Numerical Technique for Calculating Transient Position of Saltwater Front. Water Resources Research **6**:875-&, 1970.

Pinder, G. F., and W. G. Gray, Finite element simulation in surface and subsurface hydrology. Academic Press, New York, 1977.

Prasad, A., and C. T. Simmons. Unstable density-driven flow in heterogeneous porous media: A stochastic study of the Elder [1967b] "short heater" problem. Water Resources Research **39**:-, 2003.

Rathfelder, K., and L. M. Abriola. Mass Conservative Numerical-Solutions of the Head-Based Richards Equation. Water Resources Research **30**:2579-2586, 1994.

Reeves, M., D. S. Ward, N. D. Johns, and R. M. Cranwell. Theory and implementation of SWIFT II, the SANDIA waste-isolation flow and transport model for fractured media. Rep. SAND83-1159, Sandia Natl. Lab.:Albuquerque, N. M., 1986.

Reilly, T. E., and A. S. Goodman. Analysis of Saltwater Upconing beneath a Pumping Well. Journal of Hydrology **89**:169-204, 1987.

Rogers, L. L., and F. U. Dowla. Optimization of Groundwater Remediation Using Artificial Neural Networks with Parallel Solute Transport Modeling. Water Resources Research **30**:457-481, 1994.

Rosenberg, E., R. Legmann, A. Kushmaro, R. Taube, and E. Z. Ron. Petroleum Bioremediation - a Multiphase Problem. Journal of Cellular Biochemistry:187-187, 1993.

Sahni, B. M. Physics of brine coning beneath skimming wells. Ground Water **11**:19-24, 1973.

Schmorak, S., and A. Mercado. Upconing of Fresh Water-Sea Water Interface Below Pumping Wells, Field Study. Water Resources Research **5**:1290-&, 1969.

Schotting, R. J., H. Moser, and S. M. Hassanizadeh. High-concentration-gradient dispersion in porous media: experiments, analysis and approximations. Advances in Water Resources **22**:665-680, 1999.

Segol, G. A three-dimensional Galerkin finite-element model for the analysis of contaminant transport in variably saturated-unsaturated porous media. Department of Earth Sciences, University of Waterloo:Waterloo, Canada, 1976.

Segol, G., G. F. Pinder, and W. G. Gray. Galerkin-Finite Element Technique for Calculating Transient Position of Saltwater Front. Water Resources Research **11**:343-347, 1975.

Shamir, U., J. Bear, and A. Gamliel. Optimal Annual Operation of a Coastal Aquifer. Water Resources Research **20**:435-444, 1984.

Shonkwiler, R. Monte Carlo Methods. Math 4225 Class Notes:School of Mathmatics, Georgia Tech, Atlanta, GA, 2000.

Simpson, M. J., and T. P. Clement. Comparison of finite difference and finite element solutions to the variably saturated flow equation. Journal of Hydrology **270**:49-64, 2003.

Smith, A. J. Mixed convection and density-dependent seawater circulation in coastal aquifers. Water Resources Research **40**:-, 2004.

Strack, O. D. L. Some Cases of Interface Flow Towards Drains. Journal of Engineering Mathematics **6**:175-&, 1972.

Strack, O. D. L. Single-Potential Solution for Regional Interface Problems in Coastal Aquifers. Water Resources Research **12**:1165-1174, 1976.

Strobl, R. O., and G. T. Yeh. Two-dimensional modeling of saltwater intrusion, in: Peters A., G. Wittum, B. Herrling, U Meissner, C. A. Brebbia, W. G. Gray, and G. F. Pinder (eds). Comp. Meth. In Water Res. X **Proceedings Vol. 2**:Kluwer Publ. Dordrecht. 1035-1042, 1994.

Swedish Nuclear Power Inspectorate. HYDROCOIN. Progr. Rep. 1 **Stockholm**, 1984.

U.S. Nuclear Regulatory Commission. NRC model simulations in support of the Hydrologic Code Intercomparison Study (HYDROCOIN). Rep. NUREG-1249 **1**:U.S. Nucl. Regul. Comm., Washington, D. C., 1988.

van Genuchten, M. T. A Closed-Form Equation for Predicting the Hydraulic Conductivity of Unsaturated Soils. Soil Science Society of America Journal **44**:892-898, 1980.

Venosa, A. D., M. T. Suidan, B. A. Wrenn, K. L. Strohmeier, J. R. Haines, B. L. Eberhart, D. King, and E. Holder. Bioremediation of an experimental oil spill on the shoreline of delaware bay. Environmental Science & Technology **30**:1764-1775, 1996.

Voss, A., and M. Koch. Numerical simulations of topography-induced saltwater upconing in the state of Brandenburg, Germany. Physics and Chemistry of the Earth Part B-Hydrology Oceans and Atmosphere **26**:353-359, 2001.

Voss, C. I. A FE simulation model for saturated-unsaturated, fluid-density-dependent groundwater flow with energy transport or chemically-reactive single-species solute transport. U.S. Geol. Surv. Water Ressources Invest.:84-4369, 4409p, 1984.

Voss, C. I., and W. R. Souza. Variable Density Flow and Solute Transport Simulation of Regional Aquifers Containing a Narrow Fresh-Water-Saltwater Transition Zone. Water Resources Research **23**:1851-1866, 1987.

Wang, F. C. Approximate Theory for Skimming Well Formulation in Indus Plain of West Pakistan. Journal of Geophysical Research **70**:5055-&, 1965.

Willis, R., and B. A. Finney. Planning-Model for Optimal-Control of Saltwater Intrusion. Journal of Water Resources Planning and Management-Asce **114**:163-178, 1988.

Wirojanagud, P., and R. J. Charbeneau. Salt water upconing in unconfined aquifers. J. Hydraul. Eng. Am. Soc. Civ. Eng. **111**:417-434, 1985.

Witherspoon, P. A. E. Geological problems in radioactive waste isolation, a world-wide review. proceedings, workshop W3B, 28th International Geological Congress **Rep. LBL-29703**:Lawrence Berkeley Lab., Berkeley, Calif., 1991.

Wooding, R. A., S. W. Tyler, and I. White. Convection in groundwater below an evaporating salt lake .1. Onset of instability. Water Resources Research **33**:1199-1217, 1997a.

Wooding, R. A., S. W. Tyler, I. White, and P. A. Anderson. Convection in groundwater below an evaporating salt lake .2. Evolution of fingers or plumes. Water Resources Research **33**:1219-1228, 1997b.

Woods, J. A., M. D. Teubner, C. T. Simmons, and K. A. Narayan. Numerical error in groundwater flow and solute transport simulation. Water Resources Research **39**:-, 2003.

Xiang, Y. Y., J. F. Sykes, and N. R. Thomson. Alternative Formulations for Optimal Groundwater Remediation Design. Journal of Water Resources Planning and Management-Asce **121**:171-181, 1995.

Yabusaki, S. B., C. R. Cole, D. J. Holford, A. M. Monti, and S. K. Gupta. HYDROCOIN level 1: Benchmarking and verification test results with CFEST code. Rep. PNL/SRP-6681:Pac. Northwest Lab., Richland, Wash., 1988.

Yeh, G. T. On the Computation of Darcian Velocity and Mass Balance in the Finite-Element Modeling of Groundwater-Flow. Water Resources Research **17**:1529-1534, 1981.

VITA

The author was born on August 5, 1970 in Suwon, South Korea. He received his Bachelor of Science degree from the department of Mineral and Petroleum Engineering of Hanyang University in Seoul, Korea in February 1997. After his graduation, he became a graduate research and teaching assistant at the department of Civil Engineering of the University of Waterloo, Ontario, Canada where he received his Master of Science in Environmental Engineering in August 1999. Since then, he started his Ph.D. program in the School of Civil and Environmental Engineering of Georgia Institute of Technology in September 1999. He received his Master of Science in Environmental Engineering from the same school in December 2002. His research interests include saltwater intrusion in coastal aquifers, nuclear waste storage, optimization of groundwater, and waterborne pathogen transport in a watershed.